AN ABSTRACT OF THE THESIS OF

Myung Woo Han for the degree of Doctor of Philosophy

in Oceanography presented on October 29, 1987

Title: Dynamics and Chemistry of Pore Fluids in Marine Sediments of Different Tectonic Settings: Oregon Subduction Zone and Bransfield Strait Extensional Basin

Redacted for Privacy

Abstract Approved: Erwin Suess

Pore fluids of marine sediments migrate in response to thermally-induced or tectonically-induced flows, changing their chemical composition characteristically in the process. Case studies of induced pore fluid flow are presented in this thesis and their geochemical significance are discussed in four chapters. First, the anomalous pore water chemistry in the thickly sedimented eastern end of the King George Basin, Bransfield Strait, indicate strong hydrothermalism. The Bransfield Strait is a marginal basin located between the Antarctic Peninsula and the South Shetland Islands with active submarine volcanism. At all stations, both dissolved chloride and the sum of the major cations (Σ Na, Mg, Ca, K) greatly increase in the pore waters. These concentration profiles indicate that an end-member hydrothermal solution formed during seawater-basalt interaction, and was subsequently mixed with unreacted seawater during its upward migration in the sediment column. Secondly, the chemical and morpho-tectonic evidences in this basin are used to simulate a circulation model in which pore fluids move laterally across the basin from the south to the north at an average rate of 7 cm/yr. The lateral flow is fed from a recharge area through fault planes along the topographically lower southern margin of the basin where bottom water is drawn down, and discharges along the topographically higher margin in the north.

Thirdly, pore fluid venting, associated with subduction-induced sediment deformation across the active continental margin off Oregon and Washington, precipitates carbonate minerals such as is evident in carbonate chimneys and in cementation of the accreted sediments. Significant downcore depletion of interstitial Ca as well as a reduction of porosity coincide with carbonate mineral cementation. The carbonate precipitation is likely to be explained by migration and oxidation of methane and by the increase in carbonate saturation due to the release of excess pore pressure during pore fluid venting. Rates of up to 28 cm/yr are predicted from a diagenetic model applied to the vertical distribution of dissolved Ca and ammonium. Finally, this thesis presents a two-dimensional temperature distribution for the underthrust portion of the Oregon accretionary complex. A thermal model, assuming confined flow of pore fluids, yields heat fluxes that best fit the measured data across the complex. The model assumes restricted pathways of fluids and a flow rate of 20 cm/yr. The pathways are predicted along the decollement plane and along the major fault planes dipping landward in the marginal ridge. The predicted confined flow rate agrees with the measured flow rate directly over a vent site, 20 to 50 cm/yr (Suess et al., 1987a).

DYNAMICS AND CHEMISTRY OF PORE FLUIDS IN MARINE SEDIMENTS OF DIFFERENT TECTONIC SETTINGS: OREGON SUBDUCTION ZONE AND BRANSFIELD STRAIT EXTENSIONAL BASIN

by

Myung Woo Han

A THESIS

submitted to

Oregon State University

in partial fulfillment of

the requirements for the

degree of

Doctor of Philosophy

Completed October 29, 1987

Commencement June 1988

APPROVED:

Redacted for Privacy

Professor of Oceanography in charge of Major

Redacted for Privacy

Dean of College of Oceanography

Redacted for Privacy

Dean of Graduate School

Date thesis is presented October 29, 1987

Typed by Myung Woo Han and Sue Pullen

To my father

ACKNOWLEDGEMENTS

I wish to express my deep appreciation to my major professor, Dr. Erwin Suess, for his support, encouragement, and guidance that allowed me to complete this work. His integrity, warmth, compassion, and intellectual style will serve as models for me. I wish to thank Drs. Vern Kulm and Nick Pisias for their reviews on my thesis drafts. Their suggestions, though painful, improved my thesis a lot.

I particularly wish to thank Andy Ungerer for his constant help in nearly all phases of my study and life in Corvallis. The Prime computer system manager David Mandel's help is also gratefully acknowledged. Many thanks go to Marta von Breymann, Bobbi Conard, Amy Harrison, and Andy Ungerer for their help with laboratory work. I am indebted to Mrs. Jackie Poppleton for her mother-like help for me. I am also grateful for the friendship I shared with Katie Howard, Zhenlin Li, and Jim McDougall. Their support made me get through smoothly.

I thank my parents, parents-in-law, my brothers and sisters for their prayers for my well-being far away home. I am also grateful to Dr. Shi-Hyo Lee who has taken care of my family's health with no charge at all. Finally, my deepest gratitude goes to my wife Inyang, and my daughters, Ipsae and Serom; their love, encouragement, patience, and sacrifice were essential.

This study was supported by ONR grant N00014-84-C-0218, NSF grants OCE-8215147, DPP-8512395 and OCE-8609789. I thank the Alfred-Wegener-Institute for Polar Research in Bremerhaven, Federal Republic of Germany for allowing me to participate in the Antarctic Leg IV cruise to the Bransfield Strait on board *PRSV POLARSTERN*. I gratefully acknowledge financial support from the Oregon State University Foundation for my trips to Brazil and Federal Republic of Germany.

TABLE OF CONTENTS

LIST OF FIGURES

GENERAL INTRODUCTION

CHAPTER I

CHAPTER II

CHAPTER III

CHAPTER IV

LIST OF TABLES

CHAPTER I

CHAPTER III

CHAPTER IV

DYNAMICS AND CHEMISTRY OF PORE FLUIDS IN MARINE SEDIMENTS OF DIFFERENT TECTONIC SETTINGS: OREGON SUBDUCTION ZONE AND BRANSFIELD STRAIT EXTENSIONAL BASIN

GENERAL INTRODUCTION

This study addresses the dynamics of pore fluid migration and the chemistry of pore fluids in marine sediments from two contrasting tectonic settings: (1) the extensional back-arc basin in the Bransfield Strait, Antarctica, where thermally-driven fluids escape and interact with organic-rich basin sediments, and (2) the plate subduction zone along the Oregon continental margin where tectonically-driven fluids escape and interact with hemipelagic sediments of the accretionary complex. The importance of this study lies in the recognition that even slow pore fluid venting may significantly impact the dissolved mass flux from sediments to the ocean and vice versa when a large area of the total ocean floor is involved (Figs G-1 and G-2). Therefore, it is important to recognize different environments where pore fluid advection occurs in marine sediments and estimate its contribution to the overall global exchange process of elements between the geosphere and the hydrosphere.

Significant pore fluid advection in marine sediments was first reported from flanks of mid-ocean ridges (MOR) (Anderson et al., 1979; Maris and Bender, 1982; Sayles and Jenkins, 1982). The driving force of this fluid migration is well-known and directly related to the thermal energy escaping at MOR systems. The area of the combined MOR-system, however, is limited. The total area of the ocean floor, subject to pore fluid advection, has recently been expanded to include subduction zones. Strong evidence for pore fluid venting at this tectonic environment has been reported

Figure G-1

Fluid circulation zones and fluid flow processes in the crust. (Modified and expanded after COSOD-II, a position paper prepared for the meeting in Strasbourg, France, July 1987)

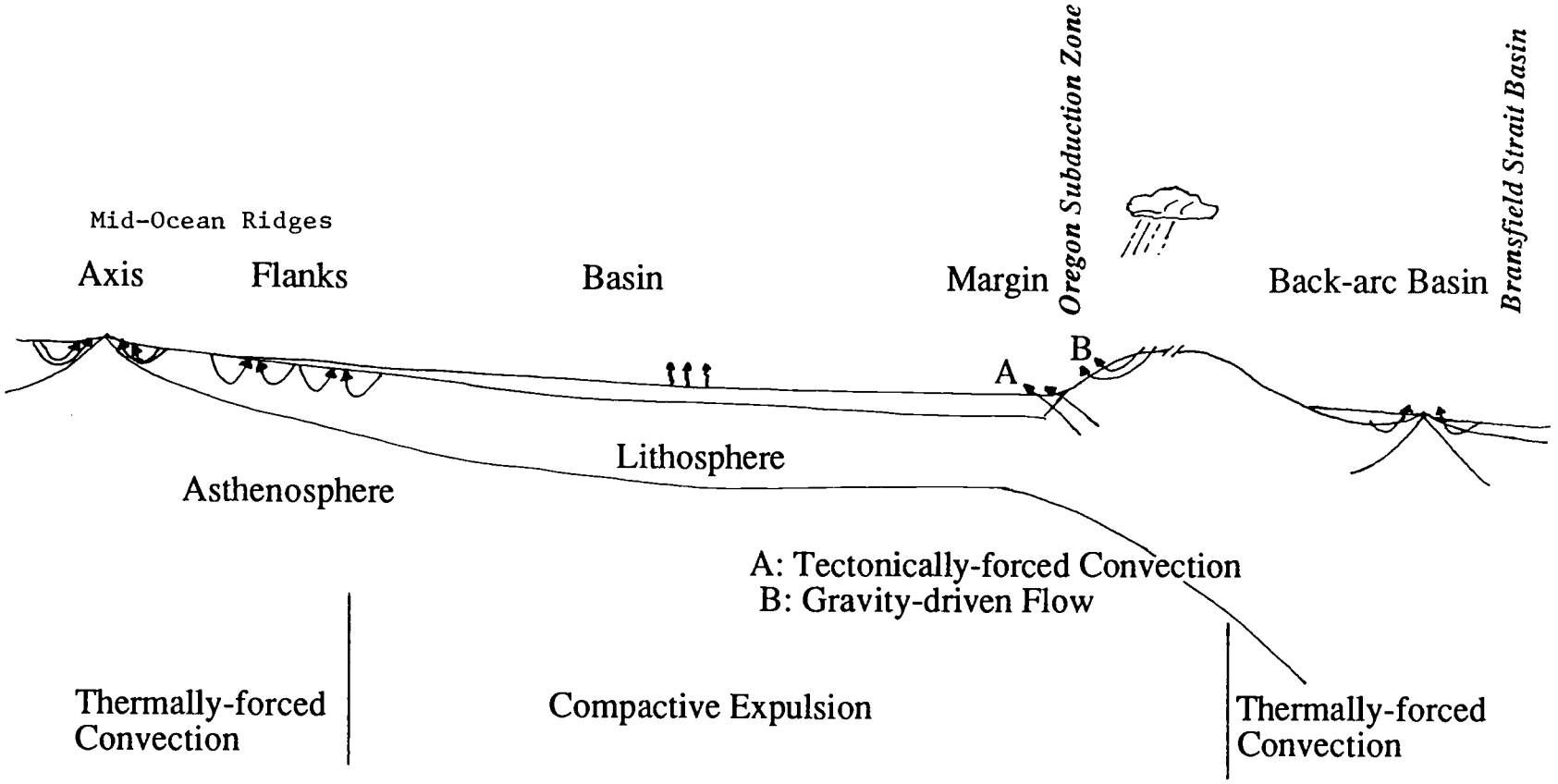
Mid-Ocean Ridges
Axis
Flanks
Basin
Margin
Oregon Subduction Zone
Back-arc Basin
Bransfield Strait Basin
A
B
Lithosphere
Asthenosphere
A: Tectonically-forced Convection
B: Gravity-driven Flow
Thermally-forced Convection
Compactive Expulsion
Thermally-forced Convection

Figure G-1

Figure G-2

Estimates of the flux of seawater through or out of the various hydrodynamic zones in Fig. G-1, and the physical processes driving fluid circulation. (After COSOD-II, a position paper prepared for the meeting in Strasbourg, France, July 1987)

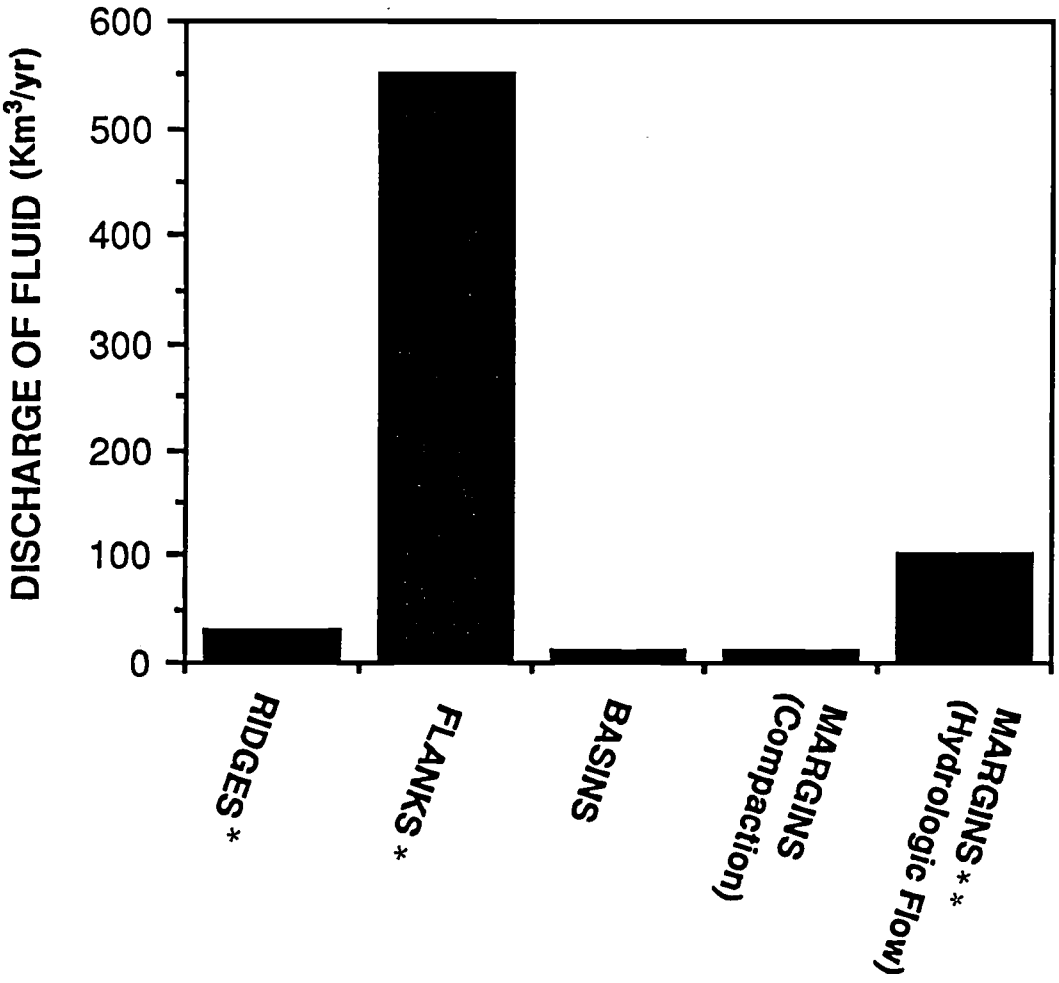

* Includes unknown discharge from back-arc basin.
** Includes unknown discharge from tectonically-forced convection.

Figure G-2

on accretionary complexes of the world's active margins (Kulm et al., 1986; Moore et al., 1986a; Cadet et al., 1987; Kastner et al., 1987). Excess pore pressure, built up by the tectonic stresses from plate convergence along subduction zones, is believed to expel fluids in these areas.

The existence of pore fluid advection in sediments has been verified mainly through downcore profiles of temperature and pore water chemistry. Non-linear profiles of temperature and pore water chemistry with depth have been attributed to pore fluid advection. Generally convex- and concave-upward shapes of concentration gradients indicate upward and downward pore fluid advections, respectively (Anderson et al., 1979; Maris and Bender, 1982; Sayles and Jenkins, 1982). However, evidence for pore fluid advection obtained by these methods contains large uncertainties and has often been contradictory as there are several problems with these verifying tools.

Diffusivities of chemical species, generally in the magnitude of 10^{-6} cm^2 /sec, are two to three orders of magnitude less than thermal diffusivities. Transport of chemical species thus tends to be more affected by irregularities in the surrounding media than transport of heat does. Therefore, temperature profiles in sediments are better suited for diagnosing pore fluid advection. Non-linear temperature profiles, however, do not necessarily imply pore fluid advection. They can equally be generated by other factors such as irregular bottom topography, changes in bottom water temperature, variable bottom water current, sedimentation effects, slumping, erosion, etc. (Noel, 1984). For profiles of pore water chemistry, in-situ production or consumption of some species by early diagenesis of organic matter may "cloud" the evidence for fluid advection. Profiles of non-reactive elements such as helium can avoid such problems, but measurement of their concentrations are difficult to obtain.

Despite all of these drawbacks, temperature and pore water chemistry, (other than direct measurements of flow rate (Suess et al., 1987a) or pore pressure (Schultheiss

and McPhail, 1986)), are still the unique tools available to diagnose pore fluid advection because they are the tracers directly affected by pore fluid migration. Two-dimensional distribution patterns of these tracers greatly improve evidence for pore fluid advection. They are superior to simple downcore profiles of temperature and pore water chemistry, which often lack areal coverage for any particular tectonic setting.

In this thesis two-dimensional distribution patterns of both tracers -- temperature and pore water chemistry -- have been established to show the extent of pore water advection in marine sediments of an extensional basin (Bransfield Strait) and a plate subduction zone (Oregon accretionary complex). The two tectonic end-member settings are suitable examples for estimation of rates of pore fluid advection. Systematic acquisition of pore water samples across the Bransfield Strait extensional basin established the spatial distribution pattern of pore water chemistry for both reactive and non-reactive species. In the Oregon subduction zone, two-dimensional temperature distributions were numerically simulated. An added advantage of establishing two-dimensional distribution patterns for these tracers is that they reveal fluid migration pathways which have rarely been investigated in marine sediments other than through fabric analysis (Moore et al., 1986b). This thesis not only proves the existence of pore fluid advection but also delineates the pathways of fluid flow and brackets the ranges of flow rates in both areas.

This thesis is divided into four chapters. Two chapters address hydrothermalism in the Bransfield Strait extensional basin and two chapters are devoted to fluid venting processes in the Oregon subduction zone. Chapter I deals with the anomalous chemistry of pore fluids resulting from hydrothermal reactions in sediments of the Bransfield Strait basin. A new way of presenting pore water chemistry data is developed which sums up the anomalies of the major cations relative to seawater. This method proves to be diagnostic of hydrothermal seawater-basalt reactions. The degree

of mixing between hydrothermal pore fluids and the bottom water of the Bransfield Strait basin is calculated from the pore fluid composition. Chapter II deals with movement of the hydrothermal pore fluids through the basin sediments. A lateral migration model of the hydrothermal pore fluids, from the southern to the northern margin of the extensional basin, is proposed in this chapter. This model is based on numerical simulation of the interstitial chloride distribution. This type of horizontal fluid flow has not previously been observed.

Chapter III deals with prominent carbonate mineral precipitation in the sediments of the Oregon/Washington accretionary complex. The pore fluid data discussed in this chapter show that the carbonate precipitation is a direct consequence of pressure release associated with pore fluid venting from the complex. This process is responsible for an overall lithification of the sediments by carbonate cement and the construction of peculiar carbonate edifices above the sea floor. The range of predicted flow rates of fluids upward through the deformed sediments is related to the type of calcium carbonate lithification, i.e. slow rates generate cement only and fast rates result in chimney formation. The uptake of dissolved calcium by the sediments of the accretionary complex allows speculation on the global calcium balance. With this consideration a new transfer pathway is defined which removes calcium directly from the oceanic crust to the accreted sediments via pore fluids without circulating through the ocean water reservoir. In Chapter IV the thermal structure of the Oregon accretionary complex is numerically simulated. The constraints of this model are in the form of measured heat flow distribution across a portion of the complex and three scenarios of heat transfer: no fluid advection (i.e., conduction only), uniform advection, and confined advection. The model which best fits the measured heat flow data assumes a restricted pathway of fluid flow of no wider than 0.5 km and a flow rate of 20 cm/yr.

CHAPTER I

HYDROTHERMAL PORE FLUIDS FROM A SEDIMENTED BACK-ARC BASIN: BRANSFIELD STRAIT, ANTARCTICA

ABSTRACT

Hydrothermal activity is clearly evident in the anomalous pore water chemistry of the thickly sedimented eastern end of the King George Basin of the Bransfield Strait, a marginal basin formed by back-arc spreading between the Antarctic Peninsula and the South Shetland Islands. Both chloride and the sum of the major cations (Σ Na, Mg, Ca, K) show significant enrichments downcore at all stations. In contrast, neither chloride nor the sum of the major cations shows any change with depth in the central basin, an area not affected by hydrothermalism. Differences in pore water chemistry between the eastern end and the central part of the basin are also found in other interstitial species such as SO_4, NH_3, PO_4, SiO_2, alkalinity, and total CO_2. These differences are less pronounced than those of the major ions because of direct involvement of these species in early diagenesis.

The pore water chemistry of major seawater ions in the eastern end of the basin appears to be influenced by end-member hydrothermal solutions formed during seawater-basalt interaction subsequently mixing with unreacted seawater in the sediment column. Basalt hydration enriches Na and Cl equally at some sites, however, large variations in the concentrations of major cations at other sites does not rule out retrograde dissolution of basalt. Both basalt hydration and retrograde alteration/dissolution occur only at low temperatures and are therefore likely to be the reactions by which the hydrothermal solutions are generated.

INTRODUCTION

Hydrothermal emanations from both sediment-starved and sediment-filled ridge crest systems, in the form of hot vents (from Corliss et al., 1979 to recently Rona et al., 1986), plumes (Lonsdale and Becker, 1985; Weiss et al., 1977) and giga plumes (Baker et al., 1987; Cann and Strens, 1987) are now well-documented and have revolutionized our concepts of basalt-seawater interaction and geochemical budgets in the ocean as these fluxes generate new sources and sinks for the transport of elements (Edmond et al., 1979; Thompson 1983; Von Damm et al., 1985a). Hydrothermal activity not manifested by such violent and spectacular features, however, is thought to be quite common from the wide-spread occurrence of altered oceanic crust (Alt et al., 1986; Staudigel et al., 1981; Muehlenbachs and Clayton, 1972; Spooner et al., 1974; Hart, 1973). The extent of net mass transport of elements during such low-temperature alteration is much less certain. Hydrothermal circulation probably occurs over ridge flanks until an appreciable sediment cover has accumulated (Sclater et al., 1976; Anderson et al., 1977). Hydrothermal mineralization (Bertine and Keene, 1975; Bonatti et al., 1979) and high-temperature hydrothermal discharge (Horibe et al., 1986; Uyeda, 1987) were also found recently from the back-arc basins in the western Pacific. Futhermore recent reports on pore fluid venting in subduction zones (Kulm et al., 1986; Moore et al., 1986a; Cadet et al., 1987) and speculations on rejuvenation of hydrothermal activity near the outer trenches where the plates bulge (Caldwell and Turcotte, 1979) suggest other tectonic settings of low-temperature hydrothermal circulation. Therefore, such off-ridge processes may also result in significant chemical mass exchange and may be equally important in geochemical budget as high-temperature on-ridge processes are.

In this paper we document the effects of low-temperature hydrothermal activity superimposed on the pore fluid composition typical for anoxic diagenesis of

organic-rich, hemipelagic sediments. Anomalous pore water chemistry was detected as shallow as 5 m in cores of the King George Basin, Antarctica, an actively spreading back-arc basin. Such shallow anomalies suggest upward migration and mixing of pore fluids generated at depth by hydrothermalism underneath the thickly sedimented basin floor. The low-temperature hydrothermal activity is probably similar to that in sedimented MOR-flanks.

Much of the low-temperature basalt-seawater interaction appears to occur at depths normally as deep as 5 Km within the oceanic crust (Hart and Staudigel, 1979). Such interaction is reflected in the pore water chemistry from sedimented MOR flanks (Maris et al., 1984; Bender et al., 1985) or from plate areas where the oceanic crust is completely sealed by sediments (Mottl et al., 1983; Lawrence et al., 1975; McDuff, 1981; McDuff and Gieskes, 1976). Commonly the anomalous pore water chemistry is treated separately for each element. This proved ambiguous and a support for actual fluid migration required very often heat flow data (i.e. high heat flow = discharge area and low heat flow = recharge area) (Maris et al., 1984; Bender et al., 1985).

With our data from the Bransfield Strait basin we take a new approach of presenting pore water chemical anomalies, which convincingly shows the evidence for hydrothermal reaction and migration without the support of heat flow data, although such data would greatly contribute towards the overall understanding of the system. We consider the chemical composition of pore fluids to result from mixing between three reservoirs: unaltered seawater, hydrothermal water, and pore water affected by early diagenesis. This allows us to identify the processes responsible for the generation of the end-member hydrothermal solutions.

GEOLOGIC SETTING

The King George Basin is one of several morpho-tectonic depressions along the

Bransfield Strait. The strait was probably formed by back-arc spreading separating the South Shetland Islands chain in the north from the Antarctic Peninsula in the south (Figs. I-1a,b). Spreading has been documented over the last 1.4 m.y. (Roach, 1978; Barker and Dalziel, 1983; Guterch et al., 1985). Prominent normal faults along the northern and southern margins run southwest to northeast, parallel to the strike of the Bransfield Strait. In the deep King George Basin normal faults develop, at least at present, predominantly along the southern basin margins (Fig. I-1c). They expose scarps as their surface expression, variable sediment thicknesses and syn-sedimentary deformation, attesting to active rifting in the basin (Chapter II).

The basin, 60 km wide and 2 km deep, has a smooth floor covered by thick turbidites, but punctuated by volcanoes and numerous dike intrusions (Fig. I-1d). The total sediment thickness in the basin is about 450 to 500 m (Guterch et al., 1985; Theilen, 1986). The sediment cover, which thickens southeastward and consists of turbidite layers which dip in the same direction, is believed to be generated from the Antarctic Peninsula and to a degree controlled by the prominent fault distribution in the south (Fig. I-1c).

The basin, located underneath the most fertile waters of the circumpolar ocean, receives abundant marine organic matter and diatomaceous silica derived from plankton, benthic algae from the shallow shelf region as well as glacial sediments of volcanogenic composition predominantly by turbidity currents (Suess et al., 1987b; Wefer et al., 1982). Distinctive and correlatable turbidite layers across the basin are thus interlayered with sediments of a more hemipelagic type. The rate of sedimentation in the basin is very rapid ranging from 260 to 460 cm/1000 yrs, based on ^{210}Pb (Mangini, unpubl. data) and ^{14}C - activities (Erlenkeuser, unpubl. data). Resuspension of shelf-derived sediment and settling in deeper waters is evident from sediment trap deployments (Gersonde and Wefer, 1987). This process contributes to the high rates

Figure I-1a

The Antarctic continent and the area of investigation, the Bransfield Strait.

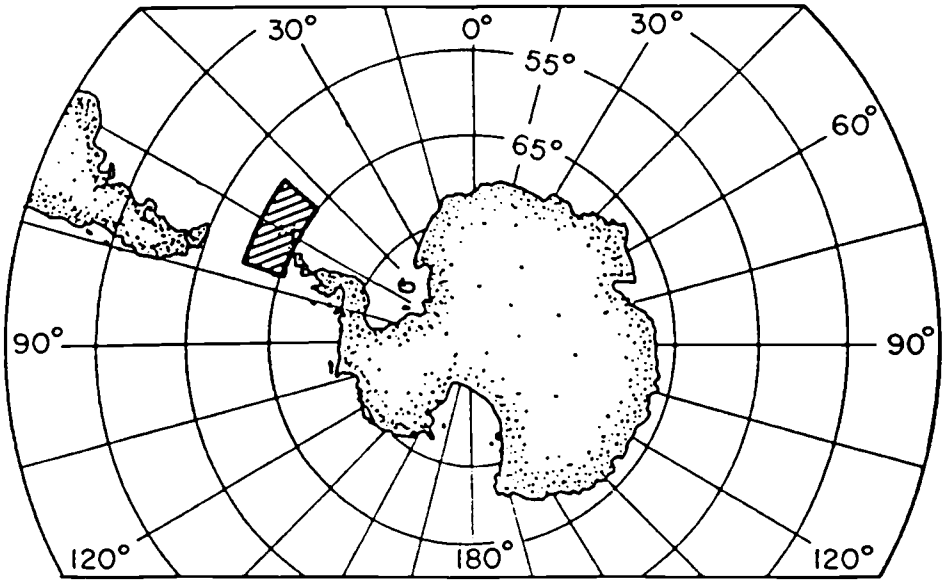

Figure I-1a

Figure I-1b

Regional tectonic map of the Bransfield Strait, Antarctica (above). The Bransfield Strait was formed by back-arc spreading separating the Shetland Islands chain in the north from the Antarctic Peninsula in the south. Subduction of the Drake plate into Shetland trench initiated the spreading behind the Shetland Island arc. The study area of the King George Basin in the Bransfield Strait is marked by a square (below). NAZ = Nazca plate, SAM = South American plate, AFR = African plate, ANT = Antarctic plate, SF = Shakleton Fracture zone, HF = Hero Fracture zone.

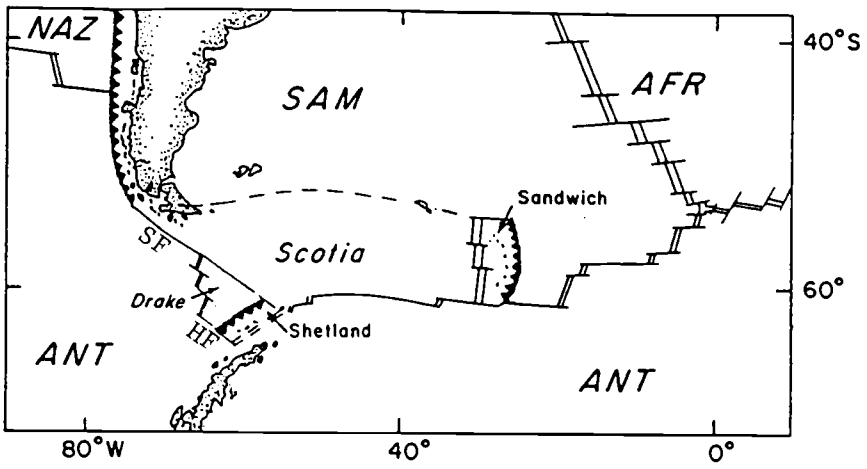
NAZ
SAM
AFR
40°S
Sandwich
SF
Scotia
Drake
HF
Shetland
60°
ANT
ANT
80°W
40°
0°

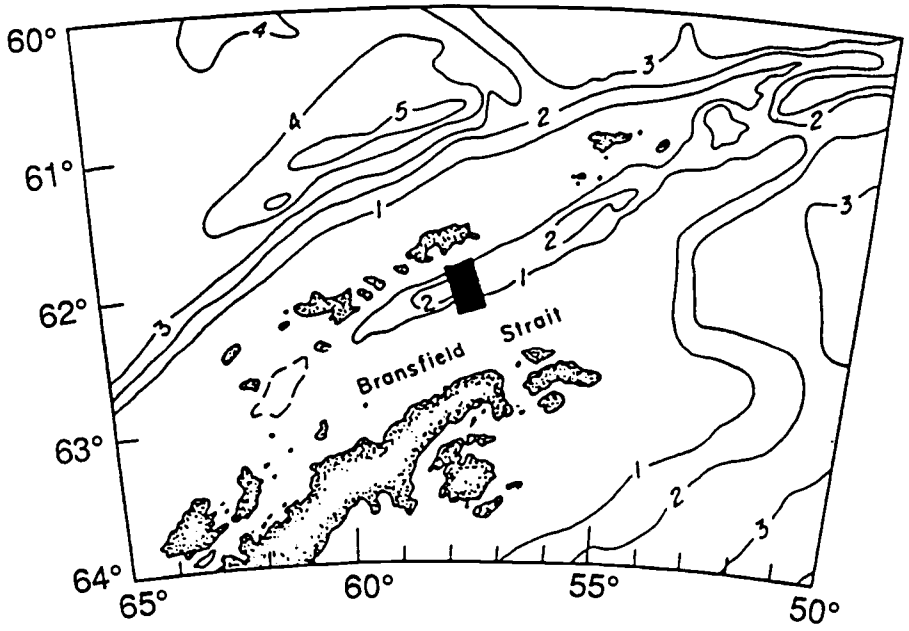
60°
61°
62°
63°
64°
65°
60°
55°
50°
Bransfield
Strait
1
2
3
4
5

Figure I-1b

of sedimentation. Downslope slumping associated with the extensional faulting, is probably another cause for exceptionally high sedimentation rate. High organic carbon accumulation rate, 9.6 gC/m^2yr, can be attributed to high seasonal primary production and a very high degree of organic matter preservation in these rapily accumulating, strongly anoxic sediments (Suess et al., 1987b).

Besides the volcanic activity observed as recently as the 1970s at Deception Island (Roobol, 1982), which is located along the axis of the Bransfield Strait with the projected intersection of the Hero Fracture Zone, submarine volcanism has been detected in the King George Basin. The major submarine volcanoes show an arch distribution from north to south at the eastern side of the basin forming a 'volcanic wall' on the southeastern side (Figs. I-1c,d). An area of very pronounced acoustic turbidity develops concentrically toward the center of the basin from the eastern 'volcanic wall' (Fig. I-1c). Two new sea mounts were discovered during our 1985 survey and subsequent dredging of fresh basalts and pillow basalts as well as the encounter of hydrothermal petroleum in our cores from within the acoustic turbidity zone all attest to vigorous ongoing volcanic activity (Suess et al., 1987b).

Sediment-covered hydrothermal systems have many unique characteristics which are not usually found in sediment-starved MOR systems. The Guaymas Basin, the best studied among these, shows the following features: (1) generation of hydrothermal petroleum (Simoneit and Lonsdale, 1982), (2) massive sill-injection into the sediment column (Einsele et al., 1980), (3) greenschist facies metamorphism of the sediments (Von Damm et al., 1985b), and (4) plumes of methane and heavier hydrocarbon compounds in the water column (Lonsdale and Becker, 1985). The King George Basin shows these features as well, however, modified in one way or another and of different intensity and magnitude than the Guaymas Basin.

Figure I-1c

Sedimentary and tectonic features in the King George Basin. In the deep King George Basin normal faults develop predominantly along the southern basin margins. The sediment cover thickens southeastward. Circular contours indicate major submarine volcanoes which are predominantly distributed in the northeastern and eastern end of the basin. Note the area of acoustic turbidity adjacent to the submarine volcanoes. "Hydrothermal" core stations, 1346 (Δ), 1340 (O), 1341(◊) and 1343 (+), are located within the acoustic turbidity zone. A "reference" core station, 1327 (*), is located in the central basin.

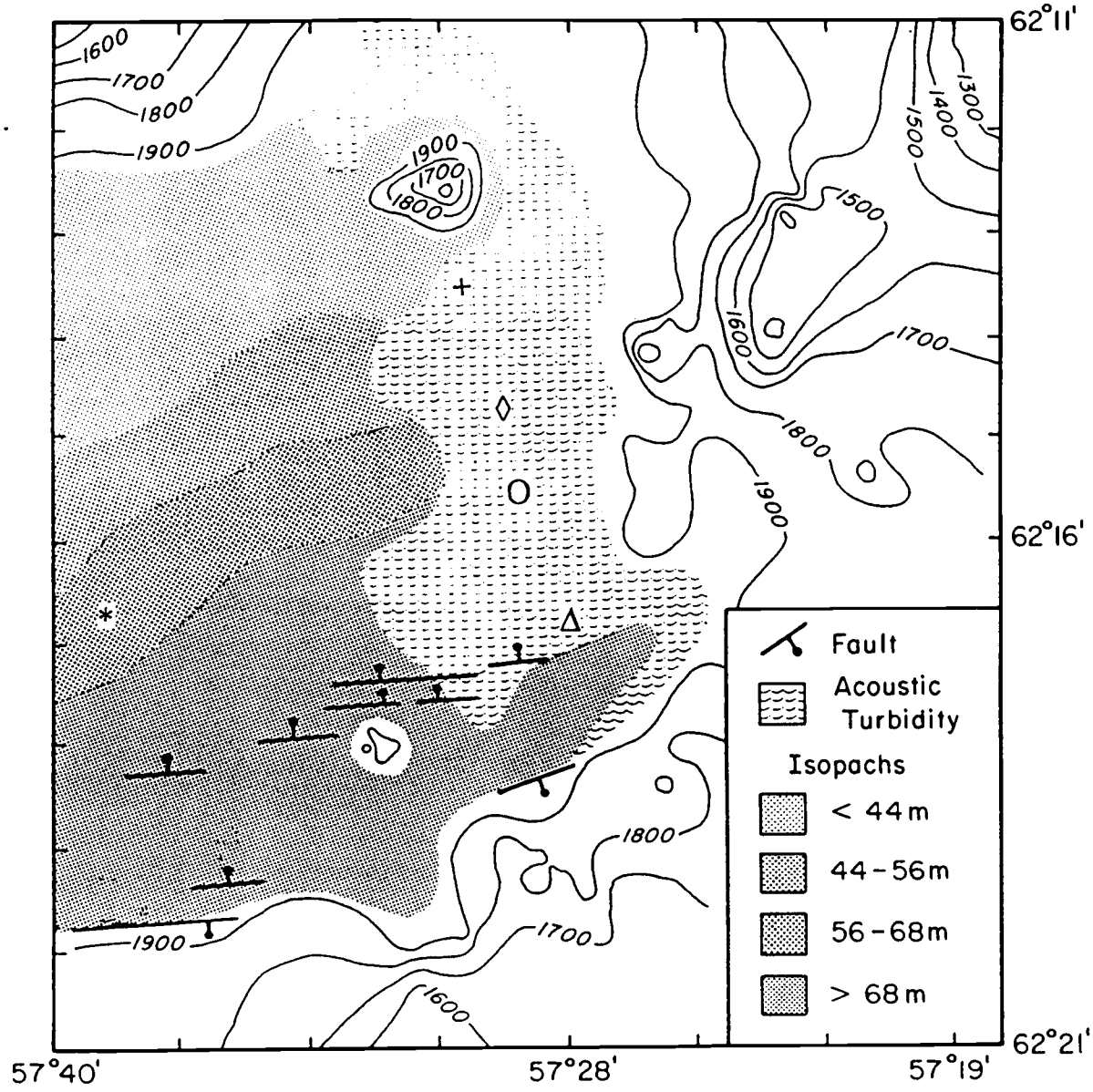
62°11'
62°16'
62°21'
57°40'
57°28'
57°19'
1600
1700
1800
1900
1300
1400
1500
Fault
Acoustic Turbidity
Isopachs
< 44 m
44 - 56m
56 - 68m
> 68 m

Figure I-1c

Figure I-1d

Bathymetry of the King George Basin. The basin, 60 km wide and 2 km deep, has a smooth floor but punctuated by volcanoes and numerous dike intrusions as shown by small isolated, unlabeled contour lines. Note change in contour intervals: 50 m at < 1900 m and 20 m at > 1900 m.

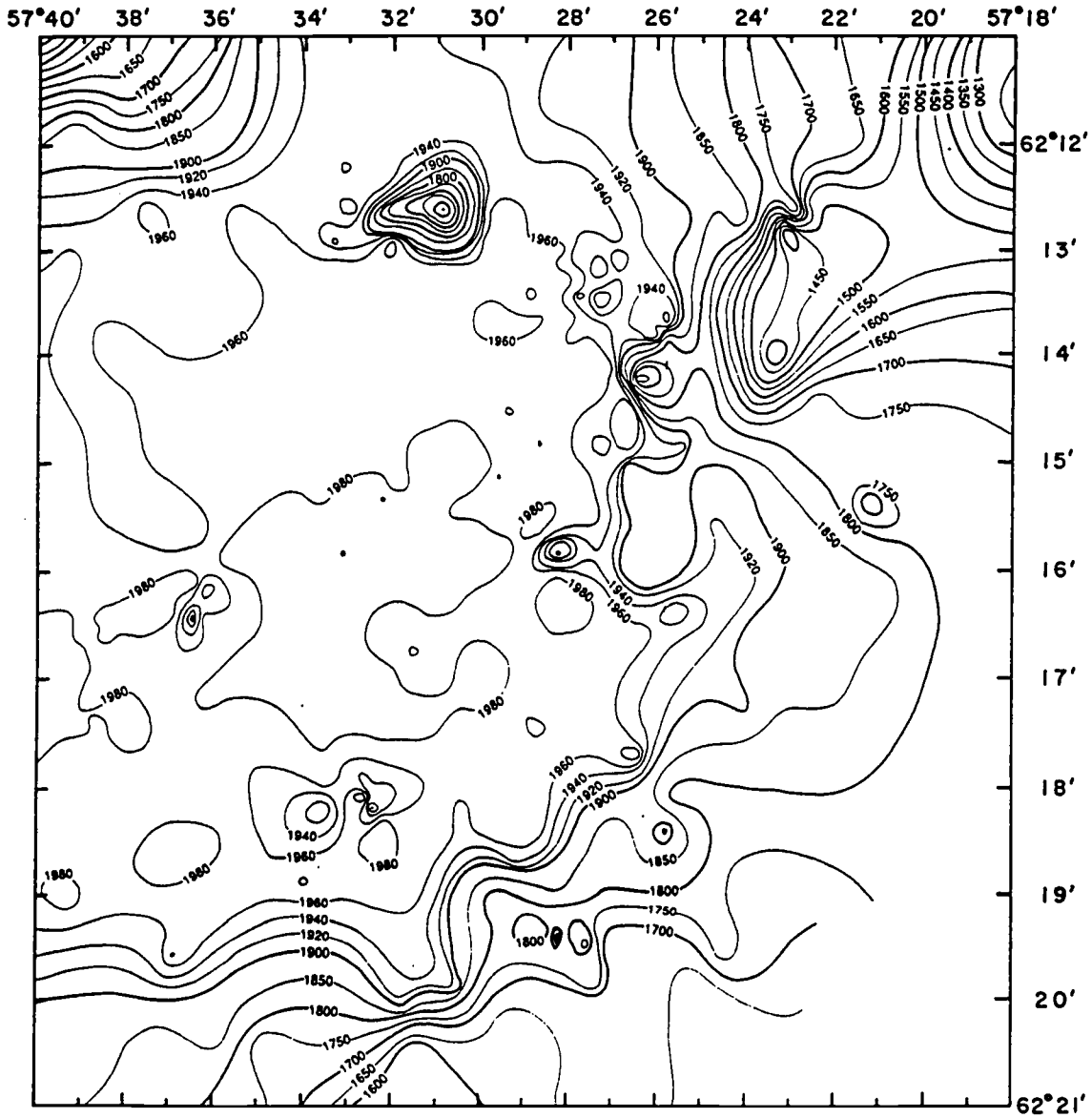
57°40'
38'
36'
34'
32'
30'
28'
26'
24'
22'
20'
57°18'
62°12'
13'
14'
15'
16'
17'
18'
19'
20'
62°21'

Figure I-1d

Hydrothermal petroleum was encountered in gravity cores (Brault and Simoneit, 1987) as well as thermogenic light hydrocarbon gases in addition to methane (Whiticar et al., 1985). Submarine volcanism associated with the process of back-arc spreading in the King George Basin must be the ultimate cause for this hydrothermal petroleum.

Evidence for hydrothermal activity is provided by anomalous ^{3}He and Mn from hydrocasts in the basin (Schlosser et al., 1987). Hydrothermalism in the thickly-sedimented King George Basin, a unique site discovered so far under polar conditions, invites comparison with the interactions among sediments, pore fluids, and intruded sills in the Guaymas Basin where they are well-documented (Lonsdale et al., 1980; Simoneit and Lonsdale, 1982; Einsele et al., 1980; Von Damm et al., 1985b; Sweeney, 1980).

METHODS

A working map of the bathymetry of the King George Basin (Fig. I-1d) was generated by a computer plot of the INDAS.10 navigation data which recorded positionings and water depths at 10 minute intervals during our survey of the basin in November 1985. A more detailed, high-resolution bathymetric chart utilizing 5 second interval data will be prepared by the Alfred-Wegener-Institute for Polar Research in Bremenhaven, West Germany. Morpho-tectonic features such as faults, submarine volcanoes, intrusions, and the distribution pattern of sediment isopachs were mapped by superimposing the 3.5 kHz records over the contour map on which the ship track was projected (Fig. I-1c).

During the cruise a transect of sediment cores, in the following called "hydrothermal" stations, was obtained from within the acoustic turbidity zone adjacent to the 'volcanic wall' (Fig. I-1c). Four gravity cores ranging from 5 to 8 m in length were acquired from the transect where hydrothermal activity was anticipated from our

Table I-1 Core locations in the King George Basin

Station	Latitude °S	Longitude °W	Water Depth (m)
1327	62 ° 16.5'	57 ° 38.7'	1978
1346	62 ° 16.8'	57 ° 29.1'	1979
1340	62 ° 15.7'	57 ° 29.2'	1980
1341	62 ° 14.8'	57 ° 28.7'	1980
1343	62 ° 13.4'	57 ° 30.3'	1970

Table I-2 Analytical methods for pore water chemistry

Element		Method	Precisions
Cl		Standard Mohr Titration with $AgNO_3$	0.05 %
Na		Flame Atomic Absorption Spectrophotometry	2 %
Mg		Flame Atomic Absorption Spectrophotometry	1%
Ca		Flame Atomic Absorption Spectrophotometry	1%
K		Flame Atomic Absorption Spectrophotometry	1%
Total CO_2		Gas Chromatography	1 %
Sulfate	SO_4	Gravimetric	1 %
Alkalinity	Alk.	Potentiometric	10 μ equiv.
Ammonia	NH_3	Colorimetric	3 %
Phosphate	PO_4	Colorimetric	0.5 %
Silicate	SiO_2	Colorimetric	1 %

previous results (Whiticar et al., 1985) (Table I-1). Pore water samples were collected from the gravity cores. Complete sets of pore water chemistry data consisting of Cl, Na, Mg, Ca, K, SO_4, NH_3, PO_4, SiO_2, total CO_2, and alkalinity were obtained from these cores (Appendix I). For comparison a gravity core was sampled from the region in the central King George Basin unaffected by hydrothermalism (Fig. I-1c). This core station will serve as a "reference" station.

Sediment samples were squeezed through 0.45 μm membrane filters for pore water extraction at approximately in situ temperatures (0 - 5 °C) immediately after core collection to avoid a temperature-of-squeezing effect (Mangelsdorf et al., 1969) and other possible artifacts. Total CO_2, NH_3, PO_4, SiO_2, and alkalinity were measured at sea; Cl, Na, Mg, Ca, K and SO_4 were measured at the shore-based laboratory. The analytical methods used are summarized in Table I-2.

In order to emphasize the difference in pore water chemistry of the major cations between the reference station and the hydrothermal stations, pore water chemistry data were presented by the sum of the major elements (Σ Cl, Na, Mg, Ca, K) v.s. each major cation. Another advantage of the representation technique is that the scatter in the plot is diagnostic for certain reactions as will be described in the sections for each major ion below.

RESULTS

The pore water composition from the four hydrothermal stations (1346, 1340, 1341, and 1343) in the tectonically active eastern end of the King George Basin is characterized by the downcore enrichment of Cl (Fig. I-2) and a corresponding increase in the sum of the major cations (Na, Mg, Ca, K) (Fig. I-3). Such a distribution of the dissolved major ions of the hydrothermal stations is significantly different from that of the reference station in the central King George Basin. Here neither Cl nor the sum of

Figure I-2

Depth profiles of interstitial Cl concentration. At all hydrothermal stations, 1346 (Δ), 1340 (O), 1341(◊) and 1343 (+), Cl shows downcore increase, 5 to 14 %, relative to the bottom water Cl. At the reference station, 1327 (*), there is no significant change in Cl with depth.

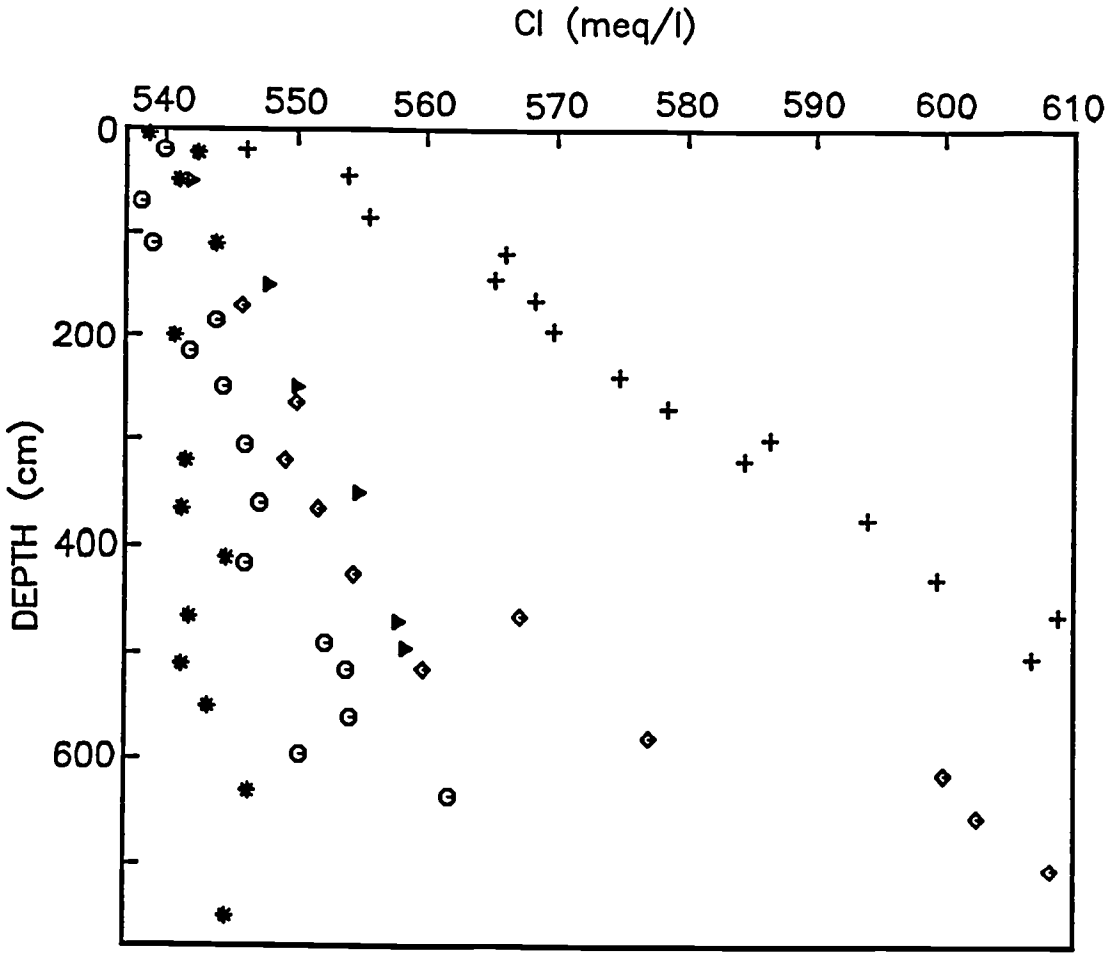

Figure I-2

Figure I-3

Depth profiles of the sum of the interstitial major cations (Σ Na, Mg, Ca, K). The sum of the major cations at all hydrothermal stations, 1346 (Δ), 1340 (O), 1341(◊) and 1343 (+), shows downcore increase (2 % to 9 %). At the reference station, 1327 (*), there is no significant change in the sum.

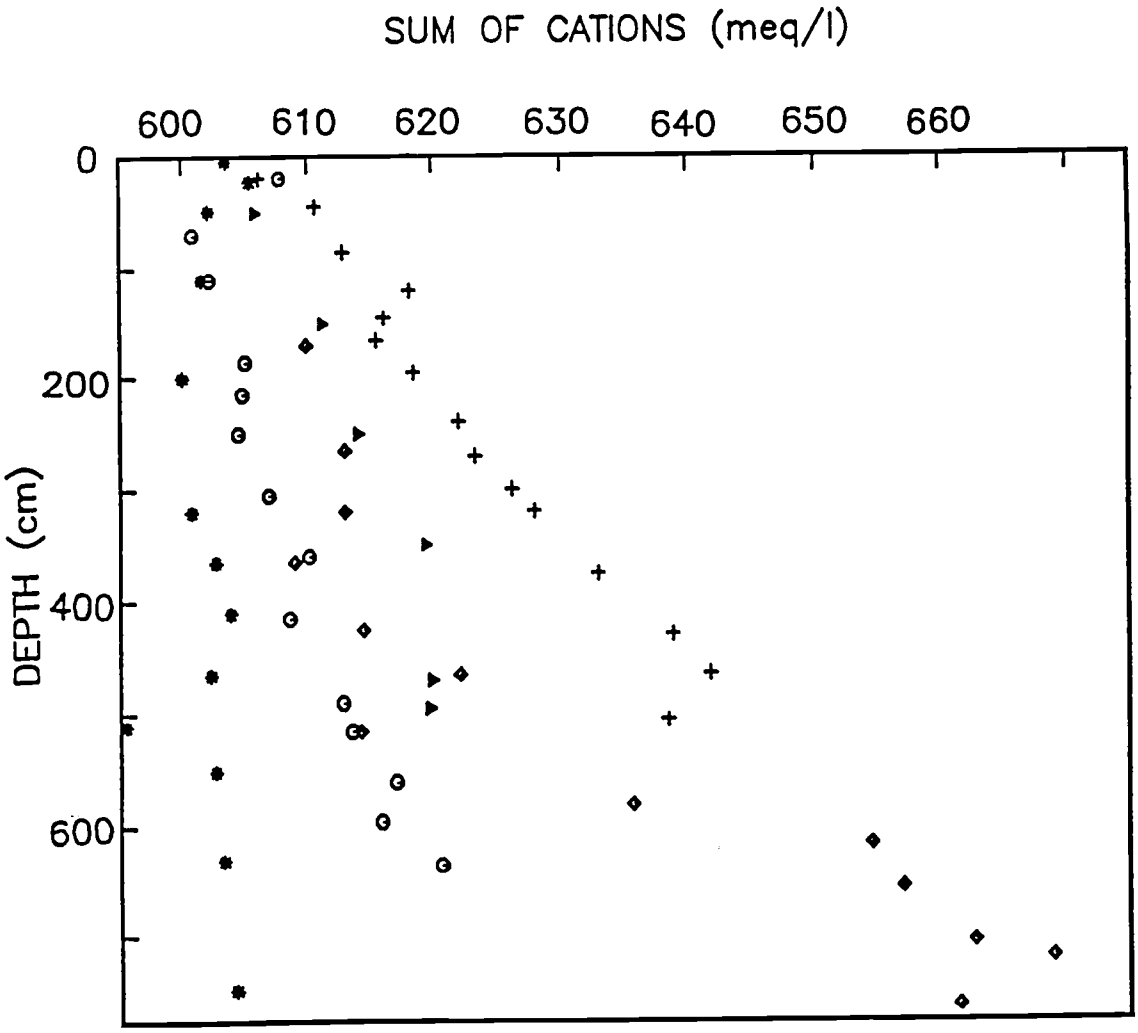
SUM OF CATIONS (meq/l)
600
610
620
630
640
650
660
0
200
400
600
DEPTH (cm)

Figure I-3

the major cations shows any change with depth (Figs. I-2 and I-3).

Differences in the pore water chemistry between the hydrothermal stations and the reference station continue to be evident in the dissolved nutrient species such as total CO_2, alkalinity, SO_4, NH_3, PO_4 and SiO_2 but less pronounced so than for the major ions. This is so because of the pervasive early diagenesis of organic matter decomposition in these near-surface sediments. Any hydrothermal signature represented by these species is masked by the diagenetic signature. Overall the concentration profiles of these species at the hydrothermal stations are highly stratified by the stresses of the two dominant processes, early diagenesis in the upper and hydrothermal reaction in the lower.

Chloride

There is no significant change in Cl in its downcore concentration at the reference station from the central basin (Fig. I-2). Chloride, being a conservative ion, is not affected by early diagenesis in marine sediments. However, at all stations from the acoustic turbidity zone where numerous extrusive and intrusive volcanic features are distributed throughout, chloride consistently increases downcore (Fig. I-2, Table I-3a). The increase is from 5 % (station 1340) to 14 % (station 1343) over the chloride content of normal bottom water. This increase reflects hydrothermal basalt-alteration reaction either at the basement or at the contact to the intrusive bodies. Hydrothermal solutions generated in laboratory experiments (Seyfried et al., 1986) as well as sampled from EPR hot springs (Michard et al., 1984; Von Damm et al., 1985a; Edmond et al., 1979) have shown both enrichment and depletion of chloride relative to normal seawater.

An experimental study by Seyfried et al. (1986) on Cl-behavior during hydrothermal alteration of basalts concludes that Cl is taken up from seawater by the formation of Cl-bearing phases such as Fe-hydroxy chloride at high temperatures (400

to 450 °C) and low water/rock ratios. As the system cools down Cl is released to the solution by retrograde alteration/dissolution of these Cl-rich mineral assemblages. According to Seyfried et al. (1986) this retrograde alteration/dissolution of basalts prevails at low temperature, less than 350 °C, and high water/rock ratios. Any increase in Cl, however, may equally be explained by basalt hydration during conductive cooling of basalts (Von Damm et al., 1985a).

Sodium

In all hydrothermal stations, except Station 1343, Na shows a downcore increase corresponding to that of Cl (Fig. I-4a, Table I-3a). For all the hydrothermal stations the axis for the sum of the cations can also be regarded as depth axis because the sum of the major cations increases with depth in all the hydrothermal stations (Fig. I-3). The ratio of the percent increase between Na and Cl is approximately one at hydrothermal stations 1346, 1340 and 1341. This suggests that hydration of basalts is very likely, at least with respect to Na and Cl, at these stations (Table I-3b). At the reference station 1327 Na does not show any change, indicating normal diagenesis.

At Station 1343 Na is significantly depleted. Depletion of Na, despite the largest Cl enrichment at this station, requires enrichment of the other major cations in order to preserve electroneutrality. Calcium is greatly enriched at Station 1343 (Fig. I-5a), but its magnitude of enrichment does not compensate for the Na depletion. No other major cation fully compensates for the Na loss. Such a behavior of Na to Cl at Station 1343 is not explained by basalt hydration. This is further illustrated by the exaggerated Na-loss when assuming that the 14 % Cl increase were due to basalt hydration. Under this assumption the corrected Na decrease would be 16 % (Table I-3a). Therefore, at Station 1343, retrograde alteration, which is characterized by Cl release in solution and Na uptake in basalt, is very likely the reaction responsible for the independent variations

of Na and Cl (Table I-3b).

Potassium

Potassium concentrations decrease downcore in the pore fluids of all hydrothermal stations except for Station 1341 which shows a downcore increase (Fig. I-4b). The hydrothermal end-member solution encountered at Stations 1346, 1340 and 1343 thus appears to be depleted in K. Reportedly K is taken up by basalt during low temperature hydrothermal reactions (Seyfried and Bischoff, 1979; Seyfried and Mottl, 1982; Staudigel and Hart, 1983). Therefore depletion of K, in addition to Cl-enrichment, indicates low-temperature hydrothermal reactions in the basin.

If the 12 % increase in both Cl and Na at station 1341 were due to basalt hydration, the corrected K-increase for the basalt hydration would reduce to only 1 % (Table I-3a). Since such a small enrichment is within the margin of accumulated errors from analyses, the percent change in K at Station 1341 is insignificant beyond that caused by basalt hydration. Thus at least at Station 1341 basalt hydration is likely to be the controlling mechanism for the end-member composition of the hydrothermal fluid rather than retrograde alteration (Table I-3b). Potassium remains essentially unchanged at Station 1327, this indicates a lack of hydrothermal reaction but instead normal diagenesis at the reference station.

Calcium

Calcium is strongly enriched in the pore fluids of all hydrothermal stations except at Station 1341 where it decreases when correction is made for water loss by basalt hydration (Fig. I-5a, Table I-3a). The largest increase in Ca was observed at Station 1343 where it partially compensates for the decrease of Na and K to maintain electroneutrality caused by the Cl increase. Generally, the overall increase in Ca at the

hydrothermal stations 1343, 1340 and 1346 agree well with the Ca-enrichment reported for hydrothermal solutions (Edmond et al., 1979, Von Damm et al., 1985a).

It is interesting to note that at Station 1327, Ca shows a scatter of the data points in direction of the Ca-axis as opposed to the clustered behavior of the Na and K data (Fig. I-5a). This scatter is due to the downcore decrease in pore water Ca. The decrease in Ca and is perfectly matched with the occurrence of calcium carbonate hexahydrate (=mineral ikaite) in the core (Suess et al., 1982). Ikaite formation is a diagenetic process which consumes calcium but has little effect on the sum of the major cations. Despite the changes in Ca, the sum of the major ions at the reference station remains essentially constant. This is distinctly different from the variability of the sum at the hydrothermal stations. This behavior of Ca clearly demonstrates the usefulness of the new type of data representation in differentiating hydrothermal from early diagenetic reactions (Figs. I-4 and I-5). For station 1341 the inference on the dominating reaction for the Ca-distribution remains inconclusive.

Magnesium

Magnesium decreases significantly downcore in the pore fluids of all hydrothermal stations, which agrees with the reported depletion of Mg in hydrothermal solutions (Fig. I-5b). Chloritization of feldspars seems to be an appropriate hydrothermal alteration reaction for such Mg-changes (Von Damm et al., 1985a). Similar to Ca, Mg shows a scatter of the data points in the direction of the Mg-axis at Station 1327. This scatter is due to an initial Mg decrease followed by an increase downcore. Such a Mg concentration profile is entirely due to diagenetic reactions involving ion-exchange with clays, as recently elucidated by von Breymann (1987). In general, early diagenetic decomposition of sedimentary organic matter causes an

Figure I-4

A plot of the sum of the interstitial major ions vs interstitial Na (a) and K (b). X-axis representing the sum of the major ions can be regarded as depth for the hydrothermal stations because the sum increases with depth as shown in Fig. I-3. Note the clustered Na and K distributions at Station 1327 (*), indicating no change in either ion nor the sum. At all hydrothermal stations, except Station 1343 (+), Na shows a downcore increase. At Station 1343 Na is significantly depleted. Potassium shows a downcore decrease at all hydrothermal stations, except Station 1341 (◊).

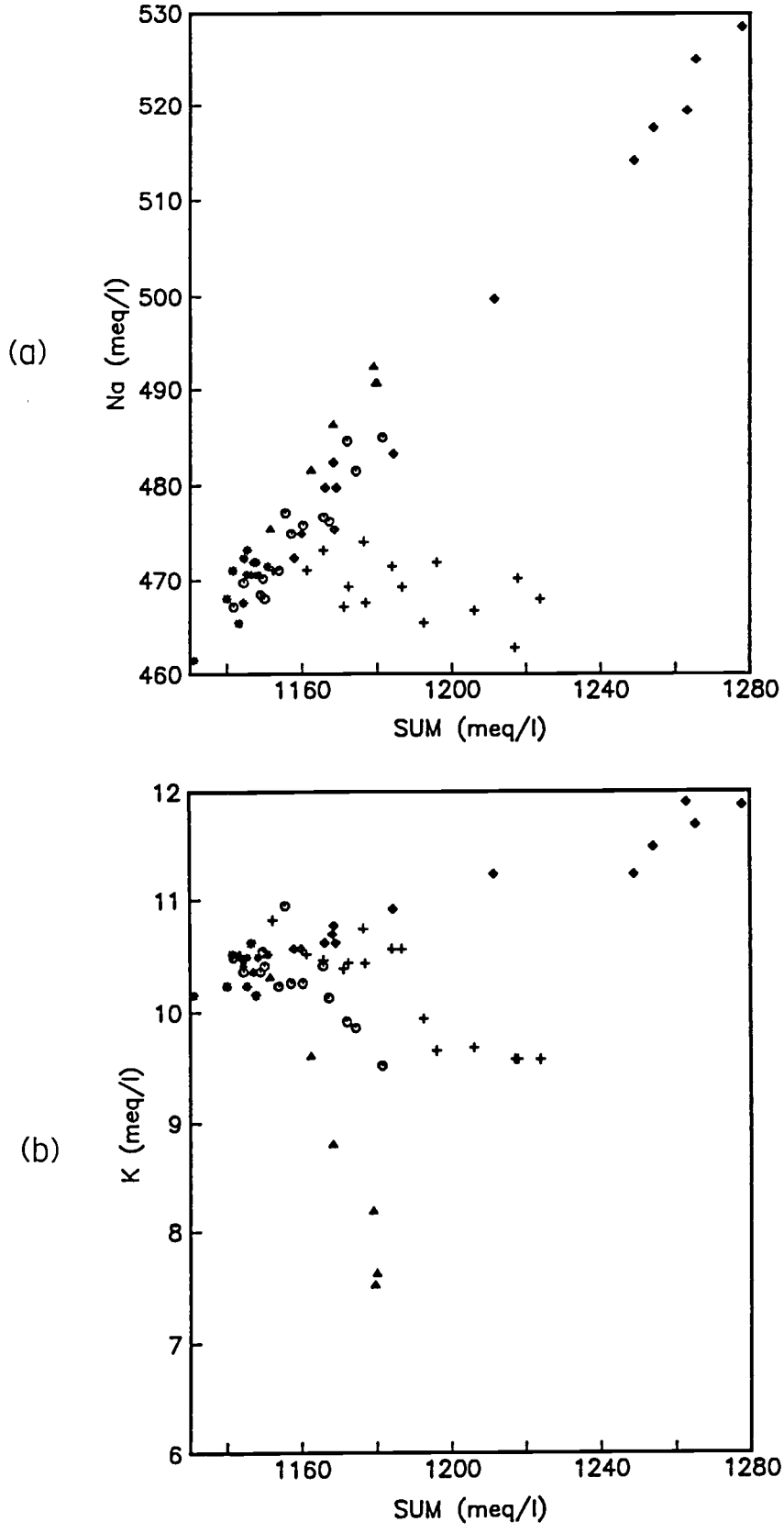
(a)
530
520
510
500
490
480
470
460
Na (meq/l)
1160
1200
1240
1280
SUM (meq/l)
(b)
12
11
10
9
8
7
6
K (meq/l)
1160
1200
1240
1280
SUM (meq/l)

Figure I-4

Figure I-5

A plot of the sum of the interstitial major ions vs interstitial Ca (a) and Mg (b). At all hydrothermal stations, except Station 1341 (◊), Ca shows a downcore increase. At Station 1341 Ca appears to remain unchanged but it decreases downcore when correction is made for water loss by hydration (Table I-3). Significant scatter of interstitial Ca along the Ca-axis at Station 1327 (*) reflects downcore decrease in interstitial Ca at this station. The constancy of the sum at Station 1327 is distinctly different from the increase of the sum at the hydrothermal stations. Overall, Mg decreases at all hydrothermal stations. Note similar scatter of Mg to that of Ca at Station 1327 (*).

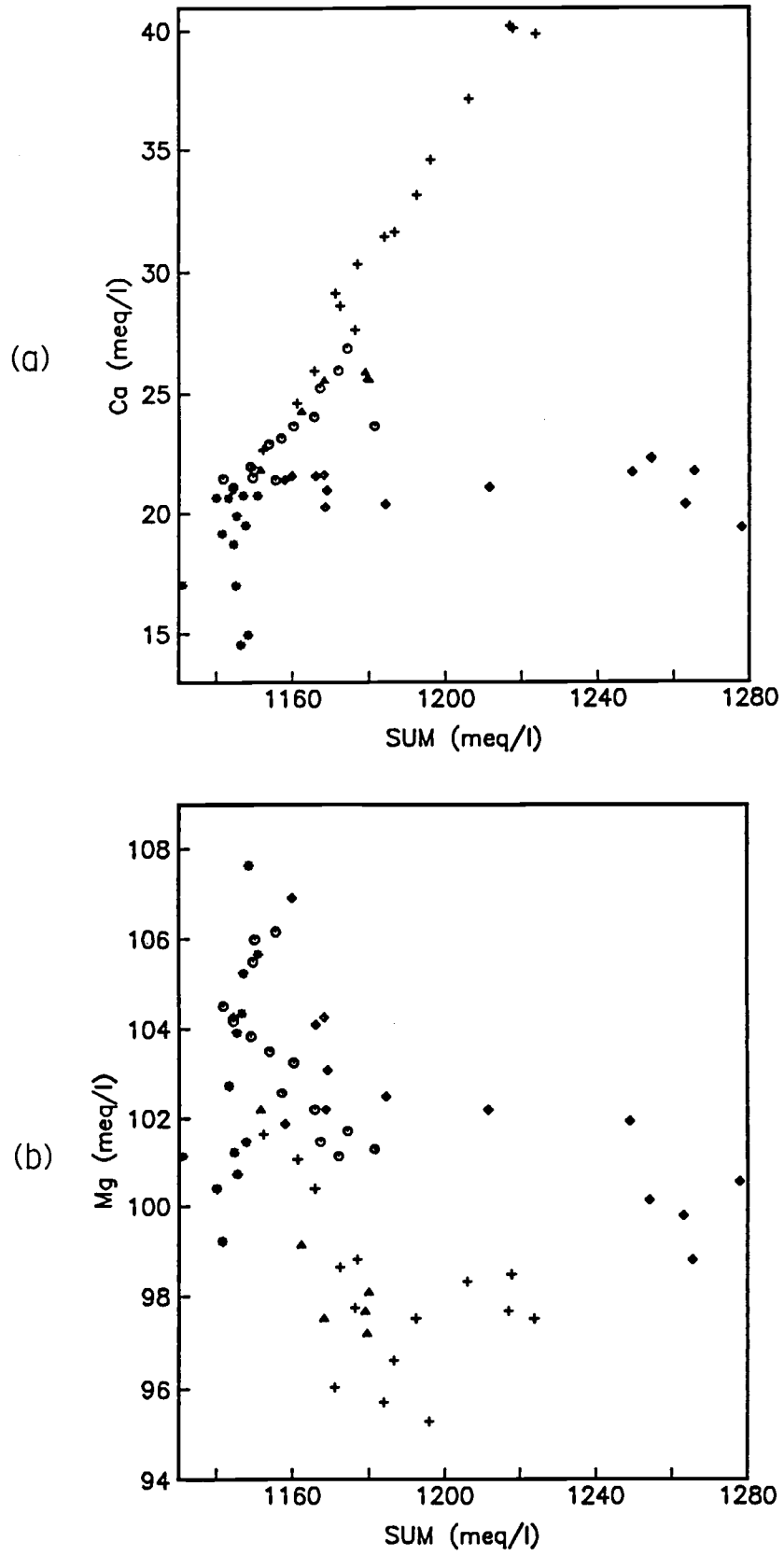
(a)
Ca (meq/l)
40
35
30
25
20
15
1160
1200
1240
1280
SUM (meq/l)
(b)
Mg (meq/l)
108
106
104
102
100
98
96
94
1160
1200
1240
1280
SUM (meq/l)

Figure I-5

Table I-3a Percent gain or loss of interstitial major ions, rounded to the nearest one %

Ion	St. 1346	St. 1340	St. 1341	St. 1343	St. 1327
Cl	+5	+4	+12	+14	±0
Na	+5	+3	+12	-2(-16*)	±0
K	-33	-10	+14(+1*)	-10	±0
Ca	+25	+26	0(-12*)	+100(+70*)	-30
Mg	-8	-5	-7	-10	-8 to +1**

* when correction is made for water loss due to basalt hydration;

** initially Mg decreases downcore but increase again at greater depths;

Table I-3b Types of reactions inferred from the changes in interstitial major ions

	St. 1346	St. 1340	St. 1341	St. 1343	St. 1327
Cl - Na	Hydration	Hydration	Hydration	Retrograde	None
Cl - K	Retrograde	Retrograde	Hydration	Retrograde	None
Cl - Ca	Retrograde	Retrograde	Retrograde	Retrograde	Ikaite Formation
Cl - Mg	Inconclusive	Inconclusive	Inconclusive	Inconclusive	Ion-exchange

increase of the total cation exchange capacity of the sediment due to removal of organic matter which blocks the clay exchange sites. Unblocking of the exchange sites causes an uptake of Mg from the pore solution and is responsible for the observed initial Mg-decrease. Subsequently, with increasing concentration changes of metabolites, -- i.e. increase in total CO_2 and decrease in SO_4-- the free Mg-ion concentration is effectively reduced by increased ion-pair formation. This process causes a re-distribution of Mg-ions by desorption from exchange sites of clay particles to maintain the ion-exchange equilibrium. The re-equilibration is responsible for the observed Mg-increase. Despite such changes in Mg at the reference station 1327 the relative constancy in the sum of the major cations, again delineates hydrothermal alteration from diagenesis, here in the form of ion-exchange reactions. However, estimates of the magnitude of hydrothermal alteration vs. ion-exchange remain inconclusive (Table I-3b).

Total CO_2 and Alkalinity

At all stations, both hydrothermal and reference sites, alkalinity and total CO_2 (TCO_2) profiles are virtual replicas of each other. This indicates that the main control of alkalinity is by the dissolved carbon dioxide species (Fig. I-6). Continuous accumulation of metabolites from the decomposition of organic matter causes the total CO_2 and alkalinity (as well as NH_3 and PO_4 which are discussed later) to increase rapidly within the upper 3 - 5 m at all stations. Hence in this upper portion it is impossible to determine whether the profiles of the TCO_2 and alkalinity indicate any effects of hydrothermal reaction. This is due to pervasive decomposition of organic matter at all stations. In the deeper portions of the cores, however, the profiles of TCO_2 and alkalinity at the hydrothermal stations distinctively differ from those at the reference station. In the deeper portions of the cores total CO_2 shows a reversal at all

Figure I-6

Depth profiles of interstitial total CO_2 (a) and total alkalinity (b). Differentiation of the hydrothermal stations from the reference station is only possible in the deeper portions of the cores where a reversal in concentration is observed for the hydrothermal stations At the reference station, 1327 (*), the high and constant TCO_2 contents at depth are controlled by the formation of calcium carbonate hexahydrate (ikaite; Suess et al., 1982). Alkalinity and total CO_2 profiles are virtual replicas of each other. This indicates that the main control of alkalinity is by the dissolved carbon dioxide species. The hydrothermal stations are 1346 (Δ), 1340 (O), 1341(◊) and 1343 (+). Alkalinity data are not available at Station 1341(◊).

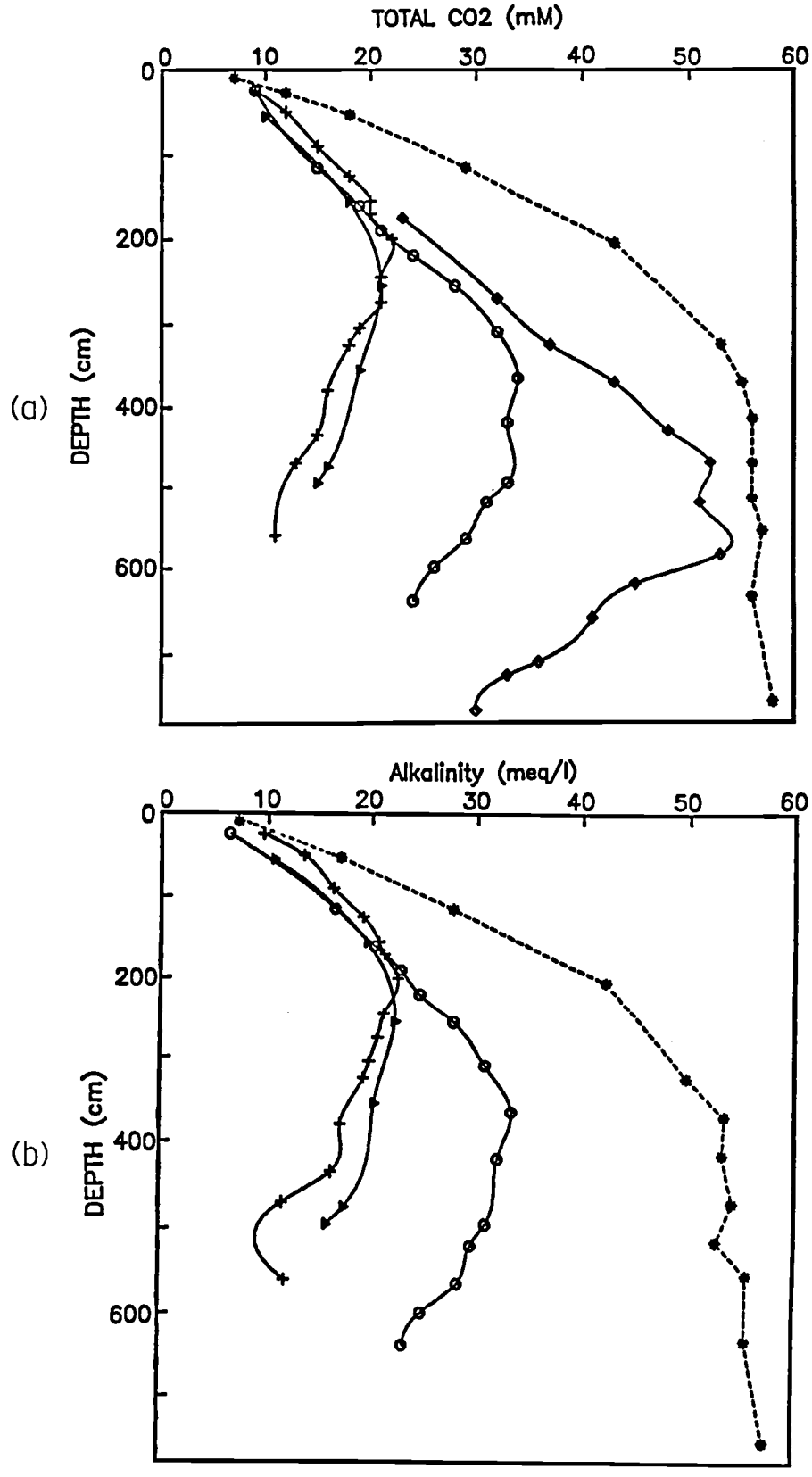
TOTAL CO2 (mM)
0
10
20
30
40
50
60
0
200
400
600
DEPTH (cm)
(a)
Alkalinity (meq/l)
0
10
20
30
40
50
60
0
200
400
600
DEPTH (cm)
(b)

Figure I-6

hydrothermal stations while it remains constant at the reference station. The reversal would not occur if diagenesis were the only process controlling TCO_2. In a typical profile for early diagenesis, TCO_2 and alkalinity would usually increase with depth either linearly or asymptotically as shown at the reference station. The asymptotic increase is due to the constraint in the lower portion by the calcite hexahydrate precipitation (Suess et al., 1982).

If the depletions of TCO_2 and alkalinity in the deeper core sections at the hydrothermal stations were caused by precipitation of another calcium carbonate phase, profiles of Ca should also show a corresponding depletion. However, they increase significantly as discussed earlier and no authigenic calcite precipitates were observed at any of the hydrothermal stations. Thus the depletions of TCO_2 and alkalinity in the deeper core sections must be due to a process other than diagenesis. Consumption of TCO_2 or dilution by fluids low in carbon dioxide would explain the observed distribution. We favor the second explanation as will be discussed in Chapter II.

In summary, the profiles of TCO_2 and alkalinity at the hydrothermal stations show a stratification caused by the two dominant processes, diagenesis in the upper and hydrothermal-related processes in the lower sections of the cores.

Sulfate

Strong sulfate reduction downcore occurs at all stations including the hydrothermal stations. Pore water sulfate reaches minimum concentrations, accompanied by the accumulation of the other metabolites NH_3, PO_4, and TCO_2. In this regard the hydrothermal stations are no different than the reference station 1327. What is unique, however, is that at all hydrothermal stations the SO_4 concentration reverses and increases again below a minimum zone (Fig. I-7a). The re-appearance of dissolved sulfate below the minima in all hydrothermal stations is a clear contradiction

Figure I-7

Depth profiles of interstitial sulfate (a) and ammonia (b) concentrations. At each station microbial sulfate reduction lowers sulfate downcore to a minimum value. Below the minimum, however, sulfate at all hydrothermal stations increases with depth. Furthermore this sulfate increment (i.e. the magnitude of increase below the minimum) shows the systematic decrease from the southern station to the northern station (1346 (Δ) - 1340 (O) - 1140(*) - 1341(◊) - 1343 (+)). NH_3 profiles of all the hydrothermal stations are indistinguishable from that of the reference station, 1327 (*), regardless of depth-in-core.

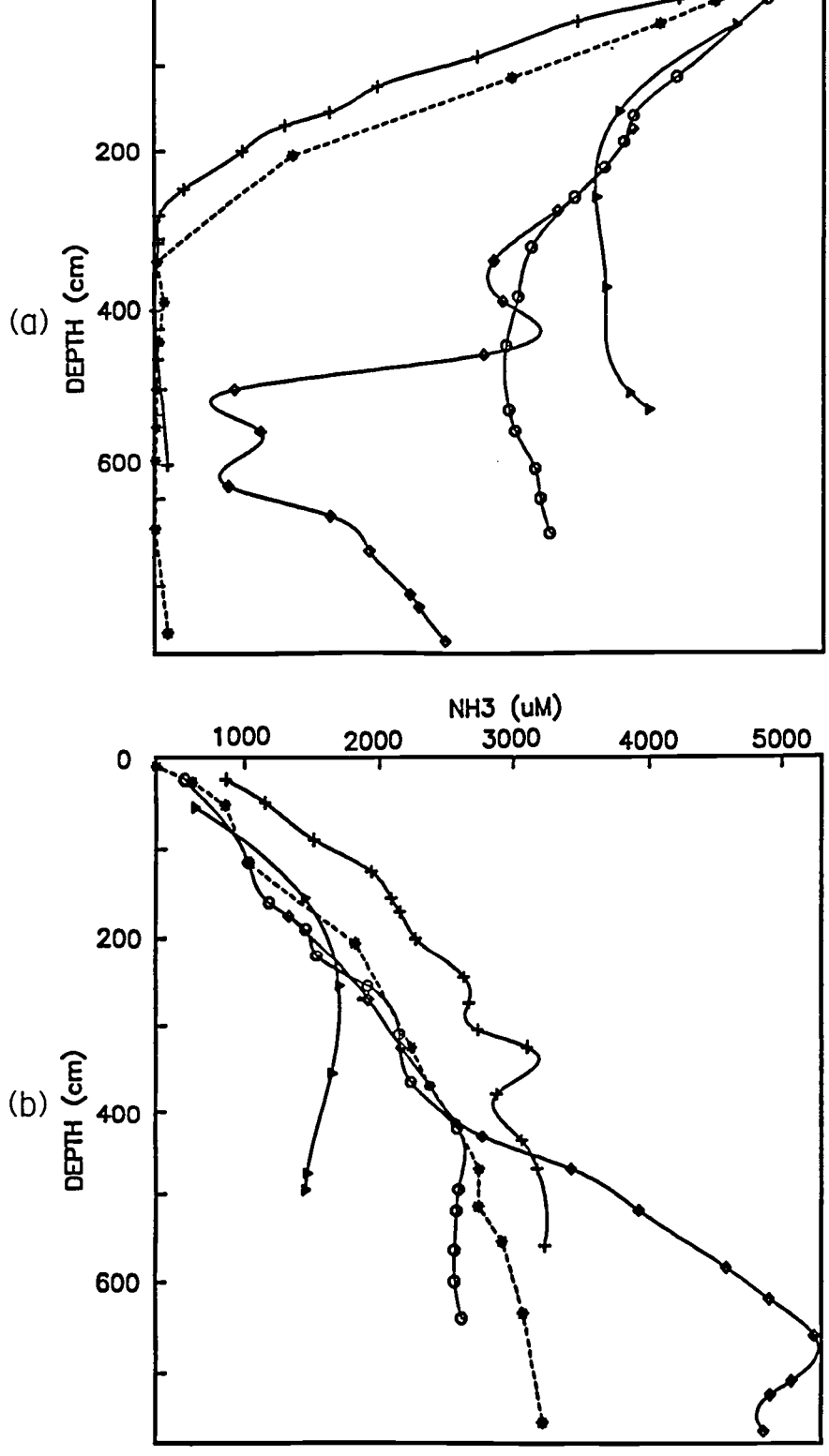
SO4 (mM)
0
5
10
15
20
25
0
200
400
600
DEPTH (cm)
(a)
NH3 (uM)
1000
2000
3000
4000
5000
0
200
400
600
DEPTH (cm)
(b)

Figure I-7

to what is known about hydrothermal reactions, because uptake of sulfate by basalts results in sulfate depletion in all types of hydrothermal solutions (Edmond et al., 1979). The unusual SO_4 distribution can not be explained by diagenesis either, because SO_4 in pore waters usually becomes exhausted or at least drops to a certain lower level with depth and then remains constant (Suess et al., 1982).

It is interesting to note that the SO_4-increase below the minima in the hydrothermal area is systematic in its magnitude from the southern to the northern stations (Fig. I-7a). The re-appearance of deep sulfate in the hydrothermal stations may only be explained by lateral flow of unreacted seawater, i.e., SO_4-rich bottom water from the southern margin of the basin toward the north. Active faults and scarps in the southern margin of the basin may facilitate recharge of deep water there. Details on the dynamics of the hydrothermal recharge circulation in the basin are discussed in Chapter II.

Ammonia

Although TCO_2 and alkalinity reverse below the SO_4-minima at all hydrothermal stations, NH_3 shows no sign of reversal. In this respect NH_3 profiles at the hydrothermal sites are indistinguishable from that of the reference station (Fig. I-7b). In the Guaymas Basin hydrothermal solutions are reported to react with sediments resulting in additional NH_3-enrichments (Von Damm et al., 1985b). The upward migration of NH_3-enriched solutions from the deep reaction source in the King George Basin may explain the continued increase in NH_3 concentration at the lower portion despite the termination of sulfate reduction.

Phosphate

The dissolved phosphate profiles at the hydrothermal stations and the reference

Figure I-8

Depth profiles of interstitial phosphate (a) and silicate (b) concentrations. Similar to dissolved NH_3, the phosphate distribution at the hydrothermal stations is indistinguishable from that of the reference station, 1327 (*). Silicate-profiles are very complex at all stations and no pattern distinguishes the hydrothermal stations from the reference station, 1327 (*).

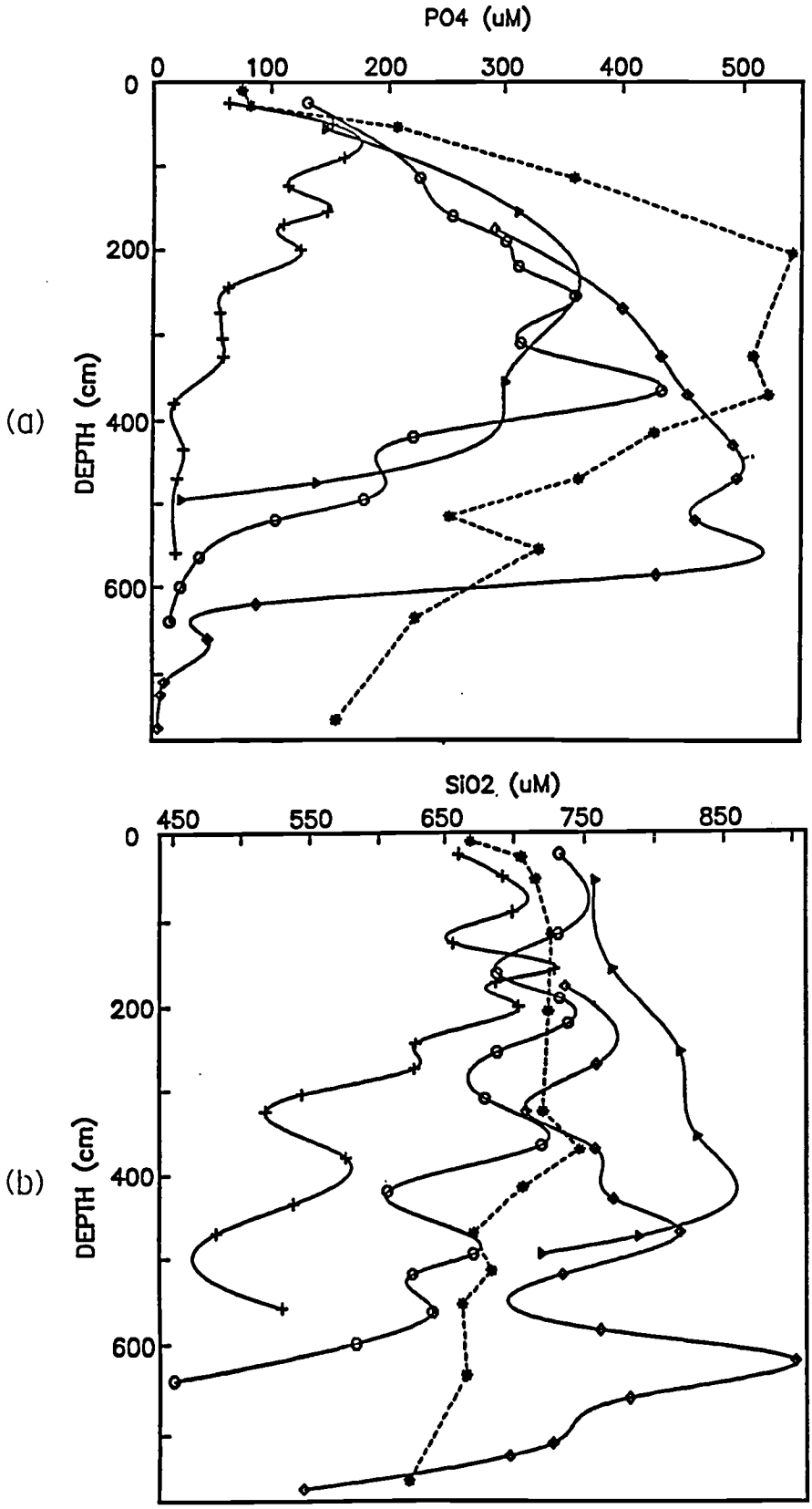
PO4 (uM)
0
100
200
300
400
500
0
200
400
600
DEPTH (cm)
(a)
SiO2 (uM)
450
550
650
750
850
0
200
400
600
DEPTH (cm)
(b)

Figure I-8

station are also indistinguishable from each other (Fig. I-8a). Phosphate increases at first and then decreases rapidly. The depths of the maximum concentrations approximately coincides with the mid-depths of the cores. The rapid depletion of PO_4 in the deeper core section at all stations may indicate that organic phosphorus is preferentially metabolized during early diagenesis of the organic matter leading to phosphorous-poor residual organic matter. At all stations in the King George Basin, PO_4 seems to be easily released within the sulfate reduction zone. This implies that organic matter remaining in the sediments beyond the sulfate reduction zone may be far more depleted in posphorus than nitrogen. If this is so, then PO_4 may not be significantly enriched in hydrothermal solutions, in contrast to NH_3, despite continued decomposition of organic matter. This would explain the dissolved PO_4 distribution at all hydrothermal stations. This is a tentative explanation because other sedimentary phosphorus sinks have not been investigated as yet.

Silicate

The dissolved SiO_2 profiles are very complex at all stations and no pattern distinguishes the hydrothermal stations from the reference station (Fig. I-8b) . Since diatoms are present in large amounts in the basin sediments it is quite possible that the pore solutions are in a non-steady state equilibrium reflecting diatom abundance and solubility rather than quartz solubility. The overall downcore decrease in SiO_2 concentration, however, seems to indicate that there is recrystallization of amorphous diatom opal to quartz in the deeper sediment column.

DISCUSSION

Summation Technique of Major Ions

Conventional element by element consideration of the pore water concentration

profiles is ambiguous if hydrothermal activities and diagenetic reactions both control the distribution of certain elements. This is especially so for the major ions in pore water. For example, the downcore Ca-enrichment and Mg-depletion in interstitial concentration profiles of sedimented MOR-flanks have been regarded as evidence for hydrothermal activity because end-member hydrothermal fluids are known to be enriched in Ca and depleted in Mg (Maris et al., 1984; Bender et al., 1985). Generally such pore water Ca- and Mg-profiles, however, can also be explained by early diagenetic reactions, though we think that in the particular cases from the EPR and the Galapagos mounds area these profiles exhibit true hydrothermal signals. Downcore Ca-enrichment in near-surface sediment has commonly been attributed to carbonate mineral dissolution, while downcore Mg-depletion to the uptake of interstitial Mg by solid phase, such as exchange of interstitial Mg with clay minerals. Dolomitization by calcite replacement is also responsible for the Ca and the Mg distribution in interstitial waters (Kastner et al., 1987).

As a new approach, the presentation of the pore water chemistry as the sum of the major ions plotted versus each major ion separately, allows effective differentiation of hydrothermal from diagenetic reactions (Figs. I-4 and I-5). This approach is efficient because of the Cl-behavior during hydrothermal reactions. During seawater-basalt reactions the Cl tends to be released to the solution phase in low-temperature reactions and taken up into solid phases at high temperatures (Seyfried et al., 1986). Basalt hydration at low temperature causes Cl and all other ions to be enriched in solution. Such Cl-enrichment in hydrothermal end-member solution are documented from many hydrothermal areas (Edmond et al., 1979, Michard et al., 1984; Von Damm et al. , 1985a). Since Cl is the most abundant ion in seawater, such behavior during hydrothermal reactions will cause changes in the sum of the major cations in order to maintain electroneutrality.

During mixing of hydrothermal solutions with unreacted seawater the major ions behave conservatively (Edmond et al., 1979), although they obviously behaved non-conservatively during the hydrothermal reactions which in the first place caused the pore solutions to be different from seawater. Thus in a sedimented hydrothermal system, the sum of the interstitial major ions would either decrease or increase downcore depending on whether hydrothermal reactions at the basement occurred at high or low temperatures. In any case the sum of interstitial major ions when plotted versus each major ion separately would show an appreciable scatter in the direction of the summation axis. This scatter would depend on the extent of enrichment or depletion of that ion in hydrothermal end-member solution. In case of early diagenetic reactions, major ions such as Ca and Mg would show scatter in the direction of each major ion but would be relatively invariant in the direction of the summation axis.

Figures I-4 and I-5 illustrate the successful delineation of hydrothermal stations from diagenetic station by this representation technique. Dissolution of evaporites or formation of gas hydrates also cause total ions to increase, but neither would cause such diverse scatter in the direction of the major ion axes as in hydrothermal solutions.

The downcore increase in the sum of the dissolved major ions in the hydrothermal area is distinctly different from the pattern of dissolved ions in non-hydrothermal background area. The main reason for this diagnosis is due to the Cl-behavior in hydrothermal reactions. It separates high-temperature alteration (Cl-decrease) from low-temperature alteration reactions (Cl-increase) and from normal diagenetic reactions (no Cl-change). The data from the Bransfield Strait, though, deal only with low-temperature reactions and normal diagenesis. Our new presentation technique would also be applicable if high-temperature hydrothermal reactions in sedimented areas would generate Cl-depleted hydrothermal solutions. This would be reflected in a downcore decrease in the sum of the major cations. Testing of our

technique by applying it to the pore water chemistry data from sedimented MORs would be interesting if there existed high-temperature hydrothermal reaction in sedimented MORs, resulting in Cl-depletion.

From the apparent lack of anomalies of Ca, Mg, and F, Bender et al. (1985) infer no significant seawater-basalt reactions during hydrothermal advection through the sedimented MOR flank at 20 °S of the East Pacific Rise. Our presentation technique would be useful to test their claim if interstitial Na and Cl data were provided in this case.

Hydrothermal Alteration Reaction

Signals for the hydrothermal reaction in the eastern King George Basin were evident in the downcore enrichments of Cl and the corresponding increase in the sum of major cations. Reported downcore changes in interstitial Cl from sediments of lakes or estuaries, however, have also been attributed to salinity fluctuation in the overlying water (Lerman and Weiler, 1970; Matisoff, 1980). Downcore enrichment of Cl at the hydrothermal stations ranges from 5 % (Station 1340) to 14 % (Station 1343). These changes can not be explained by salinity fluctuation in the overlying seawater, because the magnitude to which the salinity of the overlying seawater would have to change can only be expected in estuaries, tidal flats, or marshes. Even in these transitional, shallow-water environments the changes in Cl in response to salinity fluctuation of the overlying water are restricted to the uppermost sediment layer of less than 1 m in depth. Therefore, the downcore enrichments of Cl in the hydrothermal stations must be related to causes other than salinity fluctuation of the Bransfield Strait water.

There are two processes which can result in increased Cl concentration in pore waters: retrograde alteration and/or basalt hydration. At this point there is no independent evidence to determine which process is more influential in generating Cl-

enriched hydrothermal solution. A one-to-one enrichment on a percent basis between Cl and Na in all hydrothermal stations, except Station 1343, definitely suggests basalt hydration in the area of the Bransfield Strait. Basalt hydration is most strongly inferred at Station 1341 because of the accompanying K-distribution; (see the result section for potassium, Table I-3b). The large variation in concentration for each of the major cations between hydrothermal stations, however, does not rule out retrograde alteration/dissolution of basalt. All hydrothermal stations, except Station 1341, suggest retrograde reactions, especially Station 1343 (Table I-3b) based on the K-decrease and the Ca-increase relative to Cl. Prograde basalt alteration during high-temperature reactions in the past might have generated greatly differentiated mineral assemblages with a wide range of composition. The end-member composition of hydrothermal fluids in the King George Basin at present, though, seems to be generated by low-temperature alteration of these differentiated basalt assemblages. The potential reactions are listed in Table I-4 along with an assessment of them controlling the pore water composition.

Occurrence of both retrograde dissolution and hydration at low temperature suggest that the system in the King George Basin is a low-temperature hydrothermal system, probably at late stages of reaction. Depletion of interstitial K provides additional evidence for low-temperature reactions, the downcore decrease in K agrees with the reported K-uptake by basalt during such process (Edmond et al., 1979; Seyfried and Bischoff, 1979). If we accept the result from laboratory experiments by these authors, indicating that the change from K-release to K-uptake during seawater-basalt reaction occurs between 70-150 °C, the reaction temperature in the King George Basin may at the least be < 150 °C (Seyfried and Bischoff 1979; Menzies and Seyfried, 1979).

Table I-4 Potential low-temperature hydrothermal reactions and their likelyhood in controlling the pore water composition at the hydrothermal stations in the King George Basin.

(HOB) Hydration of Basalts

(A-1) Fe-hydroxy chloride + Na^+ + SiO_2 + Clinochlore + Clinozoisite = Plagioclase + Olivine + Ca^{++} + Cl^-

(A-2) Fe-hydroxy chloride + Albite + Clinochlore + Clinozoisite = Plagioclase + Olivine + Na^+ + SiO_2 + Cl^-

(B-1) Anorthite + Na^+ + $Si(OH)_4$ = Albite + Ca^{++} + $Al(OH)_4^-$

(B-2) Anorthite + Ca^{++} + $Al(OH)_4^-$ + $Si(OH)_4$ = Epidote + H_2O + H^+

(C-1) Epidote + $3Mg^{++}$ + $2Fe^{++}$ + H_2O = Chlorite + $2Ca^{++}$ + $Al(OH)_4^-$ + $7H^+$

(C-2) Albite + $3Mg^{++}$ + $2Fe^{++}$ + $Al(OH)_4^-$ + H_2O = Chlorite + Na^+ + $8H^+$

Station	Likely	Unlikely
1346 and 1340	(HOB), (A-2), (C-1), (C-2)	(A-1), (B-1), (B-2)
1341	(HOB), (A-2), (B-2), (C-2)	(A-1), (B-1), (C-1)
1343	(A-1), (B-1), (C-1)	(HOB),(A-2), (B-2), (C-2)

Hydrothermal End-Member Composition

An estimation of the hydrothermal end-member composition is a more difficult task for sedimented systems than for the ridge-crest hydrothermal systems. Upon upward migration through the sediments the solution is very likely to loose its hydrothermal character by mixing with pore waters affected by normal diagenesis in sediments. Ideally, therefore in characterizing fluids in sedimented hydrothermal system, we have to isolate mathematically the hydrothermal component of pore waters which are likely to be a mixture of at least three reservoirs: unreacted pore water (bottom water), hydrothermal water, and pore water affected by early diagenesis. Since dissolved species such as NH_3, PO_4, SiO_2, SO_4, and total CO_2 are primarily controlled by early diagenesis of organic matter, they are not considered in the estimation of the hydrothermal end-member composition.

If an element or dissolved species is not affected by early diagenesis, its distribution would depend only on the degree of mixing between unaltered pore water and hydrothermal water. Chloride is the best candidate for this kind of tracer. Though Cl, at the site of initial basalt-seawater reaction, behaves non-conservatively, it is resonable to assume a conservative behavior for Cl once it leaves the reaction site. Thus the Cl distribution in pore water of our shallow cores from the King George Basin is determined by the mixing between a hydrothermal component and and unaltered pore water.

The pronounced increase in Cl at all hydrothermal stations suggests Cl-enrichment in the end member hydrothermal fluid. We do not know, however, how much this Cl-enrichment would be unless the fraction of admixed hydrothermal fluid can be ascertained. Also the pattern of Cl-increase below the limit of our cores (8 m at the deepest) is not predictable. Thus our attempt to estimate a hydrothermal end-member composition based on pore water chemistry data is at best a "pseudo"

hydrothermal end-member composition (PHEMC). Nonetheless, a reasonable PHEMC and its mixing with unaltered pore water can be obtained in the following.

Chloride and the major cations (Na, Mg, Ca, K) are the basis for this attempt to estimate PHEMC. This assumes that the major cations also behave conservatively within the depth limits cored, i.e., their distribution in the pore water is controlled by mixing between PHEMC and unaltered pore water. This assumption is of course questionable, as shown for Ca and Mg as they are involved in diagenetic reactions such as calcite hexahydrate precipitation and ion-exchange with clays. However the influence of diagenetic reactions on total pore water Ca and Mg is much weaker than the hydrothermal influence and any failure of predicting mixing lines between PHEMC and unaltered pore water for either Ca or Mg would indicate the involvement of these ions in diagenetic reactions.

The PHEMC was estimated from the pore water chemistry by successive regressions followed by reiteration. The steps involved in this calculation are shown in Table I-5. First, the best regression was obtained for each major cation vs Cl (Step 1 in Table I-5) (Figs. I-9, I-10 and Table I-6). The regression between the ratio of the sum of the major cations to Cl and depth was constant, independent of depth, at each of the hydrothermal stations with confidence of greater than 80 % (Step 2 in Table I-5) (Table I-6). The regression between the ratio of each cation to Cl and depth was also constant, independent of depth, but with widely varing confidence (Step 3 in Table I-5). Among the regressions in the Step 3, however, there was at least one regression which showed confidence greater than 90 % (Table I-6). This particular regression, showing the least variation in the ion/Cl ratio, was selected for a further calculation (Step 4) and the rest was discarded. The selection reduced the system to six equations with five unknowns permitting reiteration. In Step 4, reiteration was initiated for each hydrothermal station by assigning an arbitrary concentration to that cation whose regression with Cl in Step 1

Table I-5 Procedure for the estimation of PHEMC

REGRESSION

Step 1

Na vs Cl
Mg vs Cl
Ca vs Cl
K vs Cl

pick the best regression, but keep the rest (e.g. pick Na = a Cl + b)

Step 2

Na + Mg + Ca + K / Cl vs depth

(e.g. Na + Mg + Ca + K / Cl = c)

Step 3

Na / Cl vs depth
Mg / Cl vs depth
Ca / Cl vs depth
K / Cl vs depth

pick the best regression (only one) and discard the rest (e.g. pick Mg / Cl = d)

REITERATION

Step 4

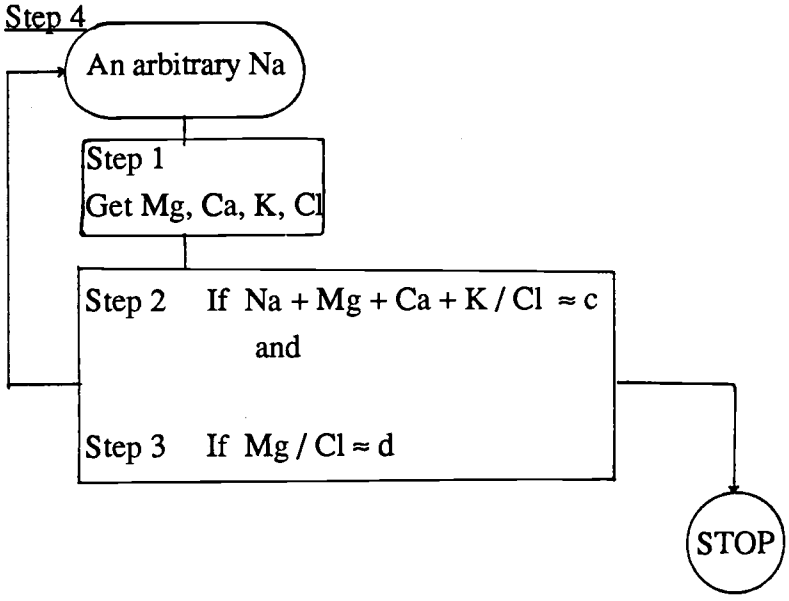

Figure I-9

Regression between interstitial Na and interstitial Cl (a). The relations between the two ions at the hydrothermal stations, 1346 (Δ), 1340 (O), 1341(◊) and 1343 (+), are, respectively: Na = 0.961 Cl - 44.246; Na = 0.683 Cl + 100.886; Na = 0.769 Cl + 52.984; and Na = -0.093 Cl + 523.061. Regression between interstitial K and interstitial Cl (b). The relations between the two ions at the hydrothermal stations, 1346 (Δ), 1340 (O), 1341(◊) and 1343 (+), are, respectively: K = -0.171 Cl +103.081; K = -0.041 Cl + 32.645; K = 0.018 Cl + 0.648; and K = -0.021 Cl + 22.506.

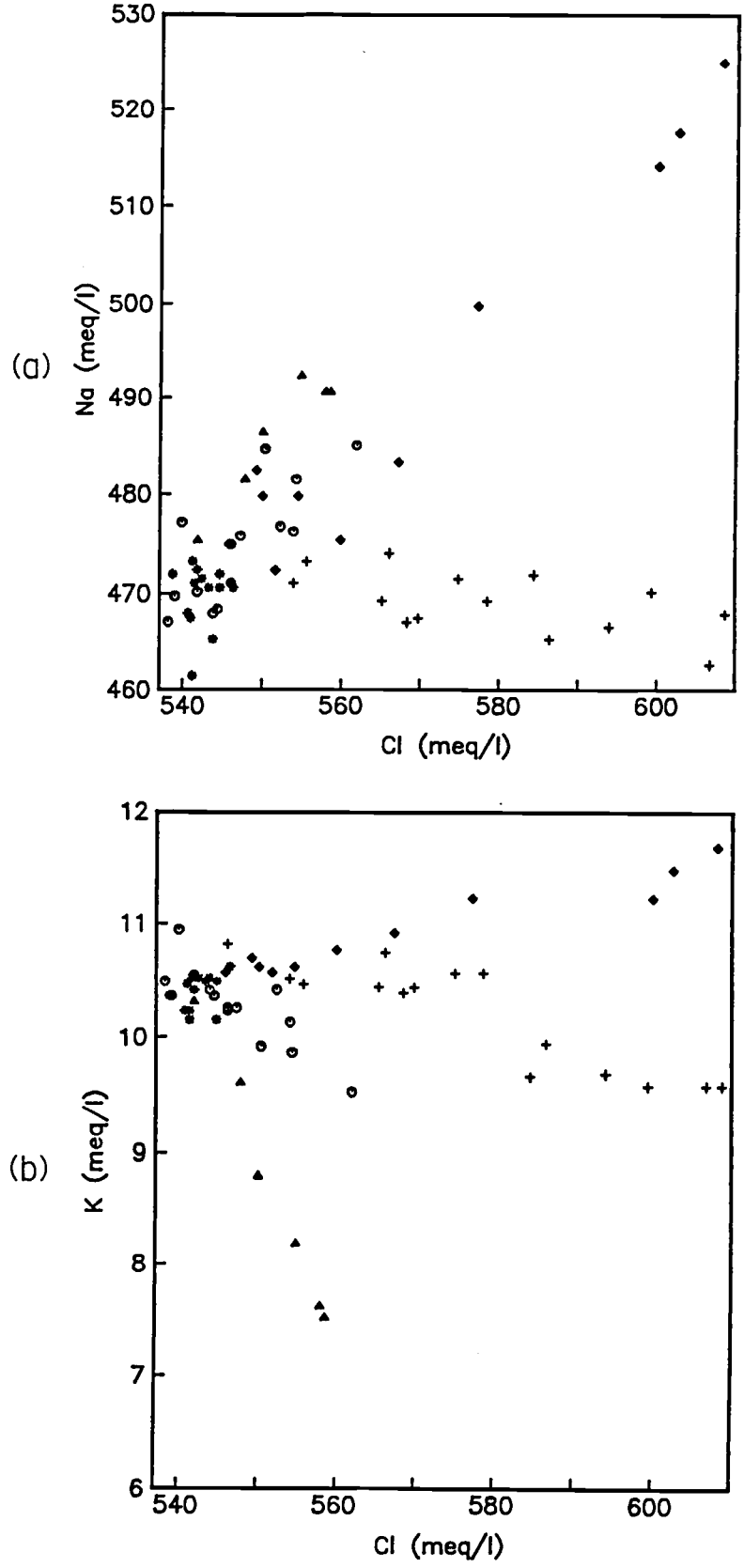
(a)
Na (meq/l)
530
520
510
500
490
480
470
460
540
560
580
600
Cl (meq/l)
(b)
K (meq/l)
12
11
10
9
8
7
6
540
560
580
600
Cl (meq/l)

Figure I-9

Figure I-10

Regression between interstitial Ca and interstitial Cl (a). The relations between the two ions at the hydrothermal stations, 1346 (Δ), 1340 (O), 1341(◊) and 1343 (+), are, respectively: Ca = 0.212 Cl - 92.334; Ca = 0.205 Cl - 89.203; Ca = -0.006 Cl + 24.391; and Ca = 0.292 Cl - 136.772. Regression between interstitial Mg and interstitial Cl (b). The relations between the two ions at the hydrothermal stations, 1346 (Δ), 1340 (O), 1341(◊) and 1343 (+), are, respectively: Mg = -0.246 Cl + 234.113; Mg = -0.209 Cl + 217.722; Mg = -0.065 Cl + 139.526; and Mg = -0.050 Cl +126.934.

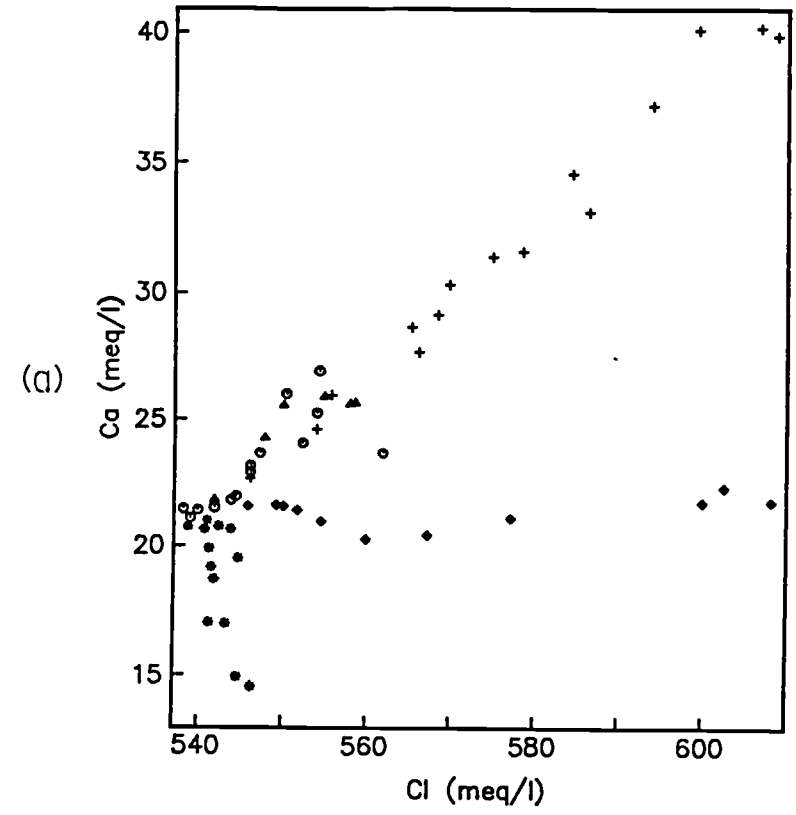
(a)
Ca (meq/l)
40
35
30
25
20
15
540
560
580
600
Cl (meq/l)

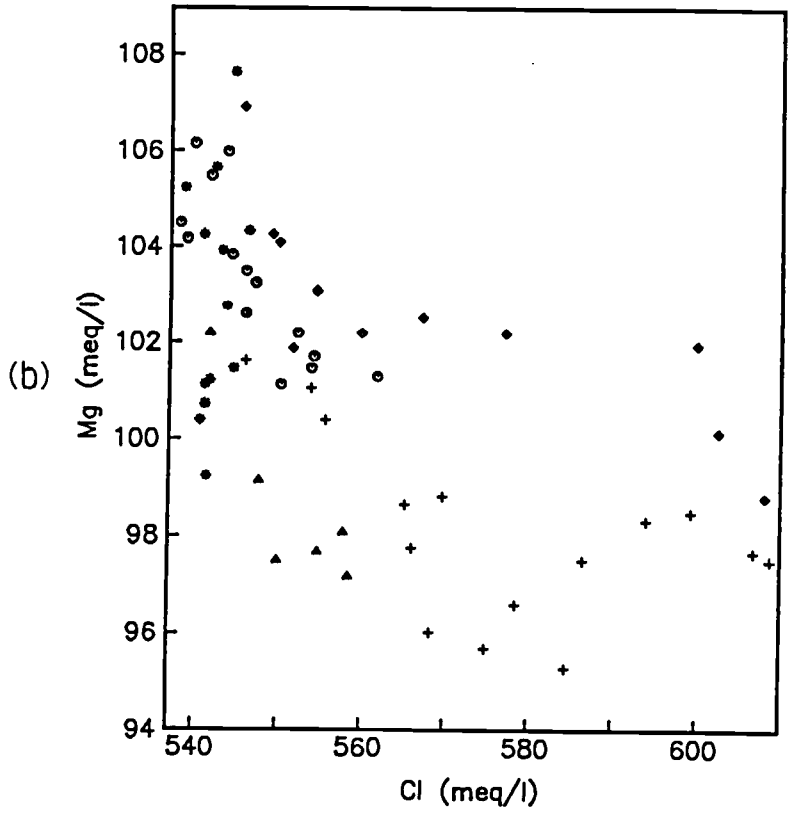
(b)
Mg (meq/l)
108
106
104
102
100
98
96
94
540
560
580
600
Cl (meq/l)

Figure I-10

Table I-6 Results of regressions between each major cation and Cl

Station	Regressions		
	Step 1	Step 2	Step 3
1346	Na = 0.961 Cl - 44.246	Na+Mg+Ca+K / Cl = 1.128	K/Cl = 0.018
	Mg = -0.246 Cl + 234.113		
	Ca = 0.212 Cl -92.334		
	K = -0.171 Cl + 103.081		
1340	Na = 0.683 Cl + 100.886	Na+Mg+Ca+K / Cl = 1.126	Mg/Cl = 0.197
	Mg = -0.209 Cl + 217.722		
	Ca = 0.205 Cl - 89.203		
	K = -0.041 Cl + 32.645		
1341	Na = 0.769 Cl + 52.984	Na+Mg+Ca+K / Cl = 1.145	Mg/Cl = 0.208
	Mg = -0.065 Cl + 139.526		
	Ca = -0.006 Cl + 24.391		
	K = 0.018 Cl + 0.648		
1343	Na = -0.093 Cl + 523.061	Na+Mg+Ca+K / Cl =1.106	Ca/Cl = 0.042
	Mg = -0.050 Cl + 126.934		
	Ca = 0.292 Cl - 136.772		
	K = -0.021 Cl + 22.506		

Table I-7 PHEMC for each hydrothermal station; the units are in meq/l.

Station	Cl	Na	Mg	Ca	K
1346	585.3	518.2	90.1	31.7	3.0
1340	581.6	498.1	96.2	30.0	8.8
1341	647.3	550.8	97.5	20.5	12.3
1343	614.3	465.9	96.2	42.6	9.6
Seawater*	550.5	479.8	109.2	21.1	10.5

*When salinity of seawater is at 19.35 ‰.

was the best. The assignment was repeated until the resulting estimates of the end-member concentrations optimally satisfied both the cation summation/Cl ratio and the ion/Cl regression selected in the Step 3.

The resulting PHEMC for each hydrothermal station is listed in Table I-7. The depth limitation from which pore water chemistry data are available, which is 8 m at the deepest, is the very reason why the estimated composition is "pseudo" hydrothermal end-member composition and a "real" composition. Magnesium in PHEMC is thus not zero as opposed to real hydrothermal end-member compositions found at the mid-ocean ridges (Michard et al., 1984; Von Damm et al., 1985b). However, slow but pervasive hydrothermal activity at low temperature in the King George Basin may never reach complete Mg removal even in real end-member hydrothermal solution.

Mixing of Hydrothermal Pore Fluids

Mixing of PHEMC fluids with unaltered pore water upon their upward migration to the surface are represented by mixing diagrams (Figs. I-11 and I-12). The Cl-concentration was used as an index for the mixing percentage at each pore water datum point under the assumption Cl behaves conservatively after leaving the reaction site.

For each element a simple conservative mixing line was drawn connecting the PHEMC and the unreacted bottom water concentration of that element. Obviously, the extent of mixing varies with depth as well as laterally from station to station. The mixing diagrams indicate that at Stations 1343 and 1340 contributions of hydrothermal waters are the greatest (Figs. I-11 and 12). Data alignment along mixing lines is quite good, indicating in most cases mixing of the PHEMC fluids with unaltered pore water upon their upward migration to the surface without interference from diagenetic reactions. Considering the error involved in the estimation of the PHEMC, the alignments of interstitial Na and K data on mixing lines at each hydrothermal station are

Figure I-11

Mixing diagrams connecting between the PHEMC and unaltered pore water (bottom water) for Na (a) and K (b). Cl-concentration was used as an index for the mixing percentage at each pore water datum point under the assumption that Cl behaves conservatively after leaving the reaction site. Symbols for the hydrothermal core stations are: 1346 (Δ), 1340 (O), 1341(◊) and 1343 (+).

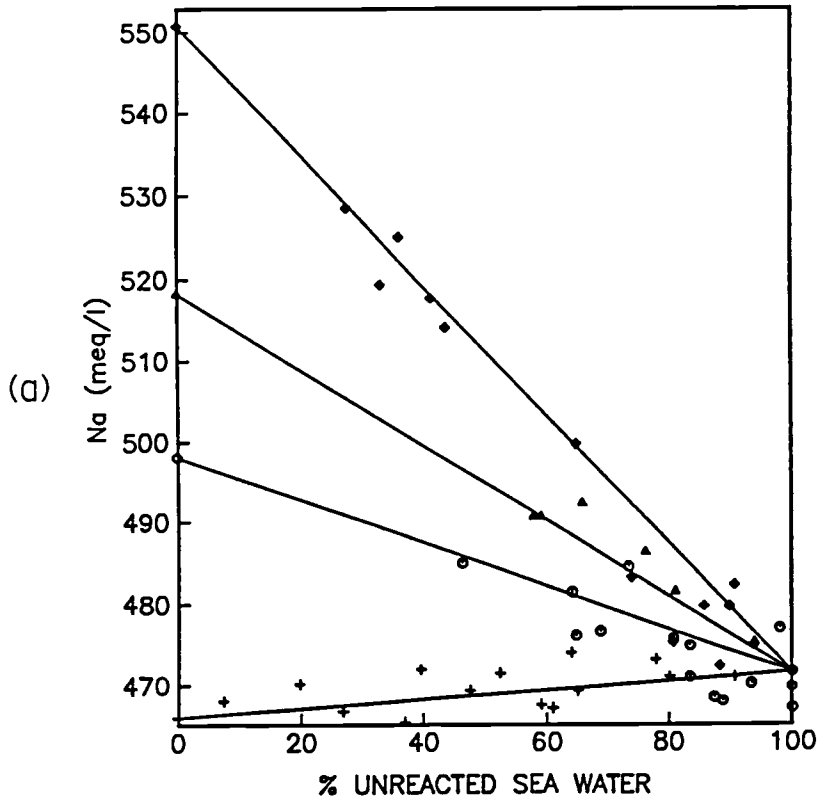
(a)
Na (meq/l)
550
540
530
520
510
500
490
480
470
0
20
40
60
80
100
% UNREACTED SEA WATER

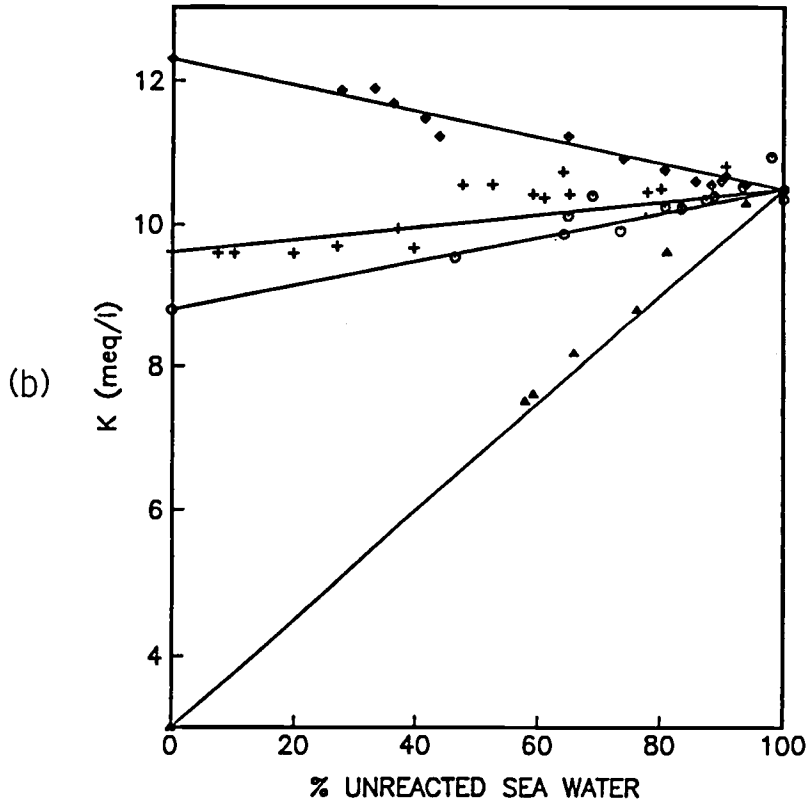
(b)
K (meq/l)
12
10
8
6
4
0
20
40
60
80
100
% UNREACTED SEA WATER

Figure I-11

Figure I-12

Mixing diagrams connecting between the PHEMC and unaltered pore water (bottom water) for Ca (a) and Mg (b). Significant departures of Ca from the mixing lines at 3 stations indicate the involvement of Ca in diagenetic reactions as well as hydrothermal processes. Departures of Mg from the mixing lines are more significant than those for Ca which indicates the involvement of Mg in diagenetic reactions as well as hydrothermal processes. Underestimation of the PHEMC-Mg may also contribute such departures of Mg. Symbols for the hydrothermal core stations are 1346 (Δ), 1340 (O), 1341(◊) and 1343 (+).

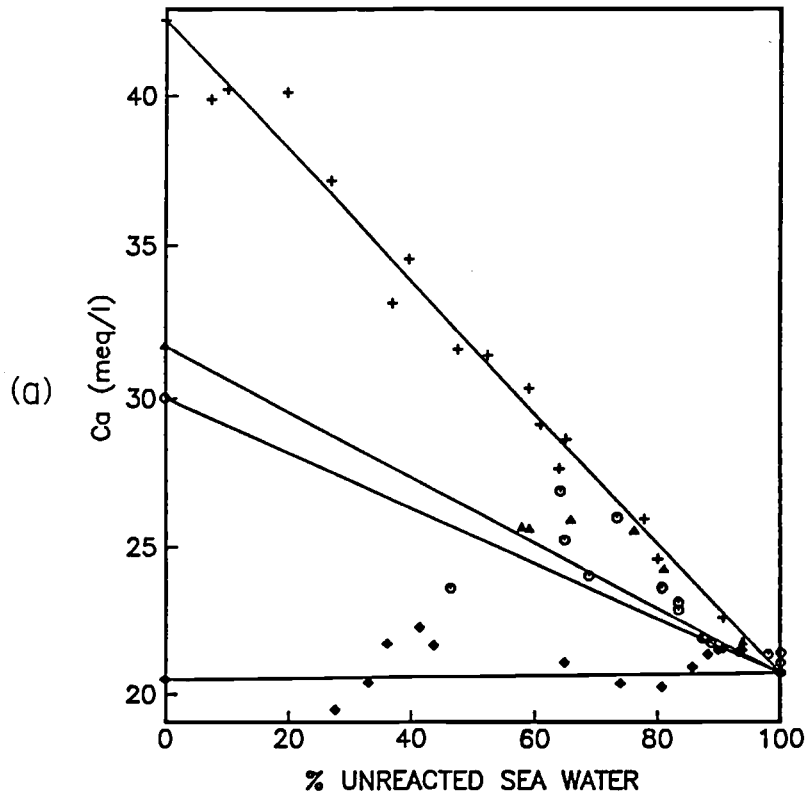
(a)
Ca (meq/l)
40
35
30
25
20
0
20
40
60
80
100
% UNREACTED SEA WATER

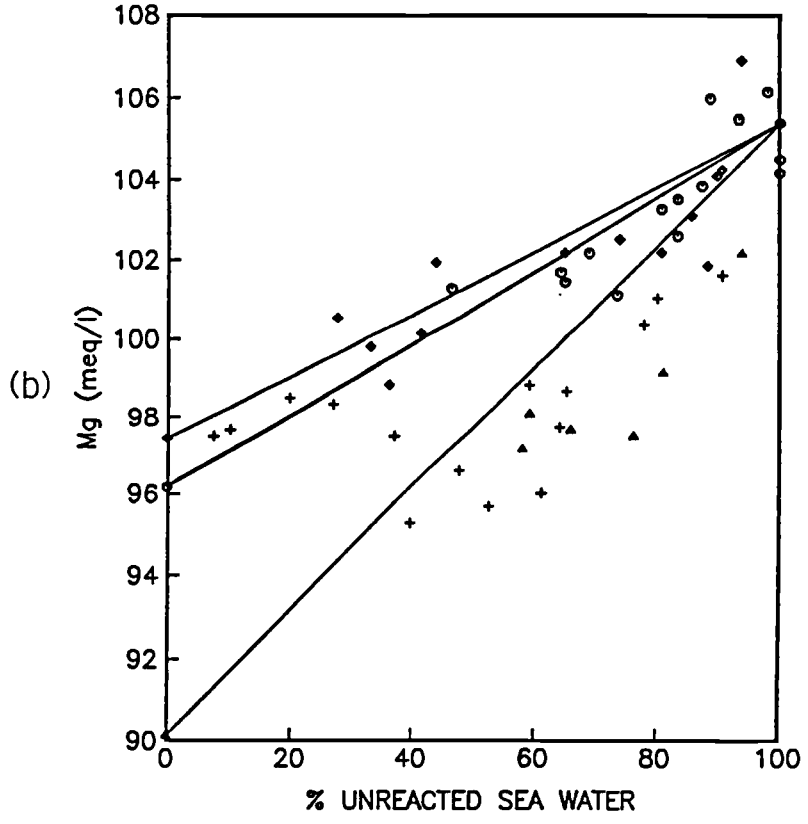
(b)
Mg (meq/l)
108
106
104
102
100
98
96
94
92
90
0
20
40
60
80
100
% UNREACTED SEA WATER

Figure I-12

excellent confirming conservative chemical behavior as was assumed (Fig. I-11).

However, there are significant departures of Ca and especially of Mg from the mixing lines in a complex fashion. This indicates their involvement in diagenetic reactions as well as hydrothermal processes (Fig. I-12). At station 1343 the deeper core section conforms to the predicted mixing model. However, the concentrations of Mg above the 20 % mixing level with unreacted seawater are substantially depleted relative to the predicted concentrations. The depletion may indicate Mg uptake by clays via ion-exchange over the shallow depth where the degree of unreacted seawater is greater than 20 %. A similar trend of Mg-depletion is also evident at station 1346.

Near the sediment-water interface the pore water chemistry data at all hydrothermal stations converge to the composition of bottom water (Figs. I-2, I-4, I-5). This indicates that the intensity of the hydrothermal fluid movement is not strong enough to imprint its signal all the way to the surface, i.e., the flow rates are not sufficient to flush out the bottom water and thus the hydrothermal water dissipates before reaching the sediment-water interface. Therefore, it seems unlikely to observe exiting hydrothermal water discharge through chimneys as in the Guaymas Basin (Lonsdale and Becker, 1985; Merewether et al., 1985). Nonetheless, anomalous ^{3}He and Mn in the bottom water (Schlosser et al., 1987) indicate that hydrothermal discharge reaches the free water column in the King George Basin, perhaps through confined venting pathways rather than diffuse flow through the sediments.

CONCLUSIONS

1. Significant downcore enrichments of both interstitial Cl and the sum of major cations in the eastern end of the King George Basin clearly indicate hydrothermal seawater-basalt reaction underneath the thickly sedimented basin. A new type of technique presenting the sum of major ions vs each major ion was applied to pore water

chemistry data from this basin. This approach differentiates the hydrothermal stations in the eastern end of the basin from the reference station in the central basin.

2. Distinctly anomalous pore water chemistry at depths as shallow as 5 m is direct evidence for the upward migration of hydrothermally-altered solutions. Upward migration of the hydrothermal solution is evident in generally good alignments of pore water data along predicted mixing lines connecting concentrations of a "pseudo" hydrothermal end-member composition (PHEMC) and unreacted pore water (bottom water). This distribution pattern of dissolved species in pore water of the hydrothermal stations is controlled by the degree of mixing between both fluid reservoirs.

3. Cl-enrichment and K-depletion suggest low temperature hydrothermal reaction in the basin (70 to 150 °C). Both basalt hydration and retrograde alteration/dissolution are likely to be the reactions by which the hydrothermal solutions are generated.

4. A low-temperature regime in the basin generates far less intense hydrothermal activities than observed at the Guaymas Basin resulting in a different mode of generation of the hydrothermal petroleum and a lack of substantial secondary reactions between hydrothermal waters and sediments. However, the encounter of the hydrothermal pore fluids as shallow as 5 m below the seafloor indicates that the hydrothermal system is still capable to migrate hydrothermal waters upward.

ACKNOWLEDGEMENTS

We thank the master and crew of the PRSV POLARSTERN, under the direction of the Alfred-Wegener-Institute for Polar Research in Bremerhaven, Federal Republic of Germany, for their outstanding and highly professional assistance at sea. This work was supported by ONR grant N00014-84-C-0218, NSF grant DPP-8512395, and NATO Grant 804/85; we also gratefully acknowledge financial support from the Oregon State University Foundation.

CHAPTER II

LATERAL MIGRATION OF PORE FLUIDS THROUGH SEDIMENTS OF AN ACTIVE BACK-ARC BASIN: BRANSFIELD STRAIT, ANTARCTICA

ABSTRACT

Vertical movements of pore fluids through sediments covering hydrothermal circulation systems have either been directly observed or inferred from chemical and thermal gradients across active spreading centers and plate convergence zones (Maris and Bender, 1982; Anderson et al., 1979; Kulm et al., 1986). Lateral movement of pore water, although an obvious connection between discharge and recharge pathways of such fluid circulation systems, has not been documented. We report on the first evidence for lateral movement of hydrothermally-altered pore fluids in sediments of the Bransfield Strait, an actively spreading back-arc basin between the Antarctic Peninsula and the South Shetland Islands. The chemical and morpho-tectonic evidence presented here shows that pore fluids move laterally through permeable turbidites from the south to the north across the basin. A numerical model suggests an average advection rate of 7 cm/yr. The lateral flow is fed from a recharge area, where bottom water is drawn down through fault planes along the topographically lower southern margin of the basin and discharges along the topographically higher margin in the north. The up-dip migration of the laterally-moving pore fluids connects recharge and discharge areas, thereby delineating a hydrothermal circulation cell in the Bransfield Strait basin. The migration toward the north is favored by the lithologic fabric and texture of the distal turbidite layers. Submarine volcanic activity related to back-arc spreading appears to drive a fluid circulation cell by thermal input.

INTRODUCTION

Information on the extent and magnitude of pore water circulation is important for refining the geochemical mass balance in the ocean because it generates new sources and sinks for net mass transport of elements (Von Damm et al., 1985a; Thompson, 1983). Recent discoveries of pore water advection and venting over large areas of

sedimented ridge flanks and in the subduction zones of the global plate tectonic framework, (Gieskes et al., 1986; Boulegue et al., 1987; Sayles and Jenkins, 1982; Maris et al., 1984) suggest the need for detailed studies of pore water circulation in order to revise and update the geochemical mass balances, although this is not a simple task.

Downcore concentration profiles of pore water chemistry across sedimented mid-ocean ridge flanks have provided evidence for either upward or downward movement of hydrothermally-altered fluids (Sayles and Jenkins, 1982; Maris et al., 1984). Although lateral migration has been regarded as an inevitable link between discharge and recharge of hydrothermal circulation, usually a complex topography and resulting complex flow pattern have prevented any lateral flow components from being identified. In many cases regional sample spacing was also inadequate, relative to the dimensions of circulation cells, for direct observation of lateral flow (Maris et al., 1984). Fortunately, a simple topography, structure and sediment blanket, consisting of distal turbidites interlayered with more hemi-pelagic sediment units, in the active back-arc basin of the central Bransfield Strait (Fig. II-1) serves as an ideal site to examine and document the lateral movement of water in a hydrothermal convection cell.

BACKGROUND AND OBJECTIVES

Active rifting associated with back-arc spreading in the Bransfield Strait during the last 1.4 m.y. has generated a series of basins with generally normal faults bounding the northern and southern margins of the strait (Barker and Dalziel, 1983; Guterch et al., 1985). In the basin of the central Bransfield Strait, however, normal faults develop, at least at present, predominantly along the southern margin. A sediment cover, thickening southward and turbidite layers dipping in the same direction, are

Figure II-1a

Bathymetry and sediment isopach map of the eastern King George Basin. The sediment cover thickens toward the south of the basin. Cores were obtained from the zone of acoustic turbidity shown in shallow seismic records: from the south to the north, 1346 (Δ) - 1340 (O) - 1140 (*) - 1341 (◊) - 1343 (+). The acoustic turbidity appears to delineate the area of hydrothermal activity and submarine volcanism in the basin. Fresh glassy pillow basalts were dredged from the surrounding extrusions; hydrothermal petroleum was detected in all cores from this area; normal faults develop along the southern margin of the basin.

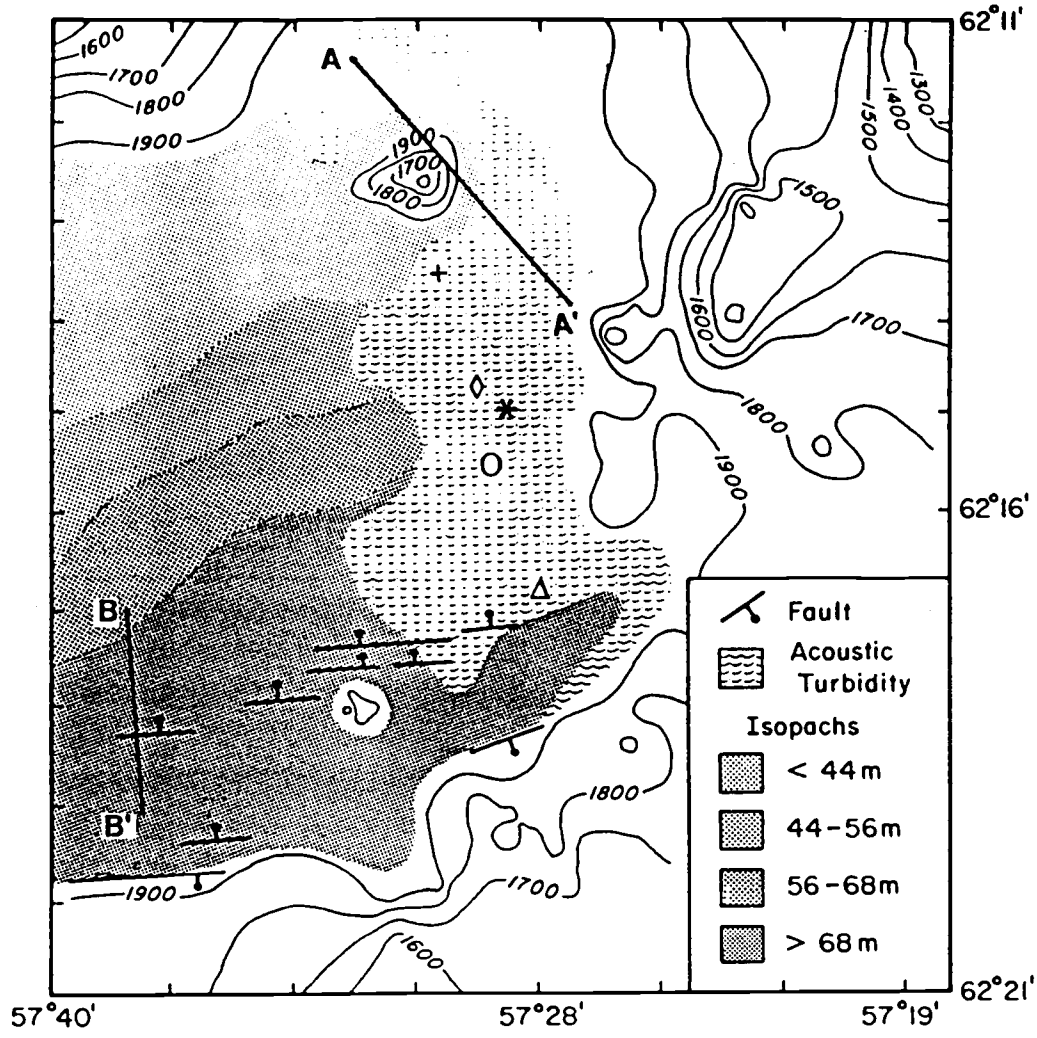
62°11'
62°16'
62°21'
57°40'
57°28'
57°19'
A
A'
B
B'
1600
1700
1800
1900
1500
1400
1300
Fault
Acoustic Turbidity
Isopachs
< 44 m
44-56m
56-68m
> 68 m

Figure II-1a

Figure II-1b

3.5 kHz records across the eastern King George Basin (line A-A' in Fig. II-1a) showing subsurface acoustic turbidity (dotted pattern); note acoutic transparency surrounding volcanic extrusion. Partial 3.5 kHz record across the central King George Basin showing southward dipping reflectors from turbidites, normal faulting, a volcanic intrusion, as well as the basin floor deepening from 1940 m to 1995 m (line B-B' in Fig. II-1a).

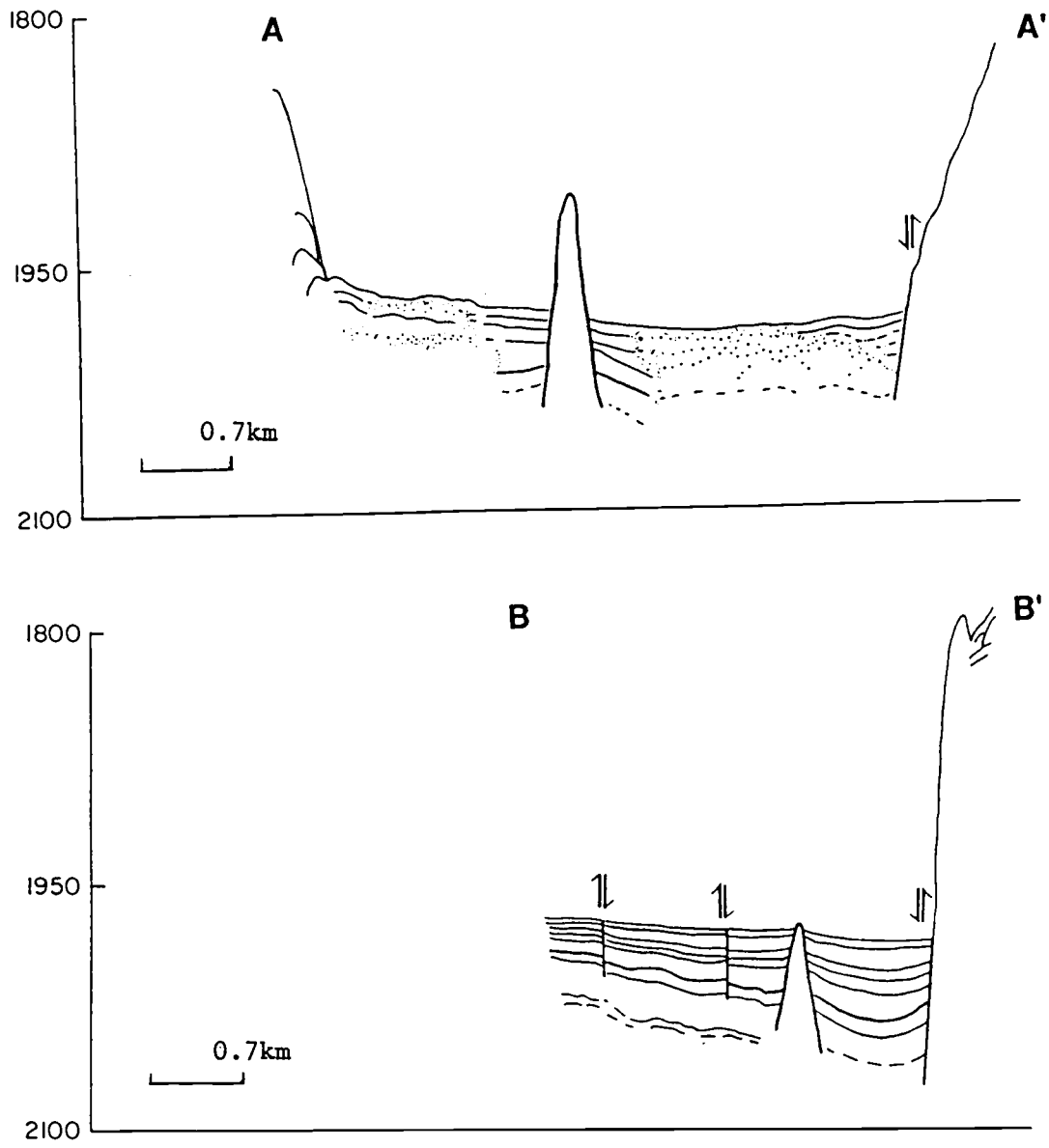

Figure II-1b

believed to be associated with this predominant fault distribution in the south (Fig. II-1). Besides the volcanic activity observed as recently as the early 1970s in Deception Island (Roobol, 1982), which is located along the axis of the Bransfield Strait with the projected intersection of the Hero Fracture Zone, submarine volcanism has been detected in the basin of the central Bransfield Strait farther east. An acoustically turbid zone -- as recorded by 3.5 kHz seismic profiling -- has developed adjacent to the volcanic features of seamounts and subsurface intrusion, which are concentrated in the eastern part of the basin (Fig. II-1). Although we suspect that the acoustic turbidity is ultimately related to such submarine volcanic activity, the specific physical cause remains speculative. For instance, acoustic turbidity zones in shallow seismic profiling are normally attributed to methane gas bubbles (Ben-Avraham, 1986), however, methane contents in the central Bransfield Strait basin are not high enough for the formation of free gas although methane and other light hydrocarbon gases have been detected (Whiticar et al., 1985).

Four cores were obtained from the acoustically anomalous zone along a NW-SE transect across the eastern part of the basin floor. In this area the extrusion of fresh pillow basalt and the seepage of thermogenic petroleum had suggested a pattern of hydrothermally-driven fluid migration (Fig. II-1). Such hydrothermal activity beneath the sedimented Bransfield Strait basin is distinctly evident in the pore water chemistry which shows a downcore Cl-enrichment, 5 to 14% over that of normal seawater chlorinity, and a corresponding increase in the sum of the major cations Na, Mg, Ca, and K. This evidence has been discussed in Chapter I.

This Chapter addresses the dynamics of lateral movement of such altered fluids and mixing with drawn-down bottom water of oceanic composition.

EVIDENCE FOR LATERAL MIGRATION

Sulfate Profiles

We first suspected lateral fluid movement from the unusual concentration profiles of pore water sulfate (Fig. II-2) because (1) all profiles developed a sulfate minimum and (2) in all cores the sulfate increments below the minima diminished systematically from the south to the north across the basin. Pore water sulfate, commonly decreases rapidly and is completely removed at depth due to sulfate reduction in these organic carbon-rich sediments. This was amply documented in pore water profiles obtained outside the acoustic turbidity zone (Suess et al., 1982; Whiticar et al., 1987). Rapid sulfate reduction by microbial activity is also reflected in the sulfate profiles from the acoustic turbidity zone by first decreasing towards the sulfate minima just below the water-sediment interface. However, the subsequent increase in sulfate is not explained readily without recharge of sulfate-containing bottom water from the basin. Besides, this sulfate increase with depth is contrary to what is expected during hydrothermal activity at depth below the sea floor, because sulfate is normally removed in hydrothermal reactions (Edmond et al., 1979).

Lateral mixing of bottom water, unaffected by sulfate reduction, with sulfate-free deep pore fluids, and possibly continued sulfate reduction along the flow path, may explain the sulfate increase at depth below the minima zone. First, the sulfate increase suggests supply from a distant source of water having a less altered sulfate composition than the pore water which is in contact with the organic carbon-rich sediments. This pore water, we suggest, moves laterally across the basin from the south to the north causing the systematic change in the sulfate increment along its path between stations (1346, 1340, 1140, 1341, and 1343). Second, the source and draw-down of sulfate-rich bottom water must be along the southern basin margin. The smooth and

Figure II-2

Concentration profiles of sulfate with depth. The sulfate minimum zone is delineated by the double-dotted line across the basin. At each station microbial sulfate reduction lowers sulfate towards the sulfate minimum zone. Below the zone, however, sulfate increases again with depth. Furthermore this sulfate increment shows a systematic decrease from the southern station to the northern station (1346 (Δ) - 1340 (O) - 1140 (*) - 1341 (◊) - 1343 (+)). Methods of analysis for the interstitial chemistry are described in Chapter I.

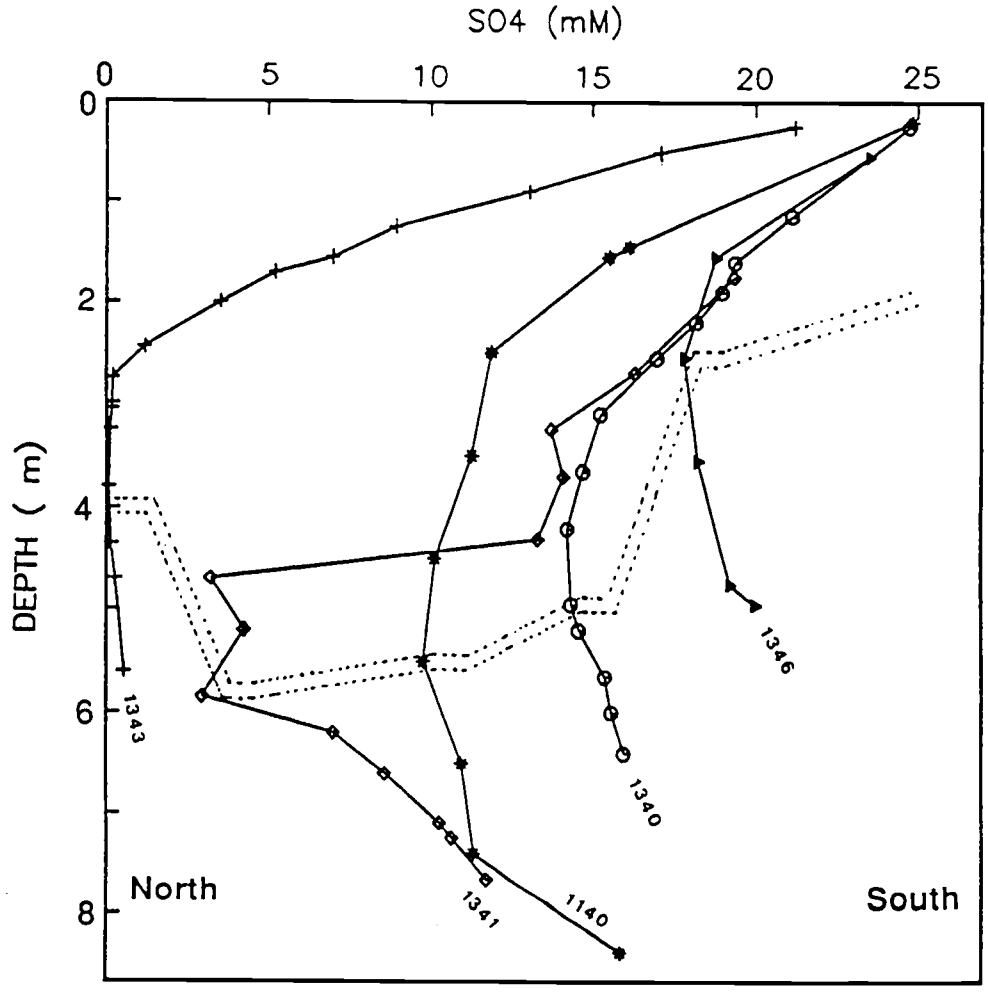
SO4 (mM)
0
5
10
15
20
25
0
2
4
6
8
DEPTH (m)
North
South
1343
1341
1140
1340
1346

Figure II-2

flat sedimented floor of the basin dips gently toward that direction (Fig. II-1) and normal faults develop predominantly along the southern margin. These faults off-set the turbidite layers and leave scarps as their surface expressions indicating that vertical tectonic movement is still active. Unlike a subaerial fluid circulation system, the topographically lower part of the Bransfield Strait basin must be the site for recharge in this particular submarine system (Stefansson, 1983). We hypothesize that bottom water is drawn down through those fault planes which constitute recharge sites and moves up-dip from a topographic low in the south to a topographic high in the north. Core 1140 located between stations 1340 and 1343 was recovered two year earlier than the ANT IV Leg 2 cruise to the area in November, 1985. The sulfate profile of the station 1140 fits surprisingly well between the profiles of the two core stations, 1341 and 1343. This agreement further supports the lateral migration scheme of pore fluids across the basin.

The two-dimensional sulfate distribution pattern suggests that lateral migration affects the sulfate above the minima zones as well. The greater influence of recharge water, rich in sulfate, is evident in a less pronounced sulfate reduction toward the southern stations (previously referred to as the sulfate increment) as well as in a more gentle sulfate reduction gradient. Sulfate gradients (dc/dz) in organic carbon-rich near-surface sediments are known to be linearly related to sedimentation rate (Berner, 1978). Accordingly, the more gentle sulfate gradients at the southernmost stations would imply slower sedimentation rates than in the north of the basin. Although detailed sedimentation rates are not available over the critical area (Whiticar et al., 1987), the thickening turbidite layers southward and the general sediment isopachs suggest instead higher sedimentation rates toward the south. Therefore, the more gentle sulfate gradients above the minima must be controlled primarily by the descending fresh bottom water than by sulfate reduction controlled by different sedimentation rates.

Chloride Profiles

Consistent with this qualitative fluid dispersal pattern inferred from the interstitial sulfate distribution, but more importantly, the dissolved chloride profiles also indicate lateral flow. Due to the chemically conservative nature of chloride its distribution pattern affords a quantification of flow rates and flow direction. Chloride is enriched in pore fluids above that of bottom water in all stations from low-temperature hydrothermal basalt seawater reactions at depth far below the coring limits (Han and Suess, 1987b; Seyfried et al., 1986). Again, there is a systematic trend from south to north in the chloride concentration profiles. The largest enrichment, e.g. 21.5 ‰ versus 19.1 ‰ Cl, was observed at station 1343 in the north; from there chloride decreased gradually southward. Such a distribution is consistent with lateral migration of pore fluids. Bottom water, having oceanic chlorinity (19.1 ‰) is drawn-down in the south, flows north, and acquires excess chloride along its path. The chloride enrichment in the northern stations (1343 and 1341) suggests either a greater extent of hydrothermal reaction or a diminishing influences of the drawn down bottom water flowing to the northern stations, or both.

Due to the conservative behavior of chloride, as opposed to sulfate, within the 6 m thick sediment package cored, the chloride distribution could be applied to a two-dimensional diffusion-advection model in order to obtain flow rates. The general flow direction was established from the sulfate distribution. Obviously, chloride must have behaved non-conservatively during hydrothermal seawater-basalt reaction, however, since the reaction site is well below the depth of core penetration, chloride is considered to behave conservatively within the spatial limits of the model. The two-dimensional model applied is:

$$D_x \, d^2C / dx^2 + D_z \, d^2C / dz^2 - u \, dC / dx - w \, dC / dz = 0 \qquad (1)$$

where C is the chloride concentration, x and z are horizontal and vertical distances, respectively; u and w are their component velocities, and D_x and D_z are diffusion coefficients, with respect to x and z. Equation (1) was solved numerically by finite difference approximations (Gerald and Wheatley, 1984). Under the known boundary conditions (constant bottom water chlorinity of 19.1 ‰ and the measured interstitial chloride data) and the given diffusion coefficients of chloride (10^{-6} cm^2/sec and 10^{-5} cm^2 /sec for D_x and D_z respectively). The numerical solution was arranged to accept arbitrary velocity vectors, hence permitting simulation of u and w by iteration. A computer program for the simulation is listed in the Appendix II and the measured interstitial chloride data in Appendix I. The results of the numerical simulation are shown in Figs. II-3 and II-4. The numerically-drived distribution of chloride simulates the pattern of measured chloride quite well when the nodal point velocities shown in Fig. II-4 are satisfied.

The absence of hydrologic information from the basin makes it impossible to compute flow rates from the governing equation of ground water flow (Bear, 1972); furthermore, the governing equation should be coupled with the energy equation (Bear, 1972) as velocity field results from pressure gradients caused by potentiometry and thermal bouyancy from the hydrothermal activity in the basin. Our numerical simulation which is, in essence, a curve fit to the two-dimensional chloride distribution, is thus a kinematic approach. Because of this approach the magnitude obtained for flow may not represent real rates. Nonetheless Fig. II-4 supports the horizontal flow of pore fluids inferred from both the sulfate and the chloride distributions, and specifies the migration pattern in detail by the flow vectors for u and w.

Figure II-3

Two-dimensional distribution pattern of the measured chlorosities (‰) (a). Two-dimensional distribution pattern of the numerically-driven chlorosities from Eq. (1) (b). The distance between coring sites is in km.

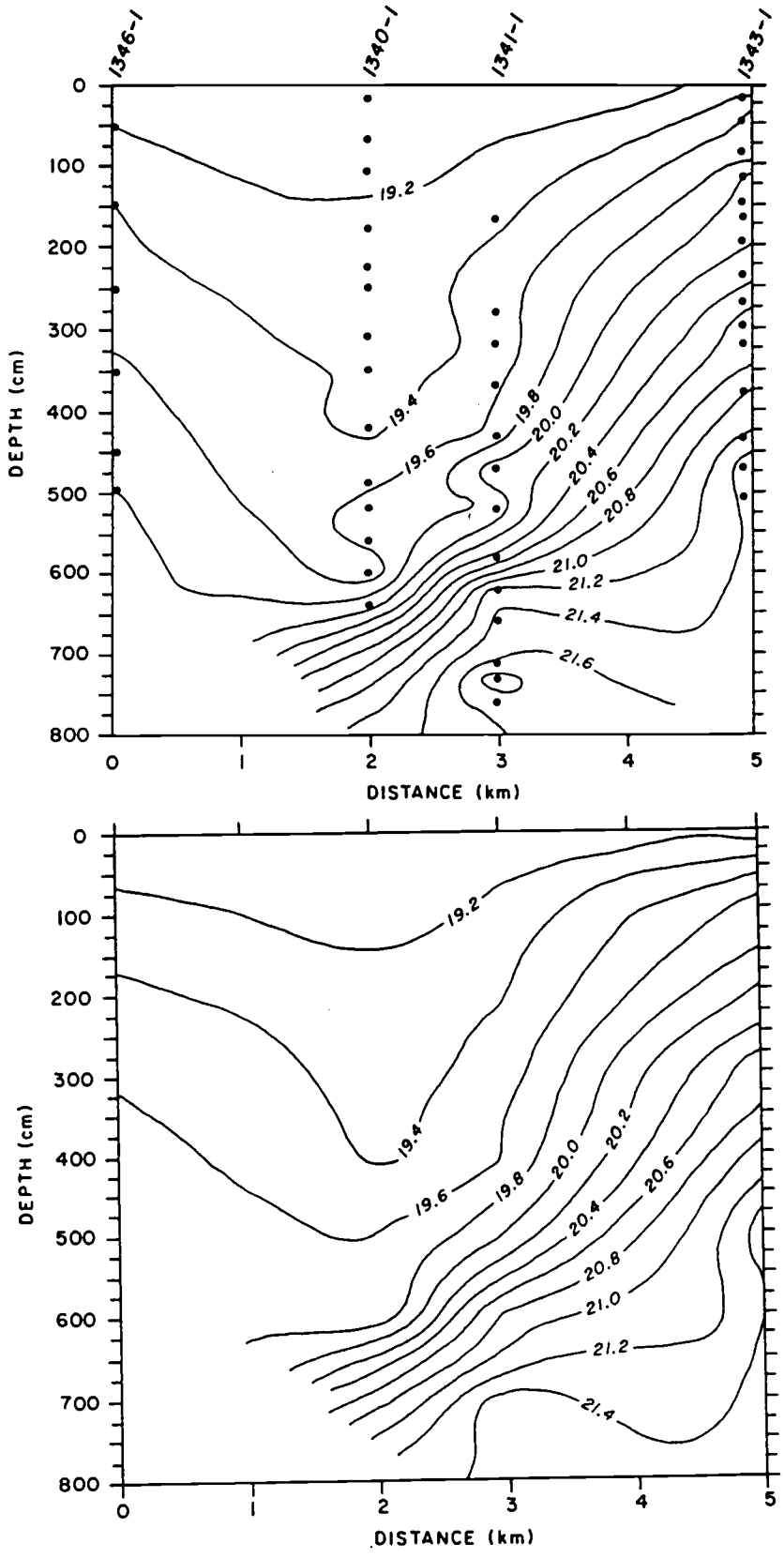
1346-1
1340-1
1341-1
1343-1
DEPTH (cm)
DISTANCE (km)
19.2
19.4
19.6
19.8
20.0
20.2
20.4
20.6
20.8
21.0
21.2
21.4
21.6

Figure II-3

Figure II-4

Velocity vectors of the predominantly lateral pore fluid flow; the component vectors shown best simulate the measured chlorosity distribution (Fig. II-3b).

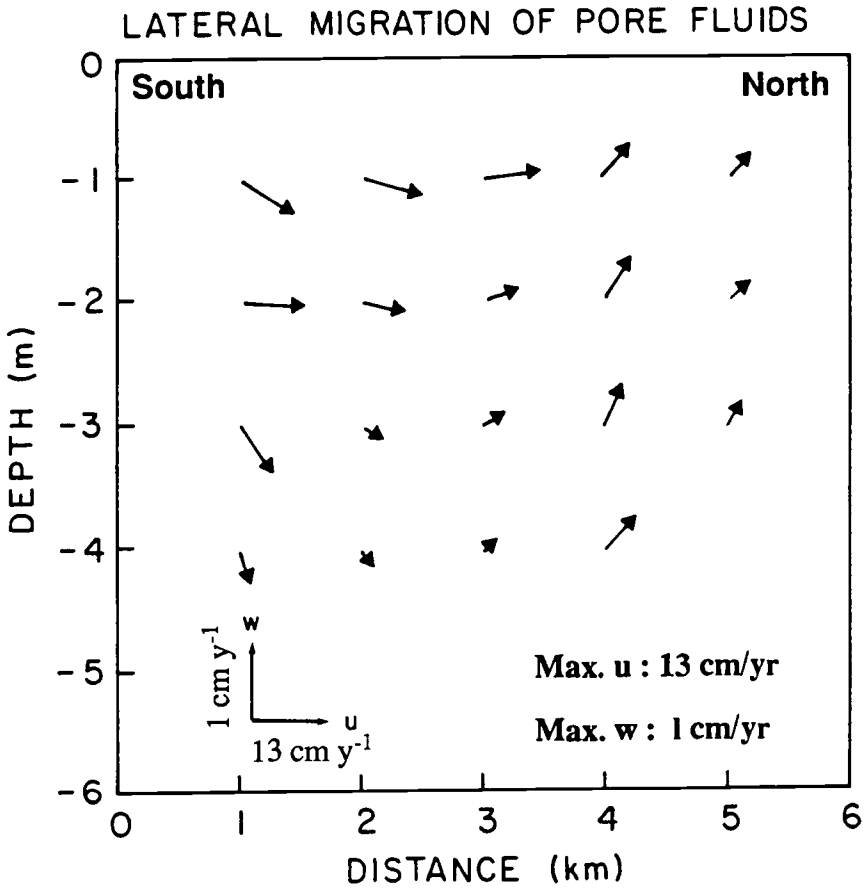
LATERAL MIGRATION OF PORE FLUIDS
South
North
DEPTH (m)
0
-1
-2
-3
-4
-5
-6
0
1
2
3
4
5
6
DISTANCE (km)
w
1 cm y-1
u
13 cm y-1
Max. u : 13 cm/yr
Max. w : 1 cm/yr

Figure II-4

Figure II-5

Lithology, sediment texture, and structural fabric of the cores 1346, 1340, 1341, and 1343. Coarse turbidite beds, with 60 - 95 % sand, are interlayered with homogeneous hemipelagic units of silty-clay . A similar lithologic sequence was also observed in a kasten core from the central Bransfield Strait basin to the west of our study area (Holler, 1985). This suggests the occurrence of the same lighologic units across the entire basin. Hydrothermal petroleum layers were encountered in the lower portions of all cores.

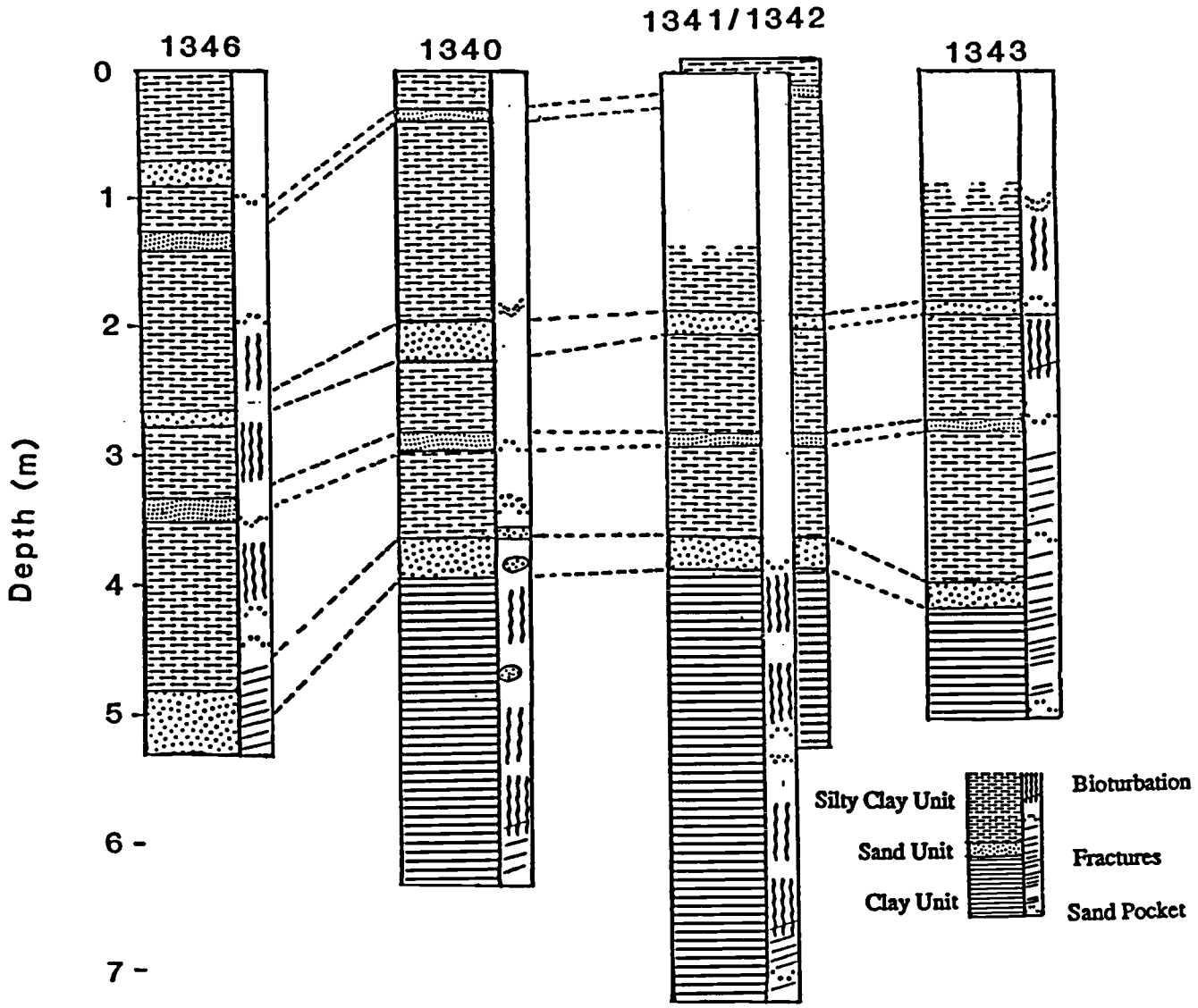
1346
1340
1341/1342
1343
0
1
2
3
4
5
6
7
Depth (m)
Silty Clay Unit
Sand Unit
Clay Unit
Bioturbation
Fractures
Sand Pocket

Figure II-5

The lateral fluid flow slows down toward the north. Consequently, a gradual increase in the upward flow component becomes apparent toward that direction resulting in up-dip migration of the pore fluids across the basin. Sediment texture of all cores across the basin (Van Enst and Laban, 1987) validates the fluid migration pattern. The textural and structural information summarized in Fig. II-5 reveals distinctive and correlatable turbidite layers (50-95% sand size fraction) whose geometry is consistent with the inferred fluid migration pattern. Interlayering of permeable turbidite with less permeable hemipelagic sediment units in the basin facilitates horizontal transport over transverse diffusive transport across the bedding from highly permeable to less permeable layers.

CONCLUSIONS

Based on the lateral migration velocity field (Fig. II-4) together with the distributions of sulfate and chloride, we propose that (1) the basin water of oceanic sulfate and chloride composition is recharged along fault planes of the southern margin; (2) upon descend it mixes with hydrothermally-altered pore water having elevated chloride and diminished sulfate contents; (3) subsequent discharge occurs along the northern margin as diffuse flow through sediments; and (4) the up-dip migration of the moving pore fluids connects recharge and discharge areas thereby delineating a horizontally-compressed hydrothermal circulation cell in the King George Basin.

This fluid flow scheme is consistent with the lithologic properties of the sediment cover (Fig. II-5), the topography, and the morpho-tectonic features of the Bransfield Strait basin (Fig. II-1). Normal faults associated with back-arc rifting develop scarps along the southern margin creating recharge sites in which the bottom water is drawn down. Toward the northern margin of the basin, active submarine volcanism favors discharge site. The rate of discharge is slow (1 cm/yr vertical component) as the model

predicts. Thus vent-type discharge is not expected, instead the upward flow would be more like a steady percolation through and from within the sediment cover. The seismic acoustic turbidity in the near surface sediments may be due to this type of pore fluid movement primarily causing density changes and probably destroying the structure of the sediments causing acoustic voids. Extensive fracturing was observed in the deeper sections of the hydrothermal cores. The up-dip migration toward the north is favored by the lithologic fabric and texture of the distal turbidite layers.

ACKNOWLEDGEMENTS

We thank the master and crew of the PRSV POLARSTERN, under the direction of the Alfred-Wegener-Institute for Polar Research in Bremerhaven, Federal Republic of Germany, for their outstanding and highly professional assistance at sea. This work was supported by ONR grant N00014-84-C-0218, NSF grant DPP-8512395, and NATO Grant 804/85; we also gratefully acknowledge financial support from the Oregon State University Foundation.

CHAPTER III

SUBDUCTION-INDUCED PORE FLUID VENTING AND THE FORMATION OF AUTHIGENIC CARBONATES ALONG THE OREGON/WASHINGTON CONTINENTAL MARGIN: IMPLICATIONS FOR THE GLOBAL Ca CYCLE

ABSTRACT

Pore fluid venting associated with subduction-induced sediment deformation causes precipitation of calcium carbonate in prominent carbonate chimneys and in cementation of the accreted sediments across the active continental margin off Oregon and Washington. A concurrent strong downcore depletion of interstitial Ca (maximum 50 % decrease over only 1.5 m depth) and reduction in porosity in the deformed sediments suggest that interstitial Ca is removed. In contrast, in the pore waters of the undeformed abyssal plain sediments, where the background level of $CaCO_3$ content is only 0.1 to 1 %, interstitial Ca is enriched (maximum 5 % increase over the same 1.5 m depth). Calcium carbonate precipitation probably occurs as the result of migration and oxidation of biogenic methane, which provides a pool for the carbonate ion, and of the increase in carbonate saturation due to release of excess pore pressure during fluid venting. Upward advection of fluids at rates of 6-28 cm/yr is predicted from a diffusion-advection- reaction model applied to the vertical distribution of dissolved Ca and NH_3 in the tectonically-deformed sediments. The range of predicted flow rates is related to the type of calcium carbonate lithification; i.e. slow rates generate cement only and fast rates result in chimney formation.

Lithification by calcium carbonate requires direct transfer of crustal Ca to the accretionary complex, leached out of basalt during alteration reaction at the basement. Such a mechanism leads us to propose that the accretionary complexes of the global plate subduction zones are a major sink for crustal Ca. When extrapolated to a global scale, Ca-removal by the subduction zones is estimated to be 31×10^{12} g/yr. This is about one-half of the commonly accepted estimates of hydrothermal Ca-input and less by a factor of fifteen than river input of dissolved Ca to the ocean. This significant sink of Ca, not previously considered in the global geochemical budget, implies that pore fluid venting in subduction zones may also act as a global sink or source for other

elements.

INTRODUCTION

Recent discoveries of carbonate chimneys and benthic communities of tube worms and giant clams associated with pore fluid venting in subduction zones (Kulm et al., 1986; Schroeder et al., 1987; Cadet et al., 1987) suggest a new mechanism that may affect the global seawater composition (i.e. pore fluid venting and exchange of elements with the subducting crust). One could foresee an important role of pore fluid venting at global subduction zones in the chemical mass balance of the oceans if the areal extent of fluid venting and the magnitude of mass transfer can be established. Although it is unclear at present if this process is similar in magnitude to that of mid-ocean ridge hydrothermal fluxes, both are ultimately related to the major tectonic processes of plate generation and consumption. Prominent carbonate precipitation and cementation of near-surface sediments associated with pore fluid venting occurs not only in the accretionary complex of the northeast Pacific but also along several other convergent margins: the Barbados accretionary complex (Moore et al., 1986a), the Nankai trough sediments (Cadet et al., 1987), and the Peru convergent margin (Kastner et al., 1987). This world-wide distribution allows us to consider a revision of the global Ca-balance (Thompson, 1983; Von Damm et al., 1985a) by including subduction-induced calcium carbonate precipitation as a major sink for calcium.

Since prominent carbonate precipitates (carbonate chimneys and crusts) in the accretionary complex off Oregon/Washington are associated with venting pore fluids, an understanding of the geochemical condition of the calcium carbonate system of the interstitial waters is essential in order to explain the formation of the pervasive carbonate lithification. Interstitial Ca in near-surface sediments is in general controlled by biogeochemical processes of early diagenesis related to organic matter decomposition

which generates an excess of total dissolved CO_2. Carbonate precipitation, as opposed to dissolution in pelagic environments, was observed in hemipelagic environments of rapid burial of sediment rich in organic matter (Kawahata and Fujioka, 1986; Moor and Gieskes, 1980; Suess et al., 1982; Stein and Smith, 1986). The mechanism for precipitation of calcium carbonate in these environments is likely associated with the biogenic methane formation (Claypool, 1974).

The Oregon/Washington accretionary complex receives hemipelagic sediments from the Columbia River drainage basin and the weathering of the Coast Range at a fairly rapid rate of around 10 cm/1000 yr (Krissek 1982; Karlin 1979). Characteristically these sediments are extremely low in detrital calcium carbonate content. Therefore the prominent chimneys, crusts and calcium carbonate cement are not due to natural sedimentation but are the result of dynamic control on the dissolved calcium carbonate system associated with pore fluid venting. Venting apparently provides favorable geochemical conditions for the precipitation in the accretionary complex. In this paper we investigate, based on pore water chemical compositions from the Oregon/Washington subduction zone, the mechanism of carbonate mineral precipitation associated with pore fluid venting. We then evaluate the potential role of this process in removing crustal Ca and finally speculate on the implications for the global balance of Ca.

GEOLOGIC SETTING AND METHODS

The Juan de Fuca oceanic plate, generated at the spreading Juan de Fuca Ridge, is presently subducted off Oregon and Washington as it converges with the North American plate at a rate of 4 cm/yr (Wells et al., 1984) (Fig. III-1). A portion of the sediments loaded on the subducting plate is off-scraped and added onto the overriding North American plate forming an accretionary complex along the lower continental

slope (Silver, 1972; Carson et al., 1974; Kulm and Fowler, 1974). The accretionary complex consists of a series of folded and thrusted ridges trending perpendicular to the convergence direction (Kulm et al., 1986; Silver, 1972; Carson et al., 1974). The ridges become progressively older from west to the east across the complex. The youngest ridges of the deformation front are less than 0.3 m.y. old and rise from 400 to 1000 m above the adjacent abyssal plain (Kulm et al., 1986; Carson et al., 1974).

The mode of occurrence and the morphology of the carbonates in near-surface sediments of the accretionary complex are diverse: slabs, crusts, and disseminated cement are found throughout the near-surface sediments. Their mineralogies, isotopic compositions, and fabric have been extensively studied (Russell et al., 1967; Scamman, 1981; Ritger et al., 1987). Conical chimneys, 1 to 2 m in height protruding above the sea floor, were found associated with the benthic communities of tube worms and giant clams on the marginal ridge of the deformation front in the Oregon accretionary complex (Kulm et al., 1986). Other carbonate chimneys were discovered on the outermost continental shelf off northern Oregon (Schroeder et al., 1987) (Fig. III-3). Generally all carbonates are strongly depleted in the carbon isotope ^{13}C. The depletion is characteristic of organic-derived calcium carbonates (Kulm et al., 1986; Suess et al., 1987a). Hollow tubes and passages with numerous grooves and flutes within all the chimneys are thought to be the imprints of venting fluids (Schroeder et al., 1987; Kulm et al., 1987). Pure carbonate precipitates which build up the chimney structures indicate an authigenic mode of formation (Schroeder et al., 1987; Ritger et al., 1987).

Figure III-1a

Subduction zone off Oregon and Washington. The Juan de Fuca plate is presently subducted off Oregon and Washington as it converges with the North American plate. An accretionary complex forms along the lower continental slope off Oregon and Washington by off-scraping sediments loaded on the subducting plate and adding onto the overriding North American plate. The areas of investigation are marked along with DSDP cores of 174 and 176.

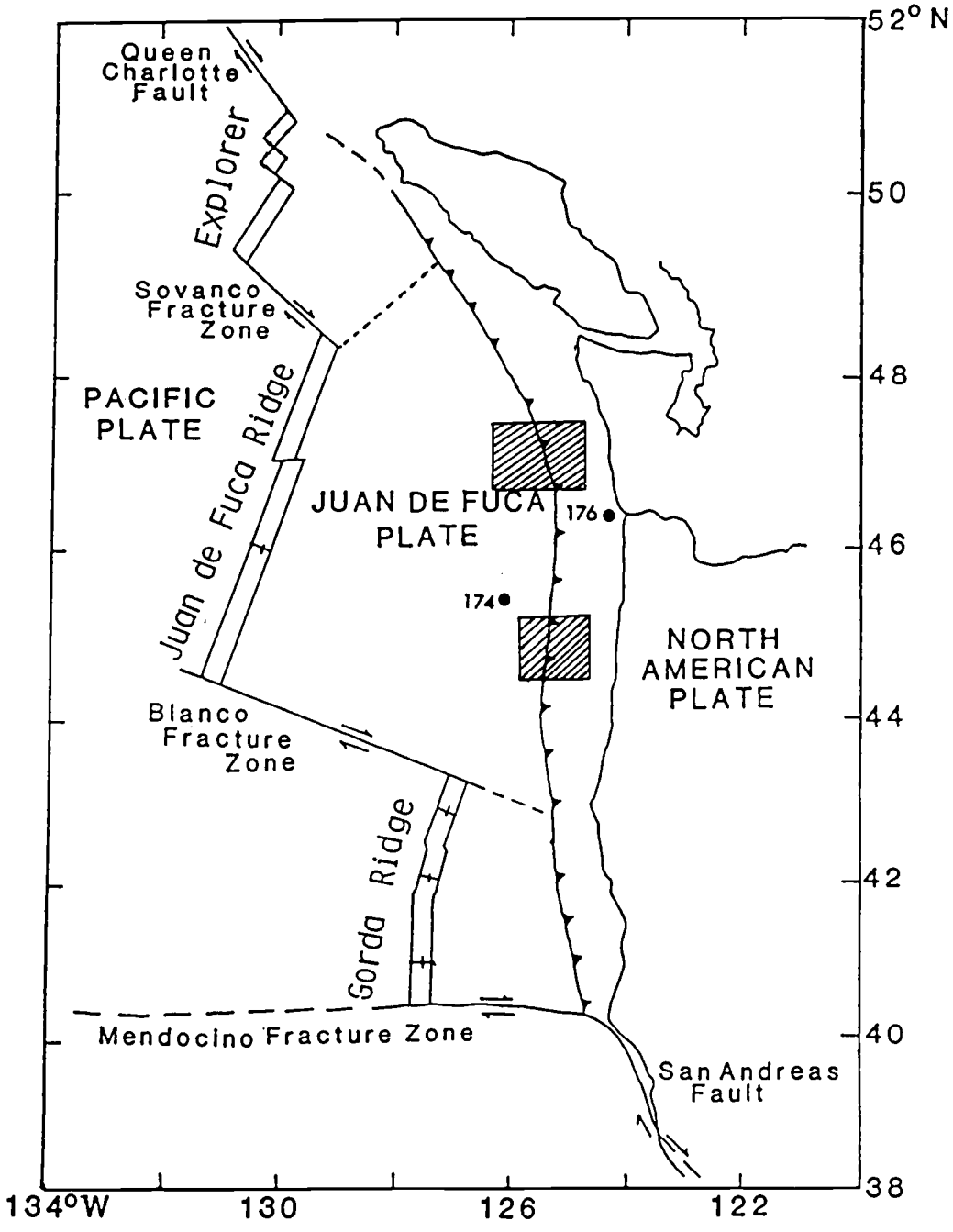

Figure III-1a

Figure III-1b

Enlarged areas of investigation in Fig. III-1a: Washington accretionary complex (above) and Oregon accretionary complex (below). Dots indicate core stations. Area A is referred to as Washington underthrust region. There are five core stations along the northern profile and four core stations along the southern profile in the area A. The circled core station along the southern profile denotes a sea mount in the location, which is interpreted as mud volcano (Kulm, personal communication). Area B is referred to as Oregon overthrust region. There are six core stations in this area. Area C is referred to as Oregon underthrust region. There are seven core stations in this area. Contours in meters.

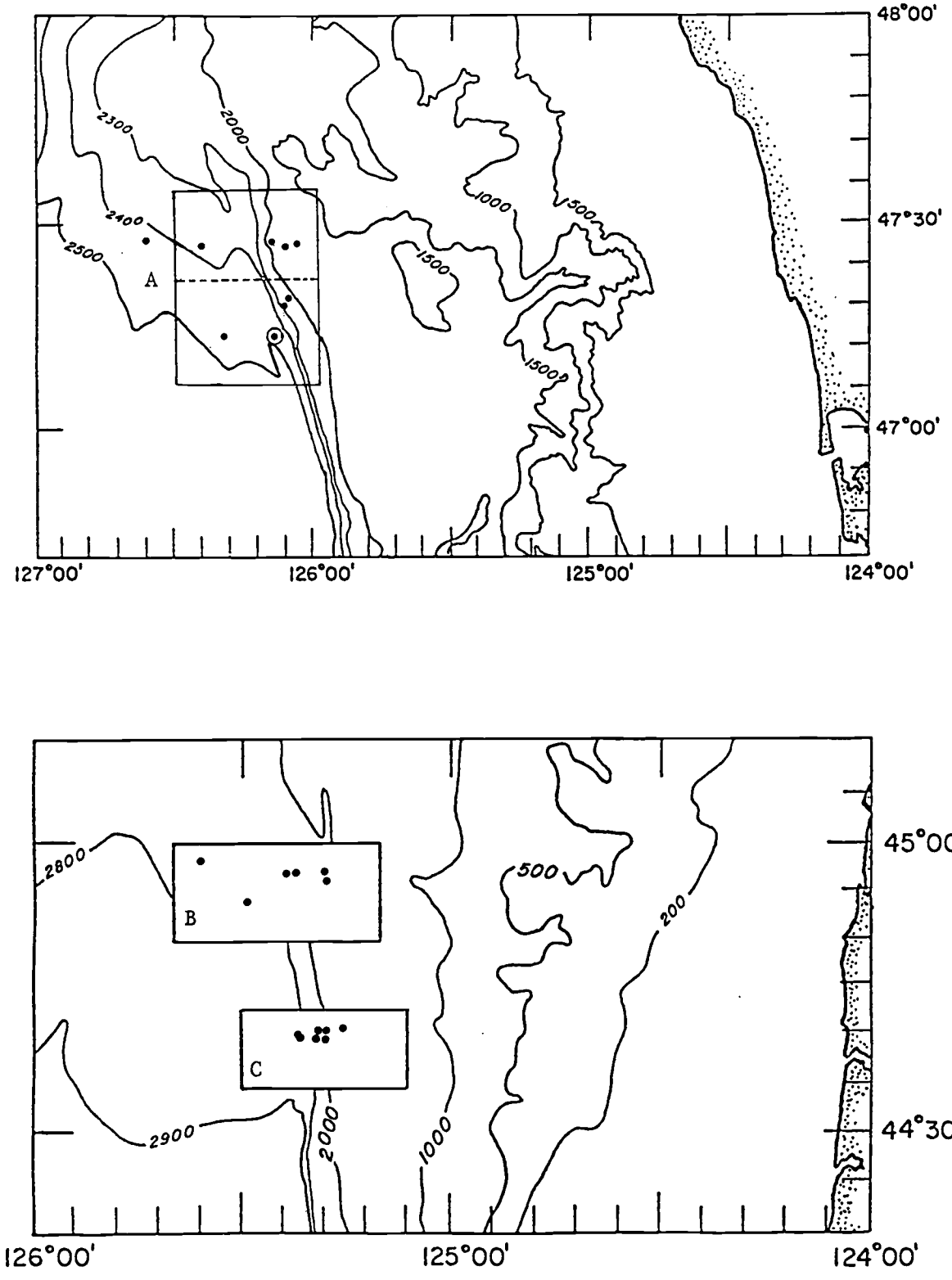

Figure III-1b

Figure III-2

Locations of core stations from Washington overthrust (a), Oregon overthrust (b), and Oregon underthrust (c). Core locations in this figure correspond to those in Fig. III-1b and are illustrated with tectonic elements of the accretionary complex, deformation front, seaward ridge, sediment pond, and second ridge.

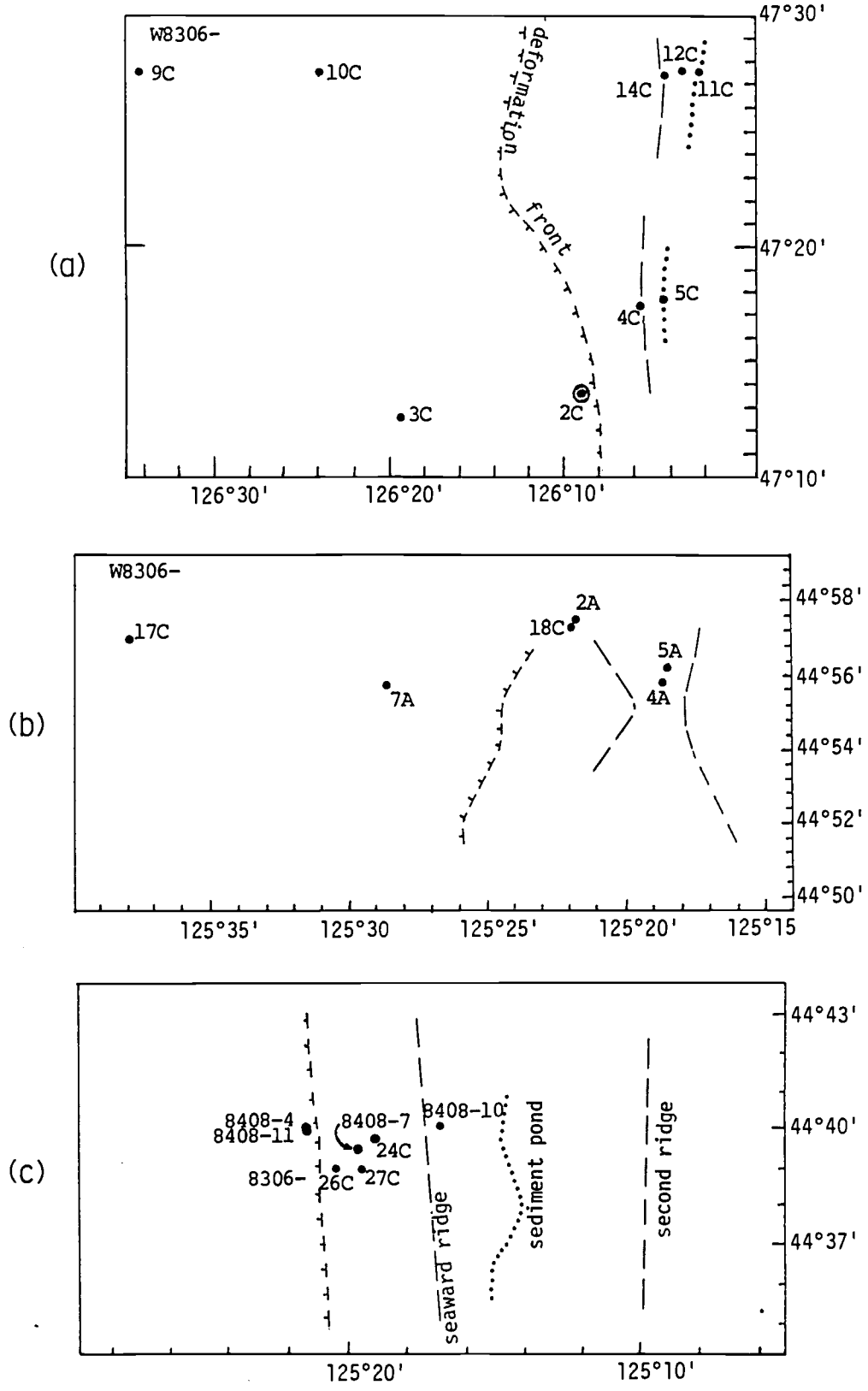
(a)
W8306-
9C
10C
12C
14C
11C
deformation front
5C
4C
3C
2C
47°30'
47°20'
47°10'
126°30'
126°20'
126°10'
(b)
W8306-
17C
2A
18C
5A
4A
7A
44°58'
44°56'
44°54'
44°52'
44°50'
125°35'
125°30
125°25'
125°20'
125°15
(c)
8408-4
8408-11
8408-7
24C
8306-
26C
27C
8408-10
seaward ridge
sediment pond
second ridge
44°43'
44°40'
44°37'
125°20'
125°10'

Figure III-2

Pore water samples and sediment cores were obtained from areas of carbonate lithification along three transects spanning the tectonic elements of the abyssal plain to the deformation ridges. Coring was done during two geological/geophysical cruises, one in June of 1983 on board the R/V WECOMA and the second in August of 1984 on board the R/V ATLANTIS II. The northern transect is in the central Washington overthrust area and consists of five stations along a northern profile and four stations along a southern profile (Fig. III-2a). Combined these stations represent the abyssal plain environment (8306-9C, -10C and -3C), the crest of the seaward deformation ridge (8306-4C), the ponded sediments behind this ridge (8306-12C and -5C), two morphologic features within the sediment pond (8306-14C = moat and 8306-11C = mound), and a sea mount on the abyssal plain (8306-2C). The central transect is in the Oregon overthrust area (Fig. III-2b). Three of the tectonic elements were sampled (Fig. III-2b): the abyssal plain (8306-17C and -7A), the crest of the seaward ridge (8306-2A and -18C), and the flanks of the second deformational ridge (8306-4A, and -5A). The southern transect is in the Oregon underthrust area (Fig. III-2c). Here the tectonic elements were cored in greater detail than in the overthrust area. Two cores were taken just seaward of the deformation front which is evident in a scarp (8408-4, and -11), four cores were taken on the seaward flank of the deformational ridge. They range from the foot of the ridge (8306-26C), across several sedimented ledges (8306-27C, -24C and 8408-7) to the landward side of the ridge, where the ponded sediments unconformably overlie the ridge flank (8408-10). The core locaitons and their tectonic environments are summarized in Table III-1. The procedure for pore water extraction and the analytical methods for measuring the dissolved species are the same as describred in Chapter I and listed in Table I-2. All analytical results are listed in Appendix III, although only Ca is discussed here in detail for all samples. Our samples

Table III-1 Core locations in the Oregon/Washington subduction zone

Station	Latitude (°N)	Longitude (°W)	Water Depth (m)	Site Description of Morphology
A. Central Washington overthrust area				
		Northern profile		
W8306-9C	47° 27.51'	126° 34.55'	2370	abyssal plain
W8306-10C	47° 27.42'	126° 23.89'	2320	deformed abyssal plain
W8306-11C	47° 27.49'	126° 02.15'	1600	sediment pond behind seaward ridge
W8306-12C	47° 27.47'	126° 03.28'	1807	mound in sediment pond
W8306-14C	47° 27.50'	126° 04.17'	1810	moat behind seaward ridge
		Southern profile		
W8306-2C	47° 13.70'	126° 08.90'	2320	sea mount on abyssal plain
W8306-3C	47° 12.50'	126° 19.36'	2445	abyssal plain
W8306-4C	47° 17.53'	126° 05.67'	1920	top of seaward ridge
W8306-5C	47° 17.74'	126° 04.29'	2050	sediment pond behind seaward ridge
B. Oregon overthrust area				
W8306-2A	44° 57.47'	125° 21.87'	2376	top of seaward ridge
W8306-4A	44° 55.91'	125° 18.64'	2008	flank of second ridge
W8306-5A	44° 56.26'	125° 18.45'	1990	flank of second ridge
W8306-7A	44° 52.82'	125° 28.64'	2758	abyssal plain
W8306-17C	44° 57.00'	125° 37.92'	2735	abyssal plain
W8306-18C	44° 57.45'	125° 21.96'	2376	top of seaward ridge

Table III-1 (continued)

Station	Latitude (°N)	Longitude (°W)	Water Depth (m)	Site Description of Morphology
C. Oregon underthrust area				
W8306-24C	44° 39.78'	125° 19.07'	2420	foot of seaward ridge
W8306-26C	44° 39.00'	125° 20.50'	2795	second ledge on seaward ridge
W8306-27C	44° 39.00'	125° 19.66'	2623	first ledge on seaward ridge
A8408-4	44° 40.00'	125° 21.60'	2860	deformed abyssal plain
A8408-7	44° 39.50'	125° 19.70'	2550	first ledge on seaward ridge
A8408-10	44° 40.00'	125° 17.10'	2180	sediment pond behind seaward ridge
A8408-11	44° 39.90'	125° 21.50'	2846	deformed abyssal plain

Figure III-3

Carbonate chimneys found in the Oregon accretionary complex. Lower continental slope vent site (a) (Kulm et al., 1986) and outermost continental shelf (b) (Schroeder et al., 1987). The conical chimney at the vent site is 1 to 2 m high and was found with the benthic communities of tube worms and giant clams in the deformation front (a). All chimneys have interior openings. Note openings in the wall of the chimney recovered from outermost continental shelf (b).

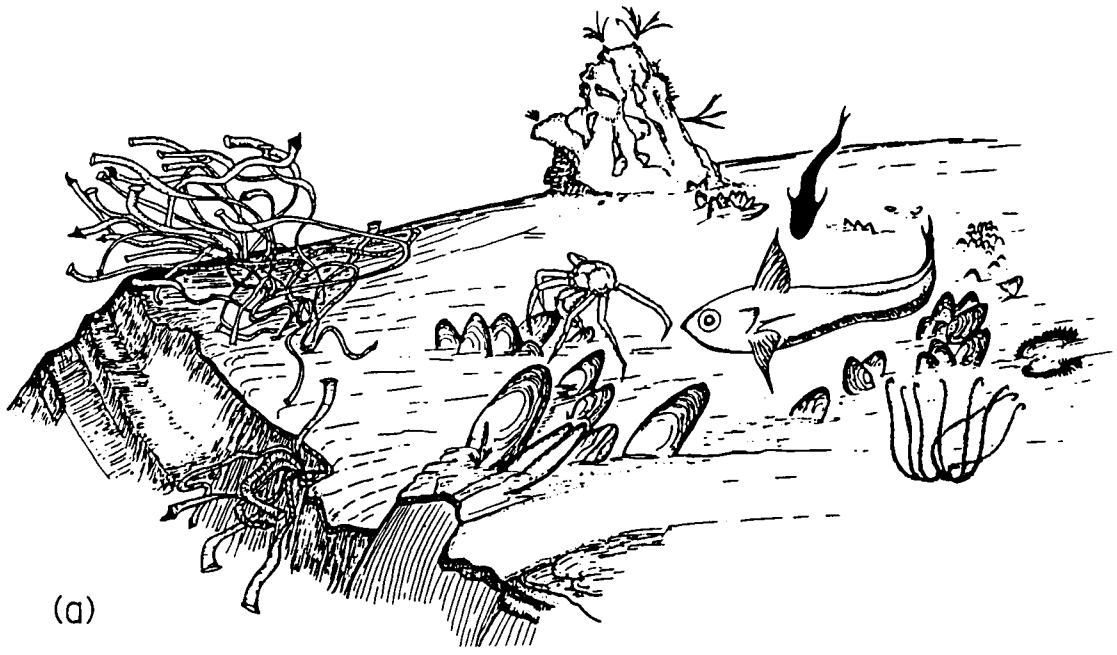

(a)

(b)

Figure III-3

from selected core locations, the dissolved NH_3, Ca, and TCO_2 are considered in the estimation of vertical advection rates and calcium carbonate saturation state.

RESULTS

Pore Water Ca

Dissolved interstitial Ca shows contrasting concentration profiles with depth across all transects of the accretionary complex (Fig. III-4): Ca decreases significantly with depth, to a minimum of 50 % of bottom water Ca over only 1.5 m sediment thickness, in the coring stations located landward of the deformation front (crest and flanks of deformational ridges) while Ca remains constant or increases with depth, to a maximum of 5 % of oceanic bottom water Ca over the same depth, in all stations from the abyssal plain and intra-basin sediments. The Ca-content in the pore waters of the seamount located in the abyssal plain shows the strongest decrease.

Though depletion of interstitial Ca in continental margin sediments has commonly been related to carbonate mineral precipitation (Watermann et al, 1972; Suess et al., 1982; Stein and Smith, 1986), such a drastic depletion of interstitial Ca over only 1.5 m sediment thickness has, to our knowledge, not been reported. The decrease in interstitial Ca in the deformed sediments of the accretionary complex suggests significant carbonate mineral precipitation and cementation.

Enrichment of interstitial Ca in the undeformed abyssal plain and intra-basin sediments indicates no significant carbonate mineral precipitation there. Measurements of $CaCO_3$-content in sediments from selected stations show that more $CaCO_3$ is contained in the deformed sediments (2 to 5 %) than is in in the undeformed sediments (0.1 to 1 %) (Fig. III-5). Samples obtained with DSRV Alvin over the vent sites contain even great amounts of $CaCO_3$, ranging from 25 to 90 % (Ritger et al., 1987).

The apparent dependence of the interstitial Ca on sediment deformation is further

Figure III- 4

Depth profiles of interstitial Ca concentration for the cores from the northern (a) and the southern (b) profiles of Washington overthrust, from the Oregon overthrust (c), and the Oregon underthrust (d). In general, interstitial Ca decreases with depth at core stations from deformed sediments and increases or remains constant at core stations from undeformed sediments.

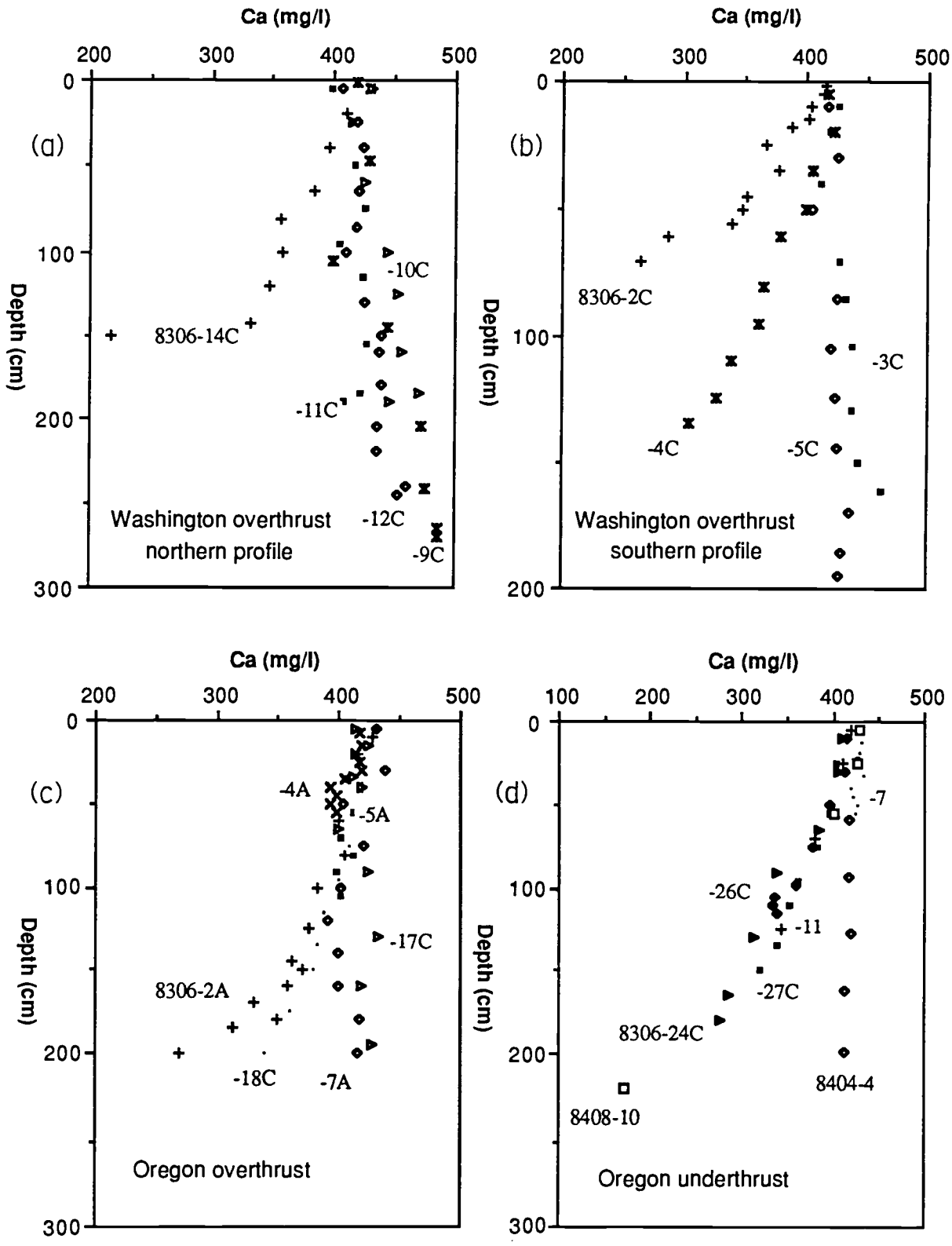
Ca (mg/l)
200
300
400
500
0
100
200
300
Depth (cm)
(a)
-10C
8306-14C
-11C
-12C
-9C
Washington overthrust
northern profile
(b)
8306-2C
-3C
-4C
-5C
Washington overthrust
southern profile
(c)
-4A
-5A
-17C
8306-2A
-18C
-7A
Oregon overthrust
100
(d)
-7
-26C
-11
-27C
8306-24C
8404-4
8408-10
Oregon underthrust

Figure III-4

Figure III-5

Downcore profiles of percent $CaCO_3$ content in sediments. High $CaCO_3$ content in deformed sediments and low $CaCO_3$ content in undeformed sediments correspond respectively to the interstitial Ca decrease in the deformed sediments and the Ca increase in the undeformed sediments.

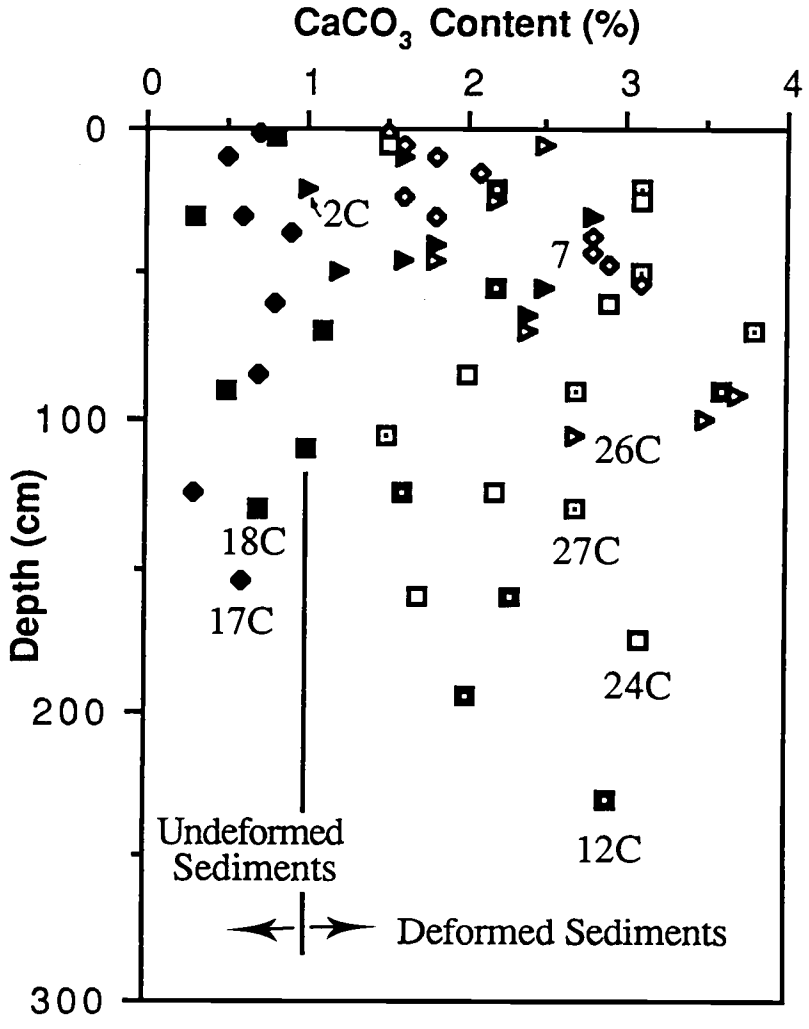
CaCO3 Content (%)
0
1
2
3
4
0
100
200
300
Depth (cm)
2C
7
26C
18C
27C
17C
24C
12C
Undeformed Sediments
Deformed Sediments

Figure III-5

Figure III-6

Porosity- and interstitial Ca-gradients. Core stations where interstitial Ca decreases with depth show greater porosity reduction than stations with interstitial Ca-enrichment.

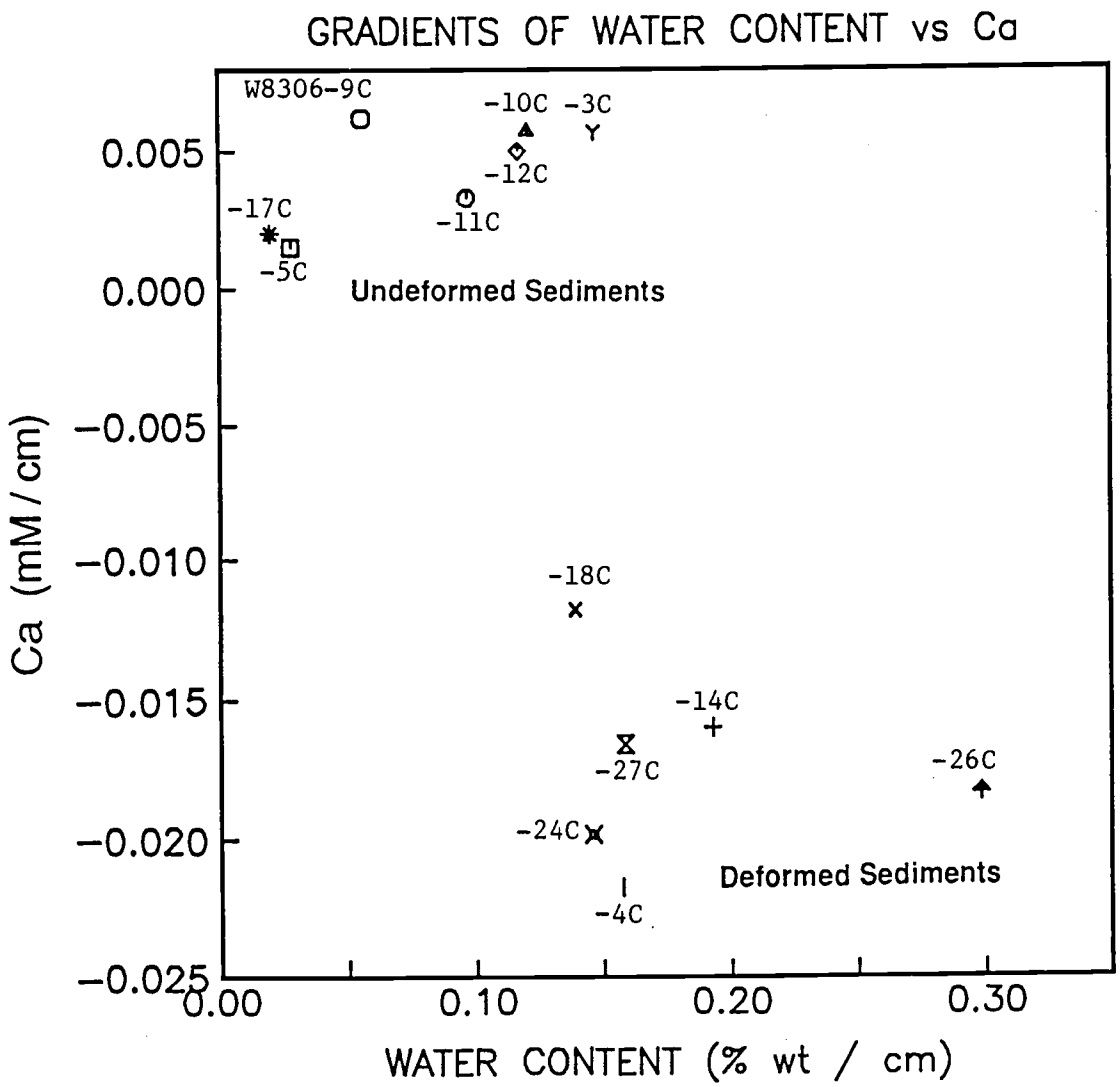
GRADIENTS OF WATER CONTENT vs Ca
W8306-9C
-10C
-3C
-12C
-17C
-11C
-5C
Undeformed Sediments
-18C
-14C
-27C
-26C
-24C
Deformed Sediments
-4C
0.005
0.000
−0.005
−0.010
−0.015
−0.020
−0.025
0.00
0.10
0.20
0.30
Ca (mM/cm)
WATER CONTENT (% wt / cm)

Figure III-6

confirmed by the relationship between the gradients of interstitial Ca with depth and the gradient of change of water content. Figure III-6 clearly shows that the depletion of interstitial Ca coincides with the reduction in water content, whereas the enrichment of interstitial Ca is observed in sediments whose water content changes little. Although expulsion of pore fluid, due to sediment deformation, is the dominant cause for the porosity reduction (Carson and Berglund, 1986), in-situ carbonate mineral precipitation and the resulting cementation of sediments may in part cause porosity reduction as well, especially in near-surface sediments. All of these contrasting relationships observed between deformed, accreted sediments and undeformed abyssal plain sediments; i.e. interstitial Ca-profiles, $CaCO_3$-contents, and porosity distributions, suggest consistently that the depletion of interstitial Ca directly reflects carbonate mineral precipitation.

MECHANISM OF CARBONATE PRECIPITATION

To simplify our consideration on the mechanism of carbonate mineral precipitation, we will only consider Ca^{2+} and CO_3^{2-} as the main components of the precipitates although dolomite and magnesian calcites are common (Russell et al., 1967; Scamman, 1981; Ritger et al., 1987). In order to identify the mechanism of carbonate mineral precipitation, we have to address briefly the origin of the two main reactants. Calcium, ultimately of crustal origin, is transported into the accreted sediments by upward advecting fluids. The CO_3^{2-}-ion may be provided by oxidation of migrated methane equally brought to the near-surface depths by venting fluids. We propose that oxidation of the migrated methane and the decrease in carbonate solubility (or conversely an increase in calcium carbonate saturation) due to the release of excess pore pressure play an important role in the formation of carbonate mineral precipitates.

Migration and Oxidation of Methane

During biochemical degradation of organic matter in sediments, the CO_2 is generated by aerobic oxidation near the sediment-water interface followed by anaerobic oxidation below generally by sulfate reduction (Claypool, 1974; Berner, 1980). When sulfate is exhausted from the interstitial water, the process of biogenic methane formation takes place by CO_2-reducing microbes, which utilize the pool of dissolved bicarbonate generated during sulfate reduction.

In the process of microbial methane formation the residual bicarbonate is progressively enriched in ^{13}C ($\delta^{13}C$ = -40 to -10 %) and biogenic methane is depleted in ^{13}C ($\delta^{13}C$ = -70 to -90 %) (Claypool and Kvenvolden, 1983). An increase in the pH due to removal of CO_2 from pore water during biogenic methane production may cause precipitation of carbonate in anoxic sediments. The carbonate originated by this methanogenic process is thus enriched in ^{13}C as the carbonate is formed from ^{13}C-enriched bicarbonate (Claypool and Kaplan, 1974).

However, carbonates with anomalously light ^{13}C ($\delta^{13}C$ = -35 to -67 %) in the deformed sediments (Schroeder et al., 1987; Ritger et al, 1987; Kulm et al., 1987) indicate that they could not have originated from this diagenetic process. The $\delta^{13}C$-depleted carbonates in near surface sediments of the accretionary complex provide two constraints: (1) the carbonates are so strongly ^{13}C-depleted that biogenic methane appears to be the only compound from which the carbonate ions could be derived, and (2) the methane must be transported toward the surface and be oxidized in order to precipitate carbonate near-surface sediments.

A parcel of venting pore fluid, driven by positive excess pore pressure, continually adjusts to the total hydrostatic pressure on its path upward through the sediment column by releasing its excess pore pressure. This release of pore pressure results in a corresponding decrease in the amount of methane dissolved in the pore

fluid. Methane may escape through ebullition and accelerate transport from depth to the surface. As methane reaches the near-surface sediments, it is oxidized by oxygen or sulfate-consuming microbes, providing an abundant source of $\delta^{13}C$-depleted carbonate ions ($\delta^{13}C$ = -30 to -70 %) (Claypool, 1974) from which anomalously $\delta^{13}C$-depleted authigenic carbonate minerals are formed. Occurrence of pyrite in carbonates suggests that anaerobic oxidation of methane by sulfate reducing microbes is the more dominent process in the Oregon subduction zone (Ritger et al, 1987).

Anomalously light carbonate minerals were also observed in Oregon continental shelf (DSDP Leg 18 site 176) at 22 m subsurface (Claypool, 1974) and slope (Russell et al., 1967). Migration of methane from depth to this horizon was proposed by Claypool (1974) to explain these $\delta^{13}C$ depleted carbonates. Fluid advection from depth to present near-surface sediments was also proposed from the ^{12}C enriched total dissolved bicarbonate in shallow pore fluids of the accretionary complex (Suess and Whiticar, 1986). These authors predicted that 30 % of the total dissolved bicarbonate resulted from methane oxidation. These results are consistent with fluid-induced carbonate lithification in the deformed sediments.

The Effect of Pressure on Carbonate Solubility

In the case of fluid filled porous media, the effective stress is the weight of the overburden, which includes the weight of the water, per unit area minus the pore pressure (Rubey and Hubbert, 1959). Thus pore fluid venting occurs when the pore pressure exceeds the weight of the overburden and continues until the pore pressure equals the weight of the overlying water. This positive excess pore pressure is likely to be generated in subduction zones where compressional stress is exerted by converging plates (Von Huene, 1985). During upward migration of pore fluid this excess pore pressure must be released. The release may be one potential mechanism by

which carbonate minerals precipitate in near-surface sediments of the deformed accretionary sediments, as the carbonate mineral solubility is proportional to pressure. The release of excess pore pressure in near-surface sediments is proportional to the rate of pore fluid venting. Thus the faster the pore fluids escape, the more likely carbonate minerals precipitate governed only by the effect of pressure on carbonate solubility.

The excess pore pressure gradient may be related to the rate of pore fluid venting by Darcy's law (Bear, 1972);

$$u = KP / \eta z \quad \text{or}$$
$$= kP / n\rho g \qquad (1)$$

where u is the rate of pore fluid flow, K is the permeability of the porous medium, P is the excess pore pressure over subsurface depth, z, k is the hydraulic conductivity, η is the viscosity of pore fluid, n is the porosity of sediments, ρ is the density of pore fluid and g is the gravitational acceleration. From Eq. (1) the venting rate and the excess pore pressure gradients are related by the expression:

$$P\ (atm) / z\ (m) = 3.3\ u\ (m/yr) \qquad (2)$$

if $k=7 \times 10^{-10}$ m/sec, n=0.7, ρ =1.05 g/cm^3, and g=9.8 m/sec^2 are fixed.

Suppose a parcel of pore fluid flows from a subsurface depth of z to the seafloor at a water depth of 2.1 km (which is the approximate water depth of the vent site where authigenic carbonate chimneys and benthic organisms were found, Kulm et al., 1986), Eq. (2) predicts that for a venting rate of 10 m/yr, the total pressure at 6 m subsurface would have to be 408 atm. This represents the sum of 198 atm from excess pore pressure plus 210 atm from overburden pressure. The thickness of 6 m for the depth

of the subsurface layer where precipitation might take place, is arbitrary. However, Scamman (1981) assumed, based on porosity reduction, that cementation would begins at shallow burial depth, probably within several meters of the sediment-water interface. If carbonate mineral precipitation was entirely controlled by thermodynamic equilibration of pure calcite, the amount of $CaCO_3$ would be equivalent to the difference in the equilibrium Ca-concentrations between 408 atm and 210 atm, i.e., between the sediment surface and 6 m of depth below sea flow. The 6 m-thickness is only for illustration and will be extended later in this section to an appropriate subsurface depth in order to establish a thermodynamic equilibrium model that best takes into account the effect of the release of excess pore pressure on $CaCO_3$ precipitation.

Details of thermodynamic equilibrium model, quantifying $CaCO_3$ precipitation by the release of pore pressure, are described in Appendix III. The result of this thermodynamic equilibrium model for $CaCO_3$-precipitation shows the following linear relationship between % $CaCO_3$ and excess pore pressure over the 6-m subsurface interval (Fig. III-7);

$$\text{Log}(\%\ CaCO_3) = -4.6564 + 1.0262\ \text{Log}(P) \qquad \text{or}$$

$$= -4.6564 + 1.0262\ \text{Log}(3.3\ u\ z) \qquad (3)$$

The amounts of $CaCO_3$ formed from fluid venting from only a 6-m thick sediment layer are very small. Figure III-7 shows that the amount of $CaCO_3$ precipitated from the release of pore pressure can not account for the measured $CaCO_3$ content in some of the sediments even at the extreme venting rate of 10 m/yr. This is due to setting the subsurface base at 6 m which implies that venting pore fluids originate from this depth. The disagreement between predicted and measured amounts of $CaCO_3$

Figure III-7

Theoretical relationship between the release of excess pore pressure and the amount of potential $CaCO_3$ precipitation (in weight %) responding to the pore pressure release. Thermodynamic equilibrium was assumed for pure calcite precipitation. The symbol ⊡ represents the relationship between excess pore pressure and precipitation of $CaCO_3$ as predicted by equations developed in Appendix III. Wet bulk density and porosity fraction of sediment are assumed as 1.3 g/cm^3 and 0.7, respectively.

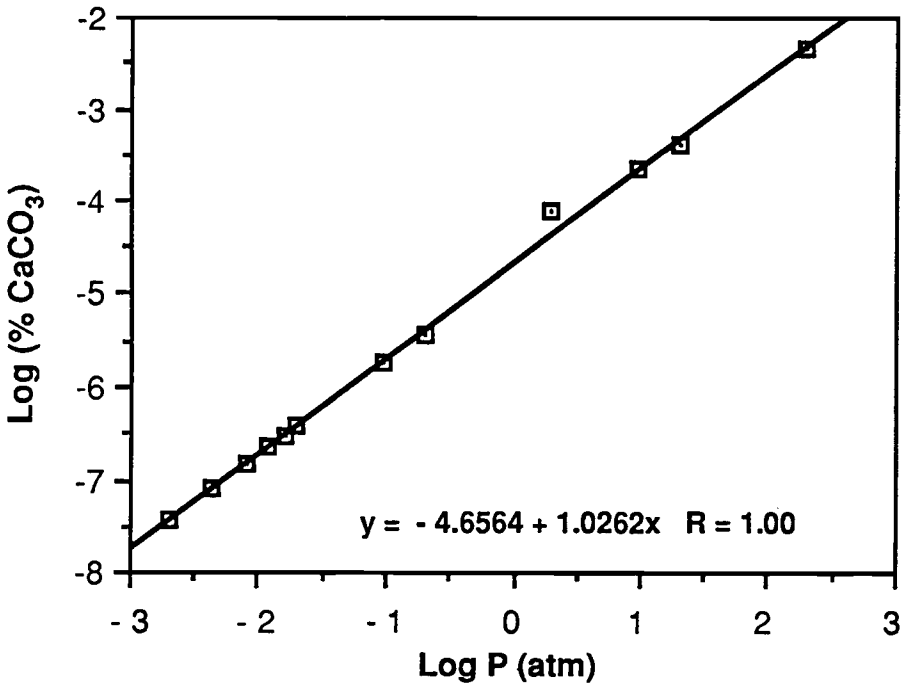

Figure III-7

Figure III-8

Theoretical relationship between $CaCO_3$ content (in weight %) of lithified sediments and the proposed depths for the origin of pore fluids. This relation is an extension of that illustrated in Fig. III-7.

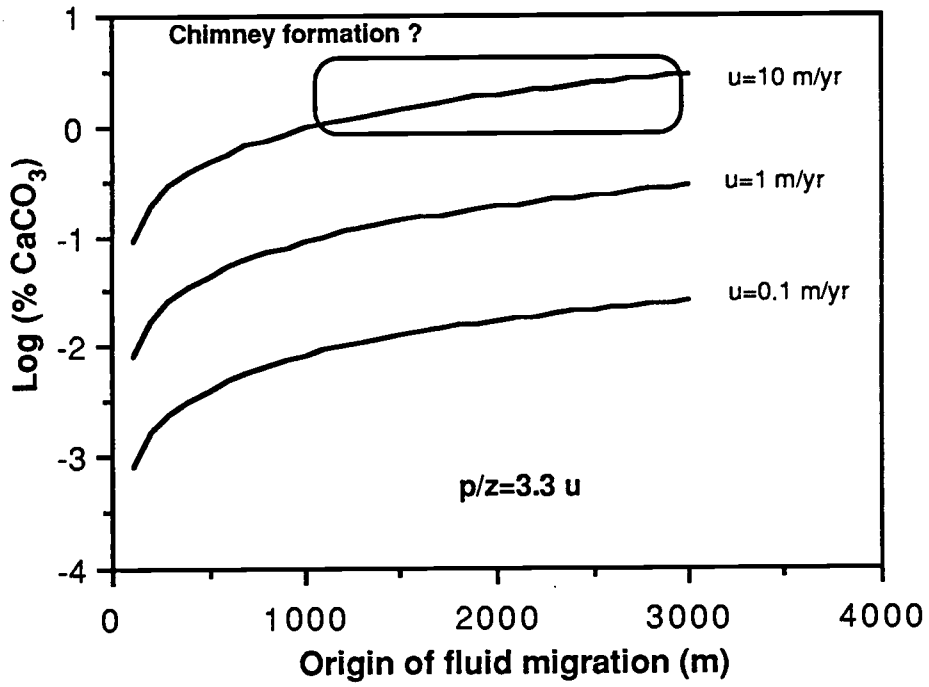
Chimney formation ?
u=10 m/yr
u=1 m/yr
u=0.1 m/yr
p/z=3.3 u
Log (% CaCO3)
1
0
-1
-2
-3
-4
0
1000
2000
3000
4000
Origin of fluid migration (m)

Figure III-8

precipitation, therefore, suggests a need for extension of the subsurface interval. The relation of Eq. (3) will still hold at any depth below the 6 m subsurface as the model assumes an exclusive thermodynamic control on carbonate precipitation in response to the release of excess pore pressure.

The thermodynamic equilibrium model for calcite precipitation in case of the extended depth below 6 m is illustrated in Fig. III-8. It shows that significant $CaCO_3$ precipitation (>> 1 %) is likely at venting rates and source depths of fluids at around 10 m/yr and 1 km, respectively. If one takes into account the restrictive assumption that carbonate precipitation is entirely controlled by equilibration of pure calcite in response to the release of excess pore pressure, then the conditions specified in Fig. III-8 are lower limits of carbonate mineral precipitation. It is interesting to note that only a fairly fast venting rate of 10 m/yr and a source depth for pore fluids of 1 km may generate chimney formation.

Interstitial calcium profiles obtained from DSDP site 174A in the Cascadia abyssal plain show a Ca-minimum (<10 mM) at subbottom depths of 50 to 350 m, but drastic Ca-enrichments, much higher than normal seawater Ca (>>10 mM), at depth greater than 350 m (Watermann et al., 1972; Claypool, 1974). Thus, venting of pore fluids from the deformation of these sediments must migrate vertically from at least a depth of 350 m and carry crustal Ca upwards in order to precipitate carbonate in near-surface sediments.

The thermodynamic equilibrium model for calcite suggests that pressure control on carbonate solubility would be a significant mechanism for the formation of the carbonate chimney should the venting rate be in the range of 10 m/yr or greater. A minimum flow rate of 277 ml/m^2day was directly measured above a vent site in the deformation front of the Oregon accretionary complex (Suess et al., 1987a). This rate is equivalent to only 20 to 50 cm/yr of vertical migration depending on the porosity. On

the other hand, a venting rate as high as 200 cm/yr was estimated from a systematic change in sulfate and methane concentrations in timed water samples that were obtained by deploying a benthic chamber above the vent site (Suess, personal communication). Evidently the high required flow rate of 10 m/yr by the thermodynamic model is not approached in any of the measured flow rates. Considering the assumption of the model that carbonate precipitation be entirely controlled by solubility of pure calcite and the release of excess pore pressure associated with pore fluid venting, any closer agreement would be fortuitous. What is significant, however, is that both the measured and the model-derived flow rates are considerably faster than any reported venting rates in other accretionary complexes, which are on the order of 1 cm/yr at most (Boulegue et al., 1987; Reck 1987).

Ritger et al. (1987) point out that normally undersaturated bottom waters, (with respect to calcite), bathe the entire accretionary complex off Oregon and Washington. Therefore carbonate mineral precipitation requires supersaturation generated from local conditions within the sediment column and not at the sediment-water interface. Calculations of the ion-concentration-product (ICP) $[Ca^{2+}] \times [CO_3^{2-}]$ in pore waters of the area do indicate supersaturation of the pore waters with respect to calcite. Pore waters from both the deformed and the undeformed abyssal plains are supersaturated with respect to calcite (Fig. III-9) (Appendix III). Again, as with other parameters, the degree of supersaturation in the deformed sediments is significantly higher than in the undeformed abyssal plain sediments. Admitting a large margin of error accumlated in these calculations and analyses, this systematic difference in the degree of saturation may suggest undersaturation of the pore waters from the undeformed abyssal plain with respect to calcite. Another possibility is that actually not calcite controls the saturation in these pore fluids but a mixed carbonate mineral phase, whose solubility is higher than that of calcite. Supersaturation with respect to calcite in sediments devoid of

Figure III-9

Degree of saturation of the pore waters from both the deformed and the undeformed abyssal plains with respect to $CaCO_3$. Pore waters from both the deformed (W8306-2C) and the undeformed (W8306-3C) abyssal plains are supersaturated with respect to $CaCO_3$. However, the pore waters from the deformed abyssal plain are systematically more saturated than those from the undeformed abyssal plain.

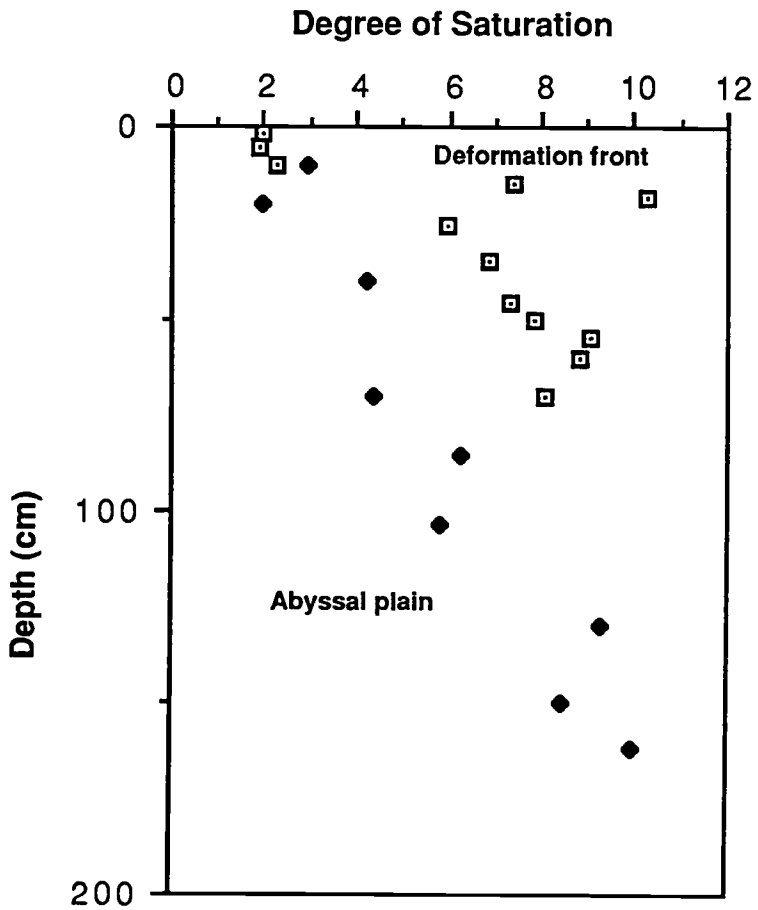
Degree of Saturation
0
2
4
6
8
10
12
0
100
200
Depth (cm)
Deformation front
Abyssal plain

Figure III-9

calcium carbonate is quite common. An apparent $CaCO_3$ saturation increase was also reported at depths of all sediments from the North American continental margin off Nova Scotia and from the central Pacific (Sayles, 1987). Sayles (1987) concludes that the ICP increases cannot be adequately described by a single thermodynamic constant. We feel that the relative difference in calcite saturation between pore waters from deformed and undeformed sediments is significant and is another indication of the enhanced clacium carbonate precipitation in sediments affected by fluid venting.

EVIDENCE FOR VENTING FROM INTERSTITIAL WATER

Venting Rates

In addition to the first direct measurement of pore fluid venting rates at the vent site in the Oregon accretionary complex (Suess et al., 1987), downcore concentration profiles of chemical species, such as Ca and NH_3 can be used to ascertain vertical flow rates. Rates of pore fluid venting, ranging from 1 to 13 cm/yr, were determined by applying one-dimensional diffusion-advection-reaction models to the downcore concentration profiles of interstitial Ca and NH_3 obtained from selected coring sites across the Oregon/Washington accretionary complex. These stations are: 8408-4 from the deformed abyssal plain of the Oregon underthrust area; 8408-7, 8306-24C, and 8306-26C from the flank of the seaward deformation ridge (also of the Oregon underthrust area), and 8306-2C from the top of the seamount on the abyssal plain off Washington.

The model equation applied to interstitial Ca profile may be written as

$$D\, d^2C / dz^2 - u\, dC / dz - k\, C = 0 \qquad (4)$$

where D is the diffusion coefficient of Ca, C is the concentration of interstitial Ca, z is

the vertical depth positive downward, u is the advection rate of pore fluid, and k is the coefficient of Ca precipitation. The solution of Eq. (4) may be written as

$$C(z) = C_1 \exp(\lambda_1 z) + C_2 \exp(\lambda_2 z) \qquad (5)$$

where,

$$\lambda = \frac{u \pm \sqrt{u^2 - 4kD}}{2D}$$

$$C(z=0) = C_1 + C_2, \text{ and}$$
$$C(z=h) = C_1 \exp(\lambda_1 h) + C_2 \exp(\lambda_2 h).$$

C (z=0) and C (z=h) are known from the measured interstitial Ca concentrations and D is assumed as 3×10^{-6} cm^2/sec. The only unknown terms in Eq. (5) are u and k. The linear concentration profile at station 8408-4 (deformed abyssal plain) was assumed to indicate that the Ca-distribution is exclusively controlled by diffusion. At this station, therefore, the u-term was removed and subsequent curve fitting of Eq. (5) to the measured Ca profile gave a value for k (the coefficient of Ca-precipitation). This k value was used in the other stations to determine u by fitting Eq. (5) to the measured Ca-profiles at those stations. Advection rates of pore fluids derived from the Ca-modeling range from 1 cm/yr to 10 cm/yr upward, but are mostly of the magnitude around 1 cm/yr (Table III-2 and Fig. III-10). Station 8306-2C, however, the site of the sea mount on Washington abyssal plain shows the fastest advection rate of 28 cm/yr. This sea mount is considered to be a mud volcano (Kulm, personal communication) which would readily explain these high vertical flow rates.

Profiles of the measured interstitial NH_3 may be described by another version of

Figure III-10

Application of a diffusion-advection-reaction model to interstitial Ca profiles. Pore water advection rate (u) was obtained by visual curve fitting of the model equation to the measured Ca concentrations. Two-layer models were applied to the Ca profile at the core station 8306-2C (sea mount) to obtain best curve fitting. Values of the model parameters used in the curve fitting are listed in Table III-2.

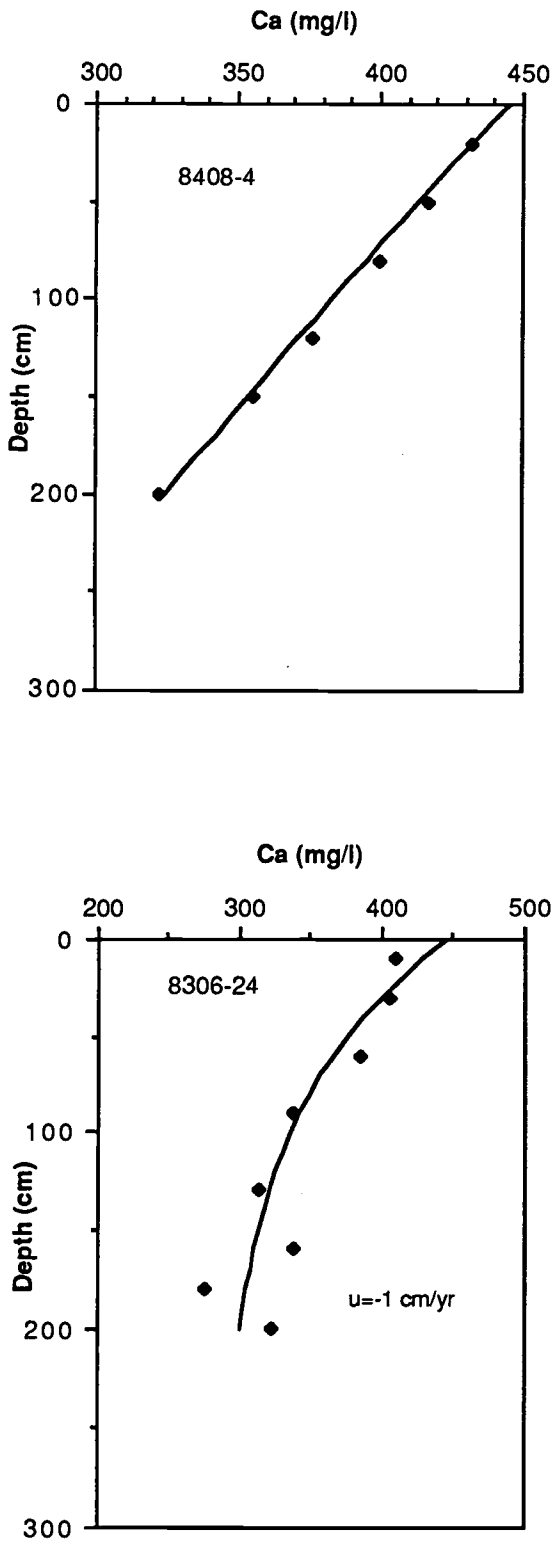

Figure III-10

(continued)

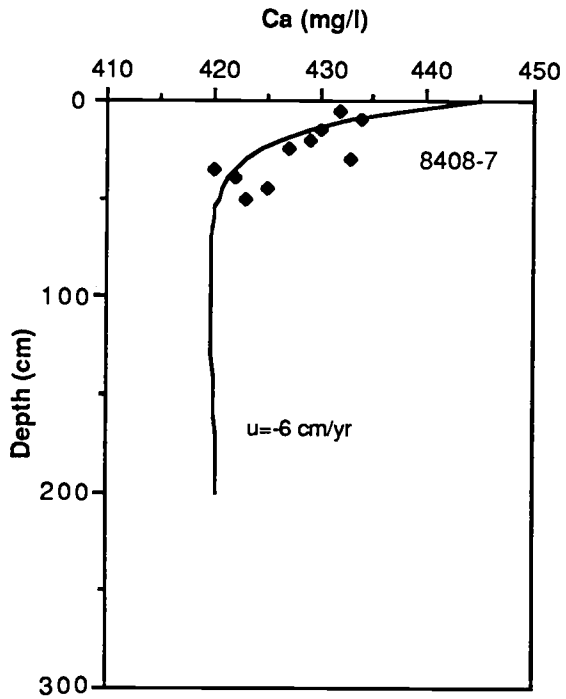
Ca (mg/l)
410
420
430
440
450
0
100
200
300
Depth (cm)
8408-7
u=-6 cm/yr

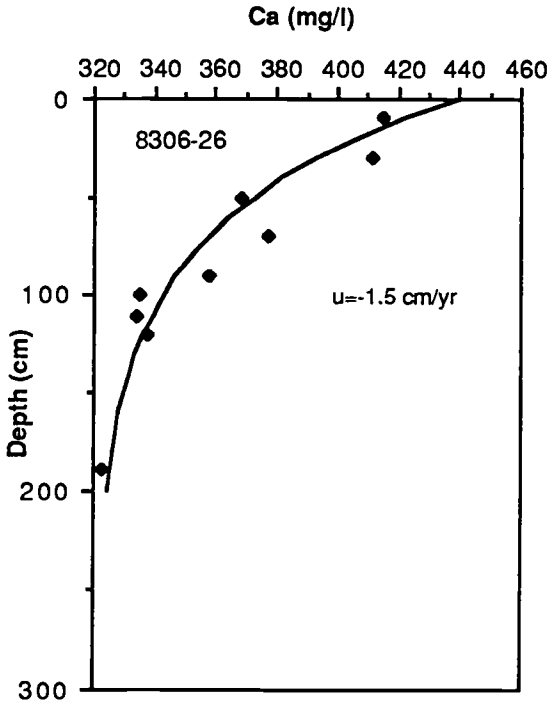
Ca (mg/l)
320
340
360
380
400
420
440
460
0
100
200
300
Depth (cm)
8306-26
u=-1.5 cm/yr

(continued)

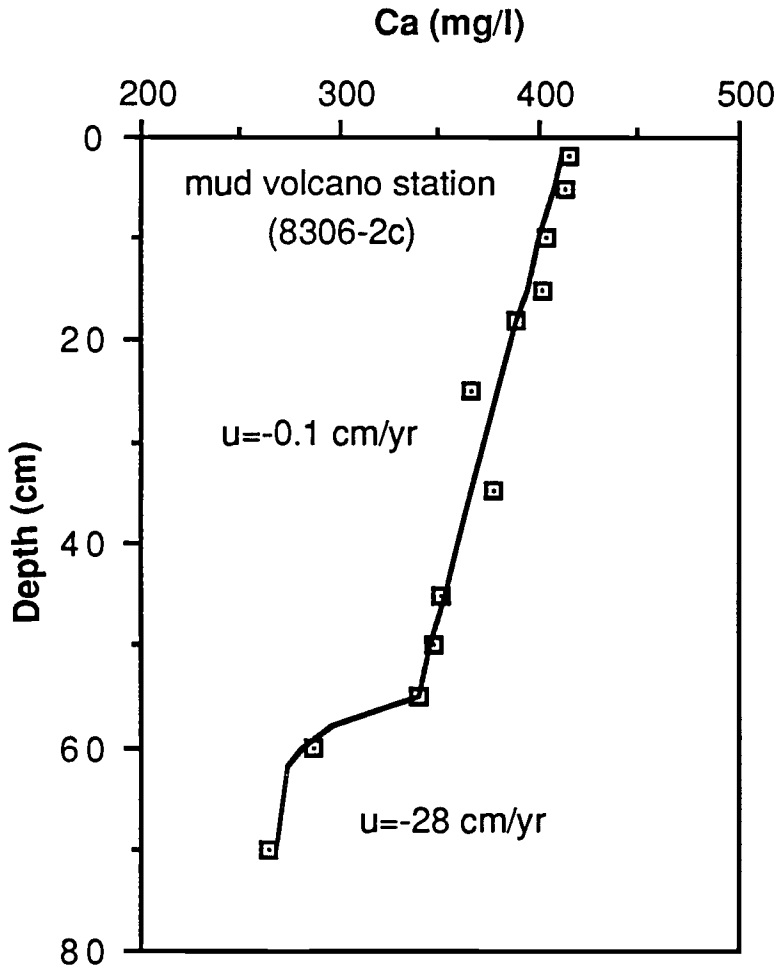
Ca (mg/l)
200
300
400
500
0
20
40
60
80
Depth (cm)
mud volcano station
(8306-2c)
u=-0.1 cm/yr
u=-28 cm/yr

Table III-2 Input parameters used for Ca and NH_3 modeling and comparison of calculated advection rates

	Ca	NH_3	Ca	NH_3	Ca	NH_3	Ca	NH_3	Ca	NH_3
	8408-4		8408-7		8306-24C		8306-26C		8306-2C	
$D(10^{-6}cm^2/sec)$	3	6	3	6	3	6	3	6	3	6
$k(10^{-4}/yr)$	1		1		1		1		1	
$J_o(umol/cm^3yr)$		0.013		0.013		0.013		0.013		0.013
$a(1/cm)$		0.006		0.05		0.01		0.01		0.01/0.01/0.02
C_o	445	0	445	0	445	0	445	0	445/325	0/0.25/1.25
$C_h(NH_3)$		1.89		0.09		1.6		1.3		0.5/1.5/1.55
$C_h(Ca)$	325		420		338		290		325/250	
u(cm/yr)	0	0	-6.0	-6.7	-1.0	-0.9	-1.5	-1.1	-0.1/-28	-0.04/-0.07/-24

Figure III-11

Application of a diffusion-advection-reaction model to interstitial NH_3 profiles. Pore water advection rates obtained from NH_3 modeling is comparable to those from Ca modeling. Three-layer models were applied to the NH_3 profile at the core station 8306-2C (sea mount) to obtain best curve fitting. Values of the model parameters used in the curve fitting are listed in Table III-2.

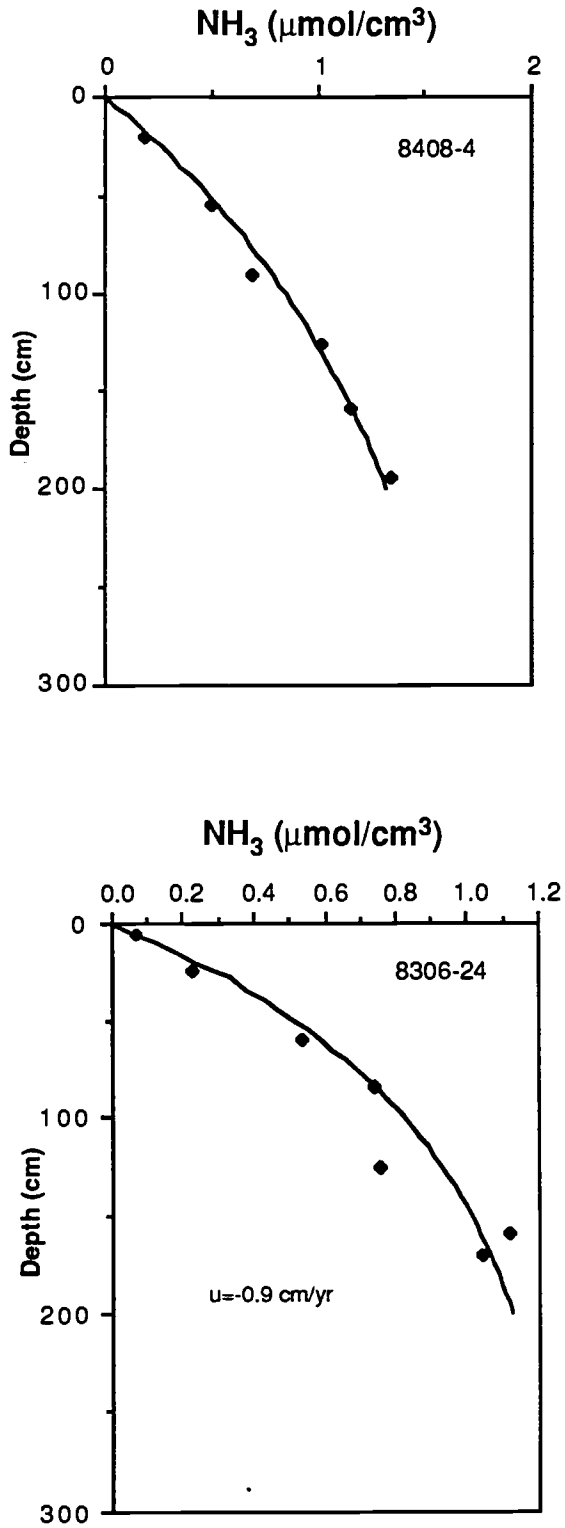

Figure III-11

(continued)

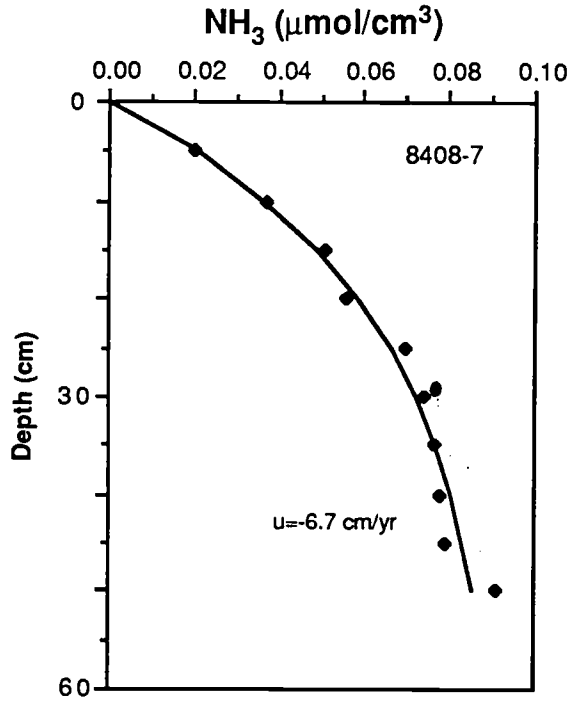
NH3 (μmol/cm3)
0.00
0.02
0.04
0.06
0.08
0.10
0
30
60
Depth (cm)
8408-7
u=-6.7 cm/yr

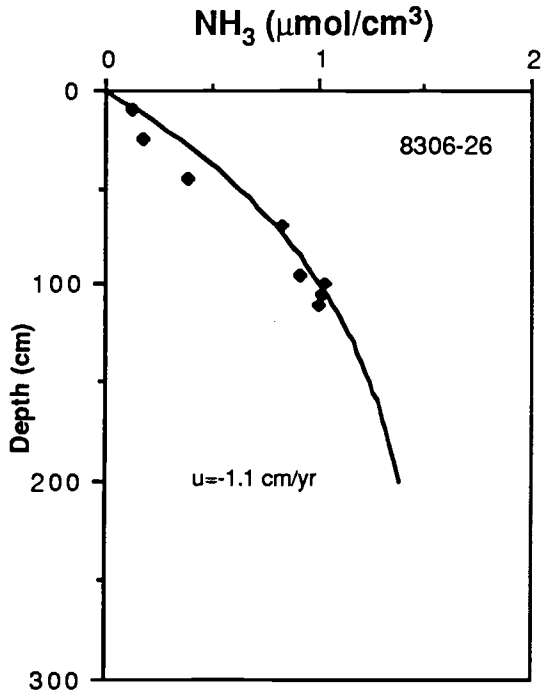
NH3 (μmol/cm3)
0
1
2
0
100
200
300
Depth (cm)
8306-26
u=-1.1 cm/yr

(continued)

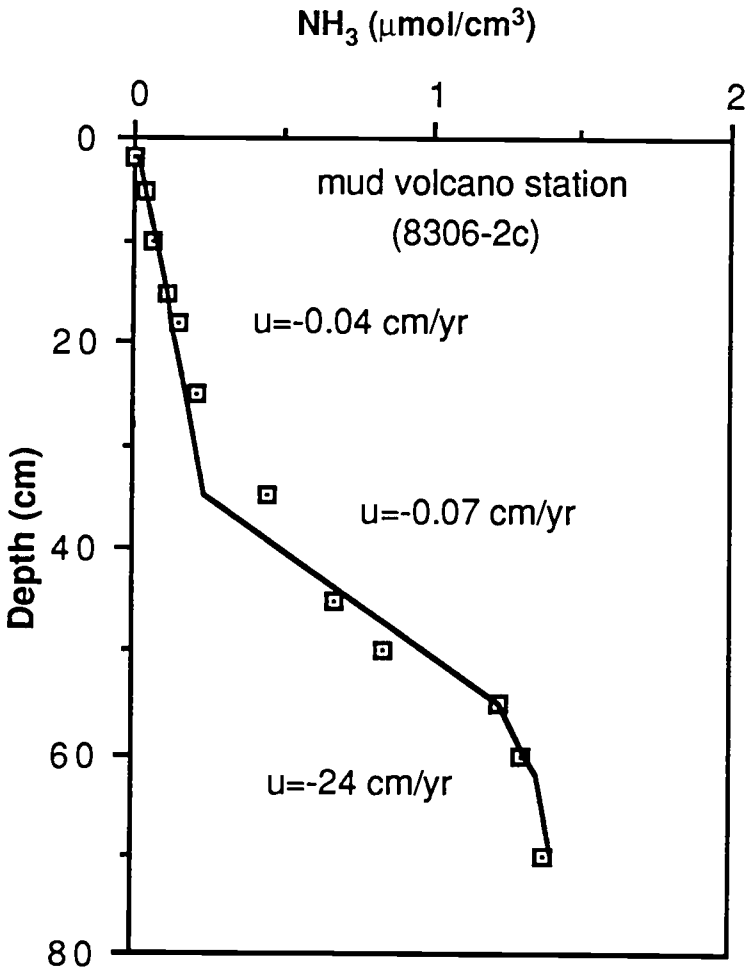
NH3 (μmol/cm3)
0
1
2
0
20
40
60
80
Depth (cm)
mud volcano station
(8306-2c)
u=-0.04 cm/yr
u=-0.07 cm/yr
u=-24 cm/yr

diffusion-advection-reaction model, which takes the following expression:

$$D\, d^2C / dz^2 - u\, dC / dz + J_0 \exp(-\alpha z) = 0 \qquad (6)$$

where J_0 is the NH_3-production rate at the sediment-water interface and α is the attenuation coefficient for concentration profile. The solution of Eq. (6) may be written as

$$C(z) = C_3 + C_4 \exp(z\, u / D) - J_0 \exp(-\alpha z) / (D\, \alpha^2 + u\, \alpha) \qquad (7)$$

where, $C(z=0) = C_3 + C_4 - J_0 / (D\, \alpha^2 + u\, \alpha)$ and

$$C(z=h) = C_3 + C_4 \exp(h\, u / D) - J_0 \exp(-\alpha h) / (D\, \alpha^2 + u\, \alpha)$$

C (z=0) and C (z=h) are known from the measured interstitial NH_3 concentrations and D is assumed as 6×10^{-6} cm^2/sec. There are three unknown terms in Eq. (7); the attenuation coefficient (α), the production rate of NH_3 at the surface (J_0) and the advection rate (u). At the station 8408-4 where the advection rate is assumed to be zero (based on the Ca profile), only J_0 and α need to be defined. Assuming values of α in the range of 0.001 to 0.01, the production rate (J_0) can subsequently be constrained at the station 8408-4 . With these constraints on J_0 and α the advection rate, u, for each station was determined when the model-derived NH_3 curve fitted best to the measured NH_3. Advection rates derived from the NH_3-modeling range from 1 to 10 cm/yr (Table III-2 and Fig. III-11). The rate for the sea mount station is 24 cm/yr. These rates are consistent with the range obtained for advection from Ca-modeling. These model-derived advection rates are 20 to 200 times slower than the rate measured right over the vent site. Considering that interstitial Ca- and NH_3-data of all the core stations

are from non-vent areas, yet from within the deformed accretionary complex, however, these model-derived advection rates appears to be reasonable. The great difference in magnitude of advection rates between a vent site and non-vent sites of the accretionary complex suggests that pore fluid expulsion is confined to small areas while pervasive upward migration of pore fluid occurs in most of the complex at much reduced rates.

Water and Ca Fluxes

Corresponding to the range of modelled advection rates, 1 to 10 cm/yr, the Ca flux can be estimated to be in the range of -0.01 to -0.05 mol/m^{2}yr by the following relation:

$$f = -\phi\,(D\,dC/dz - u\,C)_{z=0} \qquad (9)$$

where ϕ and f are porosity and Ca-flux across the sediment-water interface respectively. Although the estimated negative Ca-flux indicates flux of Ca out of the sediment, this does not necessarily mean that Ca is added to the seawater. The algebraic sign and direction of flux depend on the relative magnitudes of the diffusional and advective fluxes in Eq. (9). Domination of upward-advection over downward-diffusion results in a net upward flux of Ca, despite the negative concentration gradients of Ca. Depletion of interstitial Ca and carbonate precipitates allow us to interprete the upward-Ca flux as the rate of Ca-removal by carbonate precipitation.

An important consequence of this estimate of vertical Ca flux is that it provides a means to calculate the water flux. For the bottom-water Ca, 10.5 mM, water flux per unit surface area (horizon of 1 cm^2) is estimated to be in the range of 0.095 to 0.48 ml/cm^{2}yr upward, corresponding to the Ca flux of between 0.01 and 0.05 mol/m^{2}yr. The total volume of water vented through a unit surface area of sediment may be

estimated by the following;

$$\int_0^z \phi' \, dz' \; - \; \int_0^z \phi \, dz \qquad (10)$$

where ϕ' is initial porosity profile before deformation and ϕ is porosity profile undergoing deformation. Since it is impossible to obtain porosity profiles before and after deformation at a fixed station, profiles from two different stations, one having the least reduction in porosity and one having the greatest reduction, were chosen to maximize the effect of sediment deformation on pore fluid venting. The total volume of vented pore fluids can be calculated from the two porosity profiles. This is a first order estimate but not an unrealistic one. Stations 8306-7C and 8306-26C were chosen for this purpose. When z in Eq. (10) is set at 6 m, the total volume of pore water expelled per unit area (1 cm^2) of sediment surface is 42 cm^3, which is a 7 % volume reduction of the 600 cm^3 (1 cm^2 x 6 m) of the sediment layer.

If the sediment column of 600 cm^3 (1 cm^2 x 6 m) is deformed at a constant rate, then dividing the total volume of water vented through unit surface area, 45 ml/cm^2, by the water flux per unit surface area, as estimated above, would give the time over which the total volume of water, 45 ml is squeezed from the sediments. The time thus estimated is between 88 and 442 years, corresponding to the water flux of 0.48 to 0.095 ml/cm^2yr, respectively. With the time and the thickness of sediment column squeezed thus available, the rate of pore fluid venting may also be estimated as between 1.4 and 6.8 cm/yr. This range of venting rate is fairly close to the rates obtained from the Ca- and NH_3-modeling. Extending the sediment column to depths below 6 m would also give a similar advection rate, because the increase in the total volume of water vented is offset by the increase in thickness of sediment column.

IMPLICATIONS

Global Ca-Flux

Uncertainties in explaining the steady-state seawater composition by thermodynamic models (Sillen, 1967) and kinetic models (Broecker, 1971) were greatly reduced during the past decade by including hydrothermal sinks and sources in the element budget. The magnitude of hydrothermal fluxes generated by the seawater-basalt reaction are now regarded as first-order processes (Edmond et al., 1979; Hart and Staudigel; 1982; Von Damm et al., 1985a; Thompson, 1983). Major imbalances in previous global geochemical budgets for certain elements, such as magnesium, were considerably reduced by inclusion of hydrothermal flux estimates to the extent that no other mechanism needed to be invoked (Von Damm et al., 1985a; Drever, 1974). Therefore, much effort has since been focused on refining the flux estimates involved in the seawater-basalt reaction (Thompson, 1983).

Weathering of average igneous rock can not account for all the calcium in sedimentary rocks (Garrels and Mackenzie, 1971). An additional Ca-input of 30×10^{12} g/yr is needed to balance this excess calcium (Wolery and Sleep, 1976). Furthermore, since Ca-containing sediment is subducted (i.e., lost to the mantle) at a maximum rate of 120×10^{12} g/yr (Wolery and Sleep, 1976), an even larger Ca input is needed, i.e. 150×10^{12} g/yr, to balance the sedimentary Ca-budget (Fig. III-12). Input of hydrothermal Ca is known to be a significant source for this additionally needed Ca. The hydrothermal Ca-input required to balance the maximum rate of Ca-removal by sediment subduction was thought to be between $93 - 142 \times 10^{12}$ g/yr (Wolery and Sleep, 1976) whereas the most recent estimate for hydrothermal Ca-input, which includes fluxes from all ranges of seawater-basalt reaction, is given as 73×10^{12} g/yr

(Thompson, 1983).

Accepting this recent estimate for hydrothermal Ca-flux, the input still falls short of the total amount of Ca needed by about 77 x 10^{12} g/yr, i.e., 100 %. This shortage may indicate that the maximum rate of Ca-removal to the mantle by sediment subduction is glossly overestimated. In such a case, the hydrothermal Ca-input would be sufficient if the estimate for Ca-loss by sediment subduction were reduced to 43 x 10^{12} g/yr. This is where the discussion on the Ca-budget stands today.

Another way of reducing the Ca-shortage is by taking into account all Ca removed by carbonate mineral precipitation from pore fluids venting in accretionary complexes (Fig. III-12). At present there is no way to independently verify the rate of Ca-loss by sediment subduction, nor to update the hydrothermal Ca-input. The most recent estimate of hydrothermal Ca-input appears to be a reliable and well-refined value. Therefore, our hypothesis of Ca-removal by pore fluid venting in subduction zones becomes important as the rate of Ca-loss by sediment subduction approaches a minimum. The minimum rate of Ca-removal of 12 x 10^{12} g/yr by sediment subduction (Wolery and Sleep, 1976) requires an additional Ca supply of 42 x 10^{12} g/yr. In this case the recent estimate for hydrothermal Ca-input, 73 x 10^{12} g/yr, constitutes an excess. This surplus of Ca, as much as 31 x 10^{12} g/yr, can potentially be taken up by Ca-precipitation from pore fluid venting in subduction zones (Fig. III-12).

This newly defined Ca-sink, 31 x 10^{12} g/yr, in subduction zones is about half as much as the hydrothermal Ca-input and less by a factor of fifteen than the river input of dissolved Ca. Carbonate mineral precipitation, coupled with depletion in interstitial Ca in the Oregon/Washington subduction zone, supports such a Ca-removal process. Authigenic carbonates in the near-surface sediments of the Nankai trough which is accompanied by the depletion of interstitial Ca, yields another example for the potentially world-wide effect of convergence-induced Ca-precipitation (Kawahata and

Figure III-12

A global model for Ca mass flux.

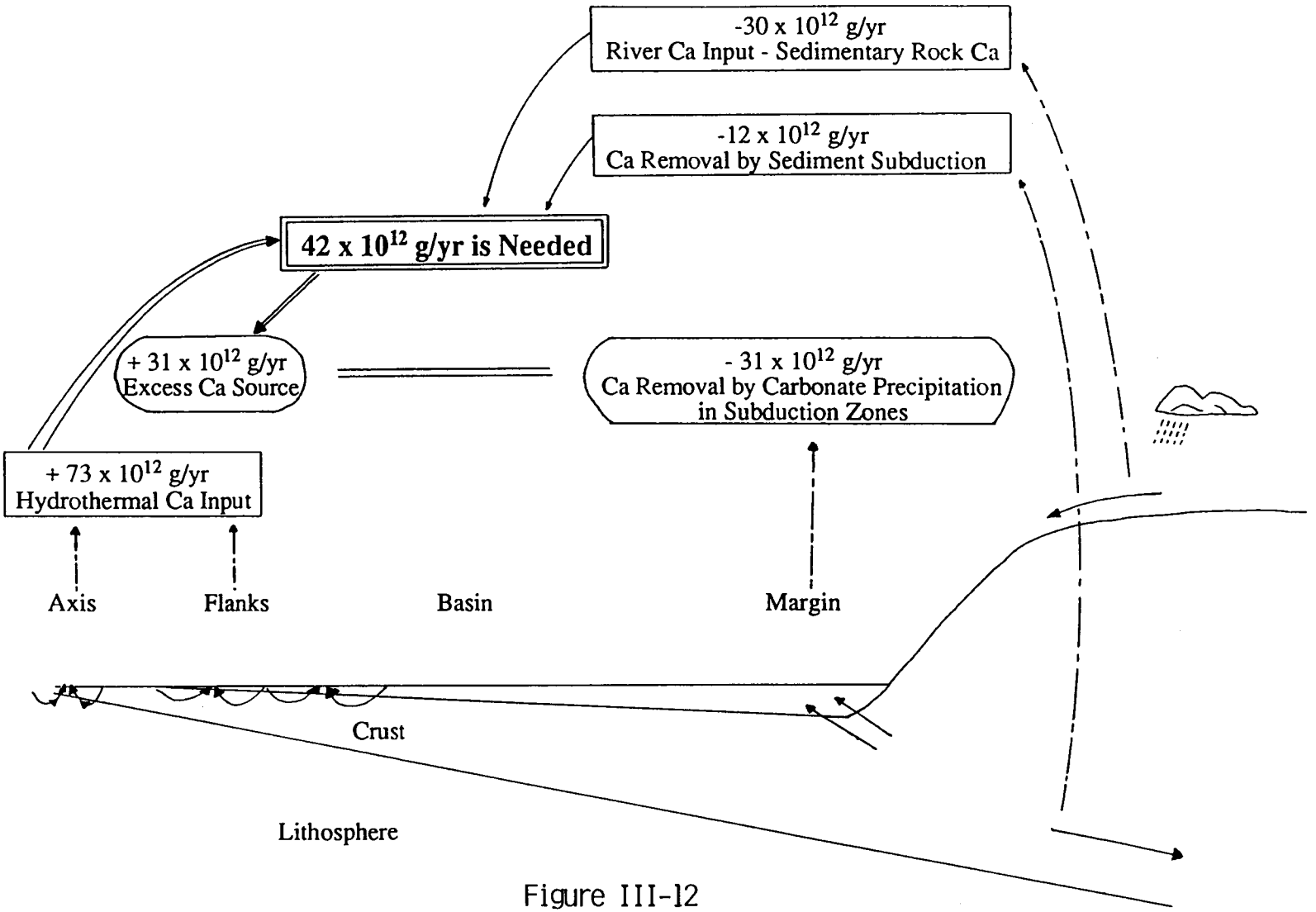

Figure III-12

Fujioka, 1986; Stein and Smith, 1986). Interstitial Ca is enriched at depth, as seen in from numerous DSDP data, by leaching from the basaltic basement and subsequent diffusive transport to overlying sediments (McDuff and Gieskes, 1976; McDuff, 1981). When pore fluid venting is initiated by the excess pore pressure in subduction zones, this crustal Ca is transported upward and is removed from the fluids to form authigenic carbonates.

The significant sink for Ca by convergence-induced carbonate precipitation, which has not previously been considered in the global element budget, implies that this process may also be of importance for the global budgets of other elements. For instance, systematic anomalies of trace metal distribution over clam colonies in the Nankai trough of the Japan subduction zone (Dron et al., 1987) may draw attention to this process.

Efficiency of Plate Motion

The remaining portion of this chapter deals with the speculation on the efficiency of plate motion as related to element fluxes. Although little is known about the driving mechanism of plate tectonics, there is no doubt that the formation of mid-ocean ridges and consumption of plates in the trench systems are consequences of plate motion. If one conjectures a "plate engine" driving a plate from the mid-ocean ridge to the trench, hydrothermal circulation and pore fluid venting would be surface manifestations as the engine consumes energy in the course of the plate-motion. The total area of the two types of ocean floor affected by plate-motion, (a) one related to the pore fluid venting driven by mechanical compressive stress and (b) one related to the hydrothermal convection driven by thermal stress, may be used for the purpose of this discussion on plate engine efficiency.

Direct application of the diffusion-advection-reaction model to the distribution

profiles of interstitital Ca yields a Ca removal rate in the range of 0.01 to 0.05 mol/m^2yr. Taking the indirectly derived absolute global removal rate of Ca from fluid venting, 31×10^{12} g/yr, the total area undergoing such a process of convergence-induced fluid venting is $3 - 15 \times 10^{16}$ cm^2.

From the systematic deviation of the measured conductive heat flow from the theoretical heat flux, hydrothermal convection is known to continue until the age of the oceanic plate is about 17 m.y. for fast-spreading plates and 23 m.y. for slow-spreading ones (Wolery and Sleep, 1976). Using the value of 2.94 km^2/yr for the newly created oceanic plate area (Chase, 1972; Williams and Von Herzen, 1974), the total area undergoing hydrothermal convection off-ridge and on-ridge is $50 - 68 \times 10^{16}$ cm^2.

If one assumes that the thermal energy which drives hydrothermal convection in the mid-ocean ridge, converts to the mechanical energy of compressional stress as the plate moves toward trench, equal surface areas undergoing hydrothermal convection and pore fluid venting would indicate an efficiency of the plate engine of 100 %. Our estimations for those areas, derived above, show that the area of pore fluid venting is 3-22 times less than the area for hydrothermal convection. Therefore, the efficiency of the plate engine may be 5 to 33 %. Although it is obvious that our approach is extremely crude, the efficiency of the specific plate motion and systematic tabulation of the data for all plates would retrieve valuable information. Introducing such a concept would help better understand plate tectonics.

SUMMARY

1. Downcore depletions of interstitial Ca and reduction in porosity with the occurrence of prominent carbonate precipitates over the accretionary complex in Oregon/ Washington subduction zone suggests that interstitial Ca is removed in the process of convergence-induced calcium carbonate precipitation.

2. The release of excess pore pressure, which drives the pore fluids, may induce calcium carbonate precipitation. Thermodynamic consideration on calcite solubility and saturation associated with the release of excess pore pressure suggests that the formation of carbonate chimneys requires the venting rate to be at least 10 m/yr with a source depth of fluid migration at least 1 km.

3. Global removal of Ca by calcium carbonate precipitation in subduction zones may be as much as 31×10^{12} g/yr, when hydrothermal Ca-input and Ca-loss to sediment subduction are assumed as 73×10^{12} g/yr and 12×10^{12} g/yr, respectively. This significant sink of Ca, not previously considered in the global Ca-budget, implies that pore fluid venting in subduction zones may also be considered in the global budgets of other elements.

4. If one conjectures a 'plate engine' driving a plate from the mid-ocean ridge to the trench, hydrothermal convection and pore fluid venting would be surface manifestations of the engine's consumption of energy in the course of plate motion. Reasonably constrained surface areas affected by thermally-driven fluid flow and by convergence-driven fluid flow, could be used to estimate efficiency of the plate engine.

CHAPTER IV

PORE FLUID VENTING AND THERMAL STRUCTURE WITHIN THE OREGON ACCRETIONARY COMPLEX

ABSTRACT

Two-dimensional temperature distribution models for the underthrust portion of the Oregon accretionary complex are presented. One thermal model, assuming confined flow, yields heat fluxes that best match the measured range of heat flow across three distinct tectonic elements of the complex. The model requires restricted pathways of less than 0.5 km for flow and a rate of 20 cm/yr. The restricted pathways are likely along the decollement plane and the major fault planes in the marginal ridge which dip landward along the deformation front. The predicted rate of 20 cm/yr for confined flow agrees well with the flow rate measured directly over a vent site (Suess et al., 1987a), although we consider the order of magnitude significant rather than absolute venting rates. The confined flow model predicts that the temperature of the basement at 5 km depth in the area of underthrusting is as low as 160 °C. Upward migration of pore fluid through the Oregon accretionary complex predicts increasing thermal gradients from the basement to the seafloor. This temperature distribution pattern with depth prevents abnormally high temperatures at the base of the accretionary complex which would have been attained without assuming upward fluid migration. The heat flow distribution patterns of all thermal models tested are similar to each other, which indicates that the geometry in this thermal model which deviates from the commonly used flat top geometry is well justified. This demonstrates the importance of using a realistic geometry of the accretionary complex in thermal modeling.

INTRODUCTION

Strong evidence for pore fluid venting in accretionary complexes has recently emerged from studies of several of the world's active margins (Kulm et al., 1986; Moore et al., 1986a; Cadet et al., 1987; Kastner et al., 1987). The venting is believed to occur in response to sediment compaction and lithification which are driven by tectonic stresses that result from plate convergence along subduction zone (Moor and Karig, 1976; Carson, 1977; Bray and Karig, 1985; Fowler et al., 1985).

Whereas heat flow data at the sea floor spreading ridges have provided strong evidence for hydrothermal circulation (Anderson et al., 1979; Williams et al., 1979; Becker and Von Herzen, 1983; Noel, 1985), heat flow data and thermal models from accretionary complexes have been available only in a few cases to support pore fluid venting (Burch and Langseth, 1981; Wang and Shi, 1984; Reck, 1987). Reck (1987) claimed, based on one-dimensional thermal modeling, that pore fluids must migrate upward through the northeast Japan accretionary complex at a rate of 0.3 cm/yr to account for abnormally high near-surface thermal gradients. One-dimensional models, however, may not adequately explain any lateral variation in heat flow across accretionary complexes as the geometry is not taken into account. Two-dimensional thermal models of subduction zones generally cover so large an area (150 km x 20 km), due to the main interest in the thermal structure of the subducting slab, that they provide no detail thermal information from within the accretionary complex (Hsui and Toksoz, 1979; Honda, 1985). Though fluid advection is included in the two-dimensional thermal models of subduction zones by Wang and Shi (1984), their rectangular model geometry is not realistic.

Models representing the thermal structure within any accretionary complex must consider the realistic geometry of the complex as the heat flow is strongly affected by surface topography. The morphology of accretionary complexes is generally

characterized by a convex cross-sectional shape which shows the decreasing surface slopes of complexes from deformation front toward arc (Zao et al., 1986) rather than the flat-top geometry. Locating fluid pathways within the model area is also important for the thermal structure of any accretionary complex because uniform versus confined fluid flow profoundly affects the temperature distribution. Reasonable locations of fluid pathways would be allowed in the model area cross-section only if the dimensions of the modelled area are large and if such pathways can be reasonably accomodated within the tectonic fabric. An example for structurally-controlled fluid pathways are benthic communities of tube worms and giant clams observed at specific locations along the Oregon accretionary complex. These organisms are supported by nutrients from the venting pore fluids. Their distribution suggests that the benthic communities are located at the exit of major fluid pathways.

The purpose of this paper is to consider several scenarios of heat distribution within a portion of the underthrust margin off Oregon. Thermal models include heat transport by fluid flow which reproduces the thermal structure within the accretionary complex. The predicted heat flow distribution across the complex is matched to the range of measured heat flow values considered typical for the various tectonic elements of the underthrust setting by Langseth (unpubl. data). The thermal model will yield the rate of pore fluid venting and possible locations and dimensions of pathways within the complex. The modeling area, 5 km deep to the basement and 5 km wide, encompasses the most critical area of the Oregon underthrust portion of the accretionary complex. This area consists of the deformation front, the adjacent undeformed abyssal plain, the first and second deformed marginal ridges, and intervening sediment pond (Kulm et al., 1986). An excellent multichannel seismic record (Snavely et al., 1986) reveals in detail the tectonic fabric associated with this portion of the margin; it was used as a basis for configuring the model geometry. The proposed major pathways of fluids were traced

toward the interior of the complex based upon the faults dips in the seismic section. A finite difference approximation method was used for the two-dimensional numerical simulation of temperature distribution within the model area. Scenarios and parameters considered in the model are: (1) presence or absence of fluid advection, (2) distribution of pathways of fluid migration, (3) variation in thermal diffusion coefficients both vertically and laterally, and (4) varying basement temperature.

METHODS

Numerical Formulation

The complete heat flow equation (Carslaw and Jaeger, 1959) can be represented as:

$$\rho c \partial T / \partial t = \nabla [K \nabla T] - \nabla [\rho \alpha T V] + h \quad (1)$$

$\rho c \partial T / \partial t$	$=$	$\nabla [K \nabla T]$	$-$	$\nabla [\rho \alpha T V]$	$+$	h	(1)
The total change in heat per unit time		Total heat conducted per unit time		Total heat convected per unit time		Internal heat produced per unit time	

For two-dimensional steady heat flow, assuming no internal heat production, Eq. (1) becomes:

$$\partial / \partial x [K_x \partial T / \partial x] + \partial / \partial y [K_x \partial T / \partial y] - \rho \alpha [u \partial T / \partial x + v \partial T / \partial y] = 0 \quad (2)$$

The variables are density, ρ, specific heat, α, temperature, T, thermal conductivity, K, the cartesian coordinates, x and y, x component advection velocity, u, and y component advection velocity, v. Eq. (2) also assumes that ρ and c are constant throughout the xy-plane of interest.

Removal of advection terms of Eq. (2) leads to a Laplace equation. Numerical solution procedures for Laplace equations can readily be found in textbooks (e.g.

Figure IV-1

The spacing of grid from which the derivatives are approximated by difference quotients.

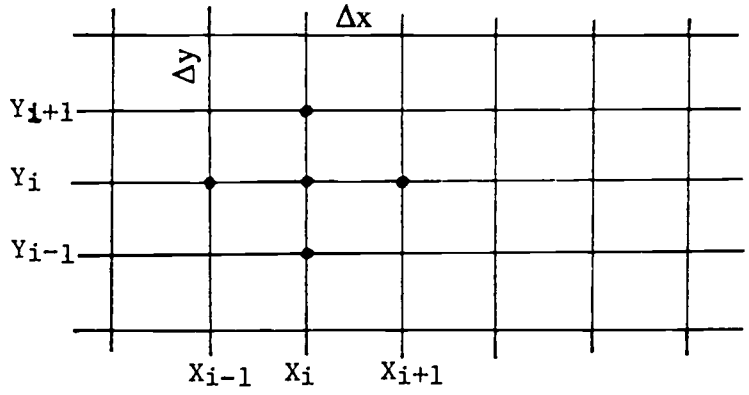

Figure IV-1

Gerald and Wheatley, 1984). However, the involvement of the advection term in Eq. (2) prevents direct application of these procedures. In order to solve Eq. (2), the derivatives in Eq. (2) are first replaced by difference quotients, converting the equation to a difference equation. A difference equation is then written corresponding to each point at the nodes of a gridwork that subdivides the region of interest at which the function values are unknown. Solving these equations simultaneously gives values for the function at each node which approximate the true values.

Let Δx and Δy be the spacing of grid in the x-direction and the y-direction respectively (Fig. IV-1), the derivatives in Eq. (2) can be replaced by difference quotients which approximate the derivatives at the points (x_i,y_j):

$$\frac{\partial^2 T}{\partial x^2} = \frac{T(x_{i+1}, y_j) - 2\,T(x_i, y_j) + T(x_{i-1}, y_j)}{(\Delta x)^2} \tag{3}$$

$$\frac{\partial^2 T}{\partial y^2} = \frac{T(x_i, y_{j+1}) - 2\,T(x_i, y_j) + T(x_i, y_{j-1})}{(\Delta y)^2} \tag{4}$$

$$\frac{\partial T}{\partial x} = \frac{T(x_{i+1}, y_j) - T(x_{i-1}, y_j)}{2\,(\Delta x)} \tag{5}$$

$$\frac{\partial T}{\partial y} = \frac{T(x_i, y_{j+1}) - T(x_i, y_{j-1})}{2\,(\Delta y)} \tag{6}$$

It is convenient to let double subscripts on T indicate the x- and y-values:

$$\frac{\partial^2 T}{\partial x^2} = \frac{T_{i+1,j} - 2T_{i,j} + T_{i-1,j}}{(\Delta x)^2} \qquad (3')$$

$$\frac{\partial^2 T}{\partial y^2} = \frac{T_{i,j+1} - 2T_{i,j} + T_{i,j-1}}{(\Delta y)^2} \qquad (4')$$

$$\frac{\partial T}{\partial x} = \frac{T_{i+1,j} - T_{i-1,j}}{2(\Delta x)} \qquad (5')$$

$$\frac{\partial T}{\partial y} = \frac{T_{i,j+1} - T_{i,j-1}}{2(\Delta y)} \qquad (6')$$

The thermal equation (Eq. 2) can be simplified if semi-constant values of thermal conductivities, K_x and K_y, are assigned for each depth layer. This approach avoids the complication of the thermal equation by relating K_x and K_y to explicit functions of x and y. Details of thermal conductivities will be described in the next section of parameters. Eq. (2) thus can be rewritten as:

$$R\,\partial^2T/\partial x^2 + \partial^2T/\partial y^2 - \rho\,\alpha/K_y\,[\,u\,\partial T/\partial x + v\,\partial T/\partial y\,] = 0 \qquad (7)$$

Where $R = K_x / K_y$

Substituting Eq. (7) with Eqs. (3'), (4'), (5'), (6'):

$$R/\Delta x^2\,(T_{i+1,j} - 2\,T_{i,j} + T_{i-1,j}) + 1/\Delta y^2\,(T_{i,j+1} - 2\,T_{i,j} + T_{i,j-1}) -$$

$$\rho\,\alpha/K_y\,\{\,u\,(T_{i+1,j} - T_{i-1,j})/2\,\Delta x + v\,(T_{i,j+1} - T_{i,j-1})/2\,\Delta y\,\} = 0 \qquad (8)$$

Rearranging Eq. (8) with respect to T's:

$$(R/\Delta x^2 - \rho\,\alpha\,u/2\,K_y\,\Delta x)\,T_{i+1,j} + (R/\Delta x^2 + \rho\,\alpha\,u/2\,K_y\,\Delta x)\,T_{i-1,j} +$$

$$(1/\Delta y^2 - \rho\,\alpha\,v/2\,K_y\,\Delta y)\,T_{i,j+1} + (1/\Delta y^2 + \rho\,\alpha\,v/2\,K_y\,\Delta y)\,T_{i,j-1} -$$

$$2\,(R/\Delta x^2 + 1/\Delta y^2)\,T_{i,j} = 0 \qquad (9)$$

Eq. (9) has the form,

$$a\,T_{i+1,j} + b\,T_{i-1,j} + c\,T_{i,j+1} + d\,T_{i,j-1} + e\,T_{i,j} = 0 \qquad (10)$$

where $a = (R/\Delta x^2 - \rho\,\alpha\,u/2\,K_y\,\Delta x)$, $b = (R/\Delta x^2 + \rho\,\alpha\,u/2\,K_y\,\Delta x)$,

$c = (1/\Delta y^2 - \rho\,\alpha\,v/2\,K_y\,\Delta y)$, $d = (1/\Delta y^2 + \rho\,\alpha\,v/2\,K_y\,\Delta y)$,

and $e = 2\,(R/\Delta x^2 + 1/\Delta y^2)$.

Five points involved in the relationship of Eq. (10) points to the right, left, above, and below the central point (x_i,y_j). This linear combination of T's can be represented pictorially as,

$$\begin{Bmatrix} & c & \\ b & e & a \\ & d & \end{Bmatrix} T_{i,j} = 0 \qquad (11)$$

The system of equations will be generated from this relation once the mesh size of the xy domain of interest is set up.

Modeling Area

Based on the multichannel seismic reflection record by Snavely et al. (1986) (Fig. IV-2), the Oregon accretionary complex is sketched as a grid to give 69 interior points with $\Delta x = \Delta y = 0.5$ km (Fig. IV-3). The area of the model, 5 km wide and 5 km deep, laterally covers the deformed ridges and the undeformed abyssal plain adjacent to the deformation front, and vertically the seismic basement which in the region appears to be located at about 4 km depth beneath the undeformed abyssal plain. The upper boundary temperatures at the sediment-water interface were assumed to be zero.

$$T_{U1} = T_{U2} = ...T_{U9} = 0$$

For the lower boundary temperatures at the basement, six different sets of temperatures were assigned corresponding to different geothermal gradients of 15, 20, 25, 30, 35 and 40 °C / km. The lower boundary temperature was set to decrease eastward by 2 °C laterally over 0.5 km of grid distance to account for cooling of the plate with aging.

Figure IV-2

Multichannel seismic record of the central Oregon margin (after Snavely et al., 1986). The fault geometry and topography are used to construct the interior fabric of the modelled area, in particular the depths and dips of potential fluid pathways.

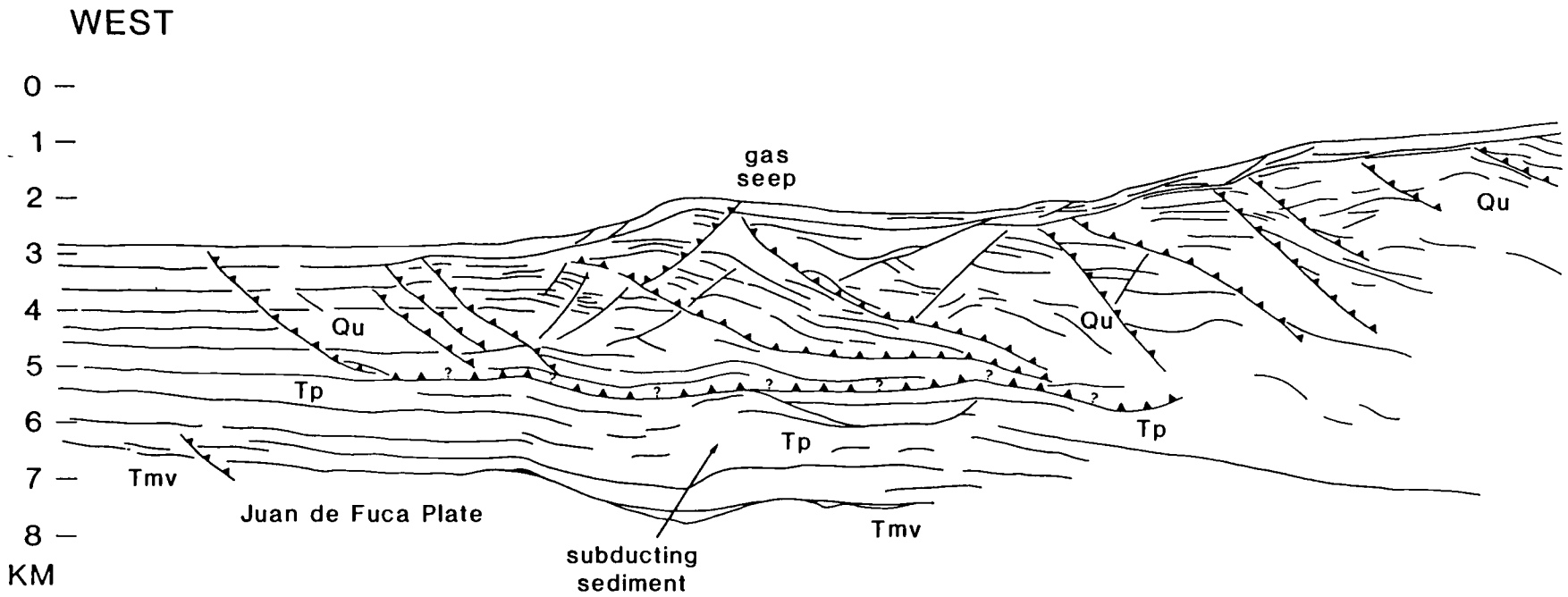
WEST
0
1
2
3
4
5
6
7
8
KM
gas
seep
Qu
Qu
Qu
Tp
Tp
Tp
Tmv
Tmv
Juan de Fuca Plate
subducting
sediment

Figure IV-2

Figure IV- 3

Modeling area with a grid of 69 nodal points. Sketch of the area is based on Fig. IV-2. The model area covers 5 km of depth to the basement and 5 km in width to encompass the undeformed abyssal plain, the deformation front, and the western slope of the second deformation ridge including the sediment pond. The vertical and the horizontal scales are one to one.

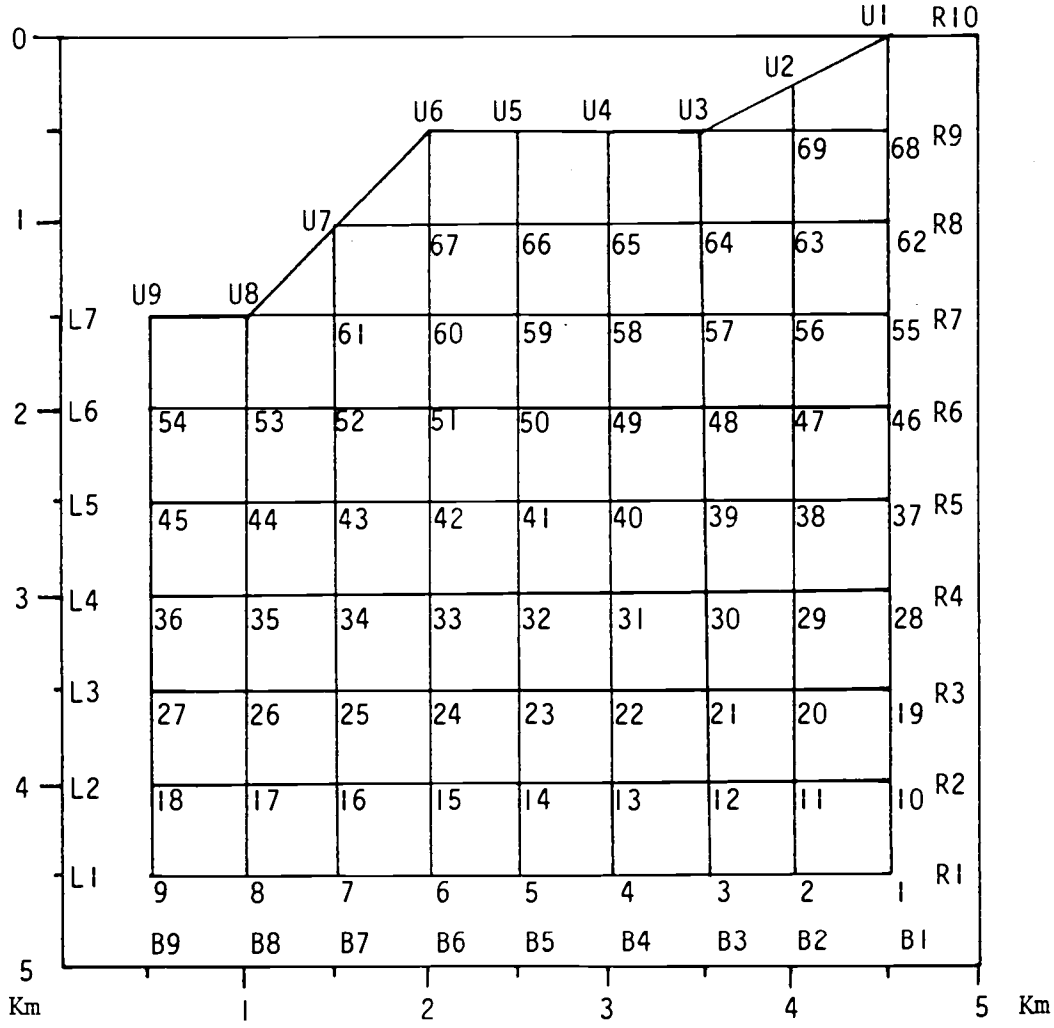
U1
R10
U2
U3
U4
U5
U6
U7
U8
U9
R9
R8
R7
R6
R5
R4
R3
R2
R1
L7
L6
L5
L4
L3
L2
L1
0
1
2
3
4
5
Km
1
2
3
4
5
Km
B9
B8
B7
B6
B5
B4
B3
B2
B1
69
68
67
66
65
64
63
62
61
60
59
58
57
56
55
54
53
52
51
50
49
48
47
46
45
44
43
42
41
40
39
38
37
36
35
34
33
32
31
30
29
28
27
26
25
24
23
22
21
20
19
18
17
16
15
14
13
12
11
10
9
8
7
6
5
4
3
2
1

Figure IV-3

For example, a geothermal gradient of 15 °C / km gave the lower boundary temperature:

$$T_{B9} = 60 \;\; T_{B8} = 58 \;\; T_{B7} = 56 \ldots\ldots \;\; T_{B1} = 44$$

The left and the right boundary conditions were given as,

$$\partial T / \partial x = 0 \qquad (12)$$

Now Eq. (10) can be written for each unknown point. The system of equations then becomes:

$$\begin{aligned}
a\,T_2 + b\,T_{R1} + c\,T_{10} + d\,T_{B1} + e\,T_1 &= 0 \\
a\,T_3 + b\,T_1 + c\,T_{11} + d\,T_{B2} + e\,T_2 &= 0 \\
a\,T_4 + b\,T_2 + c\,T_{12} + d\,T_{B3} + e\,T_3 &= 0 \\
a\,T_5 + b\,T_3 + c\,T_{13} + d\,T_{B4} + e\,T_4 &= 0 \\
&\;\;\vdots
\end{aligned} \qquad (13)$$

Fictitious exterior points (R1, R2,,,,,,, R9, L1,L2,,,,,, L9) were introduced to the right and the left boundaries to make possible the needed five-point combination shown in Eq. (11) (Fig. IV-3). The fictitious points are subsequently eliminated by using the boundary condition of Eq. (12), e.g., for the point 9,

$$(\partial T / \partial x)_{T=9} = (T_{L1} - T_9) / 2\,(0.5) = 0 \qquad (14)$$

The fictitious point L1 is thus replaced by the point 9 from Eq. (14). In the same way all fictitious points in the right and the left boundaries are eliminated by using the imposed boundary condition. Matrix representation of Eq. (13) is then:

$$
\begin{array}{cccccccccccccc}
e+b & a & & & & c & & & & & & & T_1 & -dT_{B1} \\
b & e & a & & & & c & & & & & & T_2 & -dT_{B2} \\
 & b & e & a & & & & c & & & & & T_3 & -dT_{B3} \\
 & & b & e & a & & & & c & & & & T_4 & -dT_{B4} \\
 & & & b & e+a & & & & & c & & & T_5 & -dT_{B5} \\
d & & & & & e+b & a & & & & c & & T_6 & 0 \\
 & d & & & & b & e & a & & & & c & T7 & 0 \\
 & & d & & & & b & e & a & & & c & T_8 & 0 \\
 & & & & & & & . & & & & & . & . \\
 & & & & & & & . & & & & & . & . \\
 & & & & & & & . & & & & & . & .
\end{array}
$$

Equation (15)

Sparse, diagonal coefficients dominant matrix of Eq. (15) allowed us to use the Gauss-Seidel iteration method to solve for unknown temperatures, T_1, T_2, T_3,,,,,T_{69}. The computer programs used for these calculations are named ORHEAT and are listed in the Appendix VI.

Parameters

The thermal conductivity is known to increase with depth because of consolidation and the related increase in bulk density. Therefore, the thermal

conductivity has often been related to the porosity (Lewis and Rose, 1970). The measured porosities in the Oregon accretionary complex decrease significantly from about 0.7 (porosity fraction) at the sediment-water interface to 0.4 at a depth of 4 to 6 m (Carson and Berglund, 1986). Since the porosity reaches a relatively low value shallow in the section we would expect little relative change on the 5 km scale the calculations. Thus the calculated temperature from the model should be insensitive to our assumptions concerning thermal conductivity. This insensitivity was also shown by Reck (1987). Thus semi-constant values of thermal conductivity over each depth segment of the modeling area were arbitrarily assigned in a way that they increased with depth.

The assigned depth dependent values of K_y ranged from 1.6 to 2.4 w/m °C. Measured conductivity values in sediments of the Oregon accretionary complex increase regularly from 0.8 to 1.1 W/m °C with depth over the first 6 m (Langseth, unpubl. data). The lower range of 1.6 W/m °C assumed in this model seems reasonable as this value was assigned to the uppermost grid points which are located at 0.5 km depth from the surface. K_y values of 1.7, 1.8, 1.9, 2.0, 2.2 and 2.4 were assigned to lower grid points with values increasing with depth. Considering that an assumed conductivity value of the upper mantle is usually on the order of 2.9 W/m °C (Wang and Shi, 1984), the upper value of 2.4 W/m °C used here is not unreasonable for the deeply-buried lithified sediments of the Oregon margin. The upper range of conductivity also conforms to the value used in other thermal models of convergent margins (Heasler and Surdam, 1985).

The values of K_x were assigned by the preset ratio R, K_x / K_y, of either 50 or 100. The range of R was assumed to be the approximate lower and upper extreme values possible (Garven, 1985). Values of 4.18 J / g°C and 1.025 g / cm^3 were used for the specific heat of water and the density of water, respectively, following Reck

Figure IV- 4

Sketch of the modeling area showing three characteristic tectonic elements: (a) undeformed abyssal plain, (b) the ridge at the deformation front, and (c) the intra-basin between the first and the second deformation ridges.

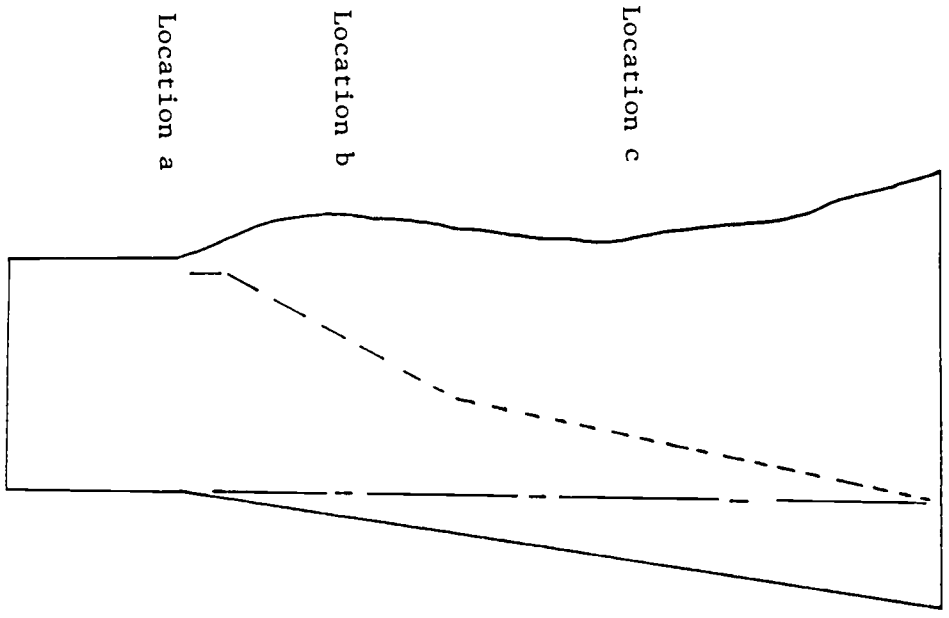

Figure IV-4

(1987). These properties were assumed to be constant over the xy-plane of the model.

For the advection parameter three different cases were considered: (1) no advection (u=v=0), (2) uniform upward advection (|u|=|v|=const), and (3) confined upward advection ($|u_1|=|v_1|$=const1 and $|u_2|=|v_2|$=const2). Thermal models with different basement temperature and different conductivity ratio; $R=K_x/K_y$, were considered for each case to generate different temperature distributions within the Oregon accretionary complex and the resulting heat flow distribution across the surface of the complex.

RESULTS

The model-derived thermal gradients in the upper 0.5 km and the resulting estimated heat flow data are listed in Tables IV-1 and IV-2. The three thermal gradients (Locations "a","b" and "c") for each basement temperature (60 ° to 160 °C) correspond to the critical tectonic elements of the Oregon unthrust area (Fig. IV-4), i.e., Location "a" = undeformed abyssal plain, Location "b" = first marginal ridge, Location "c" = intra-basin between the first and the second ridges. Ranges of measured heat flow data are available from all three sites (Langseth, unpubl. data), the model-derived heat flow data in Tables IV-1 and IV-2 are compared to these ranges. The best match between the two is considered the most realistic thermal model.

The ranges of measured heat flow data from the three locations are plotted in Fig. IV-5. For each scenario of thermal model the predicted heat flow data that are closest in the grid to the measured heat flows are also plotted in Fig. IV-5. The measured heat flow ranges show that the undeformed abyssal plain (Location "a") has the highest heat flow (100 - 125 mW/m^2), the marginal ridge (Location "b") has the lowest (50 -70 mW/m^2), and the intra-basin between the deformation ridges (Location "c") has an intermediate (75 - 100 mW/m^2) heat flux.

Table IV-1 Model-derived thermal gradients and heat flows at the three locations. $R=K_x/K_y$ is at 50.

Thermal Gradient

Basement Temperature	60			80			100			120			140			160		
Locations	a	b	c	a	b	c	a	b	c	a	b	c	a	b	c	a	b	c
No Advection							24.14	3.7	6.78	28.4	4.36	7.96	32.66	5	9.14	36.94	5.64	10.32
Advection 1 cm/yr				50.3	9.9	18.14	62.48	12.28	22.46	74.68	14.64	26.8	86.88	17.02	31.14	99.06	19.4	35.46
Advection 5 cm/yr	79.56	24.74	43.9	110.02	34.26	60.76	140.58	43.76	77.68	171.12	53.32	94.6						
Advection 10 cm/yr	92.88	34.34	56	127.96	47.24	77.04	163.14	60.24	98.24	196.32	73.22	119.42						
Confined 20/1 cm/yr				30.12	14.94	21.86	38.36	19.02	27.84	46.62	23.22	33.98	55.3	27.42	40.12	63.78	31.62	46.28

Heat Flow

No Advection							36.62	5.92	10.85	45.44	6.98	12.74	52.26	8.00	14.62	59.10	9.02	16.51
Advection 1 cm/yr				80.48	15.84	29.02	99.97	19.65	35.94	119.49	23.42	42.88	139.01	27.23	49.82	158.50	31.04	56.74
Advection 5 cm/yr	127.30	39.58	70.24	176.03	54.82	97.22	224.93	70.05	124.29	273.79	85.31	151.38						
Advection 10 cm/yr	148.61	54.94	89.60	204.74	75.58	123.26	261.02	96.38	157.18	317.31	117.15	191.07						
Confined 20/1 cm/yr				48.19	23.90	34.98	61.38	30.43	44.54	74.91	37.15	54.37	88.48	43.87	64.19	102.02	50.59	74.05

Table IV-2 Model-derived thermal gradients and heat flows at the three locations. $R=K_x/K_y$ is at 100.

Thermal Gradient

Basement Temperature	60			80			100			120			140			160		
Locations	a	b	c	a	b	c	a	b	c	a	b	c	a	b	c	a	b	c
No Advection							16.5	1.56	2.9	18.14	1.7	3.16	19.78	1.84	3.44	21.42	1.98	3.7
Advection 1 cm/yr				34.46	4.2	7.82	39.62	4.8	8.94	44.8	5.4	10.04	45.98	6	11.16	55.14	6.6	12.26
Advection 5 cm/yr	79.14	17.1	31.82	109.2	23.6	43.66	138.6	29.92	55.3	167.98	36.22	66.96						
Advection 10 cm/yr	91	26.08	46.58	124.96	35.66	63.66	159.54	45.56	81.3	194.16	55.46	98.98						
Confined 20/1 cm/yr				47.22	15.46	26.18	60.14	19.68	33.36	73.46	24.04	40.74	86.68	28.38	48.08	99.64	32.62	55.26

Heat Flow

No Advection							26.40	2.50	4.64	29.02	2.72	5.06	31.65	2.94	5.50	34.27	3.17	5.92
Advection 1 cm/yr				55.14	6.72	12.51	63.39	7.68	14.30	71.68	8.64	16.06	73.57	9.60	17.86	88.22	10.56	19.62
Advection 5 cm/yr	126.62	27.36	50.59	174.72	37.76	69.86	221.76	47.87	88.48	268.77	57.95	107.14						
Advection 10 cm/yr	145.60	41.73	74.53	199.94	57.06	101.86	255.26	72.90	130.08	310.68	88.74	158.37						
Confined 20/1 cm/yr				75.55	24.74	41.89	98.22	31.49	53.38	117.54	38.46	65.18	136.69	45.41	76.93	159.42	52.19	88.42

Figure IV- 5

Distributions of the estimated and the measured ranges of heat flow at the Locations "a", "b", and "c", representing undeformed abyssal plain, the ridge of the deformation front and intra-basin, respectively. The error bars are the range of the measured heat flows. Note that the heat flow from confined flow model best fits the measured.

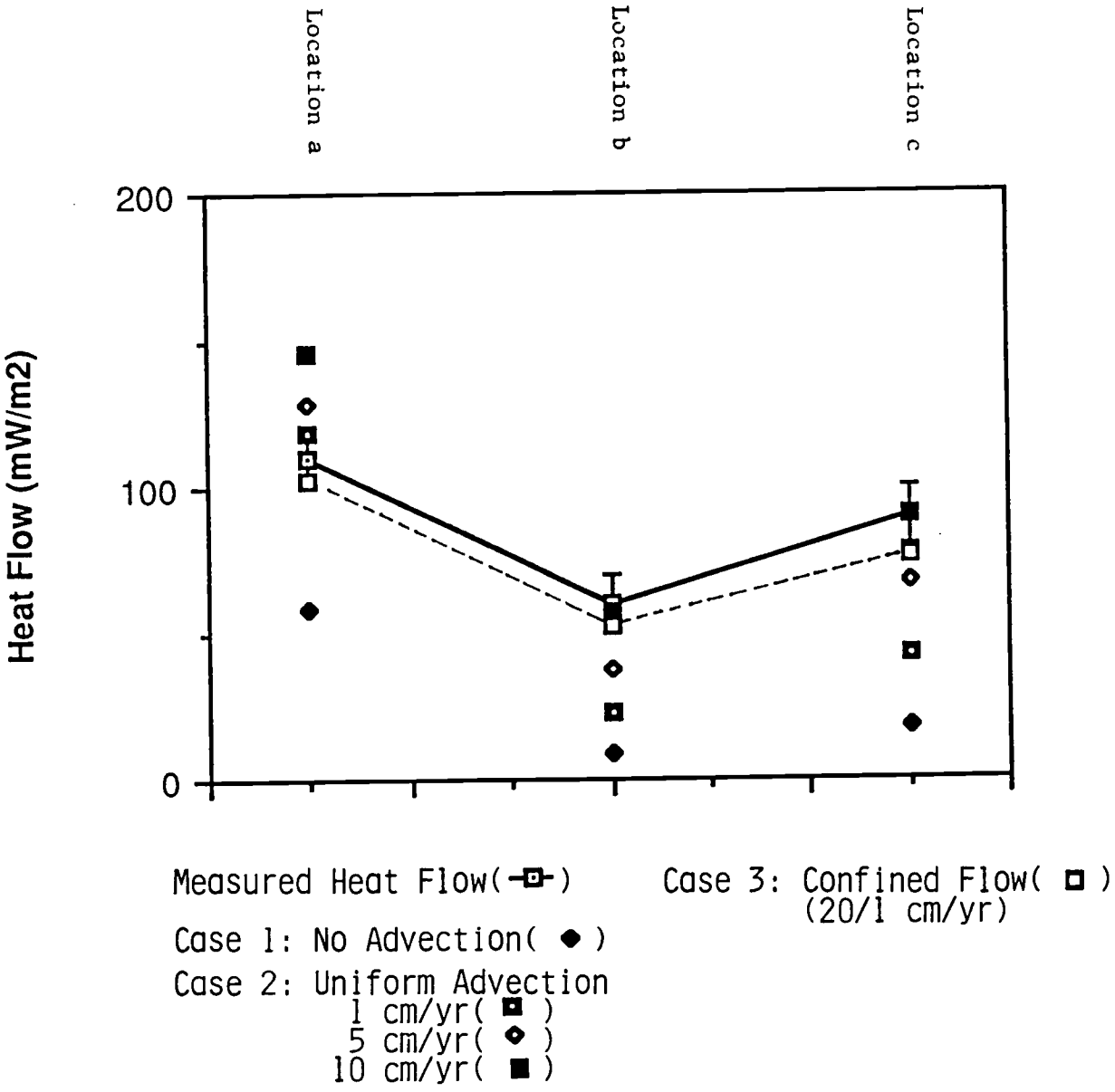
Location a
Location b
Location c
200
100
0
Heat Flow (mW/m2)
Measured Heat Flow( )
Case 1: No Advection( )
Case 2: Uniform Advection
1 cm/yr( )
5 cm/yr( )
10 cm/yr( )
Case 3: Confined Flow( )
(20/1 cm/yr)

Figure IV-5

Case 1: No Advection

In the absence of fluid advection the distribution of the predicted heat flow shows the same relative pattern as that of the measured heat flow, however, the absolute magnitudes are significantly different. This same trend in the heat flow distribution pattern is observed for all thermal models of advection but with varying magnitude (Fig. IV-5). The heat flow obtained from the thermal model simulating no-advection, underestimates the measured values at any setting of basement temperature and conductivity ratio, $R= K_x/K_y$ (Tables IV-1 and IV-2). At a basement temperature of 160 °C and K_x/K_y=50, the scenario of no-advection yields the heat flow estimates of 59.1, 9.02 and 16.5 mW/m^2 for the Locations of "a", "b" and "c", respectively. These estimates, though the highest among the heat flow data for the case of no-fluid-advection, greatly underestimate the measured heat flows. Only unrealistically high basement temperatures of > 1000 °C would yield the desired magnitude in heat flux. This result, therefore, suggests that fluid advection must be considered in the thermal model of the Oregon accretionary complex to account for the measured heat flow distribution.

Case 2: Uniform Advection

The estimated heat flow and thermal gradients data predicted by the thermal models for uniform upward advection of 1 cm/yr, 5 cm/yr, and 10 cm/yr are listed in Tables IV-1 and IV-2. Figure IV-6 illustrates the uniform upward advection through the Oregon accretionary complex as considered in this modeling procedure. For the fluid advection rate of 1 cm/yr, a temperature range for the basement of 80 to 100 °C, and a conductivity ratio of K_x/K_y =50, predicts heat flows of 80 to 119 mW/m^2 at Location "a". This value approaches the measured heat flow of 100 to 125 mW/m^2 quite closely (Fig. IV-5). However, at the Locations "b" and "c" the model

Figure IV- 6

Sketch of the modeling area undergoing uniform upward advection.

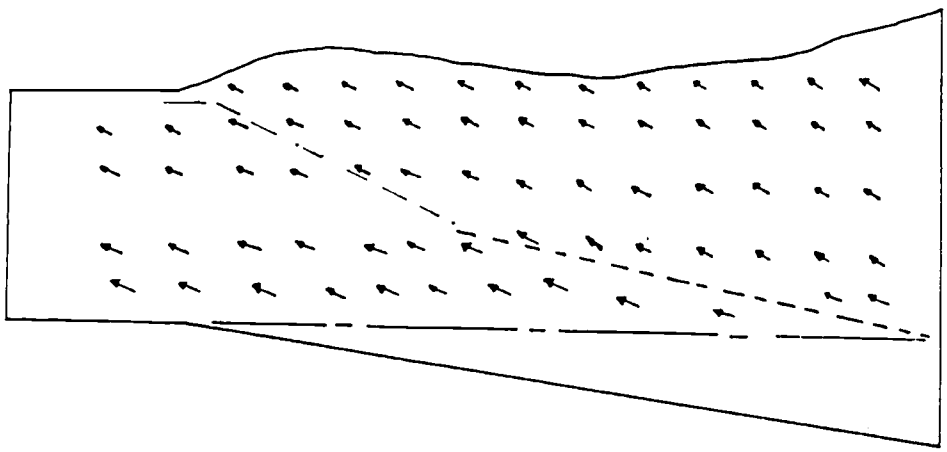

Figure IV-6

underestimates the measured heat flow by a factor of 2 to 3. The heat fluxes at these locations increase with the assumed basement temperature above 120 °C, but still remain below the measured values. On the other hand, at the basement temperature > 120 °C, the estimated heat flow at Location "a" rapidly exceeds the measured value. Therefore, a satisfactory fit of the estimated and the measured heat flow at all three locations can not be attained at realistic basement temperatures. Even at temperatures higher than the maximum value of 160 °C (used in modeling the scenario for Case 2) does not improve the fit.

For the conductivity ratio, K_x/K_y=100, no thermal model of uniform upward advection at 1 cm/yr yielded any significant heat flow in any of the locations and for the range of basement temperatures considered in the model. The increase in the basement temperature would cause the same result as described above for the ratio, K_x/K_y=50. This indicates that the case of uniform upward fluid advection of 1 cm/yr, regardless of the ratio K_x/K_y and the basement temperature, does not account for the observed heat flow distribution.

Other thermal models including uniform upward fluid advection of both 5 cm/yr and 10 cm/yr were also unable to reproduce heat flows that fit the measured values in Location "a" as well as Locations "b" and "c". In both instances (i.e. 5 and 10 cm/yr advection rate) the heat flow increases rapidly to above 150 mW/m^2 at Location a, which is well above the upper limit of the measured heat flow at that location. The boundary conditions for the respective models were basement temperature: > 60 °C and the conductivity ratios: K_x/K_y of both 50 and 100. A basement temperature lower than 60 °C would reduce the overestimated heat flow in Location a but would amplify the underestimation in Locations "b" and "c". If a large margin of error can be tolerated, the thermal model of uniform upward advection of 10 cm/yr, a basement temperature of 60 °C, and a K_x/K_y of 50 may account for the measured heat flow distribution

(Fig. IV-5).

Case 3: Confined Advection

The thermal model of confined flow generated the heat flows which best fit the measured values across the tectonic elements of the accretionary complex (Fig. IV-5). This model assumes that fluid advection of 20 cm/yr is confined to two main pathways and uniform advection,1 cm/yr, throughout the rest of the accretionary complex. Two main pathways are structurally controlled and assumed to lie (1) along the main decollement zone which is projected upward to the near-surface sedimentary melange structure at the foot of the deformation front and (2) along the major landward dipping fault planes at the landward flank of the marginal ridge (Fig. IV-7). The model-derived heat flow best simulated the measured heat flow in all three locations if the basement temperature is 160 °C and the conductivity ratio K_x/K_y either 50 or 100 (Tables IV-1 and IV- 2). The basement temperature may be lowered to 140 °C if a larger margin of error can be tolerated, and the agreement is still satisfactory. The best fit of the thermal model (based on confined fluid advection) among all types of thermal models tested here strongly suggests that confined fluid advection through the accretionary complex is a most likely process associated with compressional deformation of the Oregon underthrust margin.

DISCUSSION

Advection Rate

The most interesting result from the thermal modeling is the relatively fast fluid advection rate required to match the observed heat flow ranges. Fluids moving through confined pathways at a rate of 20 cm/yr are flowing much faster than those postulated by Reck (1987) for the northeast Japan accretionary complex, i.e., 0.3 cm/yr. The total

Figure IV-7

Sketch of the modeling area undergoing confined advection along the decollement and major fault planes. Advection rate along these pathways were set at 20 cm/yr. Advection rate in the rest of the area was set at 1 cm/yr which is not shown in the figure for simplicity.

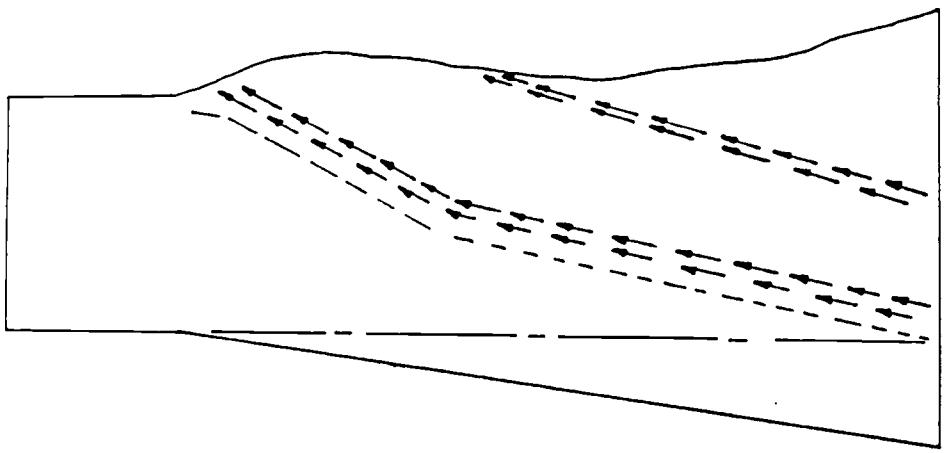

Figure IV-7

width of the two main fluid pathways in the scenario proposed here occupies 10 % of the total 5 km width of the modeling area. This is the smallest area resolvable by the data grid. If the total width of active conduit for pore fluid venting is assumed to be 5 % of the total 5 km width of the modelled area in the complex (instead of 10 % as is the case in the present model), the rate of pore fluid venting through confined pathway could then be in the order of 40 cm/yr. This illustrates that the advection rate of 20 cm/yr postulated for the Oregon accretionary complex is rather a minimum and depends strongly on the size of the active area of venting.

A minimum flow rate of 277 ml / m^2day (Suess et al., 1987a) was measured directly above a vent site in the modeling area. This rate is equivalent to 20 to 50 cm/yr depending on the porosity of the sandy matrix at the vent site, estimated to be between 50 and 20 vol. %. This independent measurement of venting in the area is surprisingly close to the advection rate of 20 cm/yr obtained by the thermal model which includes confined advection. This agreement is significant only in so far as it defines the order of magnitude of flow. Any more significance attached to the close agreement is fortuitous, because a geochemical model, addressing carbonate chimney formation in the area of venting, requires rates greater than 10 m/yr (Chapter III). What is significant, however, is that rates of pore fluid venting we derived are considerably greater in magnitude than any reported venting rates in the world's accretionary complexes only around 1 cm/yr at most (Boulegue et al., 1987; Reck, 1987). Based on all these independent results we propose that the venting rate along confined conduits in the underthrust portion of the Oregon accretionary complex is at least 20 cm/yr.

Model Geometry and Fluid Pathways

In order to refine the thermal structure within the accretionary complex a consideration of the geometry of the modeling area and the location of fluid pathways is

essential as they strongly affect the temperature distribution within the accretionary complex and the resulting heat flow across the surface of the complex. The results of the thermal modeling as used here demonstrated the need for a realistic model geometry bounding the area. All thermal models tested, even the case of no fluid advection (Case 1), generated a heat flow distribution pattern which generally agreed with the measured heat flow (Fig. IV-5). This appears to justify the model geometry used and demonstrates the importance of a realistic geometry for understanding the relatively small-scale thermal structure within the accretionary complex. Therefore, a flat-lying top boundary line, which has often been used for thermal modeling in subduction zones (Wang and Shi, 1984) can not generate a realistic detailed thermal structure. Consequently, any advection rate determined from the flat top model geometry of accretionary complexes may not be reliable.

The detailed geometry of the modeling area as employed here and based on the seismic interpretation also allows the realistic positioning of the fluid pathways within the modeling area. One of two fluid pathways was positioned along the decollement plane which was clearly revealed in the seismic profile (Fig. IV-7). The other fluid pathway was positioned along the major unconformity between the landward dipping strata of the back slope of the deformation ridge and the sediment-filled intra-basin (Fig. IV-7). The surface expression of the second major fluid pathway is located at the same position as the observed vent sites which are characterized by the benthic communities. At this point it is not certain if the projected discharge location *along the decollement* pathway suggests another concentration of benthic communities there as most of the ALVIN submersible work was focused on the landward slope of the deformation ridge. Nonetheless the *along-decollement* pathways yielded the heat flow at Location "a" that best fit the measured values.

Temperature Distribution Within the Complex

A significant difference exists in the internal thermal structure between the model based on no-advection and those with advection (Figs. IV-8 - IV-10). The 10 °C contour-spacing becomes systematically narrower with depth for the model based on no-fluid advection (Fig. IV-8). Whereas the contour spacing in general becomes narrower toward the sediment surface for the models based on fluid advection. This is pronounced especially at the Locations "a" and "c", leading to steep thermal gradients and consequently to higher heat flows (Figs. IV-9 and IV-10). The narrowing of contour spacing with depth in the Case 1 indicates that the thermal gradient becomes steeper with depth. This is quite different from the results by Reck (1987) who showed a constant thermal gradient in the modelled case based only on diffusion of heat.

In Reck's (1987) model the constant thermal gradient was due to the use of thermal conductivities that were related to porosity changes with depth. Since the porosity profile over the depth scale of kilometers did not show much variation, thermal conductivities as a consequence also varied little. This invariance of conductivities with depth causes the constant thermal gradients if only diffusion is the main heat transport mechanism. On the contrary, assigning varying thermal conductivity values, increasing by 0.1 over each 0.5 km depth increase as in the model used here, results in increasing thermal gradients with depth.

Both the varying and the constant thermal gradients with depth, however, would result in similar basement temperature, because a varying thermal gradient with gradually increasing temperature at shallow depths and a rapid increase with depth with a constant thermal gradient is averaged out. Nonetheless the two cases would result in a quite different temperature distribution within the accretionary complex, for which no independent sources of temperature data are available to validate either case. The model of no-fluid advection produces higher temperatures near to the basement than do the

Figure IV-8

Modelled temperature distribution within the Oregon underthrust area. The model parameters are: no-advection, basement temperature = 160 °C, and the ratio of $K_x/K_y = 50$.

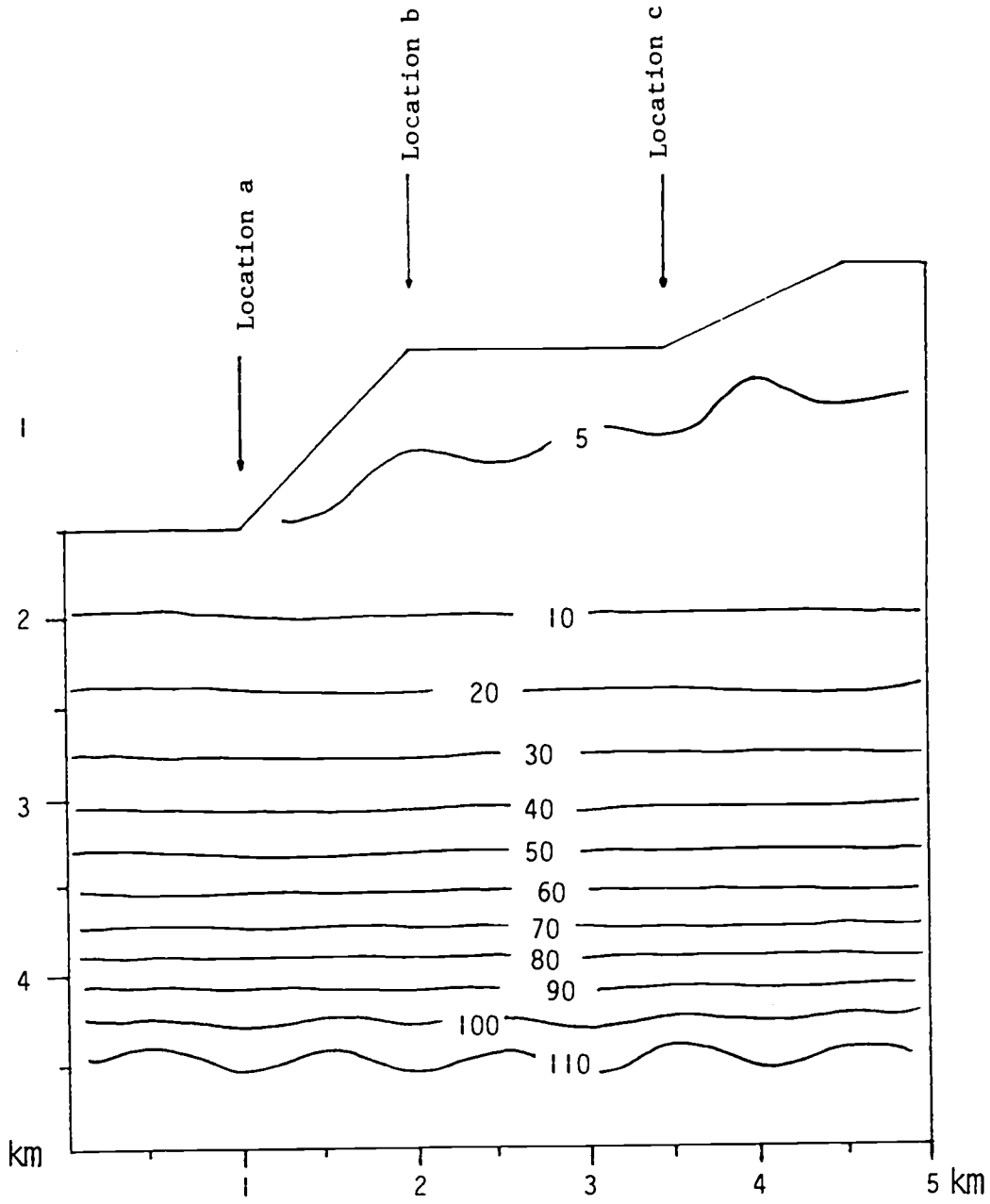
Location a
Location b
Location c
1
2
3
4
km
5
10
20
30
40
50
60
70
80
90
100
110
1
2
3
4
5 km

Figure IV-8

Figure IV-9

Modelled temperature distribution within the Oregon underthrust area. The model parameters are: advection rate = 10 cm/yr, basement temperature = 60 °C, and the ratio of $K_x/K_y = 50$.

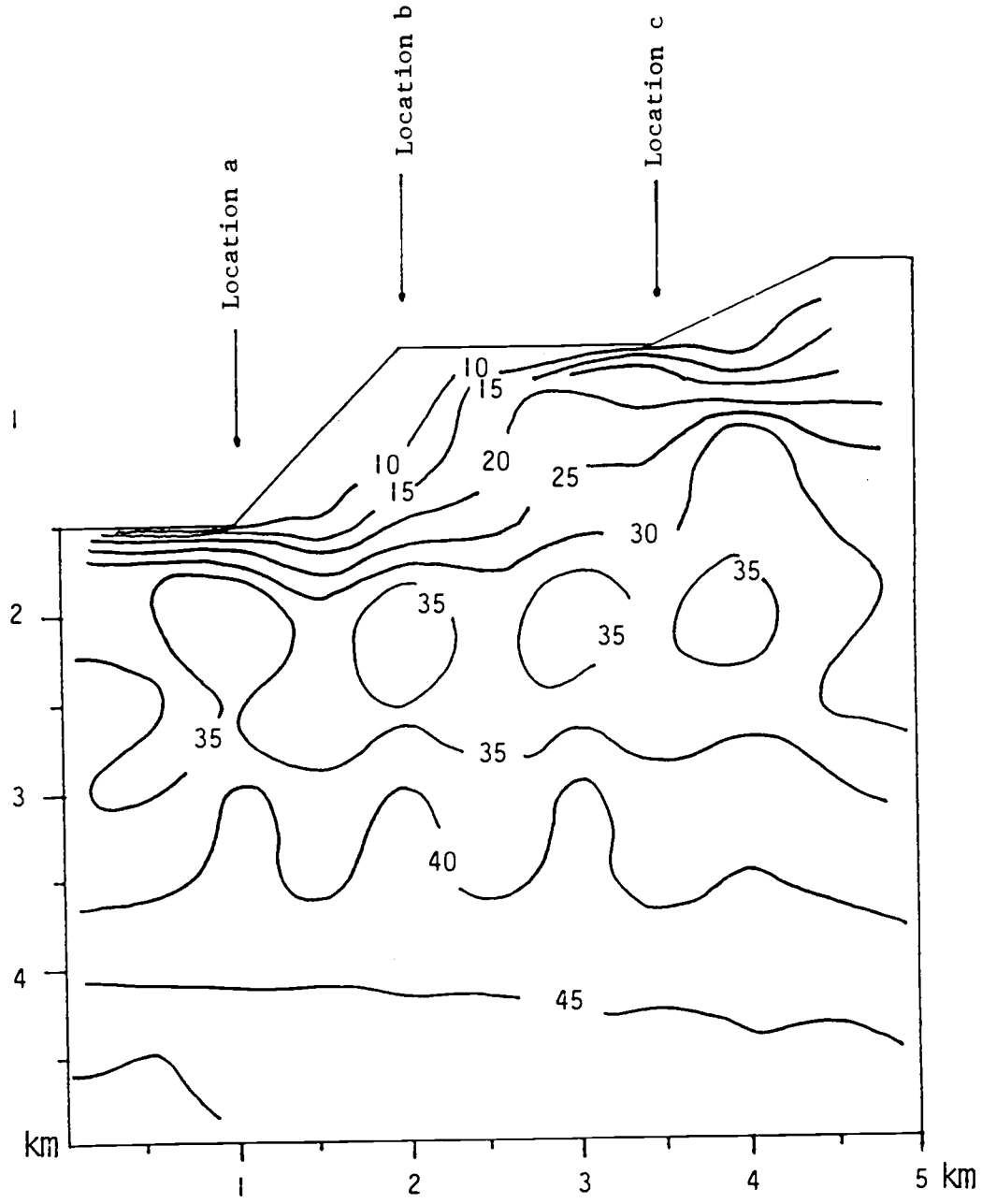
Location a
Location b
Location c
10
15
10
15
20
25
30
35
35
35
35
35
40
45
1
2
3
4
km
1
2
3
4
5 km

Figure IV-9

Figure IV-10

Modelled temperature distribution within the Oregon underthrust area. The model parameters are: confined advection rate = 20 cm/yr, basement temperature = 160 °C, and the ratio of $K_x/K_y = 50$.

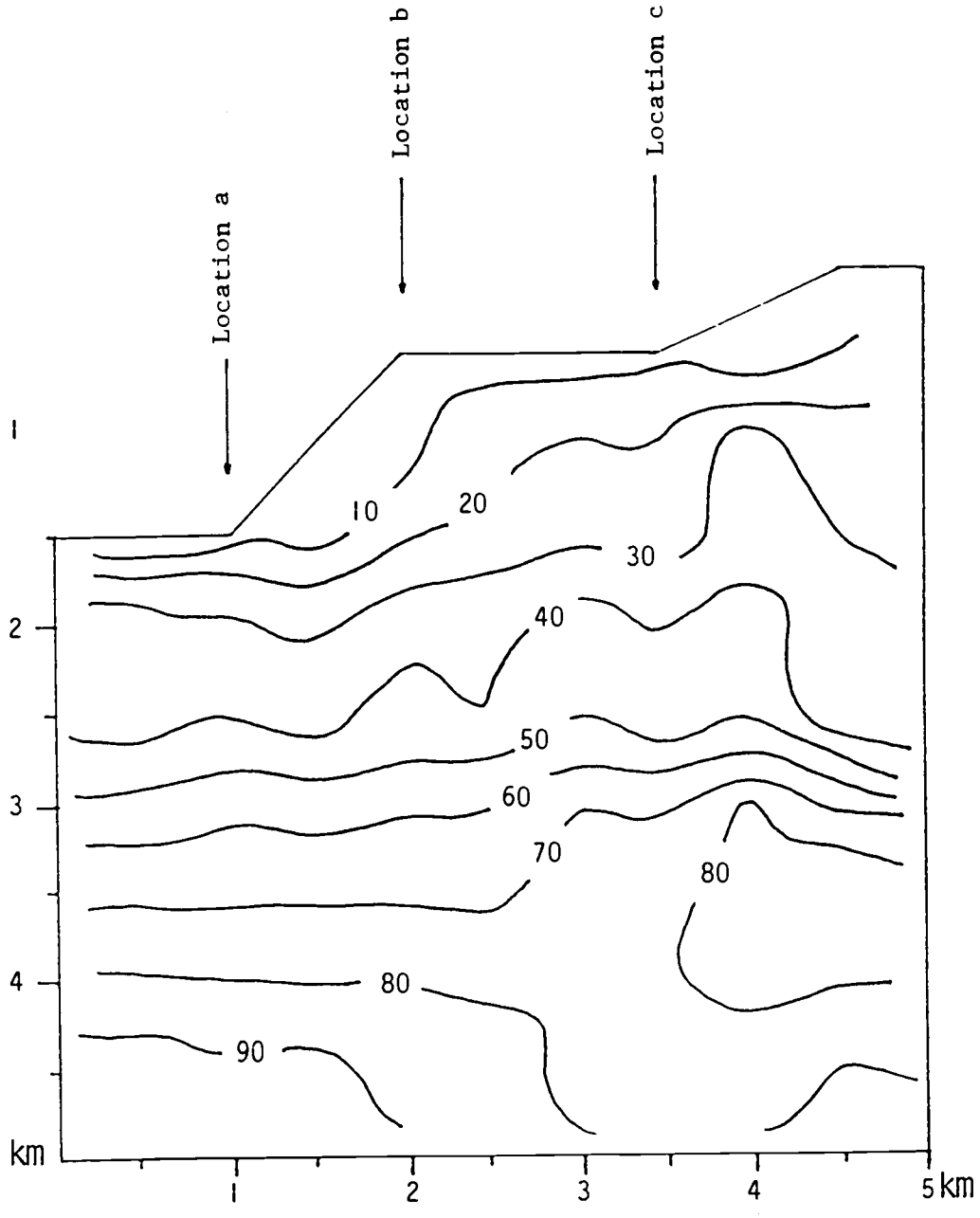
Location a
Location b
Location c
1
2
3
4
km
10
20
30
40
50
60
70
80
80
90
1
2
3
4
5 km

Figure IV-10

models based on fluid advection. At a basement temperature of 160 °C the model of no-fluid advection generates temperatures of 110 °C at nodal points closest to the basement (Fig. IV-8) while the model of uniform upward fluid advection (10 cm/yr) generates near-basement temperatures of around 90 °C (Fig. IV-9). The higher temperature predicted by the no fluid advection is consistent with Reck's (1987) result.

The decreasing thermal gradients with depth in the models which includ advection (Figs. IV-9 - IV-10) prevent build-up of abnormally high temperature at the base of the accretionary complex. This is of considerable geochemical significance and is in accord with the prediction of low temperatures at the bases of most subduction complexes (Hsui and Toksoz, 1979; Honda and Uyeda, 1983; Wang and Shi, 1984). Low basement temperatures are required for blueschist metamorphism formed at many ancient convergent margins (Miyashiro, 1973).

The thermal model based on uniform upward fluid advection at 10 cm/yr through the accretionary complex may also be accepted as a realistic scenario if a larger margin of error can be tolerated between the measured and the estimated heat flow (Fig. IV-5). The main difference between the model of confined flow at a rate of 20 cm/yr and the one of uniform upward advection at a rate of 10 cm/yr is that the former requires a basement temperature of 160 °C while the latter requires only 60 °C. Again, we do not have any independent source to validate either one of these basement temperatures. If the vent sites at restricted areas of the Oregon underthrust region play an important role in dewatering and show a systematic distribution controlled by the structural and tectonic fabric, then the case for a uniform upward advection of fluids at 10 cm/yr through the entire accretionary complex can be excluded and the basement temperature would have to be in the range of 160 °C at 5 km depth. This is equivalent to a geothermal gradient of 32 °C/km. Such a basement temperature is still low enough to promote blueschist metamorphic facies, yet high enough to also generate thermogenic

hydrocarbons (Tissot and Welte, 1978).

CONCLUSIONS

1. The heat flow obtained from the scenario of no-advection considerably underestimates the measured heat flow at any basement temperatures and the conductivity ratios of K_x/K_y used in the thermal model. This suggests that fluid advection must be considered in the dispersal of heat to account for the measured heat flow across the underthrust portion of the Oregon accretionary complex. Numerous lines of other evidence for pore fluid venting in the accretionary complex supports the suggestion.

2. The scenario of confined fluid flow simulates heat fluxes that best fit to the measured heat flows across the accretionary complex. The thermal model requires restricted pathways and a confined flow rate of 20 cm/yr and flow pathways along (1) the decollement plane and (2) the major unconformity between the landward dipping back slope of the deformation ridge and the sediment fill of the intra-basin.

3. The surface projection of the second pathway coincides with the observed vent sites of the Oregon accretionary complex which are populated by colonies of benthic organisms. The predicted rate of 20 cm/yr for confined flow agrees with the measured flow rate directly over the vent site which ranges from 20 to 50 cm/yr, although the significance of this agreement is more in the order of magnitude of flow than in the actual rates.

4. The confined flow model predicts that the basement temperature in the area of underthrusting is as low as 160 °C. Such a temperature is low enough to promote blueschist metamorphism and high enough to generate thermogenic hydrocarbons.

5. Though the confined flow model yielded the best fit between the measured and the estimated heat flows, the relative distribution pattern was the same for both scenarios.

This justifies the geometry considered in this thermal modeling (which deviates from the commonly used flat top geometry) and demonstrates the importance of using a realistic geometry for the accretionary complexes.

BIBLIOGRAPHY

Alt J. L., Muehlenbachs K. and Honnorez J., 1986, An oxygen isotopic profile through the upper kilometer of the oceanic crust, DSDP hole 504B, Earth Planet. Sci. Lett. 80:217-229.

Anderson R. N., Langseth M. G. and Sclater T. G., 1977, The mechanism of heat transfer through the floor of the Indian Ocean, J. Geopys. Res. 82:3391-3409.

Anderson R. N., Hobart M. A. and Langseth M. A., 1979, Geothermal convection through oceanic crust and sediments in the Indian Ocean, Science 204: 828-832.

Baker E. T., Massoth G. J. and Richard A. J., 1987, Cataclysmic hydrothermal venting on the Juan de Fuca Ridge, Nature 329:149-151.

Barker P. F. and Dalziel I. W. D., 1983, Progress in geodynamics in the Scotia Arc region, In: Geodynamics of the Eastern Pacific Region, Caribbean and Scotia Acrs., Ed. S. J. Ramon, Geodynamic Series 9:137-170.

Bear J., 1972, Dynamics of Fluids in Porous Media, Elsevier, New York, 674pp.

Becker K. and Von Herzen R. P., 1983, Heat flow on the western flank of the East Pacific Rise at 21 °N, J. Geophy. Res. 88:1057-1066.

Ben-Avraham Z., Shaliv G. and Nur A., 1986, Acoustic reflectivity and shallow sedimentary structure in the Sea of Galilee, Jordan Valley, Marine Geology 70: 175-189.

Bender M. L., Hudson A., Graham D. W., Barnes R. O., Leinen M. and Kahn D., 1985, Diagenesis and convection reflected in pore water chemistry on the western flank of the East Pacific Rise, 20 degree south, Earth Planet. Sci. Lett. 76:71-83.

Berner R. A., 1978, Sulfate reduction and the rate of deposition of marine sediments, Earth Planet. Sci. Lett. 37:492-498.

Berner R. A., 1980, Early Diagenesis: A Theoretical Approach, Princeton Univ.

Press., Princeton, N. J., 237pp.

Bertine K. K. and Keene J. B., 1975, Submarine barite-opal rocks of hydrothermal origin, Science 18:150-152.

Bonatti E., Kolla V., Moore W. S. and Stern C., 1979, Metallogenesis in marginal basins: Fe-rich basal deposits from the Philippine Sea, Marine Geology 32:21-37.

Boulegue J., Iiyama J. T., Charlou J. L. and Jedwab J., 1987, Nankai Trough, Japan Trench and Kuril Trench: geochemistry of fluids sampled by submersible "Nautile", Earth Planet Sci. Lett. 83:363-375.

Brault M. and Simoneit B. R. T., 1987, Hydrothermally-enhanced diagenetic transformations of biomarker distributions in sediments from the Bransfield Strait, Antarctica, submitted for AGU-Ocean Sciences Meeting.

Bray C. J. and Karig, D. E., 1985, Porosity of sediments in accretionary prisms and some implications for dewatering processes, J. Geophy. Res. 90:768-778.

Broecker W. S., 1971, A kinetic model for the chemical composition of sea water, Quaternary Res. 1:188-207.

Burch C. J. and Langseth M., 1981, Heat-flow determinations in three DSDP boreholes near the Japan trench, J. Geophys. Res. 86:9411-9419.

Cadet J. P., Kobayashi K., Lallemand S., Jolvet L., Aubouin J., Boulegue J., Dubois J., Hotta H., Ishii T., Konishi K., Niitsuma N. and Shimamura H., 1987, Deep scientific dives in the Japan and Kuril trenches, Earth Planet. Sci. Lett. 83:313-328.

Caldwell J. G. and Turcotte D. L., 1979, dependence of the thickness of the elastic oceanic lithosphere on age, J. Geophy. Res. 84:7572-7576.

Cann J. and Strens R., 1987, Venting events in hot water, Nature 329:104.

Carslaw H. S. and Jaeger J. C., 1959, Conduction of Heat in Solids, Clarenden Press,

Oxford, 510pp.

Carson B., Jennwei Y., Meyers P. B., Jr. and Barnard W. D., 1974, Initial deep-sea sediment deformation at the base of the Washington continental slope: A response to subduction, Geology 2(11):561-564.

Carson B., 1977, Tectonically induced deformation of deep sea sediments off Washington and north Oregon: mechanical consolidation, Marine Geol. 24:289-307.

Carson B. and Berglund P. L., 1986, Sediment dewatering associated with subduction-accretion: Experimental results, In: Structural Fabrics in DSDP Cores from Forearcs, Ed. J. C. Moore, Geol. Soc. Am. Memoir 166:135-150.

Chase C. G., 1972, The N plate problem of plate tectonics: Geophy. J. Royal Astron. Soc. 29:117-122.

Claypool G. E., 1974, Anoxic diagenesis and bacterial methane production in deep sea sediments, Ph.D. thesis, Univ. Calif. Los Angels, 276pp.

Claypool G. E. and Kaplan I. R., 1974, The origin and distribution of methane in marine sediments, In: Natural Gases in Marine Sediments, Ed. I. R. Kaplan, Plenum, New York, 99-139.

Claypool G. E.and Kvenvolden K. A., 1983, Methane and other hydrocarbon gases in marine sediment, Ann. Rev. Earth Planet. Sci. 11: 299-327.

Corliss J. B., Dymond J., Gordon L. I., Edmond J. M., Von Herzen R. P., Ballard R. D., Green K., Williams D., Bainbridge A., Crane K. and Van Andel T. H., 1979, Submarine thermal springs on the Galapagos Rift, Science 203:1073-1083.

Drever J. I., 1974, The magnesium problem, In: The Sea, Ed. E. J. Goldberg, Wiley, New York, 5:337-357.

Dron D., Boulegue J., Taira A. and Rangin C., 1987, Geochemistry of Tenryu Canyon

deep-sea fan biological community (kaiko), Earth Planet. Sci. Lett. 83:356-362.

Edmond J. M., Measures C. I., McDuff R. E., Chan L. H., Collier R., Grant B., Gordon L. I. andCorliss J. B., 1979, Ridge crest hydrothermal activity and the balance of the major and minor elements in the ocean; the Galapagos data, Earth Planet. Sci. Lett. 46:1-18.

Einsele G., Gieskes J. M., Curray J., Moor D., Aguayo J. E., Aubry M. P., Fornari D. J., Guerrero J. C. Kastner M., Kelts K., Lyle M., Matoba Y., Molina-Cruz A., Niemitz J., Rueda J., Saunders A., Schrader H., Simoneit B. and Vacquier V., 1980, Intrusion of basaltic sill into highly porous sediments and resulting hydrothermal activity, Nature 283:441-445.

Fowler S. R., White R. S. and Louden K. E., 1985, Sediment dewatering in the Makran accretionary prism, Earth Planet. Sci. Letters 75:427-438.

Garrels R. M. and Mackenzie F. T., 1971, Evolution of Sedimentary Rocks, Norton, New York, 397pp.

Garven G., 1985, The role of regional fluid flow in the genesis of the Pine Point Deposit, Western Canada sedimentary basin, Economic Geology 80:307-324.

Gerald C. F. and Wheatley P. O., 1984, Applied Numerical Analysis, 3rd edition, Addison-Wesley Pub. Co., Massachusetts, 579pp.

Gersonde and Wefer, 1987, Sedimentation of biogenic siliceous particles in Antarctic waters from the Atlantic sector, Marine Micropaleontology 11(4):311-332.

Gieskes J. M. et al., 1986, Hydrogeochemistry in the Barbados accretionary complex: Leg 110 ODP, EOS 67(44):120.

Guterch A., Grad M., Janik T., Perchuc E. and Pajchel T., 1985, Seismic studies of the central structure in west Antarctica 1979-1980 -preliminary results, Tectonophysics 114:411-429.

Hart R. A., 1973, A model for chemical exchange in the basalt-seawater system of

oceanic layer II, Canada. J. of Earth Sci. 10(6):799-816.

Hart S. R. and Staudigel H., 1979, Ocean crust interaction:Sites 417 and 418, DSDP Initial Reports 51-53:1169-1176.

Hart S. R. and Staudigel H., 1982, The control of alkalies and uranium in sea water by ocean crust alteration, Earth Planet. Sci. Lett. 58(2):202-212.

Heasler H. P. and Surdam R. C., 1985, Thermal evolution of coastal California with application to hydrocarbon maturation, Am. Assoc. Pet. Geol. Bull. 69: 1386-1400.

Holler P., 1985, Geotechnical properties of Antarctic deep sea sediments, Meteor Forsch-Ergebnisse Reihe C, No.39:23-36.

Honda S. and Uyeda S., 1983, Thermal processes in subduction zones- A review and preliminary approach on the origin of arc volcanism, In: Arc Volcanism, Physics and Tectonics, Eds. D. Shimozuru and I. Yokoyama, Adv. Earth Planet. Sci. 117-140.

Honda S., 1985, Thermal structure beneath Tohoku, northeast Japan- A case study for understanding the detailed thermal structure of the subduction zone, Tectonophysics 112:69-102.

Horibe Y., Kim K. R. and Craig H., 1986, Hydrothermal methane plumes in the Mariana back-arc spreading center, Nature 324:131.

Hsui A. T. and Toksoz M. N., 1979, The evolution of thermal structure beneath a subduction zone, Tectonophysics 60:43-60.

Karlin R., 1979, Sediment sources and clay mineral distributions off the Oregon coast: Evidence for a poleward slope undercurrent, Master Thesis, Oregon State Univeristy, 80pp.

Kastner M., Suess E., Garrison R. E. and Kvenvolden K., 1987, Hydrology, geochemistry and diagenesis along the convergent margin off Peru, EOS 68

(44):1499.

Kawahata H. and Fujioka F., 1986, Sediments and interstitial water at site 582 and 584, The Nankai trough and the Japan Trench landward slope, In: DSDP Initial Reports 87: 865-875.

Krissek L. A., 1982, Sources, dispersal, and contributions of fine-grained terrigenous sediments on the Oregon and Washington continental slope, Ph. D. Thesis, Oregon State University, 226pp.

Kulm L. D. and Fowler G. A., 1974, Oregon continental margin structure and stratigraphy: A test of the imbricate thrust model, In: Geology of Continental Margins, Eds. C. A. Burk and C. L. Drake, Springer-Verlag, NY, 261-283.

Kulm L. D., Suess E., Moore J. C., Carson B., Lewis B. T., Ritger S. D., Kadko D. C., Thornburg T. M., Embley R. W., Rugh W. D., Massoth G. J., Langseth M. G., Cochrane G. R., Scamman R. L., 1986, Oregon subduction zone: venting, fauna, and carbonate, Science 231:561-566.

Kulm L. D., Suess E. and Snavely P, Jr., 1987, Fluid venting structures on the northern Oregon continental shelf, NOAA Symp. Series for Undersea Res. in press.

Lawrence J. R., Gieskes J. M. and Broecker W. S., 1975, Oxygen isotope and cation composition of DSDP pore waters and the alteration of Layer II basalts, Earth Planet. Sci. Lett. 27:1-10.

Lerman A. and Weiler R. R., 1970, Diffusion and accumulation of chloride and sodium in lake Ontario sediment, Earth Planet. Sci. Lett. 10:150-156.

Lewis C. R. and Rose S. C., 1970, A theory relating high temperatures and overpressures, J. Petrol. Technol. 22:11-16.

Lonsdale P. F. and Becker K., 1985, Hydrothermal plumes, hot springs, and conductive heat flow in the southern trough of Guaymas Basin, Earth Planet.

Sci. Lett. 73:211-225.

Lonsdale P. F., Bischoff J. L., Burns V. M., Kastner M. and Sweeney R. E., 1980, A high temperature hydrothermal deposit on the seabed at a Gulf of California spreading center, Earth Planet. Sci. Lett. 49:8-20.

Mangelsdorf P. C. Jr., Wilson T. R. S. and Daniell E., 1969, Potassium enrichments in interstitial waters of recent marine sediments, Science 165:171-174.

Maris C. R. P. and Bender M. L., 1982, Upwelling of hydrothermal solutions through ridge flank sediments shown by pore water profiles, Science 216: 623-626.

Maris C. R. P., Bender M. L., Froelich P. N., Barnes R., Luedtke N. A., 1984, Chemical evidence for advection of hydrothermal solutions in the sediments of the Galapagos Mounds hydrothermal field, Geochim. Cosmochim. Acta. 48:2331-2346.

Matisoff G., 1980, Early diagenesis of Chesapeake Bay sediments: part 1 A time series study of temperature and chloride, Am. J. Sci. 280:1-25.

McDuff R. E. and Gieskes J. M., 1976, Calcium and magnesium profiles in DSDP interstitial waters: Diffusion or reaction?, Earth and Planet. Sci. Let. 33:1-10.

McDuff R. E., 1981, Major cation gradients in DSDP interstitial waters: the role of diffusive exchange between seawater and upper oceanic crust, Geochim Cosmochim. Acta 45:1705-1713.

Mehrbach C., Culberson C. H., Hawley J. E. and Pytkowicz R. M., 1973, Measurement of apparent dissociation constants of carbonic acid in seawater at atmospheric pressure, Limnol. Ocean. 18: 897-907.

Menzies M. and Seyfried W. E., 1979, Basalt-seawater interaction: trace element and strontium isotopic variations in experimentally altered glassy basalt, Earth Planet. Sci. Lett. 44:464-472.

Merewether R., Olsson M. S. and Lonsdale P. F., 1985, Acoustically detected

hydrocarbon plumes rising from 2 km depths in the Guaymas Basin, Gulf of California, J. Geophy. Res. 90:3075-3085.

Michard G. Albarede F., Michard A., Minster J. F., Charlou J. L. and Tan N., 1984, Chemistry of solutions from the 13 N East Pacific Rise hydrothermal site, Earth Planet. Scie. Lett. 67:297-307.

Miyashiro A., 1973, Metamorphism and Metamorphic Belts, George, Allen and Unwin, London, 492pp.

Moor G. W. and Gieskes J. M., 1980, Interaction between sediment and interstitial water near the Japan Trench, Leg 57, In: DSDP Initial Reports 56/57: 1269-1275.

Moor J. C. and Karig, D. E., 1976, Sedimentology, structural geology and tectonics of the Shikoku subduction zone, SW Japan, Bull. Geol. Soc. Am. 87: 1259-1268.

Moore J. C., Mascle A., Taylor E., Andrieff P., Alvarez F., Barnes R., Beck C., Behrmann J., Blanc G., Brown K., Clark M., Dolan J., Fisher A., Gieskes J. and others, 1986a, Structural and hydrologic framework of the northern Barbados ridge: results of Leg 110 ODP, Internation KAIKO conference on subduction zones, 10-15 November, Tokyo and Shimizu, 25.

Moore J. C., Roeske S., Lundberg N., Schoonmaker J, Cowan D. S., Gonzales E. and Lucas S. E., 1986b, Scaly fabrics from DSDP cores from forearcs, In: Structural Fabrics in DSDP Cores from Forearcs, Ed. J. C. Moore, Geol. Soc. Am. Memoir 166:55-73.

Mottl M. J., Lawrence J. L. and Keigwin L. D., 1983, Elemental and stable isotope composition of pore waters and carbonate sediments from DSDP sites 501/504 and 505, In: DSDP Initial Reports 69:461-473.

Muehlenbach S. K. and Clayton R. N., 1972, Oxygen isotope geochemistry of submarine greenstone, Canadian J. Earth Sci. 9:471-478.

Noel M., 1984, Origins and significance of non-linear temperature profiles in deep-sea sediments, Geophy. J. R. Astro. Soc. 76:673-690.

Noel M., 1985, Heat flow, sediment faulting and porewater advection in the Madeira Abyssal Plain, Earth Planet. Sci. Letters 73:398-406.

Plath D. C., Johnson K. S. and Pytkowicz R. M., 1980, The solubility of calcite-probably containing magnesium- in seawater, Marine Chemistry 10:9-29.

Pytkowicz R. M., 1982, Equilibria, Nonequilibria, and Natural Waters, John Wiley & Sons, New York, 351pp.

Reck, B. H., 1987, Implications of measured thermal gradients for water movement through the northeast Japan accretionary prism, J. Geophy. Res. 92(B5): 3683-3690.

Ritger S., Carson B. and Suess E., 1987, Methane-derived authigenic carbonates formed by subduction-induced pore-water expulsion along the Oregon/Washington margin, Geol. Soc. Am. 98:147-156.

Roach P. J., 1978, The nature of back-arc extension in Bransfield Strait, Geophys. J. R. Astron. Soc. 53:165.

Roobol M. J., 1982, Volcanic hazard at Deception Island, South Shetland Islands, British Ant. Survey Bulletin No. 51:237-245.

Rona P. A., Pockalny R. A. and Thompson G., 1986, Geologic setting and heat transfer of black smokers at TAG hydrothermal field, Mid-Atlantic Ridge 26 °N, EOS 67:1021.

Rubey W. W. and Hubbert M. K., 1959, Role of fluid pressure in mechanics of overthrust faulting. II. Overthrust Belt in Geosynclinal area of western Wyoming in light of fluid-pressure hypothesis, Bull. Geo. Soc. Am. 70:167-206.

Russell K. L., Deffeyes K. S. and Fowler G. A., 1967, Marine dolomite of unusual isotopic composition, Science 155:189-191.

Sayles F. L. and Jenkins W. J., 1982, Advection of pore fluids through sediments in the Equatorial East Pacific, Science 217:245-248.

Sayles, F. L., 1987, $CaCO_3$ solubility in marine sediments: Evidence for equilibrium and non-equilibrium behavior, Geochim. Cosmochim. Acta 49:877-888.

Scamman R. L., 1981, Diagenetic carbonate cementation of clastic sediments near the sediment-water interface on the lower continental slope off Washington and northern Oregon, M.S. thesis, Lehigh University, 197pp.

Schlosser P., Suess E. and Top Z., 1987, ^3He in the Bransfield Strait waters: Indication for local injection from back-arc rifting, submitted for AGU-Ocean Sciences Meeting.

Schroeder N. A. M., Kulm L. D. and Muehlberg G. E., 1987, Carbonate chimneys on the outer continental shelf: Evidence for fluid venting on the Oregon margin, Oregon Geology 49(8):91-96.

Schultheiss P. J. and McPhail S. D., 1986, Direct indication of pore-water advection from pore pressure measurements in Madeira Abyssal Plain sediments, Nature 320: 348-350.

Sclater J. G., Crowe J. and Anderson R. N., 1976, On the reliability of oceanic heat averages, J. Geophys. Res. 81:2997-3006.

Seyfried W. E., Jr., Michael E. B. and Janecky D. R., 1986, Chloride depletion and enrichments in seafloor hydrothermal fluids: Constraints from experimental basalt alteration studies, Geochim. Cosmochim. Acta 50:469-475.

Seyfried W. E. and Bischoff J. L., 1979, Low temperature basalt alteration by seawater: an experimental study at 70 C and 150 C, Geochim. Cosmochim. Acta 43:1937-1947.

Seyfried W. E. and Mottl M. J., 1982, Hydrothermal alteration of basalt by seawater under seawater dominated conditions, Geochim Cosmochim Acta 46:985-1002.

Sillen L. G., 1967, The ocean as a chemical system, Science 156:1189-1197.

Silver E. A., 1972, Pleistocene tectonic accretion of the continental slope off Washington, Marine Geol. 13:239-249.

Simoneit B. R. T. and Lonsdale P. F., 1982, Hydrothermal petroleum in mineralized mounds at the seabed of Guaymas Basin, Nature 295:198-202.

Skirrow G., 1975, The dissolved gases - carbon dioxide, In: Chemical Oceanography, Eds. J. P. Riley and G. Skirrow, Academic press, NY, 3:1-197.

Snavely P. D. Jr., Miller J., von Huene R. and Mann D., 1986, Central Oregon Margin, Lines W076-4 and 5, In: Seismic Images of Modern Convergent Margin Tectonic Structure, Ed. R. Von Huene, Am. Assoc. Petro. Geol. Studies 26:27.

Speed R., Torrini R. and Claypool G. C., 1986, Defluidization of the Barbados accretionary complex on Barbados, EOS 67:1204.

Spooner E. T. C., Beckinsdale R. D., Fyfe W. S. and Smewing J. D., 1974, ^{18}O enriched ophiolitic metabasic rocks from E. Liguria (Italy), Pindos (Greece), and Troodos (Cyprus), Contrib. Mineral Petrol. 47:41-74.

Staudigel H., Hart S. R. and Richardson, S. H., 1981, Alteration of the oceanic crust: processes and timing, Earth Planet. Sci. Lett. 52:311-325.

Staudigel H. and Hart S. R., 1983, Alteration of basalt glass: mechanisms and significance for oceanic crust-seawater budget, Geochim Cosmochim Acta 47: 337-350.

Stefansson V., 1983, Physical environment of hydrothermal systems in Iceland and on submerged oceanic ridges, In: Hydrothermal Processes at Seafloor Spreading Centers, Eds. P. A. Rona, K. Bostrom, L. Laubier and K. L. Smith Jr., Plenum Press, New York, Nato Conference Series IV 12:321-360.

Stein C. L. and Smith A. J., 1986, Authigenic carbonate nodules in the Nankai trough,

site 583, In: DSDP Initial Reports 87:659-665.

Suess E., Balzer W., Hesse K. F., Muller P. J. Ungerer C. A. and Wefer G., 1982, Calcium carbonate hexahydrate from organic-rich sediments of the Antarctic shelf: precursors of Glendonites, Science 216:1128-1131.

Suess E. and Whiticar M. J., 1986, Methane-derived CO_2 in pore fluids expelled from the Oregon subduction complex, International KAIKO conference, Nov. 1986, Tokyo and Shimizu, Japan, 36.

Suess E., Kulm L. D., Carson B. and Whiticar M. J., 1987a, Fluid flow and methane fluxes from vent sites at the Oregon subduction zone, EOS 68 (44): 1486.

Suess E., Fisk M., Whiticar M. J., Wefer G., Wittstock R., Theilen F., Schreiber R., Simoneit B. R. T., Laban C., Kadko D., Schlosser P. and Top Z., 1987b, Hydrothermalism in the Bransfield Strait, Antarctica, in prep.

Sweeney R. E., 1980, A high temperature hydrothermal deposit on the seabed at a Gulf of California spreading center, Earth Planet. Scie. Lett. 49:8-20.

Theilen R. S., 1986, Back-arc spreading structure in the Bransfield Strait, Post-cruise meeting of ANT Leg IV, Bremen, West Germany, Abstract.

Thompson G., 1983, Basalt-seawater interaction. In: Hydrothermal Processes at Seafloor Spreading Centers, Eds. P. A. Rona, K. Bostrom, L. Laubier and K. L. Smith Jr., Plenum Press, New York, Nato Conference Series IV 12: 225-278.

Tissot B. P. and Welte D. H., 1978, Petroleum Formation and Occurrence, Springer Verlag, Berlin, West Germany, 538pp.

Uyeda S., 1987, Active hydrothermal mounds in the Okinawa back-arc trough, EOS 68:737.

Van Enst J. W. and Laban C., 1987, Report on gravity core samples from ANT IV/2

expedition Bransfield Strait 1985, Rijks Geologische Dienst, Haarlem, Netherland, 55pp.

Von Breymann M. R. T, 1987, Magnesium in hemipelagic environments: Surface reactions in the sediment-pore water system, Ph. D. Thesis, Oregon State University, 216pp.

Von Damm K. L., Edmond J. M., Grant B., Measures C. I., Walden B. and Weiss R. F., 1985a, Chemistry of submarine hydrothermal solutions at 21 °N, East Pacific Rise, Geochim. Cosmochim. Acta 49:2197-2220.

Von Damm K. L., Edmond J. M., Measures C. I. and Grant B., 1985b, Chemistry of submarine hydrothermal solutions at Guaymas basin, Gulf of California, Geochim. Cosmochim. Acta 49:2221-2237.

Von Huene R, 1985, Direct measurement of pore fluid pressure, Leg 84, Guatemala and Costa Rica, In: DSDP Initial Reports 84:767-772.

Wang C. Y. and Shi Y. L., 1984, On the thermal structure of subduction complexes: A preliminary study, J. Geophys. Res. 89:7709-7718.

Watermann L. S., Sayles F. L. and Manheim F. T., 1972, Interstitial water studies on small core samples Leg 16, 17, and 18, In: DSDP Initial Reports 18: 1001-1012.

Wefer G., Suess E., Balzer W., Liebezeit G., Muller P. J., Ungerer C. A. and Zenk W., 1982, Fluxes of biogenic components from sediment trap deployment in circumpolar waters of the Drake Passage, Nature 299:145-147.

Weiss R. F., 1974, Carbon dioxide in water and seawater: the solubility of a non-ideal gas, Marine Chemistry 2:203-215.

Weiss R. F., Lonsdale P. F., Lupton J. E., Bainbridge A. E. and Craig H., 1977, Hydrothermal plumes in the Galapagos Rift, Nature 267:600-603.

Weiss R. F., 1985, Chemistry of submarine hydrothermal solutions at 21°N, East

Pacific Rise, Geochim Cosmochim. Acta 49:2197-2220 .

Wells R. E., Engebretson D. C., Snavely P. D., Jr. and Coe R. S., 1984, Cenozoic plate motions and the volcanotectonic evolution of western Oregon and Washington, Tectonophysics 3:275-294.

Whiticar M. J., Suess E. and Wehner H., 1985, Thermogenic hydrocarbon in surface sediments of the Bransfield Strait, Antarctic Peninsula, Nature 314:87-90.

Whiticar M. J., Suess E., Wefer G. and Muller P. J., 1987, Calcium carbonate hexahydrate (ikaite): History of mineral formation as recorded by stable isotopes, submitted to Geochim. Cosmochim. Acta.

Wiebe R. and Gaddy V. L., 1940, The solubility of carbon dioxide in water at various temperatures from 12 to 40 °C at pressure to 500 atmospheres, Critical phenomena, J. Am. Chem. Soc. 62:815-817.

Williams D. L. and Von Herzen R. P., 1974, Heat loss from the earth: new estimate, Geology 2:327-328.

Williams D. L., Von Herzen R. P., Sclater J. G. and R. N. Anderson, 1979, The Galapagos spreading center; lithospheric cooling and hydrothermal circulation, Geophy. J. R. Astro. Soc. 38:587-608.

Wolery T. J. and Sleep N. D., 1976, Hydrothermal circulation and geochemical flux at mid-ocean ridges, J. Geology 84:249-275.

Zhao W. L., Davis D. M., Dahlen F. A., Suppe J., 1986, Origin of convex accretionary wedges:evidence from Barbados, J. Geophys. Res. 91: 10246-10258.

APPENDICES

APPENDIX I

Pore Water Chemistry Data from the Bransfield Strait Basin, Antarctica

Pore Water Chemistry Data from the Bransfield Strait Basin, Antarctica

Core Station	Depth Interval (cm)		Total CO_2 mM	Ammonia µM	Phosphate µM	Silicate µM	Alkalinity meq/l	SO_4^{2-} mM	Ca^{2+} mg/l	Mg^{2+} mg/l	K^+ mg/l	Na^+ mg/l	Cl^- g/kg
1327-1													
	0	10	6.8	342	75	669	7.2	25.66	416	1279	405	10850	19.10
	23	28	11.8	608	82	705		22.67	416	1284	411	10840	19.23
	49	53	18.0	852	207	715	17.0	20.46	421	1267	409	10750	19.18
	110	115	29.1	1023	360	726	27.7	14.45	414	1249	411	10700	19.28
	200	205	42.9	1824	542	724	42.2	5.54	414	1220	400	10760	19.17
	320	325	53.3	2234	509	720	49.7	0.15	384	1206	411	10830	19.20
	365	370	54.6	2375	522	746	53.3	0.43	399	1224	400	10880	19.19
	410	415	55.9	2573	426	706	53.1	0.21	391	1233	397	10850	19.31
	465	470	55.8	2743	364	671	54.0	0.14	375	1230	407	10860	19.21
	510	515	55.7	2741	253	684	52.5	0.14	341	1229	397	10610	19.19
	550	555	56.6	2916	331	663	55.4	0.09	340	1263	410	10820	19.26
	630	635	55.7	3074	224	666	55.4	0.07	292	1268	415	10820	19.37
	750	755	57.9	3219	157	623	57.2	0.57	300	1308	410	10820	19.31
1340-1													
	20	25	9.3	551	131	732	6.4	24.75	429	1290	428	10970	19.14
	70	75	12.5	924	174	707	14.0		430	1270	410	10740	19.08
	110	115	15.1	1033	227	731	16.5	21.13	423	1266	405	10800	19.11
	155	160	18.6	1188	255	688	20.3	19.37	437	1277	414	10840	
	185	190	21.1	1463	302	732	22.8	18.97	437	1288	407	10760	19.28
	215	220	23.8	1543	313	738	24.6	18.18	431	1282	412	10810	19.21
	250	255	27.5	1915	361	688	27.8	16.98	440	1262	405	10770	19.30
	305	310	31.6	2146	315	679	30.8	15.24	459	1258	400	10830	19.36
	360	365	33.6	2234	432	719	33.3	14.69	474	1255	401	10940	19.40
	415	420	33.0	2580	222	607	32.0	14.21	464	1247	401	10920	19.36
	490	495	33.1	2591	180	671	30.9	14.33	482	1242	407	10960	19.58
	515	520	31.2	2576	105	626	29.5	14.57	506	1233	396	10950	19.64
	560	565	29.2	2562	40	641	28.3	15.37	539	1236	386	11070	19.65
	595	600	25.6	2562	24	584	24.9	15.58	521	1229	388	11140	19.51
	635	635	24.0	2616	15	451	23.2	15.97	474	1231	373	11150	19.92

Core Station	Depth Interval (cm)		Total CO_2 mM	Ammonia µM	Phosphate µM	Silicate µM	Alkalinity meq/l	SO_4^{2-} mM	Ca^{2+} mg/l	Mg^{2+} mg/l	K^+ mg/l	Na^+ mg/l	Cl^- g/kg
1341-1													
	170	175	22.8	1339	292	736		19.35	432	1299	413	10920	19.35
	265	270	31.8	1920	400	758		16.30	432	1265	415	11030	19.50
	320	325	37.0	2162	432	708		13.71	433	1267	418	11090	19.47
	365	370	42.5	2376	454	757		14.09	429	1238	413	10860	19.56
	425	430	47.9	2769	492	770		13.30	420	1253	415	11030	19.66
	465	470	52.2	3425	495	818		3.26	409	1246	427	11110	20.11
	515	520	50.6	3924	460	734		4.27	406	1242	421	10930	19.85
	580	585	52.8	4576	428	761		3.00	423	1242	439	11490	20.46
	615	620	44.5	4906	89	902		7.03	435	1239	439	11820	21.27
	655	660	41.1	5244	47	782		8.59	447	1217	449	11900	21.36
	705	710	35.7	5075	10	727		10.27	436	1201	457	12070	21.56
	720	725	33.4	4914	7	697		10.64	389	1222	464	12150	21.89
	765	765	30.4	4866	5	546		11.72	409	1213	465	11940	21.68
1343-1													
	20	25	9.1	860	64	660	9.6	21.22	454	1235	423	10830	19.36
	45	50	12.3	1156	152	692	13.4	17.09	493	1228	411	10830	19.64
	85	90	15.2	1524	162	699	16.3	13.04	520	1220	409	10880	19.70
	120	125	17.9	1943	115	656	19.2	8.93	554	1188	420	10900	20.07
	145	155	19.9	2087	148	728	20.7	6.99	574	1199	408	10790	20.04
	165	170	20.4	2152	111	687	21.2	5.24	584	1167	406	10740	20.15
	195	200	22.1	2272	126	703	22.5	3.55	608	1201	408	10750	20.20
	240	245	21.3	2630	64	628	21.2	1.22	630	1163	413	10840	20.38
	270	275	20.6	2666	57	627	20.6	0.22	634	1174	413	10790	20.51
	300	305	18.9	2733	59	544	19.8	0.19	664	1185	389	10700	20.79
	320	325	18.0	3100	60	518	19.3	0.15	693	1158	378	10850	20.72
	375	380	16.0	2876	18	576	17.1	0.09	744	1195	379	10730	21.06
	430	435	14.6	3060	26	538	16.2	0.17	804	1197	375	10810	21.25
	465	470	13.3	3177	21	482	11.5	0.30	799	1185	375	10760	21.58
	505	560	10.7	3233	20	530	11.8	0.58	806	1187	375	10640	21.51

Core Station	Depth Interval (cm)		Total CO_2 mM	Ammonia µM	Phosphate µM	Silicate µM	Alkalinity meq/l	SO_4^{2-} mM	Ca^{2+} mg/l	Mg^{2+} mg/l	K^+ mg/l	Na^+ mg/l	Cl^- g/kg
1346													
	50	55	10.2	628	146	757	10.6	23.51	437	1242	403	10930	19.21
	150	155	17.9	1453	312	769	19.6	18.78	486	1205	376	11070	19.42
	250	255	20.7	1704	362	818	22.2	17.82	512	1185	344	11180	19.50
	350	355	19.1	1651	301	830	20.3	18.23	519	1187	320	11320	19.67
	470	475	16.1	1472	140	788	17.5	19.21	513	1192	298	11280	19.78
	495	495	14.6	1457	24	719	15.8	19.98	514	1181	294	11280	19.80

APPENDIX II

Computer Program for the Simulation of the Distribution Pattern of the Measured Chloride in the Bransfield Strait Basin, Antarctica

Computer Program for the Simulation of the Distribution of the Measured Chloride in the Bransfield Strait Basin, Antarctica

```
C                    CHLORIDE CONCENTRATION DISTRIBUTION BY
C                        FINITE DIFFERENCE APPROXIMATION
C   PROGRAM LANGUAGE: FORTRAN 77
C   AUTHOR:              M. W. HAN
C   VERSION DATE:        FEBRUARY 9,1987
C   TYPE OF COMPUTER:    PRIME
C*************************************************
C
C    DEFINITION OF VARIABLES:
C    AB: COEFFICIENT MATRIX
C    BV: COLUMN MATRIX FOR R.H.S. VECTORS
C    NITER: NUMBER OF ITERATIONS
C    TOL: TOLERANCE
C    A,B,C,D,E: COEFFICIENTS IN THE MATRIX AB
C    AR: COEFFICIENT OF A AT THE RIGHT BOUNDARY
C    BL: COEFFICIENT OF B AT THE LEFT BOUNDARY
C    CT: COEFFICIENT OF C AT THE TOP BOUNDARY
C    DB: COEFFICIENT OF D AT THE BOTTOM BOUNDARY
C    CL: COLUMN MATRIX FOR CHLORIDE VECTORS
C    U: HORIZONTAL VELOCITY VECTORS
C    W: VERTICAL VELOCITY VECTORS
C    CLL: CHLORIDE CONC. AT LEFT BOUNDARY
C    CLR: CHLORIDE CONC. AT RIGHT BOUNDARY
C    CLT: CHLORIDE CONC. AT TOP BOUNDARY
C    CLB: CHLORIDE CONC. AT BOTTOM BOUNDARY
C    DX: HORIZONTAL DIFFUSIVITY OF CHLORIDE
C    DZ: VERTICAL DIFFUSIVITY OF CHLORIDE
C    DELX: HORIZONTAL FINITE DISTANCE
C
C*************************************************
C                    MAIN PROGRAM
```

```
C*************************************************
      DIMENSION AB(20,20),A(20,20),B(20,20),C(20,20),D(20,20)
      DIMENSION U(20,20),W(20,20),CL(20),BV(20)
      DIMENSION CLL(4),CLR(4),CLB(5)
      OPEN (5,FILE='INPUT.CL')
      OPEN (6,FILE='OUTPUT.CL')
      READ (5,60) DX,DZ,DELX,CLT,NITR,TOR
      READ (5,64) (CLB(I), I=1,5)
      READ (5,70) (CLL(I), I=1,4)
      READ (5,72) (CLR(I), I=1,4)
      DO 12 I=1,4
      DO 11 J=1,5
      READ (5,74) U(I,J), W(I,J)
   11 CONTINUE
   12 CONTINUE
      DO 14 I=1,4
      DO 13 J=1,5
      A(I,J)=2.*DX-U(I,J)*DELX
      B(I,J)=2.*DX+U(I,J)*DELX
      C(I,J)=DELX*DELX*(2.*DZ-W(I,J))
      D(I,J)=DELX*DELX*(2.*DZ+W(I,J))
   13 CONTINUE
   14 CONTINUE
      E=-4.*(DX+DZ*DELX*DELX)
      CT=2.*DZ*DELX*DELX
      BL=2.*DX
      AR=BL
      DB=CT
C     FORMULATE MATRIX AB
C
C
      DO 18 I=1,20
      DO 17 J=1,20
```

```
      AB(I,J)=0.
   17 CONTINUE
   18 CONTINUE
C     PUT E TO THE DIAGONAL OF MATRIX AB
      DO 19 I=1,20
      AB(I,I)=E
   19 CONTINUE
C     PUT A AND B TO THE ABOVE- AND BELOW- DIAGONAL
      AB(1,2)=A(1,2)
      AB(2,1)=B(1,1)
      AB(2,3)=A(1,3)
      AB(3,2)=B(1,2)
      AB(3,4)=A(1,4)
      AB(4,3)=B(1,3)
      AB(4,5)=A(1,5)
      AB(5,4)=B(1,4)
      AB(5,6)=0.
      AB(6,5)=0.
      AB(6,7)=A(2,2)
      AB(7,6)=B(2,1)
      AB(7,8)=A(2,3)
      AB(8,7)=B(2,2)
      AB(8,9)=A(2,4)
      AB(9,8)=B(2,3)
      AB(9,10)=A(2,5)
      AB(10,9)=B(2,4)
      AB(10,11)=0.
      AB(11,10)=0.
      AB(11,12)=A(3,2)
      AB(12,11)=B(3,1)
      AB(12,13)=A(3,3)
      AB(13,12)=B(3,2)
      AB(13,14)=A(3,4)
```

```
      AB(14,13)=B(3,3)
      AB(14,15)=A(3,5)
      AB(15,14)=B(3,4)
      AB(15,16)=0.
      AB(16,15)=0.
      AB(16,17)=A(4,2)
      AB(17,16)=B(4,1)
      AB(17,18)=A(4,3)
      AB(18,17)=B(4,2)
      AB(18,19)=A(4,4)
      AB(19,18)=B(4,3)
      AB(19,20)=A(4,5)
      AB(20,19)=B(4,4)
C     PUT C AND D TO THE SIDE BANDS
      DO 44 I=1,5
      AB(I,I+5)=D(2,I)
      AB(I+5,I)=C(1,I)
   44 CONTINUE
      DO 45 I=1,5
      AB(I+5,I+10)=D(3,I)
      AB(I+10,I+5)=C(2,I)
   45 CONTINUE
      DO 46 I=1,5
      AB(I+10,I+15)=D(4,I)
      AB(I+15,I+10)=C(3,I)
   46 CONTINUE
C     INSERT R.H.S. VECTORS AS A COLUMN MATRIX BV
      DO 33 I=1,20
      BV(I)=0.
   33 CONTINUE
      DO 40 I=2,5
      BV(I)=-CT*CLT
   40 CONTINUE
```

```
      BV(1)=-BL*CLL(1)-BV(2)
      BV(6)=-BL*CLL(2)
      BV(10)=-AR*CLR(2)
      BV(11)=-BL*CLL(3)
      BV(15)=-AR*CLR(3)
      BV(16)=-BL*CLL(4)-DB*CLB(1)
      BV(17)=-DB*CLB(2)
      BV(18)=-DB*CLB(3)
      BV(19)=-DB*CLB(4)
      BV(20)=-AR*CLR(4)-DB*CLB(5)
C     INPUT INITIAL GUESS FOR CL
      DO 66 I=1,5
      CL(I)=19.2
   66 CONTINUE
      DO 67 I=6,10
      CL(I)=19.4
   67 CONTINUE
      DO 68 I=11,15
      CL(I)=19.6
   68 CONTINUE
      DO 69 I=16,20
      CL(I)=19.8
   69 CONTINUE
C
C     SOLVE N LINEAR EQUATIONS BY GAUSS-SEIDEL ITERATION
      CALL GSITRN (AB,BV,CL,NITER,TOL)
C
C     PRINT THE RESULTS
      WRITE (6,95)
      K=1
      DO 89 I=1,4
      DO 88 J=1,5
      WRITE (6,100) CL(K),U(I,J),W(I,J)
```

```
      K=K+1
 88  CONTINUE
 89  CONTINUE
 60  FORMAT (2(F7.5,1X),F6.1,F5.1,I3,F6.3)
 64  FORMAT (5(F5.2,1X))
 70  FORMAT (4(F5.2,1X))
 72  FORMAT (4(F5.2,1X))
 74  FORMAT (F4.2,F7.3)
 95  FORMAT ('    Cl (g/kg)  u (m/yr)  w (m/yr)')
 100 FORMAT (2X,F10.4,F10.3,F10.3)
      STOP
      END
C
C*************************************************
C
C*************************************************
      SUBROUTINE GSITRN (AB,BV,CL,NITER,TOL)
      DIMENSION AB(20,20),BV(20),CL(20)
      DO 10 I=1,20
        SAVE=AB(I,I)
        BV(I)=BV(I)/SAVE
        DO 7 J=1,20
          AB(I,J)=AB(I,J)/SAVE
 7    CONTINUE
 10   CONTINUE
      DO 40 ITER=1,NITER
      CLMAX=0.
      DO 30 I=1,20
      SAVE=CL(I)
      CL(I)=BV(I)
      DO 20 J=1,20
      IF (J .NE. I) THEN
      CL(I)=CL(I)-AB(I,J)*CL(J)
```

```
      END IF
   20 CONTINUE
      IF (ABS(CL(I)-SAVE) .GT. CLMAX) THEN
      CLMAX=ABS(CL(I)-SAVE)
      END IF
   30 CONTINUE
      IF (CLMAX .LE. TOL) RETURN
   40 CONTINUE
      PRINT 200, TOL,NITER
  200 FORMAT(/'DID NOT MEET TOLERANCE OF ',E14.6,' IN ',I4,
     1    ' ITERATIONS'/ LAST VALUE OF T WAS RETURNED TO
     1    CALLER')
      RETURN
      END
```

0.03154 0.00315 1000.0 19.0 99 0.001

19.81 19.70 19.60 19.98 20.76

19.00 19.10 19.20 19.20

19.89 20.21 20.76 21.10

0.14 0.008

0.13 0.007

0.13 -0.002

0.06 -0.010

0.04 -0.006

0.12 0.002

0.09 0.005

0.07 -0.003

0.05 -0.012

0.03 -0.003

0.05 0.015

0.04 0.004

0.05 -0.003

0.04 -0.013

0.01 -0.004

0.02 0.010

0.01 0.005

0.01 -0.005

0.07 -0.010

0.01 -0.001

Cl (g/kg)	u (m/yr)	w (m/yr)
19.3000	0.140	0.008
19.2000	0.130	0.007
19.1000	0.130	-0.002
19.2700	0.060	-0.010
19.5800	0.040	-0.006
19.4600	0.120	0.002
19.3700	0.090	0.005
19.2800	0.070	-0.003
19.3800	0.050	-0.012
19.7900	0.030	-0.003
19.5900	0.050	0.015
19.4800	0.040	0.004
19.3500	0.050	-0.003
19.4900	0.040	-0.013
20.1300	0.010	-0.004
19.7300	0.020	0.010
19.5400	0.010	0.005
19.3800	0.010	-0.005
19.6100	0.070	-0.010
20.3500	0.010	-0.001

APPENDIX III

Pore Water Chemistry Data from the Oregon/Washington Subduction Zone

Calculation Procedure for $CaCO_3$ Precipitation

Values of K_1, K_2, and K_s as a Function of Pressure at 0 °C and 35 $^{o}/_{oo}$

Calculation Procedure for the Degree of Saturation of Pore Fluids with Respect to $CaCO_3$

Pore Water Chemistry Data from the Oregon/Washington Subduction Zone

Core Station	Depth Interval (cm)		Phosphate µM	Ammonia µM	Alkalinity meq/l	SO_4^{2-} mM	Ca^{2+} mg/l	K^+ mg/l	Mg^{2+} mg/l	Na^+ mg/l	Cl^- g/kg
W8306-2A											
	0	10	8.4	55.0	3.40	28.12	428	434	1316	11030	19.40
	10	20	7.4	111.0	3.60	27.96	415	439	1318	10950	19.53
	30	40	16.1	180.0	4.50	27.24	418	430	1315	11040	20.00
	50	60	25.1	286.0	5.40	26.40	400	426	1295	10950	19.75
	70	80	29.9	425.0	6.80	25.78	404	428	1307	11030	19.15
	90	100	32.7	630.0	8.00	24.49	382	413	1290	10870	19.75
	115	125	34.5	590.0	10.10	22.71	375	416	1290	10910	19.24
	135	145	37.7	759.0	11.70	20.94	361	404	1295	10920	19.66
	145	150	38.5	794.0		22.64	370	414	1287	11310	19.19
	155	160	39.4	839.0		20.15	358	418	1294	11020	20.17
	165	170	39.6	983.0		19.84	330	408	1289	10880	19.75
	175	180	40.1	1085.0		19.19	349	423	1299	10990	20.08
	180	185	39.2	1104.0		18.89	313	410	1289	11170	19.15
	190	200	37.8	1112.0	16.30	12.32	269	410	1287	10070	18.52
W8306-4A											
	0	8	6.1	9.4		28.64	417	412	1304	10740	19.11
	8	15	5.9	6.5		28.02	418	419	1321	11100	20.13
	15	20	5.3	13.1		29.56	414	430	1311	11100	18.69
	20	25	4.2	14.0		28.73	417	440	1308	11080	19.75
	25	30	3.8	17.7		27.89	418	447	1313	10940	19.07
	30	35	4.4	19.8		26.26	404	438	1279	10700	19.83
	35	40	3.4	29.1		29.86	392	442	1280	10810	19.66
	40	45	3.7	35.0		30.15	398	440	1293	10850	18.90
	45	50	4.8	40.6		27.49	392	435	1275	10780	19.37
	50	55	7.3	82.4		26.58	397	443	1276	10930	19.49

Core Station	Depth Interval (cm)		Phosphate µM	Ammonia µM	Alkalinity meq/l	SO_4^{2-} mM	Ca^{2+} mg/l	K^+ mg/l	Mg^{2+} mg/l	Na^+ mg/l	Cl^- g/kg
W8306-5A											
	15	20	9.7	76.0		27.36	412	426	1282	10850	19.49
	30	35	13.1	118.0		27.16	405	421	1276	11030	19.66
	50	55	15.5	155.0		26.84	411	419	1292	10900	19.10
	65	70	15.7	209.0		26.27	402	423	1303	10920	19.15
	75	80	14.7	240.0		26.31	411	418	1312	11050	19.53
	85	90	12.9	322.0		25.08	397		1273	10850	20.17
	100	105	8.3	334.0		24.46	401	446	1301	11120	19.77
W8306-7A											
	0	5	4.5	27.0	2.90	27.90	431	434	1322	11120	20.04
	20	30	10.5	141.0	3.85	27.75	438	433	1319	10860	19.75
	45	50	11.3	202.0	4.26	26.84	403	418	1304	10930	20.08
	70	75	14.3	391.0	5.18	26.38	420	431	1313	11040	19.71
	90	100	12.6	199.0	4.60	26.68	402	411	1302	10790	19.79
	110	120	23.0	423.0	6.67	25.19	391	416	1286	10840	19.32
	130	140	27.3	509.0	7.36	24.82	399	410	1298	10890	20.00
	150	160	29.6	630.0	7.89	24.08	399	418	1266	10750	20.29
	170	180	31.2	792.0	8.68	23.57	416	420	1298	10900	19.91
	195	200	32.3	965.0	9.91	22.26	415	413	1275	10940	19.87

Core Station	Depth Interval (cm)		Phosphate µM	Ammonia µM	Total CO_2 mM	SO_4^{2-} mM	Ca^{2+} mg/l	K^+ mg/l	Mg^{2+} mg/l	Na^+ mg/l	Cl^- g/kg
W8306-2C											
	0	2	5.2	2.9	2.85	28.88	415	401	1296	10940	18.78
	2	5	5.9	38.8	2.91	28.36	414	409	1291	10990	18.62
	5	10	5.2	60.6	3.01	27.79	403	403	1270	10890	18.36
	10	15	4.8	117.5	2.82	26.42	401	417	1302	11000	18.84
	15	18	5.0	147.7	3.06	27.24	388	431	1264	10960	18.77
	20	25	5.5	218.9	2.85	28.08	366	374	1196	10230	18.85
	30	35	7.8	446.9	3.34	26.62	377	404	1293	11080	19.12
	40	45	8.8	679.5	3.57	25.26	351	387	1266	11000	18.82
	45	50	7.2	837.1	3.66	26.42	347	410	1288	11400	19.79
	50	55	10.4	1230.5	4.40	27.20	339	467	1347	12270	20.87
	55	60	13.3	1308.0	5.41	24.23	287	342	1238	11050	18.84
	65	70	14.1	1385.2	5.55	21.72	265	342	1198	10770	19.17
W8306-3C											
	5	10	6.0	14.0	2.80	27.46	426	425	1313	10950	19.44
	15	20	6.8	22.0	2.70	27.38	418	411	1288	10930	19.40
	35	40	6.7	39.3	2.90	27.57	412	418	1274	10680	18.81
	65	70	11.0	64.5	3.20	27.78	428	415	1303	10860	19.44
	80	85	14.8	64.3	3.70	27.51	432	417	1306	10940	19.59
	98	104	18.7	90.8	4.10	27.38	438	413	1330	10980	19.90
	125	130	20.6	104.2	4.50	27.28	437	431	1314	10990	19.63
	145	150	21.9	152.5	5.00	27.36	443	420	1312	10970	19.77
	159	162	20.9	164.7	5.20	28.60	461	423	1350	11230	19.77

Core Station	Depth Interval (cm)		Phosphate µM	Ammonia µM	Total CO_2 mM	SO_4^{2-} mM	Ca^{2+} mg/l	K^+ mg/l	Mg^{2+} mg/l	Na^+ mg/l	Cl^- g/kg
W8306-4C											
	0	5	7.4	10.0	2.80	28.28	417	394	1282	10730	19.34
	15	20	6.9	45.0	3.20	27.08	422	432	1312	11110	19.39
	30	35	8.8	72.0	3.50	26.65	405	427	1276	10900	19.16
	45	50			3.80	26.50	400	433	1294	11150	19.04
	55	60	11.5	137.0	3.90	25.11	379	420	1252	10830	19.11
	75	80	10.3	180.0	4.60	25.76	364	425	1254	10880	19.34
	90	95	11.5	230.0	5.90	23.52	362	440	1300	11190	19.58
	105	110	9.7	248.0	5.60	21.77	339	427	1269	10980	19.03
	120	125	12.9	289.0	6.40	21.47	326	405	1249	10890	19.29
	130	135	21.9	368.0	7.40	20.22	304	391	1236	10850	19.18
W8306-5C											
	0	10	8.6	26.0	2.90	26.56	417	411	1269	10710	19.40
	25	30	20.8	59.0	3.50	26.51	426	441	1314	10970	19.62
	45	50	14.3	135.0	4.10	26.44	404	396	1253	10260	19.08
	80	85	21.8	250.0	5.60	25.48	426	414	1310	10740	19.62
	100	105	23.5	291.0	6.20	26.26	421	423	1283	10800	19.26
	120	125			6.70	25.76	423	422	1297	10740	19.04
	140	145	24.5	385.0	7.70	25.36	426	423	1312	10830	19.44
	165	170	26.4	425.0	8.40	25.14	435	400	1313	10970	18.91
	183	186	26.2	446.0	8.70	23.62	429	398	1306	10820	19.22
	190	195	25.8	452.0	8.80	24.05	428	392	1290	10620	19.08

Core Station	Depth Interval (cm)		Phosphate µM	Ammonia µM	Total CO_2 mM	SO_4^{2-} mM	Ca^{2+} mg/l	K^+ mg/l	Mg^{2+} mg/l	Na^+ mg/l	Cl^- g/kg
W8306-9C											
	0	0	6.5	23.1	2.50	27.03	419	415	1305	10810	19.40
	0	5	6.3	29.3	2.70	26.89	429	423	1317	10960	19.49
	43	47	8.9	70.8	3.50	26.59	429	408	1300	10860	19.49
	100	105	10.5	106.7	4.30	26.78	400	380	1203	9900	17.69
	140	145	12.1	154.1	4.90	26.22	445	394	1310	10780	19.22
	200	205	8.1	212.8	5.90	26.82	472	398	1345	10920	19.40
	237	242	10.8	265.1	6.80	27.57	475	409	1339	10950	19.81
	260	265	10.1	317.4	7.30	27.40	486	371	1370	10860	19.69
	265	270	5.3	322.4	7.70	27.19	486	394	1384	10950	19.82
W8306-10C											
	0	5	5.4	26.4	2.80	27.53	430	427	1307	11000	19.96
	20	25	6.9	31.4	3.00	27.93	415	415	1280	10730	19.79
	55	60	10.6	60.1	3.30	27.73	425	413	1293	10780	19.10
	95	100	14.7	133.9	4.20	26.88	445	415	1269	10940	19.24
	120	125	18.7	169.7	4.40	27.44	453	408	1300	10900	19.38
	155	160	25.4	204.1	5.00	27.45	457	396	1313	10860	19.34
	180	185	11.9	229.0	5.10	27.18	471	386	1311	10770	19.38
	185	190	10.0	234.2	5.30	28.38	447	369	1251	10330	19.55
W8306-11C											
	0	5	4.7	1.7	2.50	27.64	398	377	1228	10300	19.12
	20	25	7.4	38.8	2.90	28.30	414	396	1277	10720	19.62
	45	50	5.9	71.2	3.60	27.05	416	402	1262	10660	19.49
	70	75	7.5	114.5	4.00	26.50	426	402	1301	10910	19.44
	90	95	5.7	145.1	4.30	26.25	404	386	1218	10400	18.85
	110	115	7.8	182.4	4.70	25.36	423	389	1275	10740	19.71
	150	155	8.0	249.7	5.50	23.29	427	410	1270	10720	19.40
	180	185	13.4	317.2	6.30	24.11	422	371	1252	10610	19.40
	185	190	17.3	356.3	6.70	23.22	408	396	1217	10590	19.30

Core Station	Depth Interval (cm)		Phosphate µM	Ammonia µM	Total CO_2 mM	SO_4^{2-} mM	Ca^{2+} mg/l	K^+ mg/l	Mg^{2+} mg/l	Na^+ mg/l	Cl^- g/kg
W8306-12C											
	0	5	5.8	8.9	2.60	27.87	406	410	1245	10450	18.92
	20	25	4.8	24.6	2.80	27.48	418	419	1302	10790	19.23
	35	40	6.0	40.0	2.90	27.66	423	433	1299	10840	19.32
	60	65	13.7	97.6	3.50	27.05	420	412	1287	10950	19.32
	80	85	14.2	132.1	3.90	26.98	418	420	1288	10830	18.78
	95	100	14.7	157.8	4.20	26.98	410	416	1281	10620	19.44
	125	130	10.9	203.6	4.80	26.48	426	411	1281	10810	19.81
	145	150	15.8	239.9	5.00	25.65	440	402	1301	10780	19.32
	155	160	8.8	261.3	5.50	25.36	438	403	1312	10760	19.24
	175	180	13.2	334.4	6.00	25.11	440	386	1291	10640	19.33
	200	205	12.7	420.4	6.80	24.66	436	384	1270	10450	19.02
	215	220	19.9	441.5	7.80	24.12	435	334	1240	10420	19.20
	235	240	16.0	503.0	8.50	23.88	460	367	1321	10720	19.10
	240	245	19.4	545.2	8.70	24.19	454	348	1289	10680	19.10
W8306-14C											
	15	20	13.2	104.0	3.90	26.67	410	421	1311	11120	19.46
	35	40	13.9	138.0	4.70	25.41	396	432	1314	11350	19.58
	60	65	12.8	108.0	5.50	24.93	383	425	1305	11150	19.42
	75	80	21.0	245.0	6.70	23.07	356	374	1229	10610	19.49
	95	100	25.5	226.0	6.50	21.85	357	408	1266	11030	19.34
	115	120	25.4	273.0	8.00	20.27	347	395	1254	11150	19.24
	138	143	27.5	311.0	8.50	19.37	331	393	1249	11230	19.31
	145	150	28.2	353.0	7.90	18.37	218	394	1218	10920	19.55

Core Station	Depth Interval (cm)		Phosphate µM	Ammonia µM	Total CO_2 mM	SO_4^{2-} mM	Ca^{2+} mg/l	K^+ mg/l	Mg^{2+} mg/l	Na^+ mg/l	Cl^- g/kg
W8306-17C											
	0	5	3.9	29.3	2.80	27.08	413	395	1280	10730	19.16
	10	15	5.5	47.4	2.90	26.93	423	411	1287	10900	19.80
	30	33	5.7	9.9	2.60	26.63	412	390	1268	10510	19.35
	35	40	6.9	27.9	2.80	26.89	418	403	1302	10810	19.48
	60	65	9.6	97.0	3.40	26.74	400	397	1238	10280	19.44
	85	90	12.0	130.8	3.50	26.87	423	429	1295	10960	19.71
	125	130	17.6	186.3	4.20	26.44	432	419	1334	11360	19.88
	155	160	21.1	238.8	4.90	25.71	418	399	1276	10840	19.98
	190	195	22.9	341.6	6.50	19.78	428	410	1316	11090	19.57
W8306-18C											
	0	5	9.1	17.6	2.80	26.55	431	406	1288	10940	18.94
	30	35	17.1	142.1	4.40	27.38	404	403	1267	10660	19.70
	70	75	24.1	249.9	6.60	25.31	408	412	1304	11050	19.43
	90	95	26.5	376.1	7.70	25.00	399	413	1310	11100	19.70
	110	115	28.7	449.4	9.10	23.99	387	411	1290	10970	19.32
	130	135	32.2	573.3	10.80	22.07	382	393	1280	10950	19.36
	145	150	31.1	595.2	12.00	21.23	379	399	1314	11120	18.91
	170	175	29.9	723.1	14.20	18.59	360	388	1332	11130	19.75
	195	200	30.0	898.9	15.80	18.36	339	403	1296	11060	19.58

Core Station	Depth Interval (cm)		Phosphate µM	Ammonia µM	Total CO_2 mM	SO_4^{2-} mM	Ca^{2+} mg/l	K^+ mg/l	Mg^{2+} mg/l	Na^+ mg/l	Cl^- g/kg
W8306-24C											
	5	10	8.3	71.0	3.10	26.86	410	414	1284	10880	19.10
	25	30	21.7	230.0	5.20	25.39	406	408	1309	11060	19.28
	60	65	28.8	539.0	8.60	22.04	384	399	1249	10930	19.09
	85	90	31.6	740.0	10.60	19.97	338	381	1184	10610	18.60
	125	130	35.0	758.0	12.80	15.42	313	387	1177	10950	19.45
	160	165	34.2	1114.0	15.40	12.72	286	378	1149	10930	19.45
	175	180	33.1	1039.0	15.30	11.54	275	380	1134	11100	19.45
W8306-26C											
	5	10	11.9	126.0	4.00	26.94	415	405	1294	10970	19.74
	25	30	18.4	178.0	4.90	25.84	412	411	1293	10960	19.41
	45	50	23.6	389.0	7.80	24.52	397	408	1287	10950	18.92
	70	75	30.9	824.0	13.00	22.71	377	403	1270	10880	19.54
	92	98	32.4	923.0	15.30	21.01	358	399	1285	10920	19.17
	100	105	34.2	1037.0	16.80	20.08	335	406	1282	10980	19.52
	105	110	27.7	1013.0	17.00	19.57	334	403	1292	10920	19.67
	110	115	29.8	1002.0	18.10	19.25	338	389	1276	10900	19.45
W8306-27C											
	20	25	20.3	162.0	3.75	26.09	403	401	1288	10890	19.48
	50	55	24.0	261.0	4.83	24.68	395	401	1289	11000	19.41
	70	75	26.6	339.0	5.78	23.91	382	411	1331	11140	19.63
	90	95	27.0	402.0	6.63	22.84	361	408	1278	10990	19.49
	105	110	30.4	437.0	7.19	22.62	353	382	1254	10900	19.34
	130	135	31.7	516.0	8.45	21.53	337	386	1269	11100	18.36
	145	150	32.6	633.0	9.45	20.59	320	375	1231	10900	19.16

Core Station	Depth Interval (cm)		Ammonia µM	Total CO_2 mM	SO_4^{2-} mM	Ca^{2+} mg/l	K^+ mg/l	Mg^{2+} mg/l	Na^+ mg/l	Cl^- g/kg
A8408-4										
	20	23	192	4.47	27.16	432	426	1310	11120	19.34
	55	58	501	7.91	24.94	417	417	1290	11060	19.15
	90	93	689	9.88	23.14	400	416	1290	10960	18.84
	125	128	1022	13.84	20.84	376	419	1280	11060	18.74
	160	163	1154	15.83	19.45	356	413	1250	10930	18.93
	195	198	1340	18.35	17.67	323	413	1250	11020	19.06
A8408-7										
	0	3	20	2.76	28.31	432	413	1300	10940	19.13
	3	7	37	2.81	27.85	434	415	1290	10990	19.06
	9	13	51	2.87	28.07	430	418	1300	10930	19.21
	13	18	56	2.95	27.90	429	415	1300	10920	19.09
	21	25	70	3.10	28.12	427	414	1300	10930	18.99
	28	32	74	3.10	28.32	433	430	1290	10970	19.10
	35	40	77	2.94	29.66	420	428	1280	10870	19.04
	42	45	78	2.99	28.45	422	434	1270	10940	19.19
	46	49	79	3.02	28.71	425	420	1280	10910	19.17
	50	54	91	3.07	28.96	423	407	1280	10940	19.04
	I		80	3.06	28.49	422	418	1300	10950	19.17
	II		79	3.14	28.13	433	414	1280	10970	19.23
A8408-10										
	0	5	26	2.80	27.88	428	426	1310	11060	19.10
	20	25	150	3.93	27.08	425	441	1290	11180	19.42
	50	55	296	5.59	26.02	401	422	1250	10890	19.39
	215	220	1508	20.53	11.46	172	462	1201	11130	20.69
A8408-11										
	0	5	33	3.18	28.17	418	422	1260	10830	18.95
	20	25	172	4.36	27.19	410	411	1290	10790	19.24
	65	70	699	10.42	22.32	379	400	1270	10810	19.10
	120	125	955	12.78	20.09	342	412	1250	10840	19.35

Calculation Procedure for $CaCO_3$ Precipitation

If carbonate precipitation is assumed to be controlled by thermodynamic equilibrium of calcite with dissolved interstitial Ca, then precipitation of carbonate would depend only on pressure, temperature, pCO_2, and the ionic strength of the pore fluids. Under this assumption we have estimated the amount of calcite precipitated as a function of the release of excess pore pressure in the process of pore fluid venting. Since the carbonate precipitation was observed in near-surface sediments, the effect of temperature on calcite solubility is ignored as the temperature gradient would be small and in the range of 1 to 2 °C, at most. Thermodynamic equilibration between calcite and pore fluid requires the following reactions to be considered;

(I-1) $CO_2\,(g) = CO_2\,(aq)$ $\qquad aCO_2^* = \alpha\, pCO_2$

(I-2) $CO_2^* + H_2O = H^+ + HCO_3^-$ $\qquad aH^+\, aHCO_3^- = K_1\, aCO_2^*$

(I-3) $HCO_3^- = H^+ + CO_3^{2-}$ $\qquad aH^+\, aCO_3^{2-} = K_2\, aHCO_3^-$

(I-4) $CaCO_3 = Ca^{2+} + CO_3^{2-}$ $\qquad aCa^{2+}\, aCO_3^{2-} = K_s$

(I-5) $H_20 = H^+ + OH^-$ $\qquad aH^+\, aOH^- = 10^{-14}$

(I-6) $2aCa^{2+} + aH^+ = aHCO_3^- + 2aCO_3^{2-} + aOH^-$

(I-7) $\Delta\, Ca^{2+} = \Delta\, HCO_3^- + \Delta\, CO_3^{2-} + \Delta\, CO_2^*$

According to Plath et al. (1980), calcite solubility may be written as

(I-8) $\ln (K_{sp}/K_{sp=1atm}) = 0.07132 + 0.0080412\,P - 2.2544 \times 10^{-5}\,PT$

From Pytkowicz (1982) $K_{sp=1atm}$ is given as

(I-9) $-\log (K_s)_{p=1atm} = 6.5795 - 3.7159 \times 10^{-5}\,TS + 0.091056\,T/S - 22.10/S$

Eq. I-8 was recommended for the temperature range of 0 to 25 °C, salinity 32 to 35 ‰, and pressure 1 to 1000 atm by Pytkowicz (1982). Eq. I-8 was used, with Eq. I-9, to generate pressure dependent calcite solubility, K_{sp}, as these conditions for temperature, salinity, and pressure are applicable to the accretionary complex of the Oregon/Washington subduction zone. Salinity and temperature were assumed to be 35 ‰ and 0 °C respectively.

Henry's law constant, α, in seawater is available from Weiss (1974). The first and the second apparent dissociation constants, K_1 and K_2, are obtained from the extrapolation of the data set of Pytkowicz (1982), which are based on the data of Mehrbach et al (1973) and Plath et al. (1980);

$10^7\,K_1 = 0.0131\,P + 4.8130$ (R-SQ =0.988)
at 0 °C and 35 ‰

$10^{10}\,K_2 = 0.0040\,P + 3.1510$ (R-SQ=0.994)

at 0 °C and 35 ‰

Eq. I-6 is for electroneutrality. Eq. I-7 expresses that the change in Ca^{2+} is balanced by the change in carbon species. Eq. I-7 can be rewritten as

$$aCa^{2+}_{p} - aCa^{2+}_{p=ref} = aTCO_{2p} - aTCO_{2p=ref}$$

We need to set a reference position and obtain equilibrium concentrations of Ca^{2+} and carbon species at the reference position as we will calculate the amount of Ca^{2+} precipitated from the difference in equilibrium concentrations of Ca^{2+} between 2.1 km sea floor and a base at subsurface. The reference position thus would be either on the seafloor or at the base of the near surface sediments. The base of this near-surface-sediment was assumed at 6 m following Scamman (1981). The reference position may be set at the sea floor of the proposed vent site, where the authigenic carbonate chimney and benthic community were found at 2.1 km water depth. In order to calculate in-situ equilibrium concentrations of CO_2^*, HCO_3^-, CO_3^{2-}, pCO_2, and Ca^{2+} at the reference position of 2.1 km seafloor, however, the knowledge of CO_2 solubility coefficient and pCO_2 at the high pressure of 210 atm is essential. Limited information on these two parameters to the temperature range in 12 to 40 °C at high pressure (Weiss, 1974; Wiebe and Gaddy, 1940) forced us to reset the reference postion at a level of 0 °C and 1 atm. Our strategy is then to estimate the change in Ca^{2+} between the levels of p=210 atm and p=1 atm as well as the change in Ca^{2+} between the levels of pressure (p > 210 atm) at the subsurface, and p=1 atm. Resulting differences between those two Ca^{2+} changes would finally be an amount of Ca^{2+} precipitated as calcite.

Substitution of the equilibrium concentrations, CO_2^*, HCO_3^-, and CO_3^{2-} at 0 °C and 1 atm, to Eq. (I-7) would reshape the seven equations in terms of seven unknown parameters. The system of equations were arranged to have an equation only in terms of aH^+, and aH^+ in this equation was solved by the Newton iteration method. With the aH^+ value solved, the rest of the unknowns were solved sequentially. The entire solution process was repeated with varying excess pore pressure at the 6 m subsurface. The amount of Ca precipitated was finally converted to % $CaCO_3$ content in the sediment;

$$\% \ CaCO_3 = \frac{\text{No. moles of Ca precip. x 100g } CaCO_3 \text{ x Porosity (n)}}{\text{Wet bulk density (g/cm}^3\text{) x 1000 (cm}^3\text{)}} \text{ x 100 (cm}^3\text{)}$$

Values of K_1, K_2, and K_s as a function of pressure at 0 °C and 35 $^{o}/_{oo}$

Pressure (atm)	K1	K2	Ks
10	4.944E-07	3.191E-10	5.4439E-07
20	5.075E-07	3.231E-10	5.5476E-07
30	5.206E-07	3.271E-10	5.6533E-07
40	5.337E-07	3.311E-10	5.7610E-07
50	5.468E-07	3.351E-10	5.8707E-07
60	5.599E-07	3.391E-10	5.9825E-07
70	5.730E-07	3.431E-10	6.0964E-07
80	5.861E-07	3.471E-10	6.2126E-07
90	5.992E-07	3.511E-10	6.3309E-07
100	6.123E-07	3.551E-10	6.4515E-07
110	6.254E-07	3.591E-10	6.5743E-07
120	6.385E-07	3.631E-10	6.6995E-07
130	6.516E-07	3.671E-10	6.8271E-07
140	6.647E-07	3.711E-10	6.9572E-07
150	6.778E-07	3.751E-10	7.0897E-07
160	6.909E-07	3.791E-10	7.2247E-07
170	7.040E-07	3.831E-10	7.3623E-07
180	7.171E-07	3.871E-10	7.5025E-07
190	7.302E-07	3.911E-10	7.6454E-07
200	7.433E-07	3.951E-10	7.7910E-07
210	7.564E-07	3.991E-10	7.9394E-07
220	7.695E-07	4.031E-10	8.0906E-07
230	7.826E-07	4.071E-10	8.2447E-07
240	7.957E-07	4.111E-10	8.4018E-07
250	8.088E-07	4.151E-10	8.5618E-07
260	8.219E-07	4.191E-10	8.7249E-07
270	8.350E-07	4.231E-10	8.8910E-07
280	8.481E-07	4.271E-10	9.0604E-07
290	8.612E-07	4.311E-10	9.2329E-07
300	8.743E-07	4.351E-10	9.4088E-07
310	8.874E-07	4.391E-10	9.5880E-07
320	9.005E-07	4.431E-10	9.7706E-07
330	9.136E-07	4.471E-10	9.9567E-07
340	9.267E-07	4.511E-10	1.0146E-06
350	9.398E-07	4.551E-10	1.0340E-06
360	9.529E-07	4.591E-10	1.0536E-06
370	9.660E-07	4.631E-10	1.0737E-06
380	9.791E-07	4.671E-10	1.0942E-06
390	9.922E-07	4.711E-10	1.1150E-06
400	1.005E-06	4.751E-10	1.1362E-06

Calculation Procedure for the Degree of Saturation of Pore Fluids with Respect to $CaCO_3$

pH and TCO_2 data are available from two core stations within the accretionary complex and one in the abyssal plain. The degree of saturation of pore fluids with respect to calcite was calculated for these stations (Fig. III-9). When pH and TCO_2 are given, $aHCO_3^-$, aCO_3^{2-}, and aCO_2^* of the pore fluids become (Skirrow, 1975);

$$aHCO_3^- = TCO_2 K_1 aH^+ / z$$

$$aCO_3^{2-} = TCO_2 K_1 K_2 / z$$

$$aCO_2^* = TCO_2 aH^+ aH^+ / z$$

$$pCO_2 = aCO_2^* / z$$

where $z = aH^+ aH^+ + K_1 aH^+ + K_1 K_2$

The condition of 0 °C and 1 atm was assumed, which was the condition during pore water sampling from squeezing.

APPENDIX IV

Computer Programs for the Simulation of the Heat Flow Distribution Across the Oregon Accretionary Complex

Computer Programs for the Simulation of the Heat Flow Distribution Across the Oregon Accretionary Complex

```
C*************************************************************************
C
C   OREGON STATE UNIVERSITY
C   COLLEGE OF OCEANOGRAPHY
C
C   NAME OF PROGRAM:      ORHEAT.ZZ0
C   OBJECT OF PROGRAM:    TWO-DIMENSIONAL NUMERICAL MODEL FOR
C                         TEMPERATURE DISTRIBUTION BY FINITE
C                         DIFFERENCE METHOD
C   PROGRAM LANGUAGE:     FORTRAN 77
C   AUTHOR:               M. W. HAN
C   VERSION DATE:         JUNE 17,1987
C   TYPE OF COMPUTER:     PRIME
C*************************************************************************
C
C   DEFINITION OF VARIABLES:
C   P: DENSITY OF VENTING PORE FLUIDS
C   G: SPECIFIC HEAT OF VENTING PORE FLUIDS
C   Q: THERMAL CONDUCTIVITY OF HEAT IN Y-DIRECTION
C   R: RATIO OF CONDUCTIVITY IN X-DIRECITON TO Y-DIRECTION
C   AB: COEFFICIENT MATRIX
C   NDIM: FIRST DIMENSION OF MATRIX AB
C   N: NUMBER OF GRID POINTS IN THE X-DIRECTION
C   M: NUMBER OF GRID POINTS IN THE Y-DIRECTION
C   BT: BASEMENT TEMPERATURE
C   BV: COLUMN MATRIX FOR R.H.S. VECTORS
C   NN: NUMBER OF LINEAR EQUATIONS
C   A,B,C,D,E: COEFFICIENTS IN THE MATRIX AB
C   T: COLUMN MATRIX FOR TEMPERATURE VECTORS
C*************************************************************************
```

```
C                    MAIN PROGRAM
C*************************************************************************
      DIMENSION AB(70,70),A(7,2),B(7,2),C(7,2),D(7,2)
      DIMENSION U(2),Q(7),T(70),BV(70),BT(9),X(69),Y(69)
      OPEN (5,FILE='INPUT.ZZ0')
      OPEN (6,FILE='OUTPUT.ZZ0')
      READ (5,60) P,G,R,TOL
      READ (5,80) (Q(I), I=1,7)
      READ (5,85) (BT(I), I=1,9)
      READ (5,90) N,M,NN,NDIM,NITER
      DO 15 J=1,2
      DO 10 I=1,7
        A(I,J)=4.*R
        B(I,J)=4.*R
        C(I,J)=4.
        D(I,J)=4.
   10 CONTINUE
   15 CONTINUE
      E=-8.*(R+1)
      NP1=N+1
C
C     INITIALIZE MATRIX AB WITH ZEROS
      DO 25 I=1,NDIM
      DO 20 J=1,NDIM
        AB(I,J)=0.0
   20 CONTINUE
   25 CONTINUE
C
C     INSERT R.H.S VECTORS AS A COLUMN MATRIX BV
      DO 30 I=1,N
      BV(I)=-D(1,1)*BT(I)
   30 CONTINUE
```

```
      DO 35 I=NP1,NDIM
      BV(I)=0.
   35 CONTINUE
C     INPUT INITIAL GUESS FOR T
      DO 36 I=1,9
      T(I)=48.
   36 CONTINUE
      DO 37 I=10,18
      T(I)=28.
   37 CONTINUE
      DO 38 I=19,36
      T(I)=18.
   38 CONTINUE
      DO 39 I=37,69
      T(I)=8.
   39 CONTINUE
C
C     FORMULATE THE COEFFICIENT OF MATRIX AB
      CALL COMAT(AB,NDIM,N,A,B,C,D,E)
C
C     SOLVE N LINEAR EQUATIONS BY GAUSS-SEIDEL ITERATION
      CALL GSITRN (AB,BV,T,NN,NDIM,NITER,TOL)
C
C     PRINT THE RESULTS
      X(1)=4.5
      DO 41 I=2,9
      X(I)=X(I-1)-0.5
   41 CONTINUE
      DO 42 I=10,61
      X(I)=X(I-9)
   42 CONTINUE
      DO 43 I=62,67
```

```
      X(I)=X(I-9)
42  CONTINUE
      DO 43 I=62,67
      X(I)=X(I-7)
43  CONTINUE
      X(68)=X(62)
      X(69)=X(63)
      DO 44 I=1,9
      Y(I)=0.5
44  CONTINUE
      DO 45 I=10,18
      Y(I)=1.0
45  CONTINUE
      DO 46 I=19,27
      Y(I)=1.5
46  CONTINUE
      DO 47 I=28,36
      Y(I)=2.0
47  CONTINUE
      DO 48 I=37,45
      Y(I)=2.5
48  CONTINUE
      DO 49 I=46,54
      Y(I)=3.0
49  CONTINUE
      DO 50 I=55,61
      Y(I)=3.5
50  CONTINUE
      DO 51 I=62,67
      Y(I)=4.0
51  CONTINUE
      Y(68)=4.5
```

```
      WRITE (6,100) I,X(I),Y(I),T(I)
   40 CONTINUE
   60 FORMAT (E7.1,F4.1,F6.1,F6.3)
   80 FORMAT (7(F7.3,1X))
   85 FORMAT (9(F5.1,1X))
   90 FORMAT (4(I2,1X),I3)
   95 FORMAT ('NODE NO.  X (Km)  Y(Km)    T C')
  100 FORMAT (2X,'T',I2,F10.1,F8.1,F12.2)
      STOP
      END
C
C*********************************************************************
      SUBROUTINE COMAT (AB,NDIM,N,A,B,C,D,E)
C
C     THIS SUBROUTINE FORMS THE COEFFICIENT MATRIX FOR THE TWO-
C     DIMENSIONAL CONVECTION-ADVECTION HEAT FLOW EQUATION ON A
C     REGION THAT HAS N POINTS IN THE X DIRECTION AND M POINTS
C     IN THE Y DIRECTION.
C
C     PARAMETERS ARE:
C     AB : MATRIX THAT RETURNS COEFFICIENTS
C     NDIM:FIRST DIMENSION OF AB IN THE MAIN PROGRAM
C     N: NUMBER OF GRID POINTS IN THE X DIRECTION
C     M: NUMBER OF GRID POINTS IN THE Y DIRECTION
C
      DIMENSION AB(NDIM,NDIM),A(7,2),B(7,2),C(7,2),D(7,2)
C
C     FIRST LET'S COMPUTE SOME CONSTANTS
      NL1=N-1
      NP1=N+1
      NP2=NP1+NL1
      NP3=NP2+1
```

```
      NL1=N-1
      NP1=N+1
      NP2=NP1+NL1
      NP3=NP2+1
      NP4=NP3+NL1
      NP5=NP4+1
      NP6=NP5+NL1
      NP7=NP6+1
      NP8=NP7+NL1
      NP9=NP8+1
      NP10=NP9+NL1
C
C     PUT COEFFICIENT E FOR THE DIAGONAL
      DO 10 I=1,NDIM
        AB(I,I)=E
 10   CONTINUE
C
C     NOW PUT COEFFICIENT A AND B FOR THE ABOVE- AND BELOW-
C     DIAGONAL RESPECTIVELY
      DO 11 I=2,N
        AB(I-1,I)=A(1,1)
        AB(I,I-1)=B(1,1)
 11   CONTINUE
      DO 12 I=NP1,NP2
        AB(I-1,I)=A(2,1)
        AB(I,I-1)=B(2,1)
 12   CONTINUE
      DO 13 I=NP3,NP4
        AB(I-1,I)=A(3,2)
        AB(I,I-1)=B(3,2)
 13   CONTINUE
      DO 14 I=NP5,NP6
```

```
      AB(I-1,I)=A(4,2)
      AB(I,I-1)=B(4,2)
14    CONTINUE
      DO 15 I=NP7,NP8
      AB(I-1,I)=A(5,2)
      AB(I,I-1)=B(5,2)
15    CONTINUE
      DO 16 I=NP9,61
      AB(I-1,I)=A(6,2)
      AB(I,I-1)=B(6,2)
16    CONTINUE
      DO 17 I=62,NDIM
      AB(I-1,I)=A(7,2)
      AB(I,I-1)=B(7,2)
17    CONTINUE
C
C     NOW REPLACE SOME A AND B WITH ZEROS
      DO 20 I=N,NP10,N
      AB(I,I+1)=0.
      AB(I+1,I)=0.
20    CONTINUE
      AB(62,61)=0.
      AB(68,67)=0.
      AB(61,62)=0.
      AB(67,68)=0.
C
C     NOW REPLACE SOME DIAGONAL WITH E+A OR E+B
      AB(1,1)=E+B(1,1)
      AB(9,9)=E+A(1,1)
      AB(10,10)=E+B(2,1)
      AB(18,18)=E+A(2,1)
      AB(19,19)=E+B(3,1)
```

```
      AB(27,27)=E+A(3,2)
      AB(28,28)=E+B(4,2)
      AB(36,36)=E+A(4,2)
      AB(37,37)=E+B(5,2)
      AB(45,45)=E+A(5,2)
      AB(46,46)=E+B(6,2)
      AB(54,54)=E+A(6,2)
      AB(55,55)=E+B(6,2)
      AB(62,62)=E+B(7,2)
      AB(68,68)=E+B(7,2)
C
C     PUT C AND D IN THE SIDE BANDS
      DO 30 I=NP1,NP2
        AB(I,I-N)=D(2,1)
        AB(I-N,I)=C(2,1)
 30   CONTINUE
      DO 31 I=NP3,NP4
        AB(I,I-N)=D(3,2)
        AB(I-N,I)=C(3,2)
 31   CONTINUE
      DO 32 I=NP5,NP6
        AB(I,I-N)=D(4,2)
        AB(I-N,I)=C(4,2)
 32   CONTINUE
      DO 33 I=NP7,NP8
        AB(I,I-N)=D(5,2)
        AB(I-N,I)=C(5,2)
 33   CONTINUE
      DO 34 I=NP9,61
        AB(I,I-N)=D(6,2)
        AB(I-N,I)=C(6,2)
 34   CONTINUE
```

```
      DO 35 I=62,NDIM
        AB(I,I-N)=D(7,2)
        AB(I-N,I)=C(7,2)
 35   CONTINUE
        AB(62,68)=C(7,2)
        AB(63,69)=C(7,2)
C      REPLACE SOME C WITH ZEROS
        AB(53,62)=0.
        AB(54,63)=0.
      RETURN
      END
C
C*************************************************************************
    SUBROUTINE GSITRN (AB,BV,T,NN,NDIM,NITER,TOL)
    DIMENSION AB(NN,NN),BV(NN),T(NN)
    DO 10 I=1,NN
      SAVE=AB(I,I)
      BV(I)=BV(I)/SAVE
      DO 7 J=1,NN
        AB(I,J)=AB(I,J)/SAVE
 7  CONTINUE
 10  CONTINUE
    DO 40 ITER=1,NITER
    TMAX=0.
    DO 30 I=1,NN
    SAVE=T(I)
    T(I)=BV(I)
    DO 20 J=1,NN
    IF (J .NE. I) THEN
    T(I)=T(I)-AB(I,J)*T(J)
    END IF
 20  CONTINUE
```

```
      IF (ABS(T(I)-SAVE) .GT. TMAX) THEN
      TMAX=ABS(T(I)-SAVE)
      END IF
   30 CONTINUE
      IF (TMAX .LE. TOL) RETURN
   40 CONTINUE
      PRINT 200, TOL,NITER
  200 FORMAT(/'DID NOT MEET TOLERANCE OF ',E14.6,' IN ',I4,
     1    ' ITERATIONS'/' LAST VALUE OF T WAS RETURNED TO CALLER')
      RETURN
      END
```

1.0E+15 1.0 50.0 0.01

571.429 476.190 380.952 333.333 285.714 238.095 190.476

144.0 146.0 148.0 150.0 152.0 154.0 156.0 158.0 160.0

9 9 69 69 400

NODE NO.	X (Km)	Y(Km)	T C
T 1	4.5	0.5	124.16
T 2	4.0	0.5	124.28
T 3	3.5	0.5	124.51
T 4	3.0	0.5	124.79
T 5	2.5	0.5	125.10
T 6	2.0	0.5	125.42
T 7	1.5	0.5	125.71
T 8	1.0	0.5	125.94
T 9	0.5	0.5	126.09
T10	4.5	1.0	99.17
T11	4.0	1.0	99.19
T12	3.5	1.0	99.23
T13	3.0	1.0	99.28
T14	2.5	1.0	99.34
T15	2.0	1.0	99.40
T16	1.5	1.0	99.46
T17	1.0	1.0	99.52
T18	0.5	1.0	99.58
T19	4.5	1.5	75.51
T20	4.0	1.5	75.51
T21	3.5	1.5	75.53
T22	3.0	1.5	75.55
T23	2.5	1.5	75.58
T24	2.0	1.5	75.62
T25	1.5	1.5	75.66
T26	1.0	1.5	75.70
T27	0.5	1.5	75.75
T28	4.5	2.0	54.25
T29	4.0	2.0	54.26
T30	3.5	2.0	54.27
T31	3.0	2.0	54.29
T32	2.5	2.0	54.31
T33	2.0	2.0	54.34
T34	1.5	2.0	54.37
T35	1.0	2.0	54.42
T36	0.5	2.0	54.46
T37	4.5	2.5	35.52
T38	4.0	2.5	35.52
T39	3.5	2.5	35.52
T40	3.0	2.5	35.52
T41	2.5	2.5	35.53
T42	2.0	2.5	35.54
T43	1.5	2.5	35.55
T44	1.0	2.5	35.58
T45	0.5	2.5	35.61
T46	4.5	3.0	19.09

T47	4.0	3.0	19.06
T48	3.5	3.0	19.00
T49	3.0	3.0	18.91
T50	2.5	3.0	18.80
T51	2.0	3.0	18.68
T52	1.5	3.0	18.58
T53	1.0	3.0	18.49
T54	0.5	3.0	18.47
T55	4.5	3.5	5.73
T56	4.0	3.5	5.54
T57	3.5	3.5	5.16
T58	3.0	3.5	4.59
T59	2.5	3.5	3.82
T60	2.0	3.5	2.82
T61	1.5	3.5	1.57
T62	4.5	4.0	3.09
T63	4.0	4.0	2.85
T64	3.5	4.0	2.35
T65	3.0	4.0	1.83
T66	2.5	4.0	1.27
T67	2.0	4.0	0.67
T68	4.5	4.5	0.19
T69	4.0	4.5	0.12

```
C***********************************************
C
C   OREGON STATE UNIVERSITY
C   COLLEGE OF OCEANOGRAPHY
C
C   NAME OF PROGRAM:      ORHEAT.ZZU
C   OBJECT OF PROGRAM:    TWO-DIMENSIONAL NUMERICAL MODEL FOR
C                         TEMPERATURE DISTRIBUTION BY FINITE
C                         DIFFERENCE METHOD
C   PROGRAM LANGUAGE:     FORTRAN 77
C   AUTHOR:               M. W. HAN
C   VERSION DATE:         JUNE 17,1987
C   TYPE OF COMPUTER:     PRIME
C***********************************************************************
C
C
C    DEFINITION OF VARIABLES:
C    P: DENSITY OF VENTING PORE FLUIDS
C    G: SPECIFIC HEAT OF VENTING PORE FLUIDS
C    U: ADVECTION RATE OF VENTING PORE FLUIDS
C    Q: THERMAL CONDUCTIVITY OF HEAT IN Y-DIRECTION
C    R: RATIO OF CONDUCTIVITY IN X-DIRECITON TO Y-DIRECTION
C    AB: COEFFICIENT MATRIX
C    NDIM: FIRST DIMENSION OF MATRIX AB
C    N: NUMBER OF GRID POINTS IN THE X-DIRECTION
C    M: NUMBER OF GRID POINTS IN THE Y-DIRECTION
C    BT: BASEMENT TEMPERATURE
C    BV: COLUMN MATRIX FOR R.H.S. VECTORS
C    NN: NUMBER OF LINEAR EQUATIONS
C    A,B,C,D,E: COEFFICIENTS IN THE MATRIX AB
C    T: COLUMN MATRIX FOR TEMPERATURE VECTORS
C
C***********************************************************************
```

```
C                    MAIN PROGRAM
C*************************************************************************
      DIMENSION AB(70,70),A(7,2),B(7,2),C(7,2),D(7,2)
      DIMENSION U(2),Q(7),T(70),BV(70),BT(9),X(69),Y(69)
      DIMENSION A1(7,2),B1(7,2),C1(7,2),D1(7,2)
      OPEN (5,FILE='INPUT.ZZU')
      OPEN (6,FILE='OUTPUT.ZZU')
      READ (5,60) P,G,R,TOL
      READ (5,80) (Q(I), I=1,7)
      READ (5,85) (BT(I), I=1,9)
      READ (5,90) N,M,NN,NDIM,NITER
C     P*G*U(J=1)=P*G*U(J=2)=320.0 FOR U=1 CM YR
C     P*G*U(J=1)=P*G*U(J=2)=3200.0 FOR U=10 CM/YR
C     P*G*U(J=1)=P*G*U(J=2)=1600.0 FOR U=5 CM/YR
      DO 15 J=1,2
      DO 10 I=1,7
        A(I,J)=4.*R+320./Q(I)
        B(I,J)=4.*R-320./Q(I)
        C(I,J)=4.-320./Q(I)
        D(I,J)=4.+320./Q(I)
   10 CONTINUE
   15 CONTINUE
      DO 17 J=1,2
      DO 16 I=1,7
        A1(I,J)=4.*R-1600./Q(I)
        B1(I,J)=4.*R+1600./Q(I)
        C1(I,J)=4.+1600./Q(I)
        D1(I,J)=4.-1600./Q(I)
   16 CONTINUE
   17 CONTINUE
      E=-8.*(R+1)
      NP1=N+1
C
```

```
C    INITIALIZE MATRIX AB WITH ZEROS
     DO 25 I=1,NDIM
     DO 20 J=1,NDIM
       AB(I,J)=0.0
  20 CONTINUE
  25 CONTINUE
C
C    INSERT R.H.S VECTORS AS A COLUMN MATRIX BV
     DO 30 I=1,N
     BV(I)=-D(1,1)*BT(I)
  30 CONTINUE
     DO 35 I=NP1,NDIM
     BV(I)=0.
  35 CONTINUE
C    INPUT INITIAL GUESS FOR T
     DO 36 I=1,9
     T(I)=48.
  36 CONTINUE
     DO 37 I=10,18
     T(I)=28.
  37 CONTINUE
     DO 38 I=19,36
     T(I)=18.
  38 CONTINUE
     DO 39 I=37,69
     T(I)=8.
  39 CONTINUE
C
C    FORMULATE THE COEFFICIENT OF MATRIX AB
     CALL COMAT(AB,NDIM,N,A,B,C,D,E,A1,B1,C1,D1)
C
C    SOLVE N LINEAR EQUATIONS BY GAUSS-SEIDEL ITERATION
     CALL GSITRN (AB,BV,T,NN,NDIM,NITER,TOL)
```

```
C    SOLVE N LINEAR EQUATIONS BY GAUSS-SEIDEL ITERATION
     CALL GSITRN (AB,BV,T,NN,NDIM,NITER,TOL)
C
C    PRINT THE RESULTS
     X(1)=4.5
     DO 41 I=2,9
     X(I)=X(I-1)-0.5
 41  CONTINUE
     DO 42 I=10,61
     X(I)=X(I-9)
 42  CONTINUE
     DO 43 I=62,67
     X(I)=X(I-7)
 43  CONTINUE
     X(68)=X(62)
     X(69)=X(63)
     DO 44 I=1,9
     Y(I)=0.5
 44  CONTINUE
     DO 45 I=10,18
     Y(I)=1.0
 45  CONTINUE
     DO 46 I=19,27
     Y(I)=1.5
 46  CONTINUE
     DO 47 I=28,36
     Y(I)=2.0
 47  CONTINUE
     DO 48 I=37,45
     Y(I)=2.5
 48  CONTINUE
     DO 49 I=46,54
     Y(I)=3.0
```

```
      Y(I)=3.5
   50 CONTINUE
      DO 51 I=62,67
      Y(I)=4.0
   51 CONTINUE
      Y(68)=4.5
      Y(69)=4.5
      WRITE (6,95)
      DO 40 I=1,NN
      WRITE (6,100) I,X(I),Y(I),T(I)
   40 CONTINUE
   60 FORMAT (E7.1,F4.1,F6.1,F6.3)
   80 FORMAT (7(F7.3,1X))
   85 FORMAT (9(F5.1,1X))
   90 FORMAT (4(I2,1X),I3)
   95 FORMAT ('NODE NO.  X (Km)  Y(Km)    T C')
  100 FORMAT (2X,'T',I2,F10.1,F8.1,F12.2)
      STOP
      END
C
C*************************************************************************
      SUBROUTINE COMAT (AB,NDIM,N,A,B,C,D,E,A1,B1,C1,D1)
C
C     THIS SUBROUTINE FORMS THE COEFFICIENT MATRIX FOR THE TWO-
C     DIMENSIONAL CONVECTION-ADVECTION HEAT FLOW EQUATION ON A
C     REGION THAT HAS N POINTS IN THE X DIRECTION AND M POINTS
C     IN THE Y DIRECTION.
C
C     PARAMETERS ARE:
C     AB : MATRIX THAT RETURNS COEFFICIENTS
C     NDIM:FIRST DIMENSION OF AB IN THE MAIN PROGRAM
C     N: NUMBER OF GRID POINTS IN THE X DIRECTION
C     M: NUMBER OF GRID POINTS IN THE Y DIRECTION
```

```
C     NDIM:FIRST DIMENSION OF AB IN THE MAIN PROGRAM
C     N: NUMBER OF GRID POINTS IN THE X DIRECTION
C     M: NUMBER OF GRID POINTS IN THE Y DIRECTION
C
      DIMENSION AB(NDIM,NDIM),A(7,2),B(7,2),C(7,2),D(7,2)
      DIMENSION A1(7,2),B1(7,2),C1(7,2),D1(7,2)
C
C     FIRST LET'S COMPUTE SOME CONSTANTS
      NL1=N-1
      NP1=N+1
      NP2=NP1+NL1
      NP3=NP2+1
      NP4=NP3+NL1
      NP5=NP4+1
      NP6=NP5+NL1
      NP7=NP6+1
      NP8=NP7+NL1
      NP9=NP8+1
      NP10=NP9+NL1
C
C     PUT COEFFICIENT E FOR THE DIAGONAL
      DO 10 I=1,NDIM
        AB(I,I)=E
 10   CONTINUE
C
C     NOW PUT COEFFICIENT A AND B FOR THE ABOVE- AND BELOW-
C     DIAGONAL RESPECTIVELY
      DO 111 I=4,9
      AB(I-1,I)=A1(1,1)
      AB(I,I-1)=B1(1,1)
 111  CONTINUE
      DO 122 I=14,18
      AB(I-1,I)=A1(2,1)
```

```
      AB(I,I-1)=B1(2,1)
122   CONTINUE
      DO 133 I=23,27
      AB(I-1,I)=A1(3,2)
      AB(I,I-1)=B1(3,2)
133   CONTINUE
      DO 144 I=33,36
      AB(I-1,I)=A1(4,2)
      AB(I,I-1)=B1(4,2)
144   CONTINUE
      DO 155 I=43,45
      AB(I-1,I)=A1(5,2)
      AB(I,I-1)=B1(5,2)
155   CONTINUE
      DO 166 I=53,54
      AB(I-1,I)=A1(6,2)
      AB(I,I-1)=B1(6,2)
166   CONTINUE
      DO 11 I=2,N
      AB(I-1,I)=A(1,1)
      AB(I,I-1)=B(1,1)
11    CONTINUE
      DO 12 I=NP1,NP2
        AB(I-1,I)=A(2,1)
        AB(I,I-1)=B(2,1)
12    CONTINUE
      DO 13 I=NP3,NP4
        AB(I-1,I)=A(3,2)
        AB(I,I-1)=B(3,2)
13    CONTINUE
      DO 14 I=NP5,NP6
        AB(I-1,I)=A(4,2)
        AB(I,I-1)=B(4,2)
```

```
 14   CONTINUE
      DO 15 I=NP7,NP8
        AB(I-1,I)=A(5,2)
        AB(I,I-1)=B(5,2)
 15   CONTINUE
      DO 16 I=NP9,61
        AB(I-1,I)=A(6,2)
        AB(I,I-1)=B(6,2)
 16   CONTINUE
      DO 17 I=62,NDIM
        AB(I-1,I)=A(7,2)
        AB(I,I-1)=B(7,2)
 17   CONTINUE
C
C     NOW REPLACE SOME A AND B WITH ZEROS
      DO 20 I=N,NP10,N
        AB(I,I+1)=0.
        AB(I+1,I)=0.
 20   CONTINUE
        AB(62,61)=0.
        AB(68,67)=0.
        AB(61,62)=0.
        AB(67,68)=0.
C
C     NOW REPLACE SOME DIAGONAL WITH E+A OR E+B
        AB(1,1)=E+B(1,1)
        AB(9,9)=E+A(1,1)
        AB(10,10)=E+B(2,1)
        AB(18,18)=E+A(2,1)
        AB(19,19)=E+B(3,1)
        AB(27,27)=E+A(3,2)
        AB(28,28)=E+B(4,2)
        AB(36,36)=E+A(4,2)
```

```
      AB(37,37)=E+B(5,2)
      AB(45,45)=E+A(5,2)
      AB(46,46)=E+B(6,2)
      AB(54,54)=E+A(6,2)
      AB(55,55)=E+B(6,2)
      AB(62,62)=E+B(7,2)
      AB(68,68)=E+B(7,2)
C
C     PUT C AND D IN THE SIDE BANDS
      DO 300 I=14,18
      AB(I,I-N)=D1(2,1)
      AB(I-N,I)=C1(2,1)
300   CONTINUE
      DO 311 I=23,27
      AB(I,I-N)=D1(3,2)
      AB(I-N,I)=C1(3,2)
311   CONTINUE
      DO 322 I=33,36
      AB(I,I-N)=D1(4,2)
      AB(I-N,I)=C1(4,2)
322   CONTINUE
      DO 333 I=43,45
      AB(I,I-N)=D1(5,2)
      AB(I-N,I)=C1(5,2)
333   CONTINUE
      DO 344 I=53,54
      AB(I,I-N)=D1(6,2)
      AB(I-N,I)=C1(6,2)
344   CONTINUE
      DO 30 I=NP1,NP2
        AB(I,I-N)=D(2,1)
        AB(I-N,I)=C(2,1)
30    CONTINUE
```

```
      DO 31 I=NP3,NP4
        AB(I,I-N)=D(3,2)
        AB(I-N,I)=C(3,2)
 31   CONTINUE
      DO 32 I=NP5,NP6
        AB(I,I-N)=D(4,2)
        AB(I-N,I)=C(4,2)
 32   CONTINUE
      DO 33 I=NP7,NP8
        AB(I,I-N)=D(5,2)
        AB(I-N,I)=C(5,2)
 33   CONTINUE
      DO 34 I=NP9,61
        AB(I,I-N)=D(6,2)
        AB(I-N,I)=C(6,2)
 34   CONTINUE
      DO 35 I=62,NDIM
        AB(I,I-N)=D(7,2)
        AB(I-N,I)=C(7,2)
 35   CONTINUE
        AB(62,68)=C(7,2)
        AB(63,69)=C(7,2)
C     REPLACE SOME C WITH ZEROS
        AB(53,62)=0.
        AB(54,63)=0.
      RETURN
      END
C
C*************************************************************************
    SUBROUTINE GSITRN (AB,BV,T,NN,NDIM,NITER,TOL)
    DIMENSION AB(NN,NN),BV(NN),T(NN)
    DO 10 I=1,NN
      SAVE=AB(I,I)
```

```
      BV(I)=BV(I)/SAVE
      DO 7 J=1,NN
        AB(I,J)=AB(I,J)/SAVE
7   CONTINUE
10  CONTINUE
    DO 40 ITER=1,NITER
    TMAX=0.
    DO 30 I=1,NN
    SAVE=T(I)
    T(I)=BV(I)
    DO 20 J=1,NN
    IF (J .NE. I) THEN
    T(I)=T(I)-AB(I,J)*T(J)
    END IF
20  CONTINUE
    IF (ABS(T(I)-SAVE) .GT. TMAX) THEN
    TMAX=ABS(T(I)-SAVE)
    END IF
30  CONTINUE
    IF (TMAX .LE. TOL) RETURN
40  CONTINUE
    PRINT 200, TOL,NITER
200 FORMAT(/'DID NOT MEET TOLERANCE OF ',E14.6,' IN ',I4,
   1     ' ITERATIONS'/' LAST VALUE OF T WAS RETURNED TO CALLER')
    RETURN
    END
```

1.0E+15 1.0 50.0 0.01

571.429 476.190 380.952 333.333 285.714 238.095 190.476

144.0 146.0 148.0 150.0 152.0 154.0 156.0 158.0 160.0

9 9 69 69 400

NODE NO.	X (Km)	Y(Km)	T C
T 1	4.5	0.5	46.15
T 2	4.0	0.5	46.45
T 3	3.5	0.5	46.97
T 4	3.0	0.5	47.61
T 5	2.5	0.5	48.31
T 6	2.0	0.5	49.00
T 7	1.5	0.5	49.61
T 8	1.0	0.5	50.80
T 9	0.5	0.5	50.36
T10	4.5	1.0	42.89
T11	4.0	1.0	42.98
T12	3.5	1.0	43.14
T13	3.0	1.0	43.35
T14	2.5	1.0	43.58
T15	2.0	1.0	43.81
T16	1.5	1.0	44.01
T17	1.0	1.0	44.15
T18	0.5	1.0	44.22
T19	4.5	1.5	38.57
T20	4.0	1.5	38.60
T21	3.5	1.5	38.65
T22	3.0	1.5	38.71
T23	2.5	1.5	38.78
T24	2.0	1.5	38.85
T25	1.5	1.5	38.91
T26	1.0	1.5	38.95
T27	0.5	1.5	38.97
T28	4.5	2.0	40.89
T29	4.0	2.0	40.93
T30	3.5	2.0	41.01
T31	3.0	2.0	41.11
T32	2.5	2.0	41.21
T33	2.0	2.0	41.32
T34	1.5	2.0	41.41
T35	1.0	2.0	41.47
T36	0.5	2.0	41.50
T37	4.5	2.5	28.72
T38	4.0	2.5	28.60
T39	3.5	2.5	28.36
T40	3.0	2.5	28.05
T41	2.5	2.5	27.70
T42	2.0	2.5	27.35
T43	1.5	2.5	27.04
T44	1.0	2.5	26.81
T45	0.5	2.5	26.70
T46	4.5	3.0	38.55

T47	4.0	3.0	38.93
T48	3.5	3.0	39.66
T49	3.0	3.0	40.70
T50	2.5	3.0	41.99
T51	2.0	3.0	43.42
T52	1.5	3.0	44.82
T53	1.0	3.0	45.94
T54	0.5	3.0	46.44
T55	4.5	3.5	29.14
T56	4.0	3.5	28.89
T57	3.5	3.5	28.00
T58	3.0	3.5	26.05
T59	2.5	3.5	22.53
T60	2.0	3.5	17.17
T61	1.5	3.5	9.76
T62	4.5	4.0	38.15
T63	4.0	4.0	35.44
T64	3.5	4.0	30.19
T65	3.0	4.0	24.06
T66	2.5	4.0	16.99
T67	2.0	4.0	8.96
T68	4.5	4.5	5.17
T69	4.0	4.5	3.19

```
C***********************************************
C
C   OREGON STATE UNIVERSITY
C   COLLEGE OF OCEANOGRAPHY
C
C   NAME OF PROGRAM:      ORHEAT.ZZC
C   OBJECT OF PROGRAM:    TWO-DIMENSIONAL NUMERICAL MODEL FOR
C                         TEMPERATURE DISTRIBUTION BY FINITE
C                         DIFFERENCE METHOD
C   PROGRAM LANGUAGE:     FORTRAN 77
C   AUTHOR:               M. W. HAN
C   VERSION DATE:         JUNE 17,1987
C   TYPE OF COMPUTER:     PRIME
C***********************************************************************
C
C
C    DEFINITION OF VARIABLES:
C    P: DENSITY OF VENTING PORE FLUIDS
C    G: SPECIFIC HEAT OF VENTING PORE FLUIDS
C    U: ADVECTION RATE OF VENTING PORE FLUIDS
C    Q: THERMAL CONDUCTIVITY OF HEAT IN Y-DIRECTION
C    R: RATIO OF CONDUCTIVITY IN X-DIRECITON TO Y-DIRECTION
C    AB: COEFFICIENT MATRIX
C    NDIM: FIRST DIMENSION OF MATRIX AB
C    N: NUMBER OF GRID POINTS IN THE X-DIRECTION
C    M: NUMBER OF GRID POINTS IN THE Y-DIRECTION
C    BT: BASEMENT TEMPERATURE
C    BV: COLUMN MATRIX FOR R.H.S. VECTORS
C    NN: NUMBER OF LINEAR EQUATIONS
C    A,B,C,D,E: COEFFICIENTS IN THE MATRIX AB
C    T: COLUMN MATRIX FOR TEMPERATURE VECTORS
C
C***********************************************************************
```

```
C                    MAIN PROGRAM
C*********************************************************************
      DIMENSION AB(70,70),A(7,2),B(7,2),C(7,2),D(7,2)
      DIMENSION U(2),Q(7),T(70),BV(70),BT(9),X(69),Y(69)
      DIMENSION A1(7,2),B1(7,2),C1(7,2),D1(7,2)
      OPEN (5,FILE='INPUT.ZZC')
      OPEN (6,FILE='OUTPUT.ZZC')
      READ (5,60) P,G,R,TOL
      READ (5,80) (Q(I), I=1,7)
      READ (5,85) (BT(I), I=1,9)
      READ (5,90) N,M,NN,NDIM,NITER
C     P*G*U(J=1)=P*G*U(J=2)=320.0 FOR U=1 CM YR
C     P*G*U(J=1)=P*G*U(J=2)=3200.0 FOR U=10 CM/YR
C     P*G*U(J=1)=P*G*U(J=2)=6400.0 FOR U=20 CM/YR
      DO 15 J=1,2
      DO 10 I=1,7
        A(I,J)=4.*R+320./Q(I)
        B(I,J)=4.*R-320./Q(I)
        C(I,J)=4.-320./Q(I)
        D(I,J)=4.+320./Q(I)
   10 CONTINUE
   15 CONTINUE
      DO 17 J=1,2
      DO 16 I=1,7
        A1(I,J)=4.*R+6400./Q(I)
        B1(I,J)=4.*R-6400./Q(I)
        C1(I,J)=4.-6400./Q(I)
        D1(I,J)=4.+6400./Q(I)
   16 CONTINUE
   17 CONTINUE
      E=-8.*(R+1)
      NP1=N+1
C
```

```
C    INITIALIZE MATRIX AB WITH ZEROS
     DO 25 I=1,NDIM
     DO 20 J=1,NDIM
       AB(I,J)=0.0
  20 CONTINUE
  25 CONTINUE
C
C    INSERT R.H.S VECTORS AS A COLUMN MATRIX BV
     DO 30 I=1,N
     BV(I)=-D(1,1)*BT(I)
  30 CONTINUE
     DO 35 I=NP1,NDIM
     BV(I)=0.
  35 CONTINUE
C    INPUT INITIAL GUESS FOR T
     DO 36 I=1,9
     T(I)=48.
  36 CONTINUE
     DO 37 I=10,18
     T(I)=28.
  37 CONTINUE
     DO 38 I=19,36
     T(I)=18.
  38 CONTINUE
     DO 39 I=37,69
     T(I)=8.
  39 CONTINUE
C
C    FORMULATE THE COEFFICIENT OF MATRIX AB
     CALL COMAT(AB,NDIM,N,A,B,C,D,E,A1,B1,C1,D1)
C
C    SOLVE N LINEAR EQUATIONS BY GAUSS-SEIDEL ITERATION
     CALL GSITRN (AB,BV,T,NN,NDIM,NITER,TOL)
```

```
      CALL GSITRN (AB,BV,T,NN,NDIM,NITER,TOL)
C
C     PRINT THE RESULTS
      X(1)=4.5
      DO 41 I=2,9
      X(I)=X(I-1)-0.5
   41 CONTINUE
      DO 42 I=10,61
      X(I)=X(I-9)
   42 CONTINUE
      DO 43 I=62,67
      X(I)=X(I-7)
   43 CONTINUE
      X(68)=X(62)
      X(69)=X(63)
      DO 44 I=1,9
      Y(I)=0.5
   44 CONTINUE
      DO 45 I=10,18
      Y(I)=1.0
   45 CONTINUE
      DO 46 I=19,27
      Y(I)=1.5
   46 CONTINUE
      DO 47 I=28,36
      Y(I)=2.0
   47 CONTINUE
      DO 48 I=37,45
      Y(I)=2.5
   48 CONTINUE
      DO 49 I=46,54
      Y(I)=3.0
   49 CONTINUE
```

```
      Y(I)=3.5
   50 CONTINUE
      DO 51 I=62,67
      Y(I)=4.0
   51 CONTINUE
      Y(68)=4.5
      Y(69)=4.5
      WRITE (6,95)
      DO 40 I=1,NN
      WRITE (6,100) I,X(I),Y(I),T(I)
   40 CONTINUE
   60 FORMAT (E7.1,F4.1,F6.1,F6.3)
   80 FORMAT (7(F7.3,1X))
   85 FORMAT (9(F5.1,1X))
   90 FORMAT (4(I2,1X),I3)
   95 FORMAT ('NODE NO.  X (Km)  Y(Km)    T C')
  100 FORMAT (2X,'T',I2,F10.1,F8.1,F12.2)
      STOP
      END
C
C*************************************************************************
      SUBROUTINE COMAT (AB,NDIM,N,A,B,C,D,E,A1,B1,C1,D1)
C
C     THIS SUBROUTINE FORMS THE COEFFICIENT MATRIX FOR THE TWO-
C     DIMENSIONAL CONVECTION-ADVECTION HEAT FLOW EQUATION ON A
C     REGION THAT HAS N POINTS IN THE X DIRECTION AND M POINTS
C     IN THE Y DIRECTION.
C
C     PARAMETERS ARE:
C     AB : MATRIX THAT RETURNS COEFFICIENTS
C     NDIM:FIRST DIMENSION OF AB IN THE MAIN PROGRAM
C     N: NUMBER OF GRID POINTS IN THE X DIRECTION
C     M: NUMBER OF GRID POINTS IN THE Y DIRECTION
```

```
C     N: NUMBER OF GRID POINTS IN THE X DIRECTION
C     M: NUMBER OF GRID POINTS IN THE Y DIRECTION
C
      DIMENSION AB(NDIM,NDIM),A(7,2),B(7,2),C(7,2),D(7,2)
      DIMENSION A1(7,2),B1(7,2),C1(7,2),D1(7,2)
C
C     FIRST LET'S COMPUTE SOME CONSTANTS
      NL1=N-1
      NP1=N+1
      NP2=NP1+NL1
      NP3=NP2+1
      NP4=NP3+NL1
      NP5=NP4+1
      NP6=NP5+NL1
      NP7=NP6+1
      NP8=NP7+NL1
      NP9=NP8+1
      NP10=NP9+NL1
C
C     PUT COEFFICIENT E FOR THE DIAGONAL
      DO 10 I=1,NDIM
        AB(I,I)=E
 10   CONTINUE
C
C     NOW PUT COEFFICIENT A AND B FOR THE ABOVE- AND BELOW-
C     DIAGONAL RESPECTIVELY
      DO 11 I=2,N
        AB(I-1,I)=A(1,1)
        AB(I,I-1)=B(1,1)
 11   CONTINUE
      DO 12 I=NP1,NP2
        AB(I-1,I)=A(2,1)
        AB(I,I-1)=B(2,1)
```

```
 12   CONTINUE
      DO 13 I=NP3,NP4
       AB(I-1,I)=A(3,2)
       AB(I,I-1)=B(3,2)
 13   CONTINUE
      DO 14 I=NP5,NP6
       AB(I-1,I)=A(4,2)
       AB(I,I-1)=B(4,2)
 14   CONTINUE
      DO 15 I=NP7,NP8
       AB(I-1,I)=A(5,2)
       AB(I,I-1)=B(5,2)
 15   CONTINUE
      DO 16 I=NP9,61
       AB(I-1,I)=A(6,2)
       AB(I,I-1)=B(6,2)
 16   CONTINUE
      DO 17 I=62,NDIM
       AB(I-1,I)=A(7,2)
       AB(I,I-1)=B(7,2)
 17   CONTINUE
C
C     NOW REPLACE SOME A AND B WITH ZEROS
      DO 20 I=N,NP10,N
       AB(I,I+1)=0.
       AB(I+1,I)=0.
 20   CONTINUE
       AB(62,61)=0.
       AB(68,67)=0.
       AB(61,62)=0.
       AB(67,68)=0.
C
C     NOW REPLACE SOME DIAGONAL WITH E+A OR E+B
```

```
      AB(1,1)=E+B(1,1)
      AB(9,9)=E+A(1,1)
      AB(10,10)=E+B(2,1)
      AB(18,18)=E+A(2,1)
      AB(19,19)=E+B(3,1)
      AB(27,27)=E+A(3,2)
      AB(28,28)=E+B(4,2)
      AB(36,36)=E+A(4,2)
      AB(37,37)=E+B(5,2)
      AB(45,45)=E+A(5,2)
      AB(46,46)=E+B(6,2)
      AB(54,54)=E+A(6,2)
      AB(55,55)=E+B(6,2)
      AB(62,62)=E+B(7,2)
      AB(68,68)=E+B(7,2)
C
C     PUT C AND D IN THE SIDE BANDS
      DO 30 I=NP1,NP2
       AB(I,I-N)=D(2,1)
       AB(I-N,I)=C(2,1)
 30   CONTINUE
      DO 31 I=NP3,NP4
       AB(I,I-N)=D(3,2)
       AB(I-N,I)=C(3,2)
 31   CONTINUE
      DO 32 I=NP5,NP6
       AB(I,I-N)=D(4,2)
       AB(I-N,I)=C(4,2)
 32   CONTINUE
      DO 33 I=NP7,NP8
       AB(I,I-N)=D(5,2)
       AB(I-N,I)=C(5,2)
 33   CONTINUE
```

```
      DO 34 I=NP9,61
        AB(I,I-N)=D(6,2)
        AB(I-N,I)=C(6,2)
34    CONTINUE
      DO 35 I=62,NDIM
        AB(I,I-N)=D(7,2)
        AB(I-N,I)=C(7,2)
35    CONTINUE
        AB(62,68)=C(7,2)
        AB(63,69)=C(7,2)
C     REPLACE SOME C WITH ZEROS
        AB(53,62)=0.
        AB(54,63)=0.
C     NOW REPLACE A,B,C,D CORRESPONDING TO THE CONFINED ADVECTION
C     PATHWAYS (NODES)
      AB(1,2)=A1(1,1)
      AB(1,10)=C1(1,1)
      AB(2,3)=A1(1,1)
      AB(2,1)=B1(1,1)
      AB(2,11)=C1(1,1)
      AB(3,2)=B1(1,1)
      AB(3,12)=C1(1,1)
      AB(10,11)=A1(2,1)
      AB(10,1)=D1(2,1)
      AB(11,12)=A1(2,1)
      AB(11,10)=B1(2,1)
      AB(11,20)=C1(2,1)
      AB(11,2)=D1(2,1)
      AB(12,11)=B1(2,1)
      AB(12,21)=C1(2,1)
      AB(12,3)=D1(2,1)
      AB(20,21)=A1(3,2)
      AB(20,11)=D1(3,2)
```

AB(21,22)=A1(3,2)

AB(21,20)=B1(3,2)

AB(21,30)=C1(3,2)

AB(21,12)=D1(3,2)

AB(22,21)=B1(3,2)

AB(22,31)=C1(3,2)

AB(30,31)=A1(4,2)

AB(30,21)=D1(4,2)

AB(31,32)=A1(4,2)

AB(31,30)=B1(4,2)

AB(31,40)=C1(4,2)

AB(31,22)=D1(4,2)

AB(32,31)=B1(4,2)

AB(32,41)=C1(4,2)

AB(37,38)=A1(5,2)

AB(37,46)=C1(5,2)

AB(38,37)=B1(5,2)

AB(38,47)=C1(5,2)

AB(40,41)=A1(5,2)

AB(40,31)=D1(5,2)

AB(41,42)=A1(5,2)

AB(41,40)=B1(5,2)

AB(41,50)=C1(5,2)

AB(41,32)=D1(5,2)

AB(42,41)=B1(5,2)

AB(42,51)=C1(5,2)

AB(46,47)=A1(6,2)

AB(46,37)=D1(6,2)

AB(47,46)=B1(6,2)

AB(47,56)=C1(6,2)

AB(47,38)=D1(6,2)

AB(50,51)=A1(6,2)

AB(50,59)=C1(6,2)

```
      AB(50,41)=D1(6,2)
      AB(51,52)=A1(6,2)
      AB(51,50)=B1(6,2)
      AB(51,60)=C1(6,2)
      AB(51,42)=D1(6,2)
      AB(52,51)=B1(6,2)
      AB(52,61)=C1(6,2)
      AB(56,57)=A1(6,2)
      AB(56,63)=C1(6,2)
      AB(56,47)=D1(6,2)
      AB(57,56)=B1(6,2)
      AB(57,64)=C1(6,2)
      AB(59,60)=A1(6,2)
      AB(59,50)=D1(6,2)
      AB(60,61)=A1(6,2)
      AB(60,59)=B1(6,2)
      AB(60,51)=D1(6,2)
      AB(61,60)=B1(6,2)
      AB(61,52)=C1(6,2)
      AB(63,64)=A1(7,2)
      AB(63,56)=D1(7,2)
      AB(64,63)=B1(7,2)
      AB(64,57)=D1(7,2)
        RETURN
        END
C
C*************************************************************************
      SUBROUTINE GSITRN (AB,BV,T,NN,NDIM,NITER,TOL)
      DIMENSION AB(NN,NN),BV(NN),T(NN)
      DO 10 I=1,NN
        SAVE=AB(I,I)
        BV(I)=BV(I)/SAVE
        DO 7 J=1,NN
```

```
      AB(I,J)=AB(I,J)/SAVE
 7  CONTINUE
10  CONTINUE
    DO 40 ITER=1,NITER
    TMAX=0.
    DO 30 I=1,NN
    SAVE=T(I)
    T(I)=BV(I)
    DO 20 J=1,NN
    IF (J .NE. I) THEN
    T(I)=T(I)-AB(I,J)*T(J)
    END IF
20  CONTINUE
    IF (ABS(T(I)-SAVE) .GT. TMAX) THEN
    TMAX=ABS(T(I)-SAVE)
    END IF
30  CONTINUE
    IF (TMAX .LE. TOL) RETURN
40  CONTINUE
    PRINT 200, TOL,NITER
200 FORMAT(/'DID NOT MEET TOLERANCE OF ',E14.6,' IN ',I4,
   1    ' ITERATIONS'/' LAST VALUE OF T WAS RETURNED TO CALLER')
    RETURN
    END
```

1.0E+15 1.0 50.0 0.01

571.429 476.190 380.952 333.333 285.714 238.095 190.476

144.0 146.0 148.0 150.0 152.0 154.0 156.0 158.0 160.0

9 9 69 69 400

NODE NO.	X (Km)	Y(Km)	T C
T 1	4.5	0.5	32.72
T 2	4.0	0.5	32.47
T 3	3.5	0.5	33.44
T 4	3.0	0.5	37.27
T 5	2.5	0.5	40.35
T 6	2.0	0.5	42.76
T 7	1.5	0.5	44.55
T 8	1.0	0.5	45.74
T 9	0.5	0.5	46.35
T10	4.5	1.0	45.13
T11	4.0	1.0	40.82
T12	3.5	1.0	37.81
T13	3.0	1.0	37.72
T14	2.5	1.0	37.78
T15	2.0	1.0	37.90
T16	1.5	1.0	38.04
T17	1.0	1.0	38.16
T18	0.5	1.0	38.22
T19	4.5	1.5	42.32
T20	4.0	1.5	42.35
T21	3.5	1.5	36.37
T22	3.0	1.5	31.30
T23	2.5	1.5	31.61
T24	2.0	1.5	31.84
T25	1.5	1.5	32.01
T26	1.0	1.5	32.12
T27	0.5	1.5	32.17
T28	4.5	2.0	37.67
T29	4.0	2.0	37.93
T30	3.5	2.0	38.44
T31	3.0	2.0	33.02
T32	2.5	2.0	27.94
T33	2.0	2.0	27.67
T34	1.5	2.0	27.49
T35	1.0	2.0	27.38
T36	0.5	2.0	27.33
T37	4.5	2.5	14.19
T38	4.0	2.5	14.70
T39	3.5	2.5	18.39
T40	3.0	2.5	21.50
T41	2.5	2.5	18.82
T42	2.0	2.5	15.85
T43	1.5	2.5	16.54
T44	1.0	2.5	16.97
T45	0.5	2.5	17.19
T46	4.5	3.0	26.80

T47	4.0	3.0	22.64
T48	3.5	3.0	22.15
T49	3.0	3.0	21.91
T50	2.5	3.0	21.84
T51	2.0	3.0	18.67
T52	1.5	3.0	15.51
T53	1.0	3.0	15.20
T54	0.5	3.0	15.06
T55	4.5	3.5	14.01
T56	4.0	3.5	13.71
T57	3.5	3.5	10.93
T58	3.0	3.5	11.18
T59	2.5	3.5	11.25
T60	2.0	3.5	7.47
T61	1.5	3.5	2.30
T62	4.5	4.0	16.84
T63	4.0	4.0	17.09
T64	3.5	4.0	12.97
T65	3.0	4.0	9.71
T66	2.5	4.0	6.52
T67	2.0	4.0	3.32
T68	4.5	4.5	0.76
T69	4.0	4.5	0.47